UCLA
UCLA Electronic Theses and Dissertations

Title

Analyzing the Rest-frame Optical Emission-line and Host Galaxy Properties of ? ~ 2 Star-forming Galaxies in the MOSDEF Survey

Permalink

https://escholarship.org/uc/item/3h597829

Author

Runco, Jordan Nathaniel

Publication Date

2022

Peer reviewed|Thesis/dissertation

eScholarship.org Powered by the California Digital Library
University of California

UNIVERSITY OF CALIFORNIA

Los Angeles

Analyzing the Rest-frame Optical Emission-line and Host Galaxy Properties of $z \sim 2$ Star-forming Galaxies in the MOSDEF Survey

A dissertation submitted in partial satisfaction
of the requirements for the degree
Doctor of Philosophy in Astronomy and Astrophysics

by

Jordan Nathaniel Runco

2022

© Copyright by

Jordan Nathaniel Runco

2022

ABSTRACT OF THE DISSERTATION

Analyzing the Rest-frame Optical Emission-line and Host Galaxy Properties of $z \sim 2$ Star-forming Galaxies in the MOSDEF Survey

by

Jordan Nathaniel Runco
Doctor of Philosophy in Astronomy and Astrophysics
University of California, Los Angeles, 2022
Professor Alice E. Shapley, Chair

The study of galaxies across multiple epochs is essential for understanding the evolution of the universe. One key time period to study is $z \sim 2$, when star formation activity in the universe is at its peak. Comparing local galaxies to those in this more active time period is a critical way to learn about galaxy evolution by examining the differences and/or similarities in galaxy properties. In this thesis, I study the rest-frame optical emission-line and host galaxy properties of star-forming galaxies at $z \sim 2$ in the MOSFIRE Deep Evolution Field (MOSDEF) survey to better understand the evolution of galaxies over the past 10 Gyr of our universe's history.

First, I investigate correlations between the emission-line properties and the physical and chemical properties of $z \sim 2$ star-forming galaxies in the MOSDEF survey. It is necessary to understand the known offset of $z > 1$ galaxies on the [O III]λ5008/Hβ vs. [N II]λ6585/Hα ([N II] "BPT") diagram compared to their local counterparts because strong rest-optical emission-lines are commonly used to infer a variety of galaxy properties (e.g. gas-phase oxygen abundance). To investigate the physical driver of this shift, I defined two populations of $z \sim 2$ MOSDEF galaxies on the [N II] BPT diagram, one *on* and one *off* (i.e., offset from) the local sequence. I find that these two groups

remain separated on the [O III]λ5008/Hβ vs. [S II]$\lambda\lambda$6718,6733/Hα ([S II] BPT) diagram and the [O III]$\lambda\lambda$4960,5008/[O II]$\lambda\lambda$3727,3730 vs. ([O III]$\lambda\lambda$4960,5008+[O II]$\lambda\lambda$3727,3730)/Hβ (O_{32} vs. R_{23}) diagram, which suggests that star-forming regions in the more offset galaxies are characterized by harder ionizing spectra at fixed nebular oxygen abundance. Such a phenomenon may be tied to α-enhancement and massive stars that are chemically "young."

Second, I compare the $z \sim 2$ MOSDEF survey with the $z \sim 2$ portion of the Keck Baryonic Structure Survey (KBSS) that has been observed with MOSFIRE. Like MOSDEF, KBSS studies a large sample of star-forming galaxies at $z \sim 2$ with the MOSFIRE instrument; however, there are notable differences in survey construction and key results (e.g., the magnitude of the offset from the local star-forming sequence on the [N II] BPT diagram). Using consistent spectral-energy-distribution (SED) modeling for both surveys reveals that the MOSDEF $z \sim 2$ targeted sample has a higher median stellar mass, lower star-formation rate (SFR) and specific SFR, and redder U$-$V color compared to KBSS. However, the subsets of the surveys that have been analyzed in previous work with high S/N spectra and multiple emission lines detected are strikingly similar. Aside from stellar population age, all sample properties investigated agree within the median uncertainties. Additionally, applying uniform stellar Balmer absorption correction and emission-line fitting techniques for both samples results in the same offset on the [N II] BPT diagram. I find that the previously believed differences in key results between the two surveys can be attributed to utilizing different SED and emission-line fitting techniques.

Third, I analyze the completeness of the MOSDEF $z \sim 2$ survey. Specifically, I use SED modeling and composite spectra created from spectral stacking to test if the subset of the MOSDEF $z \sim 2$ star-forming galaxies with high S/N spectra is representative of the complete sample of star-forming galaxies. I find that the host galaxy and emission-line properties (most notably offset from the local SDSS sequence on the [N II] BPT diagram) are very similar, indicating that the smaller spectroscopic samples are representative of the full catalog of star-forming galaxies. Additionally, comparing galaxy properties obtained through SED modeling reveals that the $z \sim 2$ sample observed

by MOSDEF is representative of all $z \sim 2$ galaxies that met the selection criteria for the MOSDEF survey. Taken together, these results reveal that the emission-line trends established using high S/N $z \sim 2$ detection samples of star-forming galaxies in MOSDEF studies to date are representative of the rest-optical-magnitude-limited star-forming galaxy population at $z \sim 2$.

Fourth, I focus on two actively merging galaxies in the MOSDEF survey at $z = 1.89$. We model the SEDs of the merging galaxies to find that they are both massive with low SFRs and similar stellar population ages. Additionally, the star formation in both galaxies began and peaked within a few hundred Myr of each other, suggesting that their bursts of star formation may be connected. For one of these galaxies, GOODS-S 43114, Sérsic profile fitting and a relatively low velocity dispersion estimate indicates that it is a face-on disk; therefore, it will likely undergo a large structural change as it evolves into a massive, slowly-rotating elliptical galaxy in the present day.

Finally, as an earlier part of research I used far-IR *Herschel*/PACS spectra to investigate the profiles of six OH doublets for a large sample of 178 local galaxies. I assembled ancillary data to probe AGN luminosity, radiation field hardness, dust temperature, and dust obscuration, and find correlations between the EW(OH) and these galaxy observables. Additionally, I comment on how the origin of emission for these OH doublets, whether from radiative pumping by infrared photons or from collisional excitation, may influence these relationships.

The dissertation of Jordan Nathaniel Runco is approved.

Jean L. Turner

Steven R. Furlanetto

Matthew A. Malkan

Alice E. Shapley, Committee Chair

University of California, Los Angeles

2022

For Maren Cosens: my best friend, life partner, and quarantine buddy.

TABLE OF CONTENTS

1 Introduction **1**

1.1 The Complete MOSDEF Survey 4

1.2 The MOSDEF & KBSS Collaboration 7

1.3 Probing MOSDEF Completeness 9

1.4 A Merger at $z = 1.89$ 11

1.5 Local OH Spectroscopy 13

1.6 Roadmap 14

2 The MOSDEF Survey: A Comprehensive Analysis of the Rest-optical Emission-line Properties of $z \sim 2.3$ Star-forming Galaxies **16**

2.1 Introduction 16

2.2 Methods 20

2.2.1 MOSDEF Sample & Ancillary Measurements 20

2.2.2 SDSS Comparison Sample 23

2.3 Results 24

2.3.1 The [N II] BPT Diagram 24

2.3.2 Dividing the $z \sim 2.3$ Sample in the [N II] BPT Diagram 25

2.4 Discussion 32

2.4.1 Comparison with Previous Work 32

2.4.2 Comparison with Photoionization Models 33

2.5 Summary 47

3 Reconciling the Results of the $z \sim 2$ MOSDEF and KBSS-MOSFIRE Surveys **50**

3.1 Introduction 50

3.2 Observations & Sample Selection 54

3.2.1 The MOSDEF Survey 54

3.2.2 The KBSS Survey . . . 57
3.2.3 MOSDEF & KBSS Sample Comparison . . . 61
3.2.4 MOSDEF Sample Incompleteness . . . 63
3.2.5 SDSS Comparison Sample . . . 65
3.3 Methodology . . . 65
3.3.1 SED Fitting . . . 66
3.3.2 Emission-line Measurements . . . 68
3.4 The Physical Properties of the $z \sim 2$ Spectroscopic Samples . . . 69
3.4.1 SED Fitting Properties . . . 69
3.4.2 The [N II] BPT Diagram . . . 76
3.4.3 The [S II] BPT Diagram . . . 78
3.5 Discussion . . . 79
3.5.1 The [N II] BPT Offset . . . 80
3.5.2 SED Properties of MOSDEF and KBSS $z \sim 2$ Targeted Samples . . . 82
3.6 Summary . . . 89
3A CSF Modeling . . . 93
3B Emission-line Fitting Examples . . . 102

4 Towards a Complete Census of the $z \sim 2.3$ Star-forming Galaxy Population . . . 105
4.1 Introduction . . . 105
4.2 Observations, Sample Selection, & Methods . . . 110
4.2.1 The MOSDEF Survey . . . 110
4.2.2 SED Fitting and Derived Properties . . . 114
4.2.3 Emission-line Fitting . . . 117
4.2.4 Spectral Stacking . . . 117
4.2.5 SDSS Comparison Sample . . . 119
4.3 Results . . . 119
4.3.1 Stacking on the BPT diagrams . . . 120

4.3.2 Physical Properties of the Stacks . . . 122
4.3.3 Comparison of the $z \sim 2$ Parent and Observed Samples . . . 129
4.4 Discussion . . . 132
4.4.1 MOSDEF $z \sim 2$ Star-forming Galaxy Completeness . . . 132
4.4.2 MOSDEF $z \sim 2$ Observed Sample Completeness . . . 134
4.5 Summary . . . 137

5 A Remarkable $z = 1.89$ Merger . . . 140
5.1 Introduction . . . 140
5.2 Observations & Methods . . . 142
5.2.1 The MOSDEF Survey . . . 142
5.2.2 GOODS-S 43114 & GOODS-S 43683 Observations . . . 143
5.2.3 SED Fitting & Derived Properties . . . 145
5.2.4 SDSS Comparison Sample . . . 147
5.3 Results . . . 147
5.4 Discussion . . . 153
5.4.1 State of the Merger . . . 153
5.4.2 Implications of the Apparent Mass Discrepancy . . . 155
5.5 Summary . . . 156

6 *Herschel*/PACS OH Spectroscopy of Seyfert, LINER, and Starburst Galaxies . . . 159
6.1 Introduction . . . 159
6.2 Observations . . . 161
6.2.1 *Herschel*/PACS . . . 162
6.2.2 Galaxy Brightness & IR Line Ratios . . . 166
6.2.3 IRAS . . . 167
6.2.4 Obscuration Tracers . . . 169
6.3 Analysis & Results . . . 169

6.3.1 Measuring EW . . . 170
6.3.2 Comments on the Sample . . . 172
6.3.3 EW(OH) vs. AGN Luminosity and Radiation Field Hardness . . . 177
6.3.4 EW(OH) vs. 25-60 Color Temperature . . . 186
6.3.5 EW vs. Dust Obscuration . . . 187
6.3.6 Bivariate Linear Regression Test for EW(OH) . . . 191
6.3.7 OH79 vs. OH119 . . . 192
6.3.8 OH79 vs. OH163 . . . 193
6.4 Discussion and Interpretations . . . 194
6.4.1 OH Level Populations & the Mechanisms which Control them . . . 194
6.4.2 Interpretation of the Obscuration & Column density . . . 200
6.5 Summary . . . 201
6A Data Tables . . . 204
6B Fitting Statistics . . . 239
6C Supplemental Figures . . . 244

7 Conclusions . . . 250

LIST OF FIGURES

1.1 From Madau & Dickinson (2014): the evolution of the global star-formation rate density in the universe. The left axis shows the number of stellar masses produced in stars per year per Mpc^3 volume of space. The bottom axis shows the redshift. The top axis shows the lookback time in Gyr that corresponds to the redshift on the bottom axis. The plot shows both dust-corrected rest-frame far-ultraviolet, FUV, (green, blue, and pink) and IR (red and orange) data points. The black curve is a fit to the combined FUV and IR data. 2

1.2 From Kewley et al. (2013): a cartoon diagram showing how changing individual galaxy properties affects the observed sequence of galaxies on the [N II] BPT diagram. The properties shown are H II region ionizing spectra at fixed metallicities (EUV), H II region ionization parameter (q), H II region electron densities (n_e), and gas-phase N/O abundance ratio differences. It is shown that all of these properties can potentially be the driver of the $z > 1$ galaxy offset from the local SDSS sequence. 5

1.3 From Pettini & Pagel (2004): gas phase oxygen metallicity (i.e., 12+log(O/H)) vs. [N II]λ6585/Hα for local ($z \sim 0$) H II regions. This diagram shows at there is a clear correlation between nebular metallicity and emission-line ratio strength in the local universe. Using relationships such as this, it is possible to predict nebular metallicty when a direct measurement is not available. Due to differences in emission-line ratio sequences between $z \sim 0$ and $z \sim 2$ galaxies, it is currently unclear if these local calibrations can be used at high redshift. 6

1.4 The [N II] BPT diagram for the MOSDEF (left) and KBSS-MOSFIRE (right) $z \sim 2$ samples. Both samples are offset from the local $z \sim 0$ SDSS sequence; however, the difference in the magnitude of the offsets from previous studies is ~0.1 dex (Steidel et al., 2014; Shapley et al., 2015). 8

1.5 *HST* WFC3 image of GOODS-S 43114 and GOODS-S 43683 (labeled FW-4871 and FW-4887, respectively, in the image), reproduced from van Dokkum & Brammer (2010). The central regions of both galaxies are identified by red circles. Merger features such as diffuse, tidally-induced spiral tails and arms are visible in both galaxies. 12

2.1 Redshift distribution of the 180 star-forming MOSDEF galaxies at $z \sim 2.3$ with [N II] BPT diagram classifications (i.e., S/N $\geq$ 3 detections in Hβ, [O III]$\lambda\lambda$4960,5008, Hα, and [N II]λ6585). The dashed vertical line displays the median redshift of the sample, $z_{\rm med} = 2.29$. 22

2.2 [N II] BPT diagram. Green points indicate $1.9 \leq z \leq 2.7$ MOSDEF galaxies with S/N $\geq$ 3 for all four plotted emission-lines. Large magenta stars represent measurements of stacks from composite spectra, binned by stellar mass, for $1.9 \leq z \leq 2.7$ MOSDEF galaxies. The grayscale 2D histogram indicates local SDSS galaxies. The cyan curve is the fit to the MOSDEF sample from Shapley et al. (2015). The orange curve is a fit to the $z \sim 0$ star-forming locus (Kewley et al., 2013). The red curve is the best fit to the $z \sim 2.3$ galaxies from the Keck Baryonic Structure Survey (KBSS; Steidel et al. 2014). The black curve is the maximum starburst line from Kewley et al. (2001). The blue curve is the empirical AGN/star-forming galaxy dividing line from Kauffmann et al. (2003). 25

2.3 The sample of 122 MOSDEF galaxies that have $\geq 3\sigma$ detections in [O II]$\lambda\lambda$3727,3730, Hβ, [O III]$\lambda\lambda$4960,5008, Hα, [N II]λ6585, and [S II]$\lambda\lambda$6718,6733. Top left: we modify the MOSDEF fit from Shapley et al. (2015) by altering the y-intercept, so a curve with the same functional form splits the data set evenly into two populations. The red galaxies (*low* sample) fall close to the local SDSS sequence, while the blue galaxies (*high* sample) are shifted off the local sequence. Top right: The same two groups of data points as in the left panel. The red and blue lines indicate binned medians as described in Section 2.3.2. These lines show that the two groups are also separated in the [S II] BPT diagram, with the *high* sample higher in S2 and/or O3 than the *low* sample. Bottom center: The same two groups of data points as in the top panels. The red and blue lines again indicate binned medians as described in Section 2.3.2. The two groups are segregated in the O_{32} vs. R_{23} diagram as well, with the *high* sample having a higher median R_{23} values at fixed O_{32} where there is overlap in O_{32}. 27

2.4 Distribution of physical properties for the 122 galaxy MOSDEF sample shown in Figure 2.3 where the blue and red bins correspond to the *high* and *low* samples, respectively. The green lines are the median values for the *high* population, while the yellow lines are the median values for the *low* population. The median values with uncertainties for both populations are given in Table 2.1. The following galaxy properties are shown: **(a)** M_*, **(b)** $\log(t/\tau)$ of the stellar population using a delayed-τ star formation model, **(c)** t of the stellar population assuming a constant star formation history, **(d)** SFR(Hα), **(e)** sSFR, **(f)** $\Sigma_{\rm SFR}$, **(g)** $R_{\rm e}$, and **(h)** $n_{\rm e}$ estimated from the [O II] or [S II] doublet emission-lines. We find that the median M_*, sSFR, $\Sigma_{\rm SFR}$, and $R_{\rm e}$ differ significantly based on their location in the [N II] BPT Diagram, while the other properties are the within the uncertainties of each other. 30

2.5 Left column: $Z_* = 0.001$ (solid lines). Right column: $Z_* = 0.002$ (dashed lines). Cloudy+BPASS model emission-line ratios shown on the [N II] BPT (top row), [S II] BPT (middle row), and O_{32} vs. R_{23} diagrams (bottom row). The triangle data points on the curves increase in size as log(U) increases. To avoid overcrowding, we vary log(U) in steps of 0.20 dex and have nebular metallicity range between $-0.60 \leq$ 12+log(O/H) ≤ 0.20 in 0.10 dex steps, with additional values that extend deeper into the subsolar regime included as well (-0.80, -1.00, and -1.30). We adopt an age of $10^{8.6}$ yr because it is the approximate median age of the MOSDEF sample (given a constant star-formation history), but the results are not sensitive to age. Also plotted are the local SDSS sample (grey 2D histogram) and the *high* (blue points) and *low* (red points) MOSDEF samples with binned medians as shown in Figure 2.3. The green and yellow squares, with associated uncertainties, are the median values of the *high* and *low* populations. 36

2.6 Corner plots comparing the distributions of 12+log(O/H) and log(U) for the *high* (blue) and *low* (red) MOSDEF populations. The distributions for the sample median points, i.e. green and yellow squares in Figure 2.5, (upper left), large-N2 endpoint of the sample binned medians (top right) and small-N2 endpoint of the sample binned medians (bottom center) are included. We assume Z_* values of 0.001 and 0.002 (median points; top left panel), 0.002 and 0.003 (large-N2 points; top right panel), and 0.001 and 0.001 (low-N2 points; bottom panel) for the *high* and *low* populations, respectively. The dashed lines on the histograms mark the median value and 1σ uncertainties (16^{th} and 84^{th} percentiles) for the distributions of 12+log(O/H) and log(U), and the three contours on the diagonal mark the 1, 1.5, and 2σ regions in the 2-D 12+log(O/H)-log(U) parameter space. It is shown that moving from large- to small-N2 corresponds to decreasing nebular metallicity and increasing ionization parameter. In each of the three distributions, the *high* population has a higher 12+log(O/H) and log(U). 38

2.7 Left column: $Z_* = 0.0001$, $n_e = 250$ cm^{-3} (dotted lines). Right column: $Z_* = 0.001$, $n_e = 1000$ cm^{-3} (dot-dashed lines). Cloudy+BPASS model emission-line ratios shown on the [N II] BPT (top row), [S II] BPT (middle row), and O_{32} vs. R_{23} diagrams (bottom row). A comparison of these models with the corresponding panels in Figure 2.5 shows how raising the electron density and lowering stellar metallicity affects the predicted emission-line ratios. The correspondence between colors and symbol size and, respectively, 12+log(O/H) and log(U), matches that in Figure 2.5. Once again, we adopt an age of $10^{8.6}$ yr because it is the approximate median age of the MOSDEF sample (given a constant star-formation history) and include the local SDSS sample (grey 2D histogram), the *high* (blue) sample, and *low* (red) sample with binned medians as shown in Figure 2.3. The green and yellow squares, with associated uncertainties, are the median values of the *high* and *low* populations as shown in Figure 2.5. Aside from at roughly solar and supersolar nebular metallicities, a higher electron density has a minimal affect on the Cloudy+BPASS model grids and cannot reach the elevated O3 and O_{32} galaxies. A lower stellar metallicity is able to reach these values, suggesting that the most offset galaxies have the hardest ionizing spectrum. 46

3.1 Top: Redshift histograms. Shown in these panels are distributions of galaxies at $1.9 \leq z \leq 2.7$ for the MOSDEF (left) and KBSS (right) surveys. Blue indicates the $z \sim 2$ spectrosopic samples discussed in Sections 3.2.1 (MOSDEF) and 3.2.2 (KBSS). Green indicates galaxies that were observed and have a MOSFIRE redshift, but were not included in the $z \sim 2$ spectrosopic samples due to the various sample selection criteria discussed in Sections 3.2.1 and 3.2.2. Purple indicates galaxies that were targeted, but a robust MOSFIRE redshift was not obtained. For MOSDEF, the purple redshifts displayed are photometric redshifts. For KBSS, the purple redshifts displayed were obtained by previous rest-UV observations with Keck/LRIS. The LRIS redshifts were estimated from either Lyα or low-ionization interstellar absorption lines. Bottom: Corner plots comparing SFR(SED) vs. M_* (left) and sSFR(SED) vs. M_* (right) for the MOSDEF (red) and KBSS (blue) $z \sim 2$ targeted samples. The dashed lines on the 1D histograms mark the median values for the distributions, and the contours on the diagonal trace the 3σ regions in 2D space. Individual data points are also shown in the 2D distribution. The range of datapoints is limited by the fact that M_* and SFR(SED) are correlated and are both determined by the normalization of the SPS model to the photometry. In addition, for the 2D panels the data crowd in the upper-left portion of the distribution (left panel) and at high sSFR(SED) (right panel) because of the lower age limit for the stellar populations. In total, there are 786 MOSDEF and 850 KBSS galaxies. Note that two MOSDEF galaxies with $\log_{10}(\mathrm{SFR(SED)/M_\odot/yr^{-1}}) < -3.0$ are excluded from the left panel and one MOSDEF galaxy with $\log_{10}(\mathrm{sSFR(SED)/yr^{-1}}) < -14.0$ is excluded from the right panel to better show the data. 59

3.2 Distribution of physical properties for the MOSDEF (red) and KBSS (blue) $z \sim 2$ spectroscopic samples. The red and blue skeletal histograms represent the full spectroscopic samples (i.e., 250 galaxies for MOSDEF and 369 galaxies for KBSS), while the filled regions identify the subset of the spectroscopic samples that are on the [N II] BPT diagram (i.e., 143 galaxies for MOSDEF and 213 galaxies for KBSS). The sample medians, with uncertainties for are shown in yellow (green) for the MOSDEF (KBSS) full spectroscopic samples (i.e., the larger empty histograms), and are given in Table 3.2. The following galaxy properties are shown: (a) M_*, (b) SFR(SED), (c) sSFR(SED), (d) $\log_{10}(t/\tau)$ of the stellar population using a delayed-τ star formation model, (e) A_V, and (f) the UVJ diagram. The quiescent galaxy region in the upper left is enclosed in a solid curve, while star-forming galaxies occupy the bottom half and upper right-hand corner of the diagram. We find that all KBSS and MOSDEF sample median properties agree within the 1σ uncertainty, except for t/τ. The x-axes for panels a-e and both axes for panel f are the same as in Figure 3.7 to show how the distributions of the $z \sim 2$ spectroscopic sample compared to those for the $z \sim 2$ targeted samples. 71

3.3 Corner plot comparing the distributions of U−V and V−J colors for the MOSDEF (red) and KBSS (blue) $z \sim 2$ spectroscopic samples. The dashed lines on the 1D histograms mark the median values for the distributions of U−V and V−J colors given in Table 3.3, and the contours in the 2D panel trace the 3σ regions in UVJ color-color space. The individual data points are also shown in the 2D UVJ distribution. It is shown here that the MOSDEF and KBSS $z \sim 2$ spectroscopic samples occupy a very similar region of UVJ space, in addition to having sample medians that agree within the uncertainties. . 73

3.4 Corner plots comparing SFR(SED) vs. M_* (left) and sSFR(SED) vs. M_* (right) for the MOSDEF (red) and KBSS (blue) $z \sim 2$ spectroscopic samples. The dashed lines on the 1D histograms mark the median values for the distributions, and the contours on the diagonal trace the 3σ regions in 2D space. The individual data points are also shown in the 2D distribution. As stated for Figure 3.1, the distribution of datapoints is limited by the fact that both M_* and SFR(SED) are determined by the normalization of the SPS model to the photometry. Additionally, in 2D space the datapoints crowd in the upper-left part of the distribution (left panel) and at high sSFR(SED) (right panel) because of the lower age limit for the stellar populations. We have the same axes limits as the bottom two panels in Figure 3.1 so the distribution of galaxies in the $z \sim 2$ spectroscopic samples can easily be compared with the $z \sim 2$ targeted samples. 75

3.5 Stacked SEDs for the MOSDEF (red) and KBSS (blue) $z \sim 2$ spectroscopic samples. The SEDs are normalized at 4550 Å to show any differences in the global spectral shape. The 1σ scatter of the average SEDs is shown with shaded regions for both samples. 76

3.6 The MOSDEF (red) and KBSS (blue) $z \sim 2$ spectroscopic samples on the [N II] BPT (left) and [S II] BPT (right) diagrams. The grayscale 2D histogram indicates local SDSS galaxies. Galaxies must have S/N ≥ 3 for the Hβ, [O III]λ5008, Hα, and [N II]λ6585 ([S II]$\lambda\lambda$6718,6733) emission-lines to be included in the [N II] BPT ([S II] BPT) diagram. The yellow and green lines represent binned medians where the sample is binned in $\log_{10}$(O3N2) (left) and $\log_{10}$(O3S2) (right) for the MOSDEF and KBSS samples. The orange curve on the [N II] BPT diagram is a fit to the $z \sim 0$ star-forming locus (Kewley et al., 2013). 77

3.7 Distribution of physical properties for the MOSDEF (red) and KBSS (blue) $z \sim 2$ targeted samples. The sample medians, with uncertainties are shown in yellow (green) for the MOSDEF (KBSS) samples, and are given in Table 3.3. The following galaxy properties are shown: (a) M_*, (b) SFR(SED), (c) sSFR(SED), (d) $\log_{10}(t/\tau)$ of the stellar population using a delayed-τ star formation model, (e) A_V, and (f) the UVJ diagram. We find that the MOSDEF $z \sim 2$ targeted sample has a higher M_*, lower SFR(SED) and sSFR(SED), and a redder U−V color compared to the KBSS $z \sim 2$ targeted sample. Note that two MOSDEF galaxies with $\log_{10}(\mathrm{SFR(SED)/M_\odot/yr^{-1}}) < -3.0$ are excluded from the panel (b), and one MOSDEF galaxy with $\log_{10}(\mathrm{sSFR(SED)/yr^{-1}}) < -14.0$ is excluded from panel (c) to better show the data. 84

3.8 Corner plot comparing the distributions of U−V and V−J colors for the MOSDEF (red) and KBSS (blue) $z \sim 2$ targeted samples. The dashed lines on the 1D histograms mark the median values for the distributions of U−V and V−J colors given in Table 3.3, and the contours in the 2D panel trace the 3σ regions in UVJ color-color space. The individual data points are also shown in the 2D UVJ distribution. It is shown here that MOSDEF targeted a population of red galaxies with high U−V color that is not seen in the KBSS $z \sim 2$ targeted sample. Additionally, MOSDEF (KBSS) extends to slightly redder (bluer) regions of V−J color space. 86

3.9 Stacked SEDs for the MOSDEF (red) and KBSS (blue) $z \sim 2$ targeted samples. The SEDs are normalized at 4550 Å to show any differences in the global spectral shape. The scatter of the SEDs is shown with shaded regions for both samples. 86

3A.1 Distribution of physical properties for the MOSDEF (red) and KBSS (blue) $z \sim 2$ spectroscopic samples. The sample medians, with uncertainties are shown in yellow (green) for the MOSDEF (KBSS) samples, and are given in Table 3A.1. The following galaxy properties are shown: (a) M_*, (b) SFR(SED), (c) sSFR(SED), (d) $\log_{10}(t)$ of the stellar population using a constant star formation model, (e) A_V, and (f) the UVJ diagram. We find that the MOSDEF spectroscopic sample has a higher age, lower SFR(SED), lower sSFR(SED), and A_V, and redder U−V color compared to the KBSS spectroscopic sample. 96

3A.2 Distribution of physical properties for the MOSDEF (red) and KBSS (blue) $z \sim 2$ targeted samples. The sample medians, with uncertainties are shown in yellow (green) for the MOSDEF (KBSS) samples, and are given in Table 3A.2. The following galaxy properties are shown: (a) M_*, (b) SFR(SED), (c) sSFR(SED), (d) $\log_{10}(t)$ of the stellar population using a constant star formation model, (e) A_V, and (f) the UVJ diagram. We find that the MOSDEF $z \sim 2$ targeted sample has a higher M_* and age, lower SFR(SED) and lower sSFR(SED), and redder UVJ colors compared to the KBSS $z \sim 2$ targeted sample. 98

3A.3 Corner plots comparing the distributions of U−V and V−J colors for the $z \sim 2$ spectroscopic (left) and targeted (right) samples. MOSDEF and KBSS are shown in red and blue, respectively. The dashed lines on the 1D histograms mark the median values for the distributions of U−V and V−J colors given in Tables 3A.1 and 3A.2, and the contours in the 2D panel trace the 3σ regions in UVJ color-color space. The individual data points are also shown in the 2D distribution. Similar to Figure 3.3 and 3.8, it is shown here that while the $z \sim 2$ spectroscopic samples span a similar range in UVJ space, the MOSDEF $z \sim 2$ targeted sample extends to redder UVJ colors than the KBSS $z \sim 2$ targeted sample. 100

3A.4 Top: $z \sim 2$ targeted samples. Bottom: $z \sim 2$ spectroscopic samples. The left (right) column contains corner plots comparing SFR(SED) vs. M_* (sSFR(SED) vs. M_*). MOSDEF and KBSS are shown in red and blue, respectively. The dashed lines on the 1D histograms mark the median values for the distributions, and the contours on the diagonal trace the 3σ regions in 2D space. The individual data points are also shown in the 2D distribution. These plots utilize CSF fitting, and are analogous to Figures 3.1 ($z \sim 2$ targeted sample) and 3.4 ($z \sim 2$ spectroscopic sample). 101

3B.1 Examples showing how the MOSDEF (red) and KBSS `MOSPEC` (blue) codes fit the Hα and [N II]λ6585 emission-lines. The codes also simultaneously fit the [N II]λ6550; however, we did not use it for this study. We pick the following galaxies to highlight the following details about the code. (a) Q1603-BX379, for which we display the typical [N II]λ6585 offset between the two codes (i.e., the KBSS `MOSPEC` code is ~13% larger). The MOSDEF code uses the Gaussian fit for the preferred flux. (b) Q1549-BX223, for which we display similar [N II]λ6585 fluxes, where the MOSDEF code uses the Gaussian fit for the preferred flux. (c) AEGIS 6377, for which we display the typical [N II]λ6585 offset between the two codes where the MOSDEF code uses the Gaussian fit for the preferred flux. (d) AEGIS 33172, for which we display similar [N II]λ6585 fluxes, where the MOSDEF code uses the Gaussian flux for the preferred flux. Panel (c) shows that the Gaussian peaks for [N II]λ6585 do not always perfectly agree in the two codes. 104

4.1 Redshift distributions for the different MOSDEF samples analyzed in this study. The left panel shows the MOSDEF $z \sim 2$ N2 stacked sample (green; $z_{\rm med} = 2.28$), $z \sim 2$ spectroscopic sample (purple; $z_{\rm med} = 2.29$), and $z \sim 2$ N2 BPT detection sample (blue; $z_{\rm med} = 2.29$). The right panel shows the MOSDEF $z \sim 2$ observed sample (black; $z_{\rm med} = 2.29$) and $z \sim 2$ parent sample (red; $z_{\rm med} = 2.31$). 114

4.2 The [N II] BPT (top left), [S II] BPT (top right), and O_{32} vs. R_{23} (bottom) diagrams. The N2 and S2 $z \sim 2$ stacked samples are shown with green squares. The grey 2D histograms show the local SDSS $z \sim 0$ star-forming galaxies. The blue points identify the 143, 156, and 181 galaxies with 3σ S/N for all relevant lines on the [N II] BPT, [S II] BPT, and O_{32} vs. R_{23} diagrams, respectively. An additional requirement for a robust Hα detection is needed for dust corrections on the O_{32} vs. R_{23} diagram. The blue triangles are the binned medians from Runco et al. (2021a), binned in O3N2 (O3S2) on the [N II] ([S II]) BPT diagram. The red curve on the [N II] BPT diagram is a fit to early MOSDEF data from Shapley et al. (2015), while the yellow curve is a fit to the SDSS $z \sim 0$ star-forming locus (Kewley et al., 2013). 121

4.3 Distribution of physical properties and sample medians with 1σ uncertainties for the MOSDEF N2 $z \sim 2$ stacked sample (green), the $z \sim 2$ spectroscopic sample (purple), and the 143 galaxy subset of the $z \sim 2$ spectroscopic sample shown on the [N II] BPT diagram in Figure 4.2 (blue), i.e., the N2 BPT detection sample. The values for the sample medians are given in Table 4.2. For the panels with 1D histograms, the y-axis is normalized so the area under the histogram for each sample adds up to one. Distributions for the following galaxy properties are shown: **(a)** M_*, **(b)** $\log_{10}(t/\tau)$ of the stellar population assuming a delayed-τ star formation model, **(c)** A_V, **(d)** SFR(SED), **(e)** sSFR(SED), **(f)** the UVJ diagram. The box on the UVJ diagram separates the quiescent region (upper left) from the star-forming region (bottom half and upper right). The galaxy properties shown here are estimated using emission-line corrected photometry for all galaxies in the figure. 123

4.4 Corner plots for SFR(SED) vs. M_* (upper left), sSFR(SED) vs. M_* (upper right), A_V vs. M_* (bottom left), and U−V vs. V−J (bottom right). Shown on these diagrams are the $z \sim 2$ stacked sample (green), $z \sim 2$ spectroscopic sample (purple), and $z \sim 2$ N2 BPT detections (blue). The galaxy properties shown here are estimated using emission-line corrected photometry for all galaxies in the figure. 126

4.5 $\log_{10}$(N2) vs. M_* (upper left), $\log_{10}$(O3N2) vs. M_* (upper right), and Hα/Hβ vs. M_* (bottom). The blue points identify the 143 galaxies in Figure 4.2 with 3σ S/N for all relevant lines on the [N II] BPT diagram. The green squares show the $z \sim 2$ N2 BPT stacks. Fits to the stacks are included in the $\log_{10}$(N2) vs. M_* and $\log_{10}$(O3N2) vs. M_* panels. Also included are the MOSDEF $z \sim 2$ stacks from Sanders et al. (2021) (upper left and upper right panels) and the sliding median for the MOSDEF $z \sim 2$ sample from Shapley et al. (2022) (bottom panel). The stellar mass values shown here are estimated using emission-line corrected photometry for all galaxies in the figure. 128

4.6 Distribution of physical properties and sample medians with 1σ uncertainties for the MOSDEF $z \sim 2$ parent sample (red) and the $z \sim 2$ observed sample (black). The values for the sample medians are given in Table 4.3. For the panels with 1D histograms, the y-axis is normalized so the area under the histogram for each sample adds up to one. The distributions for the following galaxy properties are shown: **(a)** M_*, **(b)** $\log_{10}(t/\tau)$ of the stellar population assuming a delayed-τ star formation model, **(c)** A_V, **(d)** SFR(SED), **(e)** sSFR(SED), **(f)** the UVJ diagram. The box on the UVJ diagram separates the quiescent region (upper left) from the star-forming region (bottom half and upper right). Additionally, the sample medians on the UVJ diagram are orange ($z \sim 2$ parent sample) and grey ($z \sim 2$ observed sample). The galaxy properties shown here are estimated using emission-line uncorrected photometry for all galaxies in the figure. 130

4.7 Corner plots for SFR(SED) . M_* (upper left), sSFR(SED) vs. M_* (upper right), A_V vs. M_* (bottom left), and U−V vs. V−J (bottom right). Shown on these diagrams are the $z \sim 2$ parent sample (red) and $z \sim 2$ observed sample (black). The galaxy properties shown here are estimated using emission-line uncorrected photometry for all galaxies in the figure. 133

4.8 Corner plots for SFR(SED) vs. M_* (upper left), sSFR(SED) vs. M_* (upper right), A_V vs. M_* (bottom left), and U−V vs. V−J (bottom right). Shown on these diagrams are the $z \sim 2$ observed sample (black), $z \sim 2$ star-forming observed sample (brown), and the $z \sim 2$ N2 stacked sample (green). The galaxy properties shown here are estimated using emission-line corrected photometry for the majority of the galaxies with a MOSFIRE redshift. Otherwise, emission-line uncorrected photometry is used for the minority of galaxies without the $z_{\rm MOSFIRE}$. 136

5.1 Left: MOSFIRE J-band spectrum (black) for GOODS-S 43114 along with the section of the GOODS-S 43114 FAST fit (blue) and GOODS-S 43683 FAST fit (green) that overlaps with the spectra. Here we see the Hγ and Hδ absorption features. Right: The full broadband GOODS-S 43114 FAST fit (blue) with photometry points (red) and full broadband GOODS-S 43683 FAST fit (green) with photometry points (orange). 144

5.2 The 2D F160W image from the 3D-*HST* catalog with the MOSFIRE slit (yellow), GOODS-S 43114 centroid (blue) and GOODS-S 43683 centroid (green) identified. . . 145

5.3 Left: UVJ diagram. GOODS-S 43114 and GOODS-S 43683 are shown by the orange triangle and square, respectively. The dashed boxes identify the five bins of galaxies from Zick et al. (2018): quiescent (red), post-starburst (yellow), dusty galaxies with lower sSFRs (green), dust star-forming (purple), and non-dusty star-forming (blue). Both GOODS-S 43114 and GOODS-S 43683 fall into the post-starburst bin. The black line identifies the quiescent box defined in (Williams et al., 2009). Right: H$\delta_{\rm A}$ vs. D_n4000. The circles are color matched to identify the five bins of galaxies shown in the UVJ diagram. The blue, red, and green lines identify three delayed-τ SFHs, where τ = 0.1, 0.2, and 1.0 Gyr, respectively. The grayscale 2D histogram indicates local SDSS galaxies. 150

5.4 SFR(SED) vs. z displaying the SFHs assuming a delayed-τ model for GOODS-S 43114 (blue) and GOODS-S 43683 (green). The black circle identifies the moment of observation (i.e., $z = 1.89$). The rapid burst of star formation followed by rapid quenching over the course of ~500 Myr or less gives an approximation on when the first pericentric passage took place. 152

5.5 Fit to the MOSFIRE J-band spectrum using `ppxf` to estimate σ_e. The MOSFIRE spectrum is shown in black while the fit is shown in red. The residuals to the fit are given as green points. The spectrum and fit are centered at a relative flux of 1, while the residuals are centered at a relative flux of 0. 152

6.1 OH rotational Grotrian diagram showing the transitions discussed in this paper. Each rotational level is split into two sublevels due to Λ doubling and each sublevel is split again due to the hyperfine structure. The rotational ladder has two branches due to spin splitting (Λ + s, Λ − s) where Λ = 1 and s = 1/2. The integer next to the hyperfine branches of each energy level is the total angular-momentum quantum number, F. The red, blue, purple, and black numbers are the wavelength of the transition in units of μm. Red indicates that the doublet was seen primarily in absorption, blue indicates primarily emission, purple indicates that neither emission or absorption was strongly favored, and black indicates transitions not analyzed in this study but are mentioned in Section 6.4. 163

6.2 Examples of the variety of spectra observed with PACS. These spectra are the central spaxel of the observations of the 5 × 5 array. From left to right: Top: doublet absorption (Centaurus A: Seyfert-2); absorption where the doublet is blended into one line (NGC 3079: LINER); doublet emission (IC 5135: Seyfert-1.9); emission where the doublet is blended into one line (NGC 1068: Seyfert-1h). Bottom: doublet absorption (NGC 4945: Seyfert-2); P-Cygni profile with the emission and absorption components approximately equal in strength (NGC 1266: LINER); P-Cygni profile with a stronger absorption component than emission (IRAS 01003-2238: Seyfert-2); reverse P-Cygni profile with emission and absorption components approximately equal in strength (Circinus: Seyfert-1h). The top axis is the restframe wavelength, the bottom axis the velocity centered in the middle of the OH doublet, and the y-axis is the difference between the flux of the OH doublet and the flux of the continuum, normalized by the factor indicated in the upper-left corner of each panel. The gray line is the data. The green shaded region is the integrated line flux used to estimate the EW of the transition. The velocities are given relative to the blue peak of the doublet, that is v = 0 km/s coincides with the left peak of the doublet when no redshift or blueshift are detected. The two vertical dashed lines show the galaxy rest wavelength of the doublet. 171

6.3 EW of the OH doublet vs. the logarithm of the [Ne V] 14.32μm/[Ne II] 12.81μm emission-line ratio. Galaxies must have detections in EW(OH), [Ne V] 14.32μm, and [Ne II] 12.81μm to be included in the plot and fits. The weighted log-linear fits, using the parameters given in Table 6B.6, are shown for fits with p < 0.05. We do not show the fit for slopes with a p-value > 0.05. For OH79, MCG-01-24-012 is an outlier (EW = 0.242μm), and is cut off to better show the rest of the data. 179

6.4 EW of the OH doublet vs. the logarithm of the [O IV] 25.89μm/[O III] 88.36μm emission-line ratio. Galaxies must have detections in EW(OH), [O IV] 25.89μm, and [O III] 88.36μm to be included in the plot and fits. The weighted log-linear fits, using the parameters given in Table 6B.6, are shown for fits with p < 0.05. We do not show the fit for slopes with a p-value > 0.05. 180

6.5 EW of the OH doublet vs. log($L_{2-10\mathrm{keV}}$ (erg/s)). Galaxies must have detections in EW(OH) and $L_{2-10\mathrm{keV}}$ to be included in the plot and fits. The weighted log-linear fits, using the parameters given in Table 6B.7, are shown for fits with p < 0.05. For both EW(OH79) and EW(OH119), $|r| \leq 0.5$, which indicates that $L_{2-10\mathrm{keV}}$ is an uncertain predictor of these doublets. We do not show the fit for slopes with a p-value > 0.05. For OH79, MCG-01-24-012 is an outlier (EW = 0.242μm), and is cut off to better show the rest of the data. 183

6.6 EW of the OH doublet vs. log($L_{[\mathrm{O\ IV}]25.89\mu\mathrm{m}}$ (erg/s)). Galaxies must have detections in EW(OH) and $L_{[\mathrm{O\ IV}]25.89\mu\mathrm{m}}$ to be included in the plot and fits. The weighted log-linear fits, using the parameters given in Table 6B.7, are shown for fits with p < 0.05. We do not show the fit for slopes with a p-value > 0.05. For OH79, MCG-01-24-012 is an outlier (EW = 0.242μm), and is cut off to better show the rest of the data. 184

6.7 EW of the OH doublet vs. the logarithm of the dust temperature traced by the IRAS $f_{25\mu\mathrm{m}}/f_{60\mu\mathrm{m}}$ ratio. Galaxies must have detections in EW(OH), IRAS 25μm flux, and IRAS 60μm flux to be included in the plot and fits. The weighted linear fits, using the parameters given in Table 6B.8, are shown for fits with p < 0.05. We do not show the fit for slopes with a p-value > 0.05. For OH79, MCG-01-24-012 is an outlier (EW = 0.242μm), and is cut off to better show the rest of the data. 187

6.8 EW of the OH doublet vs. the strength of the 9.7μm silicate feature. Galaxies must have detections in EW(OH) and S_{sil} to be included in the plot and fits. The weighted log-linear fits, using the parameters given in Table 6B.9, are shown for fits with p < 0.05. We do not show the fit for slopes with a p-value > 0.05. For OH79, MCG-01-24-012 is an outlier (EW = 0.242μm), and is cut off to better show the rest of the data. 189

6.9 EW(OH119) vs. EW(OH79). Only galaxies with detections for both doublets are shown. The error bars for Mrk 478 is cut off to better show the rest of the data. 192

6.10 EW(OH163) vs. EW(OH79). Only galaxies with detections for both doublets are shown. 193

6C.1 EW of the OH doublet vs. the logarithm of the [O IV] 25.89μm/[Ne II] 12.81μm emission-line ratio. Galaxies must have detections in EW(OH), [O IV] 25.89μm, and [Ne II] 12.81μm to be included in the plot and fits. The weighted log-linear fits, using the parameters given in Table 6B.6, are shown for fits with p < 0.05. We do not show the fit for slopes with a p-value > 0.05. For OH79, MCG-01-24-012 is an outlier (EW = 0.242μm), and is cut off to better show the rest of the data. 244

6C.2 Same as Figure 6C.1 for the [Ne V] 24.32μm/[Ne II] 12.81μm emission-line ratio. . . 245

6C.3 Same as Figure 6C.1 for the [Ne III] 15.56μm/[Ne II] 12.81μm emission-line ratio. . . 246

6C.4 EW of the OH doublet vs. log($L_{[\mathrm{Ne\ V}]14.32\mu\mathrm{m}}$ (erg/s)). Galaxies must have detections in EW(OH) and $L_{[\mathrm{Ne\ V}]14.32\mu\mathrm{m}}$ to be included in the plot and fits. The weighted log-linear fits, using the parameters given in Table 6B.7, are shown for fits with p < 0.05. We do not show the fit for slopes with a p-value > 0.05. For OH79, MCG-01-24-012 is an outlier (EW = 0.242μm), and is cut off to better show the rest of the data. 247

6C.5 Same as Figure 6C.4 for the [Ne V] 24.32μm emission-line luminosity. 248

6C.6 EW of the OH doublet vs. the ratio of Hα to Hβ. Galaxies must have detections in EW(OH), Hα, and Hβ to be included in the plot and fits. The weighted log-linear fits, using the parameters given in Table 6B.9, are shown for fits with p < 0.05. We do not show the fit for slopes with a p-value > 0.05. 249

LIST OF TABLES

2.1 Median Values for Physical Properties of the *High* and *Low* Samples 31

2.2 Single Z_* Cloudy+BPASS Median Values for Physical Properties of the *High* and *Low* Samples 37

3.1 $U_{\rm n}G\mathcal{R}$ Diagram Statistics 64

3.2 Median Values for Physical Properties of the MOSDEF and KBSS $z \sim 2$ Spectroscopic Samples 72

3.3 Median Values for Physical Properties of the MOSDEF and KBSS $z \sim 2$ Targeted Samples 85

3A.1 Median Values for Physical Properties of the MOSDEF and KBSS $z \sim 2$ Spectroscopic Samples (CSF Models) 97

3A.2 Median Values for Physical Properties of the MOSDEF and KBSS $z \sim 2$ Targeted Samples (CSF Models) 99

4.1 MOSDEF Samples 115

4.2 Median Values for Physical Properties of the MOSDEF $z \sim 2$ N2 Stacked, Spectroscopic, and N2 BPT Detection Samples 124

4.3 Median Values for Physical Properties of the MOSDEF $z \sim 2$ Parent and Observed Samples 131

5.1 GOODS-S 43114 & GOODS-S 43683 Physical Properties 148

6.1 Fine Structure Transitions 162

6.2 List of Objects Showing P-Cygni Features 175

6.3 Percent of P-Cygni Features Found for each OH Transition 176

6A.1 The Sample 204

6A.2 IRAS Data 211

6A.3 9.7μm Silicate & Balmer Data 220

6A.4 Derived OH Integrated Flux Values 227
6A.5 Derived EW(OH) Values 233
6B.6 Best-fit Parameters for EW(OH) vs. Emission-Line Ratio Fluxes 240
6B.7 Best-fit Parameters for EW(OH) vs. the X-ray and IR Emission-Line Luminosities . . 241
6B.8 Best-fit Parameters for Figure 6.7 (EW(OH) vs. IRAS $f_{25\mu m}/f_{60\mu m}$ Dust Temperature Tracer) 242
6B.9 Best-fit Parameters for EW(OH) vs. Dust Extinction 243
6B.10 Bivariate Regression Results 243

ACKNOWLEDGMENTS

I would like to thank Professor Alice Shapley for being a wonderful research advisor and mentor. Over these past four years you have provided so much support and fostered my abilities in analyzing data, scientific writing, and giving clear presentations. Also thank you to Dr. Matthew Malkan for being my advisor for my first research project at UCLA, and helping me begin my graduate school journey. I would not be the scientist I am today and would not have interacted with so many wonderful collaborators without both of your guidance.

I would like to thank the many people in the UCLA Physics and Astronomy department. The astronomy grad community was invaluable with the friendship, resources, and general support amongst each other. I am especially grateful to my seven person cohort, and the lifelong friends I have made from it. I appreciate the friendliness of the feeling of belonging from the faculty. Lastly, I am grateful for the many people that make up the administration staff who have helped me fill out the seemingly endless number of forms to remain employed as a graduate student at UCLA.

I love and thank my family. My parents for their never ending support while I chase my dreams, and instilling the importance of education from an early age. My fiancée Maren, for always being there for me. You push me to be the best version of myself that I can be. I am grateful that we went through our graduate school journey together. My cat Obi for screaming at me and occasionally trying to close my laptop when I would work too much. You also had a pretty good attendance for most of my Zoom meetings.

I acknowledge that the results presented in this thesis are based on works that have been published or will soon be published in scientific journal with additional co-authors. Chapter 2 is a reprint of Runco et al. (2021b) which appears in the Monthly Notices of the Royal Astronomical Society (MNRAS) journal. Chapter 3 is a reprint of Runco et al. (2021a) which appears in the MNRAS

journal. Chapter 5 is a material in preparation for publication in the MNRAS journal. Chapter 4 is a material in preparation for publication in the MNRAS journal. Chapter 6 is a reprint of Runco et al. (2020) which appears in the Astrophysical Journal (ApJ).

Finally, I acknowledge that some of the data presented herein were obtained at the W. M. Keck Observatory, which is operated as a scientific partnership among the California Institute of Technology, the University of California and the National Aeronautics and Space Administration. The Observatory was made possible by the generous financial support of the W. M. Keck Foundation.

VITA

2013–2015 **Undergraduate Student Researcher**, Department of Physics, California Polytechnic State University, San Luis Obispo

2015 **B.S., Physics**, California Polytechnic State University, San Luis Obispo

2016–2020 **Teaching Assistant**, Department of Physics and Astronomy, University of California, Los Angeles

2018 **M.S., Astronomy**, University of California, Los Angeles

2020–present **Graduate Student Researcher**, Department of Physics and Astronomy, University of California, Los Angeles

PUBLICATIONS

Herscel/PACS OH Spectroscopy of Seyfert, LINER, and Starburst Galaxies

Jordan Runco, Matthew Malkan, Juan Fernández-Ontiveros, et al. 2020, ApJ, 905, 1, 57

The MOSDEF Survey: A Comprehensive Analysis of the Rest-optical Emission-line Properties of $z \sim 2.3$ Star-forming Galaxies

Jordan Runco, Alice Shapley, Ryan Sanders, et al. 2021, MNRAS, 502, 2, 2600-2614

Reconciling the Results of the $z \sim 2$ MOSDEF and KBSS-MOSFIRE Surveys

Jordan Runco, Naveen Reddy, Alice Shapley, et al. 2022, MNRAS, accepted

The MOSDEF Survey: A Remarkable $z = 1.89$ Merger

Jordan Runco, Alice Shapley, Mariska Kriek, et al. 2022, in prep.

The MOSDEF Survey: Towards a Complete Census of the $z \sim 2.3$ Star-forming Galaxy Population

Jordan Runco, Alice Shapley, Ryan Sanders, et al. 2022, in prep.

CHAPTER 1

Introduction

Tracing the formation and evolution of galaxies across cosmic time remains a key goal for extragalactic astronomy. The global star-formation rate density is known to peak at $z \sim 2$ (Madau & Dickinson 2014; see Figure 1.1), but we still do not have a complete model for the evolution of the individual star-formation histories that combine to create the global rise and fall of the universe's activity level. Studies of both local and distant galaxies with similar metrics are required to construct an evolutionary history of the universe. Local galaxies are very well studied at optical wavelengths, and the commissioning of multi-object near-infrared (IR) spectrographs on large ground-based telescopes has given us the ability to characterize the rest-frame optical emission-line properties of high-redshift galaxies in large statistical samples. Such statistical studies enable us to make direct comparisons between galaxies today and those in the distant past, as we can study the same emission-lines over different cosmic epochs.

This development in instrumentation capabilities within the past decade is important because rest-frame optical emission-line spectroscopy is one of the most powerful observational tools to help better understand galaxy formation and evolution. Rest-frame optical emission-lines provide a wealth of information about a galaxy, including star-formation rate (SFR), metallicity, electron density, active galactic nuclei (AGN) activity, virial and non-virial dynamics (e.g., outflows), and dust extinction. Therefore, knowledge about the emission-line properties of star-forming galaxies across cosmic time is essential for understanding the evolution of the stellar and gaseous content in galaxies. "Cosmic noon," (Grogin et al., 2011), i.e., $z \sim 2$ in particular, is an important epoch to

study, as the era of peak star formation could be the key for connecting the early universe to today.

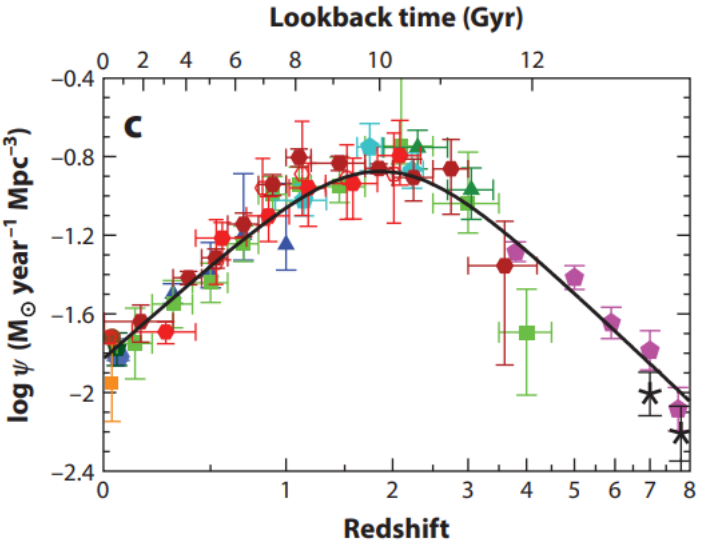

Figure 1.1: From Madau & Dickinson (2014): the evolution of the global star-formation rate density in the universe. The left axis shows the number of stellar masses produced in stars per year per Mpc^3 volume of space. The bottom axis shows the redshift. The top axis shows the lookback time in Gyr that corresponds to the redshift on the bottom axis. The plot shows both dust-corrected rest-frame far-ultraviolet, FUV, (green, blue, and pink) and IR (red and orange) data points. The black curve is a fit to the combined FUV and IR data.

In this dissertation, I aim to study the rest-optical emission-line properties of $z \sim 2$ star-forming galaxies in the MOSFIRE Deep Evolution Field (MOSDEF) survey. MOSDEF is currently one of the largest ground-based high redshift spectroscopic surveys, conducting observations using the MultiObject Spectrometer For Infra-Red Exploration (MOSFIRE; McLean et al. 2012) instrument on the Keck I telescope at the W.M. Keck Observatory on Mauna Kea. The survey took place over 48.5 nights from December 2012 to May 2016, with observations of ∼1500 galaxies at z ∼1.4-3.8 (half at $z \sim 2$). Within this redshift range, the Universe was only 1.5 to 4.5 billion years old. Specifically, galaxies were targeted across three redshift ranges ($1.37 \leq z \leq 1.70$, $2.09 \leq z \leq 2.61$, and $2.95 \leq z \leq 3.80$), which were selected to optimise the detection of strong rest-optical emission-lines (e.g., [O II]$\lambda\lambda$3727,3730, Hβ, [O III]$\lambda\lambda$4960,5008, Hα, [N II]λ6585, and [S II]$\lambda\lambda$6718,6733) within windows of atmospheric transmission. The portions of spectra that

fall outside of these windows get absorbed by the atmosphere and cannot be observed by ground based telescopes. MOSDEF used the Y-, J-, H-, and K_s-bands, which have wavelength ranges of 0.97-1.12μm, 1.15-1.35μm, 1.46-1.81μm, and 1.93-2.45μm, respectively. For the lowest (i.e., $z \sim 1.5$) and middle (i.e., $z \sim 2$) redshift bins, MOSDEF is able to observe the full rest-optical spectrum. At $z \sim 1.5$ ($z \sim 2$), MOSDEF observes [O II]$\lambda\lambda$3727,3730, in the Y-band (J-band), Hβ and [O III]$\lambda\lambda$4960,5008 in the J-band (H-band), and Hα, [N II]λ6585, and [S II]$\lambda\lambda$6718,6733 in the H-band (K_s-band). At $z \sim 3$, we can only observe [O II]$\lambda\lambda$3727,3730, in the H-band and Hβ and [O III]$\lambda\lambda$4960,5008 in the K_s-band. Longer-wavelength lines such as Hα, [N II]λ6585, and [S II]$\lambda\lambda$6718,6733 are shifted outside of the MOSFIRE wavelength range at $z > 3$. In this thesis, I will focus on the middle redshift bin (i.e., galaxies at $z \sim 2$).

MOSDEF selected objects from five well-studied extragalactic legacy fields covered by the CANDELS and 3D-HST surveys: AEGIS, COSMOS, GOODS-N, GOODS-S, and UDS (Grogin et al., 2011; Koekemoer et al., 2011; Momcheva et al., 2016). These fields were chosen because they contain a wide variety of available ancillary data, including galaxy size measurements from the catalogs of van der Wel et al. (2014), X-ray luminosities, and multi-wavelength photometry spanning from the UV to the far-IR. The MOSDEF survey used the *Hubble Space Telescope* (*HST*) WFC3 F160W filter (H-band at $z \sim 2$, rest-optical at $z \sim 0$) to select galaxies from the 3D-HST catalogs (Skelton et al., 2014), using a brightness limit of $H_{AB} = 24.0$, 24.5, and 25.0, respectively, for the lowest, middle and highest redshift bins.

The MOSDEF team has conducted a wide variety of studies using the MOSFIRE rest-optical data, including AGN properties (e.g., Coil et al. 2015; Azadi et al. 2017; Leung et al. 2017), merger demographics (e.g., Wilson et al. 2019; Horstman et al. 2021), dust content in the interstellar medium (ISM; e.g., Reddy et al. 2015, 2020; Shivaei et al. 2020, 2022; Shapley et al. 2022), dynamics (e.g., Price et al. 2016, 2020), stellar properties of quiescent galaxies (e.g., Kriek et al. 2016; Zick et al. 2018), and ISM properties of star-forming galaxies (e.g., Shapley et al. 2015, 2019; Sanders et al. 2016, 2018, 2020a,b; Topping et al. 2021). For the bulk of my thesis, I focus on

analyzing the rest-optical emission-line and host galaxy properties of $z \sim 2$ star-forming galaxies in the MOSDEF survey. I extend previous studies in this field (e.g., Shapley et al. 2015; Sanders et al. 2016), to gain a comprehensive understanding of $z \sim 2$ star-forming galaxies and compare their rest-optical emission-lines and host galaxy properties to those of local $z \sim 0$ analogs that exist today. The ultimate goal of this work is to better understand how galaxies evolve across cosmic time.

1.1 The Complete MOSDEF Survey

"BPT" diagrams, first introduced by Baldwin et al. (1981), probe the mechanism for ionization in a galaxy. There are three "BPT" diagrams proposed by Veilleux & Osterbrock (1987) based on the following line ratios: [O III]λ5008/Hβ vs. [N II]λ6585/Hα ([N II] BPT diagram), [O III]λ5008/Hβ vs. [S II]$\lambda\lambda$6718,6733/Hα ([S II] BPT Diagram), and [O III]λ5008/Hβ vs. [O I]λ6300/Hα. BPT diagrams measure the intensity ratio of different combinations of rest-optical emission-lines, which allows us to probe the ionizing spectrum and excitation mechanism of the galaxy. AGNs have a harder ionizing spectrum than massive stars. Therefore these two types of galaxies occupy different areas on these diagrams. This difference is especially well known for the [N II] BPT diagram. Another diagram commonly used to describe star-forming galaxies is the [O III]$\lambda\lambda$4960,5008/[O II]$\lambda\lambda$3727,3730 vs. ([O III]$\lambda\lambda$4960,5008+[O II]$\lambda\lambda$3727,3730)/Hβ (O_{32} vs. R_{23}) diagram. O_{32} and R_{23} are rough tracers for ionization parameter and metallicity, respectively, so this diagram allows us to probe these physical quantities in star-forming galaxies (e.g., Lilly et al. 2003; Nakajima et al. 2013).

Previous studies have found that the location of galaxies on the [N II] BPT diagram is redshift dependent, as galaxies with $z > 1$ are found to be offset from the large baseline sample of local galaxies observed by the Sloan Digital Sky Survey (SDSS; e.g., Shapley et al. 2005, 2015; Erb et al. 2006b; Liu et al. 2008; Steidel et al. 2014). There have been many proposed ideas to explain this systematic offset. Possible explanations include variations in physical properties of

galaxies such as interstellar pressure, H II region electron densities, density structure, H II region ionization parameter, hardness of the H II region ionizing spectra at fixed metallicities, gas-phase N/O abundance ratio differences, unresolved AGN activity, and shocks (e.g., Liu et al. 2008; Brinchmann et al. 2008; Wright et al. 2010; Kewley et al. 2013; Yeh et al. 2013; Masters et al. 2014; Coil et al. 2015; Sanders et al. 2016; Steidel et al. 2016; Kashino et al. 2017; Freeman et al. 2019). Galaxy selection effects could also be potential factors in this offset (Juneau et al., 2014). Figure 1.2 (from Kewley et al. 2013) illustrates how changing individual galaxy properties can change the shape and/or location of the observed sequence of galaxies the [N II] BPT diagram.

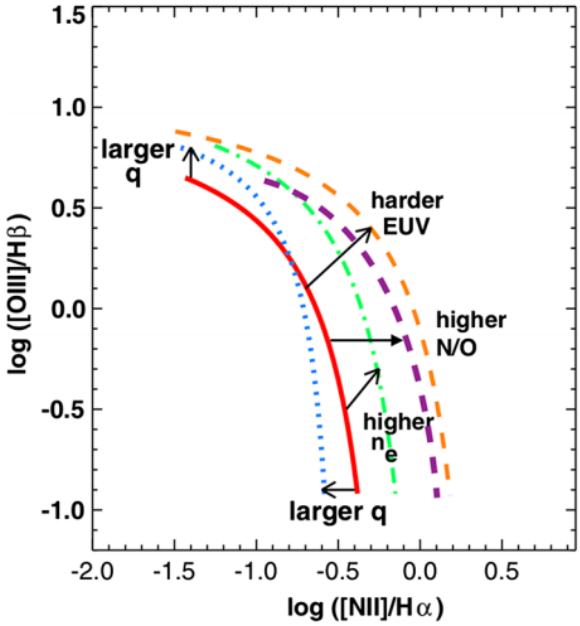

Figure 1.2: From Kewley et al. (2013): a cartoon diagram showing how changing individual galaxy properties affects the observed sequence of galaxies on the [N II] BPT diagram. The properties shown are H II region ionizing spectra at fixed metallicities (EUV), H II region ionization parameter (q), H II region electron densities (n_e), and gas-phase N/O abundance ratio differences. It is shown that all of these properties can potentially be the driver of the $z > 1$ galaxy offset from the local SDSS sequence.

Understanding this offset is vital because these strong rest-optical emission-lines are used as empirical tracers for many physical properties of the ISM. One important quantity to study is metallicity, as probed by the gas-phase oxygen abundance. Strong emission-line ratios are used as

empirical calibrations for inferring the gas-phase oxygen abundance in local galaxies (e.g., Pettini & Pagel 2004; see Figure 1.3). In addition, metallicity has been found to increase along the sequence of local galaxies on the [N II] BPT diagram from high [O III]λ5008/Hβ and low [N II]λ6585/Hα to low [O III]λ5008/Hβ and high [N II]λ6585/Hα (Masters et al., 2016). Due to the observed offset for $z > 1$ galaxies, it is unclear if local calibrations can be accurately applied to the high redshift universe. Therefore, it is essential to gain a complete understanding of why high redshift galaxies have elevated [N II]/Hα and [O III]/Hβ compared to the local SDSS sample.

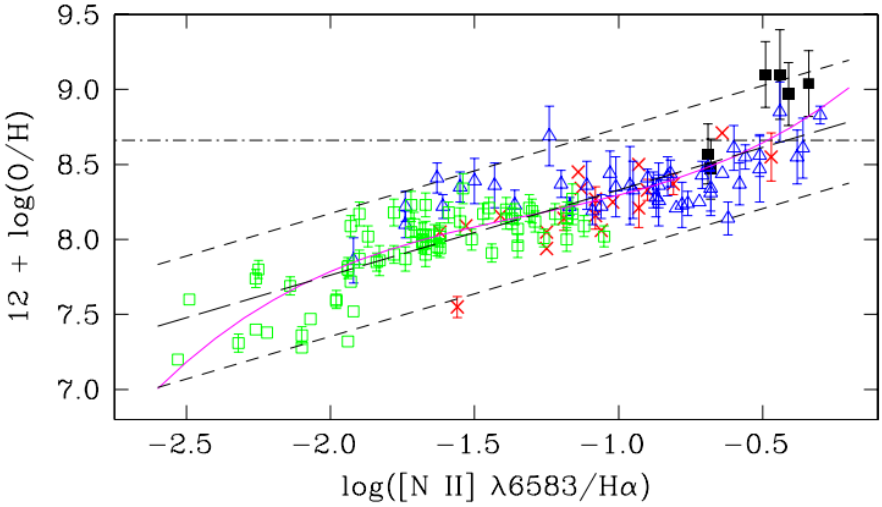

Figure 1.3: From Pettini & Pagel (2004): gas phase oxygen metallicity (i.e., 12+log(O/H)) vs. [N II]λ6585/Hα for local ($z \sim 0$) H II regions. This diagram shows at there is a clear correlation between nebular metallicity and emission-line ratio strength in the local universe. Using relationships such as this, it is possible to predict nebular metallicty when a direct measurement is not available. Due to differences in emission-line ratio sequences between $z \sim 0$ and $z \sim 2$ galaxies, it is currently unclear if these local calibrations can be used at high redshift.

With full spectroscopic coverage of all the emission-lines needed to complete the [N II] BPT, [S II] BPT, and O_{32} vs. R_{23} diagrams at $z \sim 2$ range, the MOSDEF survey provides an ideal dataset of high redshift galaxies to help explore the observed offset on the [N II] BPT diagram. In Chapter 2, I investigate the emission-line properties of the complete MOSDEF sample. I combine the MOSFIRE rest-optical spectra with ancillary data from the CANDELS and 3D-HST surveys to investigate the possibility of evolving physical conditions within the galaxies and to help uncover

the physical driver behind the [N II] BPT offset. Previous studies (e.g., Shapley et al. 2015; Sanders et al. 2016) conducted similar analysis on early MOSDEF data before all of the observations were completed and the data was available. I extend the work from these earlier studies, utilizing a MOSDEF sample that is approximately twice as large as its predecessors. With this larger dataset, I investigate the emission-line and host galaxy properties of the full $z \sim 2$ MOSDEF star-forming galaxy sample.

1.2 The MOSDEF & KBSS Collaboration

MOSDEF is not the only survey investigating the emission-line properties of high redshift galaxies. Using the Keck Baryonic Structure Survey (KBSS), the KBSS-MOSFIRE team also used MOSFIRE to investigate a large sample of ~1500 star-forming galaxies in a similar z ~1.5-3.5 redshift range (Steidel et al., 2014), with half the sample at $z \sim 2$. KBSS observes a different set of galaxies than MOSDEF, targeting 15 independent KBSS fields. These fields were selected based on the presence of a bright ($V \sim 16 - 17$) QSO at $z = 2.7 \pm 0.1$, and nearby galaxies were selected primarily based on rest-UV ($U_{\rm n}G\mathcal{R}$) colors and a rest-UV magnitude limit.

Both surveys find an offset between $z \sim 2$ star-forming galaxies and the local SDSS sequence on the [N II] BPT diagram. KBSS and recent MOSDEF studies agree that the main driver for the observed offset is a harder ionizing spectrum at fixed nebular oxygen abundance, which is caused by α-enhancement in the massive stars in $z \sim 2$ star-forming galaxies (Steidel et al., 2014, 2016; Strom et al., 2017; Shapley et al., 2019; Topping et al., 2020a; Reddy et al., 2022). However, there are still differences in key published results. Most noteworthy is that the MOSDEF and KBSS surveys have found quantitatively different offsets on the [N II] BPT diagram between the emission-line sequences for local and $z \sim 2$ star-forming galaxies, with the KBSS sample showing higher emission-line ratios on average by approximately 0.1 dex (Steidel et al., 2014; Shapley et al., 2015; Strom et al., 2017). This offset in the emission-line properties suggests that the galaxies in the two surveys might probe different subsets of the $z \sim 2$ star-forming galaxy population.

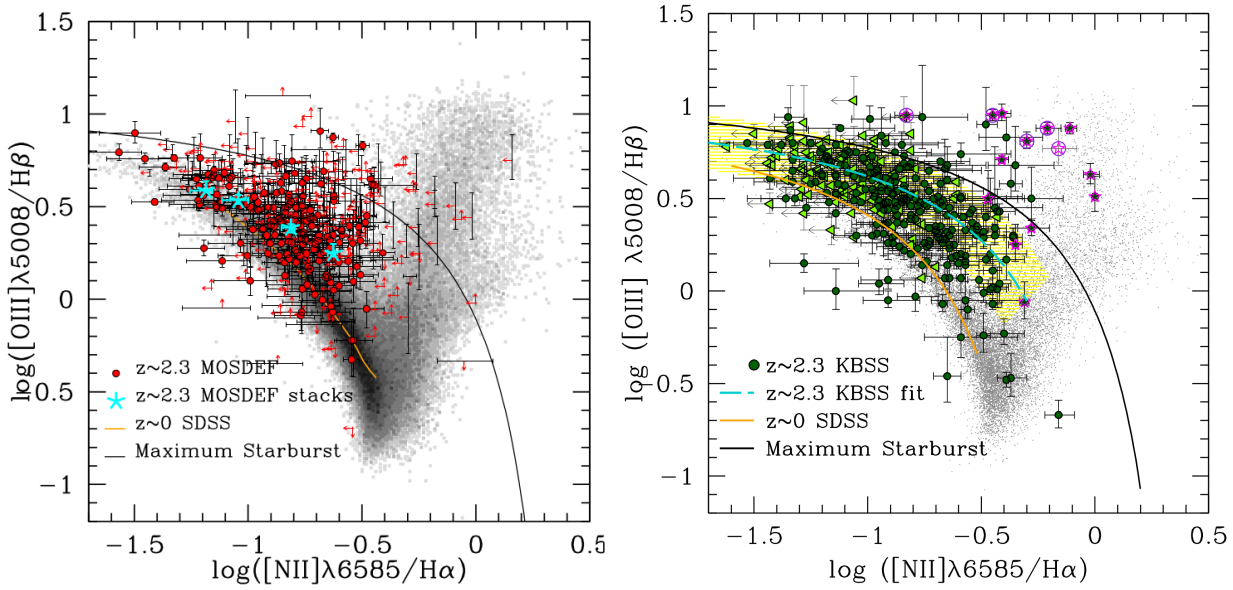

Figure 1.4: The [N II] BPT diagram for the MOSDEF (left) and KBSS-MOSFIRE (right) $z \sim 2$ samples. Both samples are offset from the local $z \sim 0$ SDSS sequence; however, the difference in the magnitude of the offsets from previous studies is ~0.1 dex (Steidel et al., 2014; Shapley et al., 2015).

As previously mentioned, gaining a complete understanding of this offset is important because strong rest-optical emission-lines trace many of the physical properties used to characterize the ISM. In the local universe, many calibrations exist between rest-optical emission-lines and the ISM properties (e.g., nebular gas-phase oxygen abundance; Pettini & Pagel 2004, see Figure 1.3). Until a full understanding of the [N II] BPT offset is obtained, it will remain unclear if these local calibrations can be used in the $z > 1$ universe (Bian et al., 2018; Sanders et al., 2020a).

To fully understand the physical driver of the offset on the [N II] BPT and the correlation between $z \sim 2$ galaxy properties and rest-optical emission-lines (e.g., nebular gas-phase oxygen abundance), a dataset of unprecedented size is needed. Chapter 3 is the beginning of a collaboration between MOSDEF and KBSS, with the goal of achieving such sample. With ~3000 galaxies observed between $1.4 \lesssim z \lesssim 3.8$ (about half at $z \sim 2$) over approximately 100 nights, the combined MOSDEF-KBSS sample represents the largest total investment of *Keck*/MOSFIRE time. In addition, the joint MOSDEF-KBSS sample would yield a sample with a statistical size capable of determining robust

trends in galaxy properties and relationships in the $z \sim 2$ universe approaching what already exists locally.

However, because of differences in selection methods of the two surveys (MOSDEF is a H-band (rest-optical) limited survey while KBSS is primarily selected based on $U_{\rm n}G\mathcal{R}$ (rest-UV) colors as well as results from previous studies (primarily concerning the [N II] BPT diagram; e.g., Steidel et al. 2014; Shapley et al. 2015; Strom et al. 2017), a comprehensive comparison of the two samples to search for possible biases is necessary before they can be combined. Here I perform a uniform comparison of the two samples to understand if any systematic differences between them exist, and, if so, how to merge the samples in a way that mitigates those differences for future work. In Chapter 3, I analyze the MOSDEF and KBSS samples utilizing consistent methodologies for emission-line fitting and stellar population synthesis modeling applied to emission-line-corrected photometry. This controlled approach removes any systematic biases originating from the different analysis methods used in past studies, and isolates the inherent differences of the galaxies in the samples. From the consistent emission-line measurements, I compare the locations of MOSDEF and KBSS samples on the [N II] and [S II] BPT diagrams. For the [N II] BPT diagram, I quantify the differences in the magnitude of their perpendicular offsets from the local $z \sim 0$ SDSS sequence. From the consistent fitting to the spectral energy distribution (SED), I compare the physical properties of the galaxies. The combination of these two analyses enables the discovery of a more precise difference in the emission-line properties (in particular the [N II] BPT offset) and if this difference is correlated with specific galaxy properties.

1.3 Probing MOSDEF Completeness

Over the course of the MOSDEF-KBSS comparison described in Chapter 3, we discovered that there is an incompleteness in the MOSDEF survey. Specifically, it was found that the MOSDEF $z \sim 2$ star-forming galaxies with high signal-to-noise (S/N) spectra (250 galaxies) are have different average properties — higher stellar mass (M_*), SFR(SED), and specific star formation rate (sSFR),

younger stellar population age, and redder UVJ colors — compared to the full sample of galaxies (786) observed at $z \sim 2$. This suggests that the subset of star-forming galaxies with high S/N might not be representative of star-forming galaxies in the $z \sim 2$ universe. In addition, the subset of $z \sim 2$ star-forming galaxies with high S/N comprised only ~32% of the observed $z \sim 2$ sample from which it was drawn. One caveat in terms of determining the unbiased properties of *star-forming* galaxies observed by the MOSDEF survey from the previous study in Chapter 3 is that the full observed sample contains AGN, quiescent galaxies, and galaxies with poor spectra where it was not possible to estimate a redshift from the observed MOSFIRE spectrum. Therefore, in Chapter 4 I utilize spectral stacking to analyze the emission-lines and host galaxy properties of all $z \sim 2$ star-forming galaxies (i.e., the MOSDEF observed sample with AGNs, quiescent galaxies, and galaxies lacking MOSFIRE spectroscopic redshifts removed). All of the galaxies in these stacks have good enough S/N in their MOSFIRE spectra to obtain a robust redshift, but not all of the emission-lines in the spectrum have the level of S/N (typically 3) needed to be considered an individual detection and therefore included in past published emission-line ratio work.

This analysis serves two purposes. First, it reveals if the subsample with high S/N spectra (as analyzed in, e.g., Sanders et al. 2018, 2021) is representative of the observed sample when the latter is restricted to star-forming galaxies like the high S/N subsample. Second, a large dataset gives better statistics for making more robust $z \sim 2$ calibrations (e.g., between emission-line ratios and nebular metallicity) similar to what exists locally. In this Chapter, I track the location of the stacked spectra on the [N II] BPT, [S II] BPT, and O_{32} vs. R_{23} diagrams and compare them to previous studies. Additionally, I compare line ratios commonly used as metallicity calibrations, specifically [N II]λ6585/Hα and ([O III]λ5008/Hβ)/([N II]λ6585/Hα), and dust attenuation tracers (Hα/Hβ) to past MOSDEF studies that use smaller high S/N samples as well as $z \sim 0$ galaxies.

In this Chapter I also investigate the properties of all galaxies at $1.9 \leq z \leq 2.7$ that could have been targeted for observation by the MOSDEF survey. As previously stated, the MOSDEF $z \sim 2$ observed sample contains 786 galaxies; however, there are ~3800 galaxies in this redshift range

that meet the H-band (rest-optical) magnitude limit and could have been targeted. Due to the limit on the number of observing nights allocated to the MOSDEF survey, it was not possible to observe this full ~3800 galaxy parent sample. Using available photometric data, I compare the galaxy properties of the 786 galaxy MOSDEF $z \sim 2$ observed sample with the full ~3800 galaxy parent sample to investigate if the galaxies selected for observation by MOSDEF are representative of the $z \sim 2$ universe.

1.4 A Merger at $z = 1.89$

In large surveys, there are bound to be some unexpected observations. In MOSDEF, one example of this is the observation of GOODS-S 43114. This galaxy is of interest because it shows visible signs of merging with GOODS-S 43683 based on *HST* WFC3 F160W 2D imaging, and the centroids of both galaxies are only ~18 kpc apart. Additionally, this galaxy pair is identified as a merger in van Dokkum & Brammer (2010) and the CANDELS morphology catalog (Kartaltepe et al., 2015). Figure 1.5 shows the *HST* WFC3 image of the merger (reproduced from van Dokkum & Brammer 2010).

It is important to study mergers because galaxy mass growth is attributed to both merging events and the smooth accretion of baryons and dark matter within the current ΛCDM cosmological framework. Therefore, mergers are an important component of structure formation modeling (e.g., Hopkins et al. 2010), and a current goal for observational galaxy evolution is to obtain empirical constraints on merger rates as a function of galaxy mass and redshift (e.g., Lotz et al. 2011). Merging systems have been observed out to $z \sim 6$ (Ventou et al., 2017), approximately ~0.9 Gyr after the big bang.

GOODS-S 43114 was observed with the MOSFIRE J-, H-, and K_s-bands, such that the strong rest-optical emission-lines typically targeted by MOSDEF (i.e., [O II]$\lambda\lambda$3727,3730, Hβ, [O III]$\lambda\lambda$4960,5008, Hα, [N II]λ6585, and [S II]$\lambda\lambda$6718,6733) fell outside of the MOSFIRE windows of observation. Instead, MOSDEF observed the Hγ and Hδ Balmer absorption lines in the J-band.

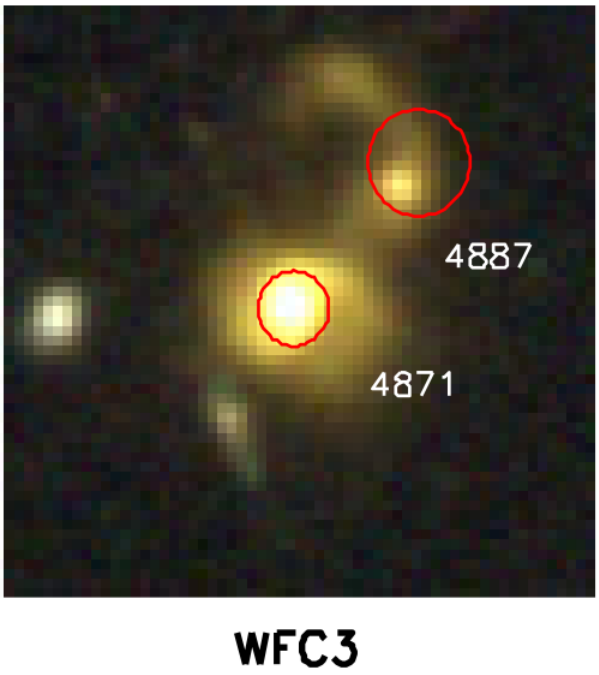

Figure 1.5: *HST* WFC3 image of GOODS-S 43114 and GOODS-S 43683 (labeled FW-4871 and FW-4887, respectively, in the image), reproduced from van Dokkum & Brammer (2010). The central regions of both galaxies are identified by red circles. Merger features such as diffuse, tidally-induced spiral tails and arms are visible in both galaxies.

These absorption lines are of interest because they contain information about the past star-formation history in a galaxy. Estimating the age of a stellar population can be difficult because age and metallicity of the stellar population have similar effects on the observed spectra (Worthey, 1994). However, Balmer lines are relatively insensitive to metals due to their dependence on main-sequence turnoff temperature instead of red giant branch temperature (Worthey & Ottaviani, 1997). Lower level Balmer lines (e.g., Hβ) are more strongly affected by nebular emission from ionized gas, especially in early-type galaxies, making higher order Balmer lines such as Hγ and Hδ more ideal for estimating stellar population age (Gonzalez 1993). The equivalent width of the Hδ absorption line (H$\delta_{\rm A}$) peaks when A-type stars dominate the spectrum, which occurs when a short burst of star formation is followed by rapid quenching.

In Chapter 5 I use SED fitting to study the galaxy properties of GOODS-S 43114 and GOODS-S

43683. In addition, I model the Hδ absorption line for GOODS-S 43114. The combination of these analyses will enable me to gain a better understanding of the physical properties of the merging system, as well as the star formation histories and state of the merger itself. Tn this study I will also fit the MOSFIRE J-band spectrum to obtain an estimate of the velocity dispersion (σ_e; i.e., the mean velocity of stars, gas, and dust) of GOODS-S 43114. Quantifying σ_e is important because it enables us to estimate the dynamical mass (M_{dyn}; i.e., the mass estimated by the gravitational potential) of the galaxy. At high redshift, S/N constraints make it difficult to measure σ_e, and subsequently M_{dyn} (e.g., such analysis was not previously possible with the *HST* grism spectra used in van Dokkum & Brammer 2010). The dynamical mass is an important quantity to obtain as it is the most direct probe of dark matter halos and constrains the cosmological cold dark matter in hierarchical structure formation for galaxy evolution models (e.g., Gnerucci et al. 2011). Therefore, in Chapter 5 I aim to obtain a measurement of both velocity dispersion and dynamical mass.

1.5 Local OH Spectroscopy

It is widely accepted that most massive galaxies likely host a supermassive black hole (SMBH) at or near the center[1]. The SMBH in a galaxy can be referred to as "active" if there is a significant amount of accretion of gas and dust on to it. When this occurs, these galaxies host an AGN. Despite the gravitational sphere of influence of a SMBH being on the pc scale (galaxy sizes are on the kpc scale), AGNs are thought to play a important role in the evolution of massive galaxies through a process called feedback (Somerville & Davé, 2015).

One key mode of feedback is AGN-driven outflows of gas and dust, which is capable of quenching the growth of the SMBH and star formation in the host galaxy by displacing a large fraction of the ISM (Di Matteo et al., 2005; Sturm et al., 2011; Veilleux et al., 2013). Molecular gas observed in the mid- to far-IR can be used as a direct probe of these outflows (Spoon et al., 2013). Many

[1]Irregular galaxies do not always contain a SMBH. Dwarf galaxies have not been found to host an SMBH. Galaxy mergers in progress can result in a SMBH being outside of the central region of the galaxy; however, it is likely in the process of migrating to the central region.

different molecules have been found to trace outflows, but OH is regarded as one of the best due to its fast radiative rates, large dipole moment, and the fact that there are 14 OH transitions between 34-163 μm in the eight lowest-energy rotational levels.

Since we still do not have a full theoretical understanding of the observed OH spectra, in Chapter 6 I aim to take an empirical approach to uncover which observed galaxy properties may predict the conditions of OH in molecular gas. The OH molecule is a known outflow tracer, therefore, a more comprehensive understanding of the what physically influences the OH line profiles is important because it could help pave the way to better constraining the properties of molecular outflows. Some relationships between far-IR OH molecular line properties (primarily focused on the 119μm OH doublet) and host galaxy properties (e.g., AGN luminosity and 9.7μm silicate absorption Veilleux et al. 2013 and Stone et al. 2016) have already been found. Therefore, in Chapter 6 I look to build on this knowledge of OH molecular spectroscopy by investigating possible correlations between EW(OH) and host galaxy properties such as AGN luminosity, radiation field hardness, dust temperature, and dust obscuration. I quantify the EW of six OH lines in the far-IR spectrum – 65μm, 71μm, 79μm, 84μm, 119μm, and 163μm – and use a large sample of archival data taken with the Photoconductor Array Camera and Spectrometer (PACS) instrument (Poglitsch et al., 2010) on the *Herschel Space Observatory* (Pilbratt et al., 2010). Additionally, I discuss how correlations between EW(OH) and these host galaxy properties are related to the method of excitation for these transitions.

1.6 Roadmap

To summarize, my thesis focuses on the study of rest-optical spectroscopy and physical properties of star-forming galaxies at $z \sim 2$ in the MOSDEF survey and the characterization of far-IR OH doublet lines in $z \sim 0$ galaxies. Chapter 2 analyzes the rest-optical emission-line, physical, and chemical properties of the complete MOSDEF survey to understand the physical driver of the [N II] BPT offset. Chapter 3 compares the MOSDEF and KBSS $z \sim 2$ star-forming samples to uncover

key results in previously published works (e.g., magnitude of the [N II] BPT offset) do not agree. Chapter 4 explores the compleness of the MOSDEF survey, comparing the full sample of star-forming galaxies to the subset with high S/N spectra as well as comparing the full parent sample to the smaller subset targeted by MOSDEF. Chapter 5 investigates a unique galaxy in the MOSDEF survey which is undergoing a merger at $z = 1.89$. Finally, Chapter 6 explores the far-IR OH profiles in a diverse galaxy population, looking for trends between EW(OH) and galaxy observables.

CHAPTER 2

The MOSDEF Survey: A Comprehensive Analysis of the Rest-optical Emission-line Properties of $z \sim 2.3$ Star-forming Galaxies

2.1 Introduction

Rest-frame optical emission-line spectroscopy is one of the most important observational tools for understanding galaxy formation and evolution. Such spectra provide a wealth of information about a galaxy, including its star-formation rate (SFR), dust extinction, active galactic nucleus (AGN) activity, virial and non-virial dynamics (e.g., outflows) and properties of the ionized interstellar medium such as the metallicity, electron density (n_e), and ionization parameter (U; i.e., the ratio of ionizing photon density to hydrogen, and therefore electron, density). Accordingly, knowledge about the emission-line properties of star-forming galaxies across cosmic time is essential for understanding the evolution of the stellar and gaseous content in galaxies. It is of particular interest to study rest-optical emission-line spectra of galaxies at $z \sim 2$, which represents the epoch of peak star formation in the universe (Madau & Dickinson, 2014) and a time before the modern Hubble sequence was fully in place.

In early work, Baldwin et al. (1981) showed how diagnostic diagrams measuring the intensity ratios of [O III]λ5008/Hβ vs. [N II]λ6585/Hα, i.e., the "[N II] BPT diagram," can be used to distinguish between star formation and AGN activity as the ionizing source for a galaxy. Other

authors have also considered the [O III]λ5008/Hβ vs. [S II]$\lambda\lambda$6718,6733/Hα diagram (originally introduced in Veilleux & Osterbrock 1987 and referred to hereafter as the "[S II] BPT diagram") when investigating the ionization mechanism of a galaxy. Indeed, the shape of the ionizing spectrum as well as the typical ionization parameter are different in gas excited by an AGN as opposed to by hot stars. Accordingly, AGNs and star-forming galaxies occupy distinct regions within rest-optical emission-line diagrams. These diagnostic diagrams also reveal information about the physical properties of the galaxies. For example, stellar mass (M_*) and metallicity have been found to increase with decreasing [O III]λ5008/Hβ and increasing [N II]λ6585/Hα along the local star-forming sequence in the [N II] BPT diagram (e.g., Masters et al. 2016).

Another diagnostic diagram commonly used to characterize the properties of star-forming galaxies is the [O III]$\lambda\lambda$4960,5008/[O II]$\lambda\lambda$3727,3730 (O_{32}) vs. ([O III]$\lambda\lambda$4960,5008+[O II]$\lambda\lambda$3727,3730)/Hβ (R_{23}) diagram. O_{32} and R_{23} are rough tracers for ionization parameter and metallicity, respectively. This diagram allows us to probe such physical quantities in star-forming galaxies (e.g., Lilly et al. 2003; Nakajima et al. 2013). For local galaxies, there is an increase in metallicity from the high excitation end (high O_{32} & R_{23}) to the low excitation tail (low O_{32} & R_{23}) on this diagram (Andrews & Martini, 2013; Shapley et al., 2015).

Early studies with Keck/NIRSPEC found that the location of galaxies on the [N II] BPT diagram is redshift dependent, as galaxies with $z > 1$ are found to be offset from local Sloan Digital Sky Survey (SDSS; York et al. 2000) galaxies, showing elevated [O III]λ5008/Hβ at fixed [N II]λ6585/Hα (or vice versa; e.g., Shapley et al. 2005; Erb et al. 2006b; Liu et al. 2008). Based on new observations with multi-object near-infrared spectrographs on 8-10-meter class telescopes, the sample of high-redshift galaxies with measurements of the BPT diagram emission lines now numbers in the hundreds. Of note, two large surveys of the high-redshift BPT diagram include the MOSFIRE Deep Evolution Field (MOSDEF; Kriek et al. 2015) survey and the Keck Baryonic Structure Survey (KBSS; Steidel et al. 2014), which find, based on much more robust statistical evidence, that high-redshift galaxies tend to have elevated [O III]λ5008/Hβ and/or [N II]λ6585/Hα compared

to local galaxies (Steidel et al., 2014; Shapley et al., 2015, 2019; Sanders et al., 2016; Strom et al., 2017).

Understanding this offset in emission-line ratios is vital because we use strong rest-optical emission-lines as empirical tracers for many physical properties (e.g., gas-phase oxygen abundance Pettini & Pagel 2004) of the interstellar medium (ISM). Due to the observed offset for $z > 1$ galaxies, it is unclear if local metallicity calibrations, e.g., Pettini & Pagel (2004), yield accurate metallicities when applied in the high-redshift universe. Therefore, it is essential to gain a complete understanding of why high-redshift galaxies have elevated [O III]λ5008/Hβ and/or [N II]λ6585/Hα compared to the local SDSS sample.

There have been many proposed explanations of this systematic offset. Possible explanations include variations in physical properties of galaxies such as H II region electron densities (or proportionally pressures), density structure, H II region ionization parameter, H II region ionizing spectra at fixed metallicities, gas-phase N/O abundance ratio differences, unresolved AGN activity, and shocks (e.g., Liu et al. 2008; Brinchmann et al. 2008; Wright et al. 2010; Kewley et al. 2013; Yeh et al. 2013; Masters et al. 2014; Coil et al. 2015; Sanders et al. 2016; Steidel et al. 2016; Strom et al. 2017; Freeman et al. 2019; Kashino et al. 2019; Shapley et al. 2019; Topping et al. 2020a). Galaxy selection effects could also be potential factors in this offset (Juneau et al., 2014).

Preliminary results from the MOSDEF survey (Shapley et al., 2015; Sanders et al., 2016) suggested that the offset in emission-line ratios is primarily due to elevated N/O at fixed O/H abundance patterns in $z \sim 2.3$ galaxies relative to local ones. Studies using KBSS data (Steidel et al., 2016; Strom et al., 2017, 2018) argued for a harder ionizing spectrum at fixed nebular metallicity as the main cause of the offset while other works using the Fiber Multi-Object Spectrograph (FMOS)-COSMOS survey (Kashino et al., 2017, 2019) or local analogues of high redshift galaxies (Bian et al., 2020) attribute the observed [N II] BPT offset to a higher ionization parameter. More recent results from the MOSDEF survey using the complete MOSDEF data set now suggest a harder ionizing spectrum drives the BPT offset (Shapley et al., 2019; Sanders et al., 2020a,b; Topping

et al., 2020a).

The completed MOSDEF survey provides an ideal data set of high-redshift galaxies to help explore the observed offset on the [N II] BPT diagram. This survey provides access to spectra of ∼1500 galaxies in the $z \sim 1.4-3.8$ redshift range, with full spectroscopic coverage of all the emission-lines needed to complete the [N II] BPT, [S II] BPT, and O_{32} vs. R_{23} diagrams in the $z \sim 1.4 - 2.6$ redshift range.

In this work, we improve upon the previous $z > 1$ BPT offset studies based on early MOSDEF data by Shapley et al. (2015) and Sanders et al. (2016). We now have the full MOSDEF sample in hand and apply a more careful spectral energy distribution (SED) fitting method that incorporates corrections to broadband photometric measurements for rest-optical emission-line fluxes. Accordingly, we derive unbiased age and stellar mass measurements, and can conduct a more thorough and complete investigation of the emission-line ratio properties of the MOSDEF sample. As an example of the level of improvement enabled by the full MOSDEF sample, the initial work by, Shapley et al. (2015) explored the location of 53 star-forming galaxies at $1.9 \leq z \leq 2.7$ on the [N II] BPT diagram, and investigated the M_*, specific SFR (sSFR), and SFR surface density (Σ_{SFR}) of the sample. In this study, the sample increases to 180 star-forming galaxies on the [N II] BPT diagram, and we also investigate additional galaxy parameters such as the galaxy effective radius (R_e), SFR, n_e, and stellar population age. Sanders et al. (2016) investigated how a sample of 53 star-forming galaxies at $1.9 \leq z \leq 2.7$ translated from the [N II] BPT diagram to the [S II] BPT diagram and O_{32} vs. R_{23} diagram. In the current study, that number is more than doubled to 122. Our more comprehensive analysis enables a better understanding of the observed offset between the MOSDEF sample and local galaxies on the [N II] BPT diagram. Through the analysis outlined above, we aim to determine the underlying physical causes of this offset.

The paper is organized as follows. In Section 2.2, we briefly describe the MOSDEF survey, and review our survey sample selection and data reduction. Section 2.3 presents the results of this study. Section 2.4 discusses the results and how they relate to photoionization models. Section

2.5 presents a summary of key results and looks ahead to future analyses. We adopt the following abbreviations for emission-line ratios used frequently throughout the paper.

$$\mathrm{N2} = [\mathrm{N\ II}]\lambda 6585/\mathrm{H}\alpha \tag{2.1}$$

$$\mathrm{S2} = [\mathrm{S\ II}]\lambda\lambda 6718, 6733/\mathrm{H}\alpha \tag{2.2}$$

$$\mathrm{O3} = [\mathrm{O\ III}]\lambda 5008/\mathrm{H}\beta \tag{2.3}$$

$$\mathrm{R_{23}} = ([\mathrm{O\ III}]\lambda\lambda 4960, 5008 + [\mathrm{O\ II}]\lambda\lambda 3727, 3730)/\mathrm{H}\beta \tag{2.4}$$

$$\mathrm{O_{32}} = [\mathrm{O\ III}]\lambda\lambda 4960, 5008/[\mathrm{O\ II}]\lambda\lambda 3727, 3730 \tag{2.5}$$

$$\mathrm{O3N2} = \mathrm{O3/N2} \tag{2.6}$$

O_{32} and R_{23} have already been defined, but we include them here for completeness. All emission-line wavelengths are vacuum wavelengths. Throughout this paper, we adopt a Λ-CDM cosmology with $H_0 = 70$ km s^{-1} Mpc^{-1}, $\Omega_m = 0.3$, and $\Omega_\Lambda = 0.7$. Also, we assume the solar abundance pattern from Asplund et al. (2009).

2.2 Methods

2.2.1 MOSDEF Sample & Ancillary Measurements

The MOSDEF survey was a 48.5-night observing program spanning multiple years (2012-2016), using the MultiObject Spectrometer For Infra-Red Exploration (MOSFIRE; McLean et al. 2012) on the 10 m Keck I telescope telescope. The survey targets three redshift ranges: $1.37 \leq z \leq 1.70$, $2.09 \leq z \leq 2.61$, and $2.95 \leq z \leq 3.80$. These ranges are chosen to optimize the detection of strong rest-optical emission lines within windows of atmospheric transmission. There are 354, 678, and 266 galaxies that have been spectroscopically confirmed in the MOSDEF low, medium, and high-redshift ranges, respectively. The sample is H-band magnitude limited, and is located in the well-studied CANDELS and 3D-*HST* legacy fields (Grogin et al., 2011; Koekemoer et al., 2011; Momcheva et al., 2016): AEGIS, COSMOS, GOODS-N, GOODS-S, and UDS. The ancillary data

from these fields enables us to probe other properties of the sample (e.g., galaxy size and stellar mass).

In this study, we restrict the sample to the central redshift bin, spanning the redshift range to $1.9 \leq z \leq 2.7$ to reflect the scatter between target photometric and measured spectroscopic redshifts (i.e., the fact that not all spectroscopic redshifts, when actually measured, fell precisely within the target $2.09 \leq z \leq 2.61$ window). For galaxies in this redshift range, [O II]$\lambda\lambda$3727,3730, Hβ, [O III]$\lambda\lambda$4960,5008, Hα, [N II]λ6585, and [S II]$\lambda\lambda$6718,6733 features are captured within the J, H, and K near-IR filter wavelength ranges. For MOSFIRE, the J, H, and K filters have typical respective wavelength coverages of 1.142-1.365 μm, 1.450-1.826 μm, and 1.897-2.427 μm and spectral resolutions of R = 3000, 3650, and 3600.

We imposed further restrictions to reach our final sample. Galaxies containing an AGN were identified and removed from the sample based on their IR colors, X-ray luminosity, or if N2 > 0.5 (Coil et al., 2015; Azadi et al., 2017; Leung et al., 2017). We also require a S/N $\geq$ 3 for each emission-line in our analysis. These criteria yielded a sample of 180 galaxies for initial classification in the [N II] BPT diagram, of which 122 galaxies are additionally detected in [S II]$\lambda\lambda$6718,6733 and [O II]$\lambda\lambda$3727,3730 and have size measurements from the *Hubble Space Telescope* (*HST*). The redshift distribution of the 180 MOSDEF star-forming galaxies at $z \sim 2.3$ with [N II] BPT diagram classifications is shown in Figure 2.1.

We correct Hα and Hβ line fluxes for stellar Balmer absorption as described in Kriek et al. (2015) and Reddy et al. (2015). We also dust correct emission-line ratios for which the member features differ significantly in wavelength, including O_{32} and R_{23}. For such corrections, we assumed the Cardelli et al. (1989) dust attenuation curve and an unreddened Hα/Hβ ratio of 2.86. In the case of emission-line ratios for which the lines are close in wavelength (O3, N2, and S2) dust correction was not applied.

In this study, we investigate additional galaxy photometric, spectroscopic, and structural properties

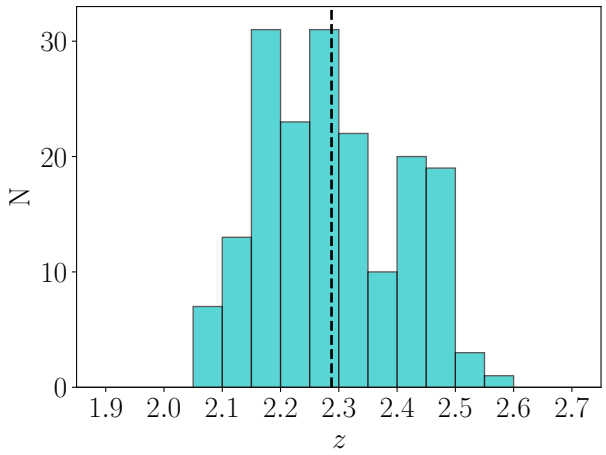

Figure 2.1: Redshift distribution of the 180 star-forming MOSDEF galaxies at $z \sim 2.3$ with [N II] BPT diagram classifications (i.e., S/N $\geq$ 3 detections in Hβ, [O III]$\lambda\lambda$4960,5008, Hα, and [N II]λ6585). The dashed vertical line displays the median redshift of the sample, $z_{\rm med} = 2.29$.

for the MOSDEF sample in order to try to better understand the observed rest-optical emission-line properties. The Hao et al. (2011) calibration for a Chabrier (2003) initial mass function (IMF) and solar metallicity is used to estimate SFR(Hα) from stellar-Balmer-absorption-corrected, dust-corrected, and slit-loss-corrected Hα luminosities (Reddy et al., 2015; Kriek et al., 2015; Shivaei et al., 2015). We used the SED fitting code, FAST (Kriek et al., 2009) to obtain key stellar population parameters including stellar mass and age. For this modeling, as a default we assumed star-formation histories of the delayed-τ form, where SFR $\propto t \times e^{-t/\tau}$. Here t is the time since the onset of star formation (i.e., age), and τ is the characteristic star-formation timescale. Given the range of best-fit τ values, the meaning of absolute ages is not necessarily clear. In order to obtain a better gauge of the relative maturities of the galaxy stellar populations in our sample, we used both normalized ages (i.e., t/τ), and also the age (t) obtained from constant star formation (CSF) models. Galaxy sizes, $R_{\rm e}$, are taken as the F160W galaxy half-light radii from the van der Wel et al. (2014) catalog, which were estimated using single-component Sérsic profile fits to the two-dimensional light distribution of galaxies in the CANDELS and 3D-*HST* fields. We combine

SFR(Hα) and R_e to estimate the SFR surface denisty, Σ_{SFR} as:

$$\Sigma_{SFR} = \frac{SFR(H\alpha)}{2\pi R_e^2} \tag{2.7}$$

We estimate the sSFR using SFR(Hα) and M_*, both of which are described above.

The electron density, n_e, is estimated with the [O II] and [S II] emission-line doublets using the method described in Sanders et al. (2016). In that study, the [O II] and [S II] electron densities agree within the uncertainties; both reliable tracers of the density within H II regions. [O II] is the preferred choice because the doublet typically has a higher S/N. We only use [S II] measurements when we do not have adequate [O II] data. This scenario arises for the following reasons:

1. Low S/N. A S/N $\geq$ 3 is required for each emission-line in the doublet to estimate n_e; however, a less restrictive requirement of S/N $\geq$ 3 for the overall doublet is sufficient for a galaxy to be included in the [S II] BPT and O_{32} vs. R_{23} diagrams. We only require S/N $\geq$ 3 for the individual doublet members when investigating the n_e of the sample.

2. Rejection of the [O II] doublet based on visual inspection. Such cases occur when skylines affect the [O II] doublet but not the [S II] doublet, spurious detections, and poor fits.

We set the lower limit for n_e to be 1 cm^{-3}.

2.2.2 SDSS Comparison Sample

Throughout this study, we compare our high-redshift MOSDEF sample to local galaxies. For this comparison, we use archival data from the SDSS Data Release 7 (DR7; Abazajian et al. 2009). We obtain galaxy properties and emission-line measurements from the MPA-JHU DR7 release of spectrum measurements[13]. SDSS galaxies are selected within the $0.04 \leq z \leq 0.10$ redshift range. We impose similar restrictions on our SDSS sample to those applied to the MOSDEF sample by requiring that each emission-line used in the analysis has a S/N $\geq$ 3. For the SDSS sample,

[13]https://wwwmpa.mpa-garching.mpg.de/SDSS/DR7/

we remove AGN using equation 1 from Kauffmann et al. (2003). Galaxies are also identified as having an AGN component if N2 > 0.5. These criteria result in a comparison sample of 103,422 SDSS galaxies when considering the [N II] BPT diagram alone, and 74,726 SDSS galaxies when considering galaxies with simultaneous detections across all three emission-line diagrams analyzed in this work ([N II] BPT, [S II] BPT, and O_{32} vs. R_{23}).

2.3 Results

2.3.1 The [N II] BPT Diagram

We start by investigating the locations of $z \sim 2.3$ star-forming galaxies in the [N II] BPT diagram based on the complete MOSDEF sample (Figure 2.2). We include the 180 galaxies with $\geq 3\sigma$ detections for all four emission-lines (Hβ, [O III]$\lambda\lambda$4960,5008, Hα, and [N II]λ6585) and the corresponding SDSS sample with the same four emission-lines detected. Similar to previous MOSDEF studies (e.g., Shapley et al. 2015; Sanders et al. 2016; Shapley et al. 2019; Topping et al. 2020a) and other studies from the literature (e.g., Shapley et al. 2005; Erb et al. 2006b; Steidel et al. 2014), there is a systematic offset observed for the high-redshift MOSDEF sample from the local sequence (Figure 2.2). The MOSDEF galaxies appear on average to be shifted towards the AGN region of the diagram with elevated N2 and/or O3 values, with some galaxies on the AGN side of the Kauffmann et al. (2003) AGN/SF boundary. There are even a small number of galaxies past the maximum starburst line from Kewley et al. (2001) as well.

To search for any biases in the sample based on the $\geq 3\sigma$ detection requirement in all four [N II] BPT lines, we construct spectral stacks for all MOSDEF galaxies at $1.9 \leq z \leq 2.7$ with Hα emission detected at S/N $\geq$ 3. There are four spectral stacks, divided into bins of stellar mass (see Sanders et al. 2018 for a full description of the method for constructing composite spectra). The emission-line ratios measured from stacked spectra follow the distribution of datapoints measured from MOSDEF galaxies with individual detections in all [N II] BPT lines. Therefore, the sample of individual detections seems to represent the parent $z \sim 2.3$ MOSDEF data set with minimal

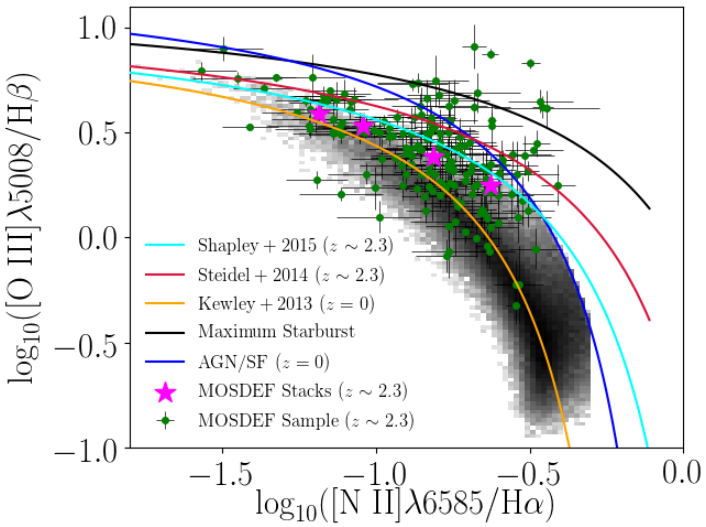

Figure 2.2: [N II] BPT diagram. Green points indicate $1.9 \leq z \leq 2.7$ MOSDEF galaxies with S/N ≥ 3 for all four plotted emission-lines. Large magenta stars represent measurements of stacks from composite spectra, binned by stellar mass, for $1.9 \leq z \leq 2.7$ MOSDEF galaxies. The grayscale 2D histogram indicates local SDSS galaxies. The cyan curve is the fit to the MOSDEF sample from Shapley et al. (2015). The orange curve is a fit to the $z \sim 0$ star-forming locus (Kewley et al., 2013). The red curve is the best fit to the $z \sim 2.3$ galaxies from the Keck Baryonic Structure Survey (KBSS; Steidel et al. 2014). The black curve is the maximum starburst line from Kewley et al. (2001). The blue curve is the empirical AGN/star-forming galaxy dividing line from Kauffmann et al. (2003).

bias. The four stacks, similarly to the individually detected galaxies, are offset from the local SDSS sample with elevated N2 and/or O3 values.

2.3.2 Dividing the $z \sim 2.3$ Sample in the [N II] BPT Diagram

Figure 2.2 shows that on the [N II] BPT diagram, part of the MOSDEF sample sits on or near the local SDSS sequence, while the remainder of the galaxies lie off the SDSS sequence and are shifted towards the local AGN region. We now investigate if the location of a high-redshift galaxy – either on or offset from the local SDSS sequence – is connected with other physical properties of the galaxy. For this analysis, we examine how galaxies on the [N II] BPT diagram populate the [S II] BPT and O_{32} vs. R_{23} diagrams, and therefore require the sample to have $\geq 3\sigma$ detections for all emission-lines on these diagrams: [O II]$\lambda\lambda$3727,3730, Hβ, [O III]$\lambda\lambda$4960,5008, Hα, [N II]λ6585,

and [S II]$\lambda\lambda$6718,6733. There are 123 MOSDEF galaxies that meet this criterion. One galaxy was removed because it does not have a R_e measurement, which brings the final sample to 122 MOSDEF galaxies.

For this analysis, we split the final sample of 122 galaxies into two groups using the functional form presented in Shapley et al. (2015), and adjusting the y-intercept so that our sample is divided in half. The equation used to split the MOSDEF sample into two groups of 61 galaxies each is

$$\log\big([\text{O III}]/\text{H}\beta\big) = \frac{0.67}{\log([\text{N II}]/\text{H}\alpha) - 0.20} + 1.065 \tag{2.8}$$

The new curve is 0.055 dex lower in [O III]λ5008/Hβ compared to equation 1 in Shapley et al. (2015). This splitting of the sample on the [N II] BPT diagram is shown in the upper left panel of Figure 2.3, where galaxies above the curve are indicated with blue symbols and those below with red symbols. Hereafter, we refer to the galaxies above the curve on the [N II] BPT diagram as the *high* sample, and the group below the curve as the *low* sample, following the nomenclature in Topping et al. (2020a). We plot the two samples on both the [S II] BPT diagram (upper right panel of Figure 2.3) and the O_{32} vs. R_{23} diagram (bottom panel of Figure 2.3). We also include binned median lines for both the *high* (blue) and *low* (red) populations. These binned medians are binned by $\log_{10}$(O3N2) for the [N II] BPT diagram, $\log_{10}$(O3) − $\log_{10}$(S2) for the [S II] BPT diagram, and $\log_{10}(O_{32}) + \log_{10}(R_{23})$ for the O_{32} vs. R_{23} diagram. The binning schemes above were adopted because they divide our sample into subgroups segregated roughly along the local star-forming sequence. For both the *high* and *low* samples, each of which contain 61 galaxies, there are four equally sized bins (three bins of 15 galaxies and one bin of 16).

For completeness, we checked for potential bias between the smaller sample of 122 galaxies with detections across all three emission-line diagrams and the parent sample of 180 galaxies defined based on detections in the [N II] BPT diagram alone. Of the 58 galaxies that were removed, 32 are above the curve dividing our sample (Equation 2.8) and 26 are below it on the [N II] BPT diagram. Because these two groups are approximately equal in size, we can expect that the smaller subset with [O II] and [S II] also detected (122 galaxies) has approximately the same average BPT offset

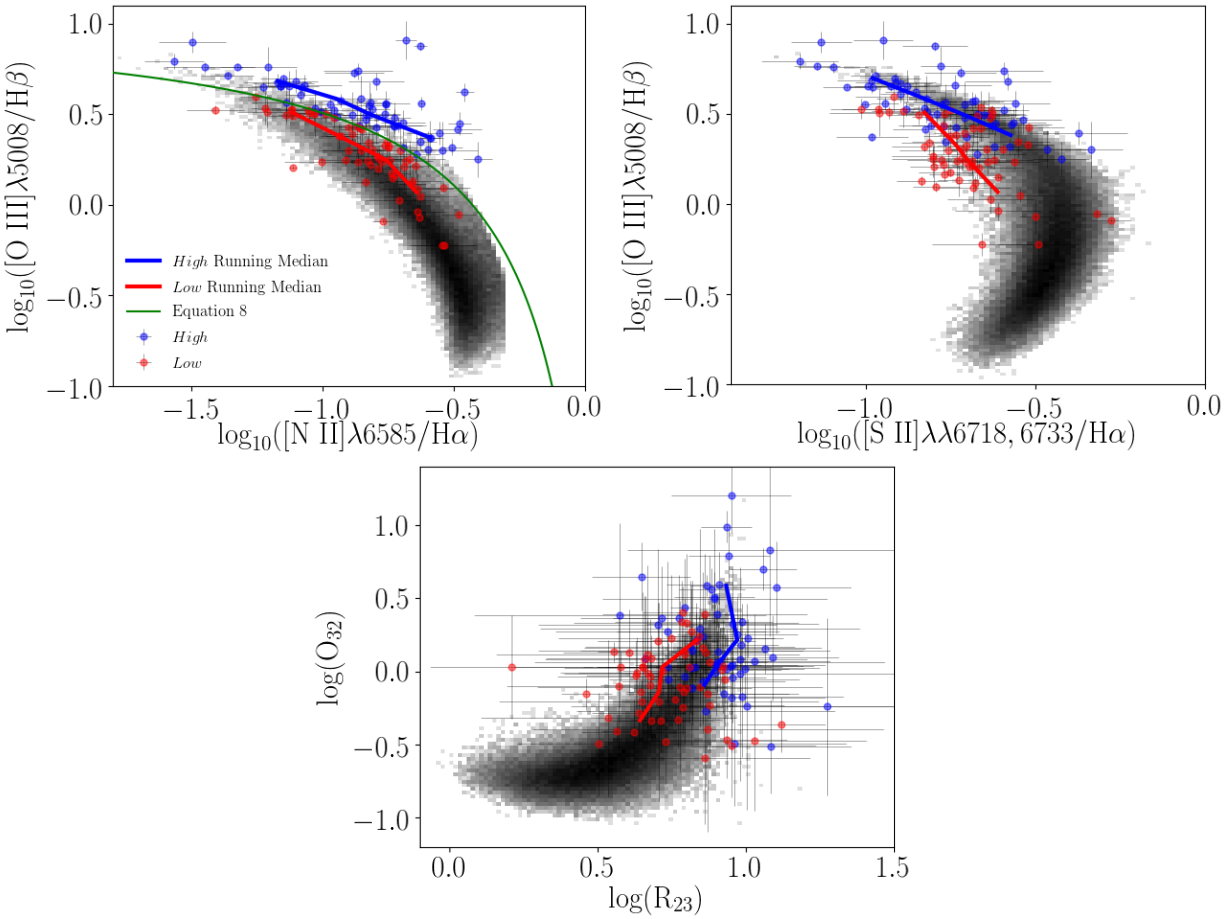

Figure 2.3: The sample of 122 MOSDEF galaxies that have $\geq 3\sigma$ detections in [O II]$\lambda\lambda$3727,3730, Hβ, [O III]$\lambda\lambda$4960,5008, Hα, [N II]λ6585, and [S II]$\lambda\lambda$6718,6733. Top left: we modify the MOSDEF fit from Shapley et al. (2015) by altering the y-intercept, so a curve with the same functional form splits the data set evenly into two populations. The red galaxies (*low* sample) fall close to the local SDSS sequence, while the blue galaxies (*high* sample) are shifted off the local sequence. Top right: The same two groups of data points as in the left panel. The red and blue lines indicate binned medians as described in Section 2.3.2. These lines show that the two groups are also separated in the [S II] BPT diagram, with the *high* sample higher in S2 and/or O3 than the *low* sample. Bottom center: The same two groups of data points as in the top panels. The red and blue lines again indicate binned medians as described in Section 2.3.2. The two groups are segregated in the O_{32} vs. R_{23} diagram as well, with the *high* sample having a higher median R_{23} values at fixed O_{32} where there is overlap in O_{32}.

as the larger [N II] BPT only sample (180 galaxies). Therefore, we can conclude that the cuts to create the sample of 122 galaxies with detections across all three emission-line diagrams do not introduce biases when compared to the larger parent sample of 180 galaxies.

2.3.2.1 Division in the Other Diagrams

We find separation between the *high* and *low* samples on both the [S II] BPT and O_{32} vs. R_{23} diagrams. For the [S II] BPT diagram, the *high* sample has a systematically higher S2 at fixed O3 (or vice versa). For the O_{32} vs. R_{23} diagram, the *high* sample has a systematically higher R_{23} value at fixed O_{32}.

Our new results on the [S II] BPT and O_{32} vs. R_{23} diagrams update the early MOSDEF results from Sanders et al. (2016). In this earlier work, based on a significantly smaller sample of only 53 galaxies, subsamples split in the [N II] BPT diagram were found to be well mixed in the [S II] BPT and O_{32} vs. R_{23} diagrams. In contrast, our results are consistent with those of Strom et al. (2017), based on the KBSS survey. In that study, the sample was split into two groups based on [N II] BPT diagram location – large and small offset from the local SDSS sequence. These subsamples were found to remain separated on the [S II] BPT diagram. Strom et al. (2017) did not investigate if this segregation remained on the O_{32} vs. R_{23} diagram. Section 2.4 contains a more in-depth comparison with the results from Strom et al. (2017) and a discussion of the implications for the underlying causes of the observed shift in the high-redshift [N II] BPT diagram.

2.3.2.2 Physical Properties of the Galaxies

The fact that there is a segregation in all three plots in Figure 2.3 implies that there are some key differences between galaxies offset from the local SDSS sequence and galaxies that overlap with it. We now investigate several galaxy physical properties to uncover any differences between the galaxies that fall into these two categories. In this study, as described in Section 2.2.1, we focus on: M_*, $\log(t/\tau)$ of the stellar population inferred from a delayed-τ star formation model, t of the stellar population assuming a constant star formation history, SFR(Hα), sSFR, $\Sigma_{\rm SFR}$, $R_{\rm e}$, and $n_{\rm e}$. We have

measurements of these properties for all 122 galaxies in the sample except for n_e. As discussed in Section 2.2.1, a more stringent requirement of a S/N $\geq$ 3 for each component of the [O II] or [S II] doublets is needed to estimate n_e while a S/N $\geq$ 3 for the combined doublet is needed to be plotted on the [S II] BPT and O_{32} vs. R_{23} diagrams. Accordingly, while our fiducial sample for analysis contains 122 galaxies, only 90 of them (44 *high* and 46 *low*) have reliable n_e estimates.

We show how the *high* and *low* samples divide in the space of each of these parameters using histograms, marking the median value of the parameter with solid lines for each *high* and *low* population (Figure 2.4). Showing the data in this format clearly highlights how the *high* and *low* samples separately distribute in each of the galaxy parameters and, accordingly, which of the galaxy parameters are correlated with the location of galaxies on the [N II] BPT diagram. The median values for the *high* and *low* populations are listed with 1σ uncertainties derived from bootstrap resampling in Table 2.1. We also list the probabilities, based on the Kolmogorov-Smirnov (K-S) test, of the null hypothesis that the *high* and *low* samples are drawn from the same parent distribution.

While the distributions of the *high* and *low* samples significantly overlap for some galaxy parameters, there are several parameters for which the *high* and *low* distributions are measurably offset in the median and spread. These results indicate that *high* sample of MOSDEF galaxies tend to have a smaller R_e and M_*, but a larger sSFR and Σ_{SFR} compared to the *low* sample. We also note that even though R_e, sSFR, and Σ_{SFR} are correlated with M_*, at fixed M_* the *high* sample is still found to be smaller with larger sSFR and Σ_{SFR} values compared to the *low* sample. The variation in median Σ_{SFR} between the two samples can be attributed to the difference in median R_e. At fixed size, the median SFR(Hα) values for the *high* and *low* populations agree within the uncertainties. With smaller significance, the *high* sample is also younger (smaller median t/τ and CSF t). We find no mutual correlation for either n_e or SFR with the the location of galaxies on the [N II] BPT diagram.

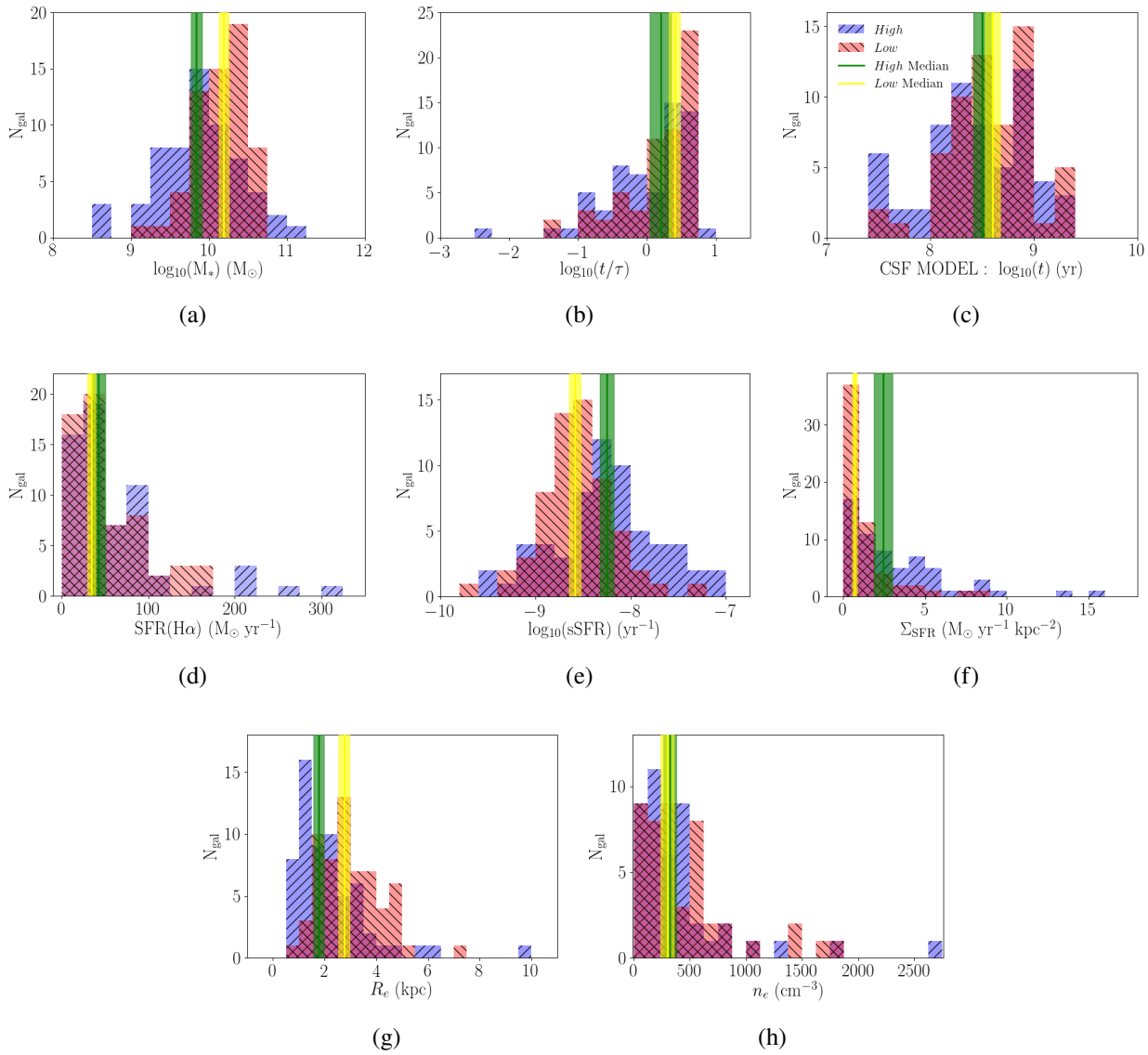

Figure 2.4: Distribution of physical properties for the 122 galaxy MOSDEF sample shown in Figure 2.3 where the blue and red bins correspond to the *high* and *low* samples, respectively. The green lines are the median values for the *high* population, while the yellow lines are the median values for the *low* population. The median values with uncertainties for both populations are given in Table 2.1. The following galaxy properties are shown: **(a)** M_*, **(b)** $\log(t/\tau)$ of the stellar population using a delayed-τ star formation model, **(c)** t of the stellar population assuming a constant star formation history, **(d)** SFR(Hα), **(e)** sSFR, **(f)** $\Sigma_{\rm SFR}$, **(g)** $R_{\rm e}$, and **(h)** $n_{\rm e}$ estimated from the [O II] or [S II] doublet emission-lines. We find that the median M_*, sSFR, $\Sigma_{\rm SFR}$, and $R_{\rm e}$ differ significantly based on their location in the [N II] BPT Diagram, while the other properties are the within the uncertainties of each other.

Table 2.1: Median Values for Physical Properties of the *High* and *Low* Samples

Physical Property (1)	*High* Median (2)	*Low* Median (3)	p-value (4)	Statistical significance (σ) (5)
$\log_{10}(M_*/M_\odot)$	9.84 ± 0.07	10.19 ± 0.06	0.0040	2.9σ
$\log_{10}(t/\tau)$	0.20 ± 0.16	0.40 ± 0.08	0.2480	1.2σ
CSF $\log_{10}(t/\mathrm{yr})$	8.50 ± 0.08	8.60 ± 0.07	0.1671	1.4σ
SFR(Hα) ($M_\odot$ yr^{-1})	42.7 ± 7.5	34.3 ± 4.9	0.7923	0.3σ
sSFR (yr^{-1})	-8.25 ± 0.07	-8.58 ± 0.06	0.0002	3.7σ
Σ_{SFR} ($M_\odot$ yr^{-1} kpc^{-2})	2.45 ± 0.56	0.70 ± 0.15	0.0002	3.7σ
R_e (kpc)	1.77 ± 0.20	2.75 ± 0.21	0.00004	4.1σ
n_e (cm^{-3})	322 ± 58	300 ± 59	0.5341	0.6σ

Note. — Col. (1): Physical property of the galaxies in the sample shown in Figure 2.4. Col. (2): Median value with uncertainty of the *high* sample. Col. (3): Median value with uncertainty of the *low* sample. Col. (4): Two-tailed p-value, based on the K-S test, estimating the probability that the null hypothesis can be rejected. Col. (5): Statistical significance (i.e. the σ value) that the p-value corresponds to.

2.4 Discussion

2.4.1 Comparison with Previous Work

We have divided the $z \sim 2.3$ MOSDEF sample according to location in the [N II] BPT diagram. When separated in this manner, our sample also shows segregation in the [S II] BPT and O_{32} vs. R_{23} diagrams. These results update earlier MOSDEF work (Shapley et al., 2015; Sanders et al., 2016), and are in agreement with more recent MOSDEF studies (e.g., Shapley et al. 2019; Topping et al. 2020a). Our findings for the population segregation on the [S II] BPT diagram are also in agreement with those of Strom et al. (2017), in which a similar segregation in the [S II] BPT diagram is found for $z \sim 2.3$ star-forming galaxies from the KBSS survey when separated by [N II] BPT location. Strom et al. (2017) did not consider the relative positions of the KBSS equivalent of our *high* and *low* galaxies on the O_{32} vs. R_{23} diagram. However, these authors do show how photoionization models with different input parameters (i.e., varying ionizing spectrum at fixed nebular metallicity) vary across the O_{32} vs. R_{23} parameter space. Specifically, it is shown that models with harder ionizing spectra at fixed nebular metallicity are offset towards higher R_{23} at fixed O_{32}. Strom et al. (2017) additionally show that models with harder ionizing spectra produce higher O3 at both fixed S2 and N2. These separations are at least qualitatively similar to that observed between our *high* and *low* samples.

The suggested implication of these segregations on both [S II] BPT and O_{32} vs. R_{23} diagrams is a harder ionizing spectrum at fixed O/H, relative to local galaxies (e.g., Strom et al. 2017; Shapley et al. 2019; Topping et al. 2020a). A harder ionizing spectrum at fixed nebular metallicity in $z \sim 2.3$ galaxies may arise due to α-enhancement (i.e., super-solar O/Fe values) in the massive stars exciting the ionized gas in star-forming regions. Such abundance patterns may arise naturally in high-redshift galaxies, given the young median ages of their stellar populations (e.g., Steidel et al. 2016; Sanders et al. 2020a; Topping et al. 2020a).

We have also shown in Figure 2.4 that the *high* sample is associated with more compact (i.e., smaller

R_e and higher Σ_{SFR}), and intense (i.e., higher sSFR) star formation than the *low* sample. These differences between the two populations exist at fixed stellar mass as well. It will be important to explore the links between these global galaxy properties and the abundance patterns of massive stars using realistic galaxy formation simulations (e.g., FIRE-2; Hopkins et al. 2018).

2.4.2 Comparison with Photoionization Models

2.4.2.1 Modeling Methodology

We use photoionization models to explain simultaneously the joint distributions of *high* and *low* galaxies in the [N II] and [S II] BPT and O_{32} vs. R_{23} diagrams. For this analysis, we use a combination of the code Cloudy (v17.01; Ferland et al. 2017) and the Binary Population And Spectral Synthesis (BPASS) v2.2.1 models (Eldridge et al., 2017; Stanway & Eldridge, 2018). BPASS generates the spectra of model stellar populations, which we used as the input ionizing spectrum to Cloudy. We assume a constant star-formation history in the BPASS models, as constructed in Topping et al. (2020a). Additionally, we use stellar population models that follow a Chabrier (2003) IMF and set 100 $M_\odot$ as the high-mass cutoff.

Using the BPASS input ionizing spectrum, Cloudy predicts the rest-optical emission-line strengths for different combinations of physical properties. For this analysis, we set the N/O abundance ratio using equation (2) in Pilyugin et al. (2012), use the Asplund et al. (2009) [S II] abundance pattern, and assume that $n_e = 250$ cm^{-3}, which is characteristic of $z \sim 2.3$ galaxies (Sanders et al., 2016; Strom et al., 2017; Harshan et al., 2020). This value for n_e is slightly lower than the median values of our *high* and *low* samples; however, it is within the uncertainties of the *low* population and not significantly less than the lower limit of the *high* population median. The best-fit n_e values from this study also agree within the uncertainties with the those reported in Sanders et al. (2016) and Strom et al. (2017). In addition, we use Cloudy to estimate the contribution from the nebular continuum and added this into the BPASS stellar population models. To estimate this nebular contribution, we assume that $\log(U) = -2.5$ and $\log(Z_{neb}/Z_\odot) = -0.2$, which are typical

of $z \sim 2.3$ galaxies (Sanders et al., 2016). Changing these conditions does not significantly affect the nebular continuum, which is small contribution to the overall spectrum. Therefore, adjustments to the initial parameters for the nebular continuum have minimal impact on the final model fitting (Topping et al., 2020a). As a sanity check on our models, we are able to reproduce the results from Steidel et al. (2016) using their initial input parameters.

For our Cloudy+BPASS model grids, we varied the following parameters: stellar metallicity (Z_*), t (i.e., age) of the stellar population assuming a constant star formation history, gas-phase oxygen abundance ($Z_{\rm neb}$), and ionization parameter (U). We find that our choice of t over the range 10^7 to $10^{9.8}$ yr (Topping et al., 2020a) has a negligible effect of the position of models on all three diagrams, so we chose a value of $10^{8.6}$ yr because it is approximately the median t (assuming a constant star-formation history) of the $z \sim 2.3$ MOSDEF sample in this study.

In the photoionization model grids, ionization parameter and nebular metallicity range between $-3.60 \leq \log(U) \leq -1.40$ and $-1.3 \leq \log(Z_{\rm neb}/Z_\odot) \leq 0.20$, respectively. Within the ranges of interest ($-3.40 \leq \log(U) \leq -2.40$ and $-1.00 \leq \log(Z_{\rm neb}/Z_\odot) \leq 0.00$), these grids are finely sampled in steps of 0.02 dex. Outside of these regions, $\log(U)$ changes in steps of 0.20 dex. We also include three additional values for $\log(Z_{\rm neb}/Z_\odot)$: 0.10 and 0.20, extending up towards higher metallicity, and -1.30 to round out the low-metallicity extreme. The stellar metallicity of the BPASS models includes discrete values of Z_* = 0.00001, 0.0001, 0.001, 0.002, 0.003, 0.004, 0.006, 0.008, 0.01, 0.014, 0.02, and 0.03. We assume Asplund et al. (2009) solar abundance (i.e., Z_* = 0.014).

2.4.2.2 Fixed Z_* Models

In a recent MOSDEF study, Topping et al. (2020a) combined rest-UV and rest-optical spectra for a sample of 62 star-forming galaxies at $z \sim 2.3$ and constructed *high* and *low* samples using a similar methodology as this study (i.e. based on offset from the local sequence on the [N II] BPT diagram). Fitting composite rest-frame UV spectra from their *high* and *low* stacked spectra resulted in best-fit

Z_* values of 0.001 and 0.002, respectively. Best-fit $Z_{\rm neb}$ and log(U) values were then based on comparing the emission-line ratios measured from the stacked spectra with those generated by the same Cloudy photoionization model described above assuming the stellar metallicities obtained from the rest-UV spectra. We do not have rest-UV spectra for the full sample of 122 galaxies in our emission-line analysis, and therefore cannot obtain tight constraints on the median Z_* for the *high* and *low* samples of this work from our rest-optical data alone. Accordingly, we adopt the best-fit Z_* values from Topping et al. (2020a) for our two MOSDEF populations. This is a reasonable assumption because 45/62 (73%) of the galaxies in Topping et al. (2020a) are in this work, and the *high* and *low* samples are reasonably well matched to the corresponding samples in Topping et al. (2020a).

Figure 2.5 shows Cloudy+BPASS photoionization models overplotted with our data, assuming Z_* values of 0.001 (left column; *high* sample) and 0.002 (right column; *low* sample). Using the solar value of 12+log(O/H) = 8.69 (Asplund et al., 2009), we convert log($Z_{\rm neb}/Z_\odot$) to 12+log(O/H). Each curve corresponds to a different 12+log(O/H) value, as indicated by color. The triangular points along each nebular metallicity curve comprise the sequence of log(U) values. The points are smallest for log(U) = −3.60 and largest for −1.40, therefore, increasing in size as log(U) increases. The Cloudy+BPASS model grids are overplotted on the MOSDEF and SDSS data. The green and yellow squares on the [N II] BPT, [S II] BPT, and O_{32} vs. R_{23} diagrams indicate, respectively, the median values of the *high* and *low* samples. Uncertainties for these median values were obtained through bootstrap resampling and perturbing each resampled data point by its individual error according to a normal distribution. The sample median was calculated for each bootstrapped, perturbed sample, and then the 16$^{\rm th}$ and 84$^{\rm th}$ percentiles of the distribution of medians were taken as the lower and upper bounds, respectively, as the 1σ confidence interval on the plotted median value.

Using stellar metallicities of 0.001 and 0.002, respectively, for the *high* and *low* populations, we then estimate the best-fit 12+log(O/H) and log(U) values for the sample median data points using

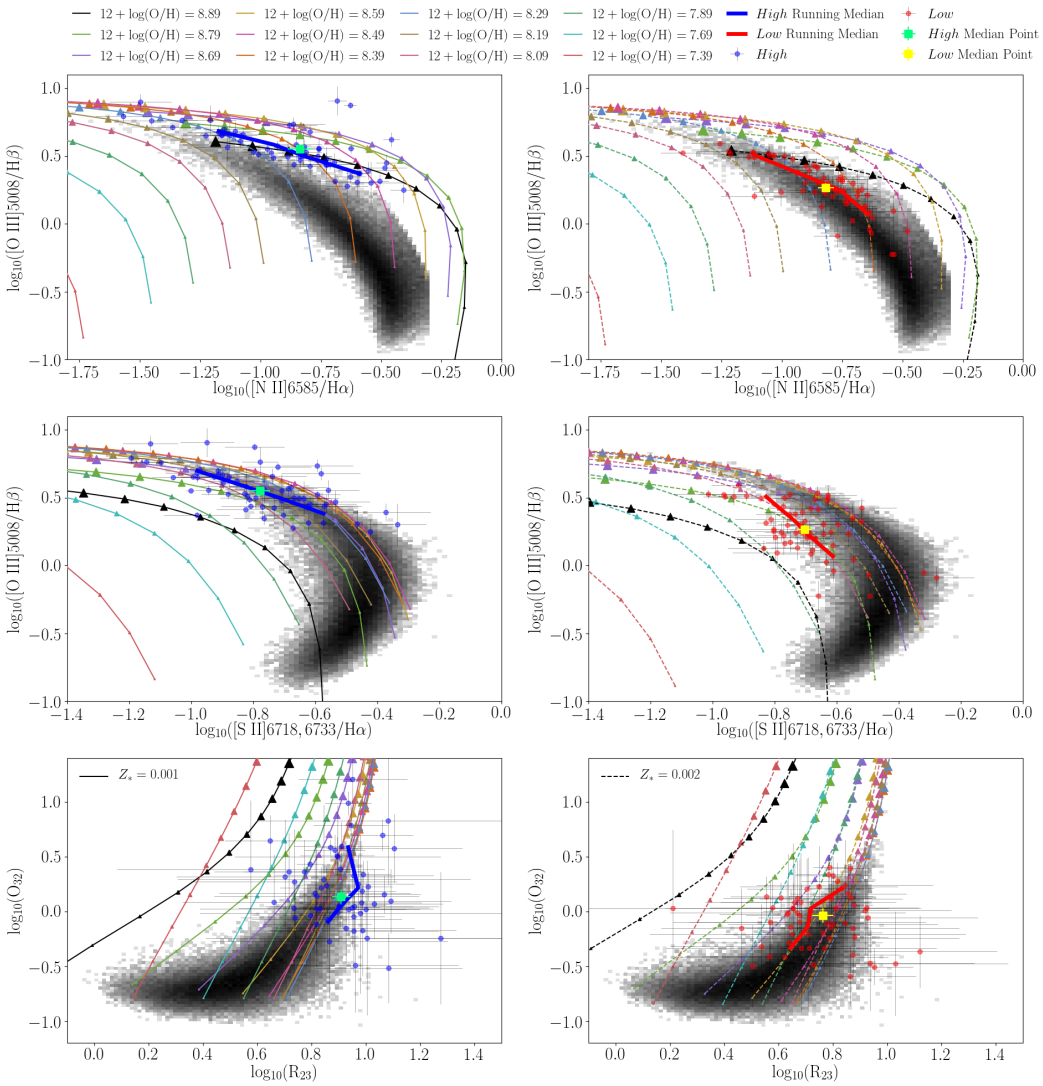

Figure 2.5: Left column: $Z_* = 0.001$ (solid lines). Right column: $Z_* = 0.002$ (dashed lines). Cloudy+BPASS model emission-line ratios shown on the [N II] BPT (top row), [S II] BPT (middle row), and O_{32} vs. R_{23} diagrams (bottom row). The triangle data points on the curves increase in size as $\log(U)$ increases. To avoid overcrowding, we vary $\log(U)$ in steps of 0.20 dex and have nebular metallicity range between $-0.60 \leq 12+\log(O/H) \leq 0.20$ in 0.10 dex steps, with additional values that extend deeper into the subsolar regime included as well (-0.80, -1.00, and -1.30). We adopt an age of $10^{8.6}$ yr because it is the approximate median age of the MOSDEF sample (given a constant star-formation history), but the results are not sensitive to age. Also plotted are the local SDSS sample (grey 2D histogram) and the *high* (blue points) and *low* (red points) MOSDEF samples with binned medians as shown in Figure 2.3. The green and yellow squares, with associated uncertainties, are the median values of the *high* and *low* populations.

Table 2.2: Single Z_* Cloudy+BPASS Median Values for Physical Properties of the *High* and *Low* Samples

	Physical Property	*High* Median	*Low* Median
	(1)	(2)	(3)
Median Points	Z_*	0.001	0.002
	12+log(O/H)	$8.37^{+0.04}_{-0.04}$	$8.31^{+0.04}_{-0.02}$
	log(U)	$-2.88^{+0.04}_{-0.04}$	$-3.08^{+0.02}_{-0.04}$
Large-N2	Z_*	0.002	0.003
	12+log(O/H)	$8.49^{+0.02}_{-0.04}$	$8.41^{+0.02}_{-0.02}$
	log(U)	$-3.04^{+0.04}_{-0.04}$	$-3.26^{+0.04}_{-0.04}$
Small-N2	Z_*	0.001	0.001
	12+log(O/H)	$8.31^{+0.04}_{-0.04}$	$8.23^{+0.02}_{-0.02}$
	log(U)	$-2.60^{+0.06}_{-0.06}$	$-2.98^{+0.02}_{-0.02}$

Note. — Col. (1): Physical property of the sample. Col. (2): Median value with uncertainty of the *high* sample. Col. (3): Median value with uncertainty of the *low* sample. For Columns (2) & (3), the Z_* values were selected and were not obtained from fitting the data. Also, the more finely spaced grids that vary 12+log(O/H) and log(U) in steps of 0.02 dex were used.

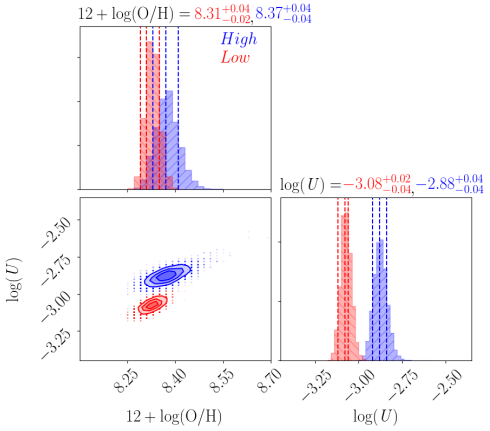

(a) Median data points

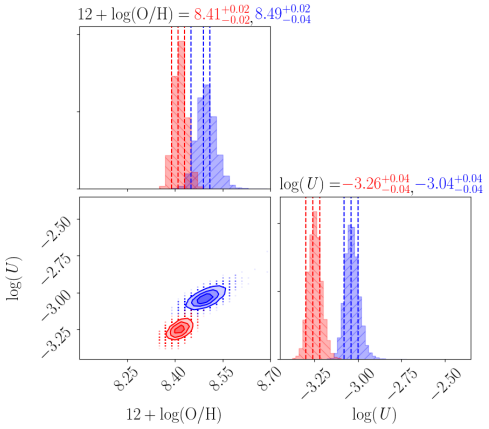

(b) Large-N2 data points

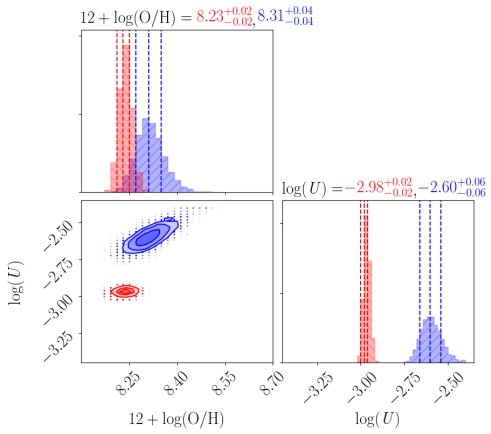

(c) Small-N2 data points

Figure 2.6: Corner plots comparing the distributions of 12+log(O/H) and log(U) for the *high* (blue) and *low* (red) MOSDEF populations. The distributions for the sample median points, i.e. green and yellow squares in Figure 2.5, (upper left), large-N2 endpoint of the sample binned medians (top right) and small-N2 endpoint of the sample binned medians (bottom center) are included. We assume Z_* values of 0.001 and 0.002 (median points; top left panel), 0.002 and 0.003 (large-N2 points; top right panel), and 0.001 and 0.001 (low-N2 points; bottom panel) for the *high* and *low* populations, respectively. The dashed lines on the histograms mark the median value and 1σ uncertainties (16$^{\text{th}}$ and 84$^{\text{th}}$ percentiles) for the distributions of 12+log(O/H) and log(U), and the three contours on the diagonal mark the 1, 1.5, and 2σ regions in the 2-D 12+log(O/H)-log(U) parameter space. It is shown that moving from large- to small-N2 corresponds to decreasing nebular metallicity and increasing ionization parameter. In each of the three distributions, the *high* population has a higher 12+log(O/H) and log(U).

a χ^2 method that compares the N2, S2, O3, and O_{32} emission-line ratios between the models and data. R_{23} is not used because it is not independent of the other emission-line ratios (i.e., R_{23} can be found from a combination of O3 and O_{32}). While Figure 2.5 displays 12+log(O/H) and log(U) in large steps, we use the finer grids of 0.02 dex spacing for both physical properties when estimating the best-fit sample values. The results for the best-fit 12+log(O/H) and log(U) values with 1σ uncertainties from the bootstrap resampling are shown in Table 2.2. The corner plot showing the distributions of these two properties obtained using the bootstrapped, perturbed N2, S2, O3, and O32 medians are shown in the top left panel of Figure 2.6.

We find that both 12+log(O/H) and log(U) are larger for the median data point of the *high* population (12+log(O/H) = $8.37^{+0.04}_{-0.04}$, log(U) = $-2.88^{+0.04}_{-0.04}$) compared to the median data point of the *low* population (12+log(O/H) = $8.31^{+0.04}_{-0.02}$, log(U) = $-3.08^{+0.02}_{-0.04}$). The difference in log(U) between the two samples is more statistically significant than the difference in 12+log(O/H), as median values of the latter agree within the uncertainties. Because the median electron densities of the *high* and *low* sample agree within the uncertainties (see Table 2.1), the difference in log(U) can be attributed to the *high* population having a higher number density of ionizing photons. This is a reasonable assumption given that the *high* sample has a lower median stellar metallicity (i.e., a harder median ionizing spectrum and greater ionizing photon production efficiency) in addition to more concentrated star formation (i.e., higher Σ_{SFR}) compared to the *low* sample. The *high* population also appears to be more α-enhanced, due to it having a lower Z_* but a higher 12+log(O/H) compared to the *low* population. Based on the variation of best-fit 12+log(O/H) and log(U) values between the *high* and *low* median data points, we conclude that quantifying both of these physical parameters, in addition to stellar metallicity (i.e., the hardenss of the ionizing spectrum), is important when explaining the distribution of high-redshift galaxies in the [N II] BPT diagram. It is worth noting that we have shown the *high* population to be less massive (i.e., smaller M_*) but more metal-rich (i.e., larger 12+log(O/H)) compared to the *low* population. This combination of physical properties is the opposite of what is expected based on results from previous studies investigating the mass-metallicity relationship (e.g., Tremonti et al. 2004; Steidel et al. 2014; Sanders et al. 2018, 2020a),

which show that M_* and 12+log(O/H) have a positive relationship. However, the differences in mass and metallicity between the *high* and *low* samples reflect the scatter in the mass-metallicity relationship.

To check the validity of our assumption that the N/O ratio is consistent between the *high* and *low* populations, we estimate log(N/O) for the sample medians based on the [N II]λ6585/[O II]$\lambda\lambda$3727,3730 tracer. We use the Strom et al. (2018) calibration to convert log([N II]λ6585/[O II]$\lambda\lambda$3727,3730) to log(N/O), and find that log(N/O) = -1.13 ± 0.05 and -1.08 ± 0.04 for the *high* and *low* samples, respectively. The consistency in log(N/O) between the *high* and *low* samples validates our Cloudy+BPASS model assumptions and rules out N/O variations as the primary driver of the [N II] BPT offset. This conclusion agrees with results from other current MOSDEF studies (e.g., Shapley et al. 2019; Sanders et al. 2020a,b; Topping et al. 2020b) as well as other $z \sim 2$ studies (e.g., KBSS; Steidel et al. 2014; Strom et al. 2017, 2018).

For the most part, these results are in agreement with Topping et al. (2020a). The best fit 12+log(O/H) and log(U) values from both studies are in agreement within 1σ, except for the log(U) of the two *high* populations, which agree within 2σ. However, this study finds a larger difference in log(U) between the *high* and *low* samples, 0.20 dex, compared to Topping et al. (2020a), 0.07 dex. On the other hand, Topping et al. (2020a) find a larger variance in 12+log(O/H) between the two populations, 0.10 dex, compared to this study, 0.06 dex. These differences are due to the slightly different median rest-optical line ratios for the *high* and *low* populations in Topping et al. (2020a) and in the current work.

To characterize the variation of physical properties within each of our *high* and *low* populations, we apply the same methodology of finding the best-fit 12+log(O/H) and log(U) values, but in this case for the two endpoints of the binned medians for the *high* and *low* samples in the [N II] BPT diagram. We use the same binning method for the [N II] BPT diagram (i.e., four equally sized bins based on O3N2 strength; see Section 2.3.2 above for complete details on binning) when calculating the median O3, N2, S2, and O_{32} emission-line ratios for the endpoints of both binned

median lines. Uncertainties for the line ratios of the median endpoints are estimated using the same methodology of bootstrap resampling coupled with perturbation of the datapoints of individual galaxies according to their error bars, as described above. On the [N II] BPT diagram, the binned medians move primarily in the N2 direction, therefore, we refer to the endpoints of both binned median lines as "large-N2" and "small-N2". It is important to note that the large-N2 endpoints of both *high* and *low* binned median lines have larger S2, and smaller O_{32} compared to the small-N2 endpoints. In other words, while the binning method was not the same on all three diagrams in Figure 2.3 (i.e., the four bins do not necessarily contain the same galaxies), the large-N2 bins on the [N II] BPT diagram have significant overlap with (and therefore roughly correspond to) the larger-S2, and smaller-O_{32} endpoints of the binned median lines on the [S II] BPT and O_{32} vs. R_{23} diagrams.

The results of Topping et al. (2020b) suggest that a positive correlation exists between N2 and Z_* (i.e., stellar metallicity tends to be higher at larger N2 values). Therefore, we vary the Z_* values that we assume for the large-N2 and small-N2 endpoints of the binned median lines accordingly. For the *low* population, we assume stellar metallicities of 0.003 and 0.001 (i.e., ±0.001 from the median Z_*) for the large-N2 and small-N2 points, respectively. Similarly, for the *high* population, we assume stellar metallicity values of 0.002 and 0.001 for the large-N2 and small-N2 points, respectively. We do not lower the stellar metallicity of the small-N2 point of the *high* population to our next available Z_* model value (0.0001, a factor of 10 lower than the next highest Z_* value) because the results from Topping et al. (2020b) do not suggest that such a significant variation in stellar metallicity is observed. It is important to note that while we do vary Z_* in accordance with the results from Topping et al. (2020a), the best-fit 12+log(O/H) and log(U) for the large-N2 and small-N2 endpoints of the *high* and *low* populations do not change significantly if we use Z_* = 0.001 and 0.002 (i.e., the Z_* values used for the median *high* and *low* population data points). We will discuss this systematic effect of how our choice in Z_* influences the best-fit 12+log(O/H) and log(U) in more detail below in Sections 2.4.2.3 and 2.4.2.4.

Median 12+log(O/H) and log(U) values for the large-N2 and small-N2 endpoints of the *high* and *low* populations are included in Table 2.2. The corner plots showing the distributions of 12+log(O/H) and log(U) for the large-N2 and small-N2 endpoints are shown in the top right and bottom panels, respectively, of Figure 2.6. In both samples we find an anti-correlation between 12+log(O/H) and log(U) along the binned median lines. Moving from large-N2 to small-N2 (therefore also large-S2 to small-S2 and small-O_{32} to large-O_{32}) leads to a lower 12+log(O/H) but a higher log(U). This anti-correlation between log(U) and 12+log(O/H) has been observed in local star-forming galaxies and H II regions (Pérez-Montero, 2014). In addition, this trend is consistent with the idea that the high O_{32} tail of the local sequence on the O_{32} vs. R_{23} diagram includes galaxies with low metallicity, and high ionization parameter (Shapley et al., 2015). Also, on the [N II] BPT diagram both stellar and nebular metallicity decrease along the local sequence (i.e., from low O3 and high N2 to high O3 and low N2).

2.4.2.3 Variable Z_* Models

As described above, thus far we have assumed Z_* values of 0.001 and 0.002 for the *high* and *low* population median points to match the best-fit values from modeling the rest-frame UV spectra of $z \sim 2.3$ MOSDEF galaxies (Topping et al., 2020a). While this is a reasonable assumption, we also investigate how relaxing our requirement on stellar metallicity affects the best-fit nebular metallicity and ionization parameter values of the two populations. For this additional analysis, we use the same χ^2 method described above (i.e., fitting the N2, S2, O3, and O_{32} emission-line ratios). However, we not only fit for 12+log(O/H) and log(U), but also treat Z_* as a free parameter. We investigate two different model grids: one that allows a small range of Z_* for the *high* and *low* samples, including the best-fit stellar metallicities from Topping et al. (2020a) for each population and those that are adjacent to the best-fit values, and a fully unrestricted method that allows all Z_* values used by the BPASS models ranging from 0.00001 to 0.03.

This analysis shows that when we relax the constraints provided by rest-UV spectra (both with limited freedom and in a fully unconstrained manner), the rest-optical emission lines tend to favor

higher stellar metallicities. When we allow for limited freedom in Z_* the stellar metallicities for the *high* and *low* samples prefer the largest allowed Z_* – i.e., 0.002 and 0.003, respectively. When all stellar metallicity values are allowed, the *high* and *low* populations favor Z_* values about 4-5 times greater than those found by Topping et al. (2020a) based on fitting rest-UV spectra. These shifts demonstrate the importance of imposing external constraints from a more direct probe of massive stars and stellar metallicity, i.e., the the rest-UV continuum, as opposed to relying only on a joint fit of rest-optical emission lines. We also note that, while the best-fit values of Z_* increase when stellar metallicity is allowed to vary, the *low* population still always favors a higher Z_* than the *high* population.

The best-fit 12+log(O/H) and log(U) values for the single-Z_* and limited freedom Z_* models are significantly consistent (i.e., within 1σ) for both the *high* and *low* populations. For the *high* sample, the best-fit values for the single-Z_* and fully unconstrained Z_* models are significantly consistent as well. For the *low* sample, only some of the best-fit values for the single-Z_* and fully unconstrained Z_* models are consistent within 1σ; however, all values are consistent within 2σ. In addition, similar to what we find for the single-Z_* models, we find that O/H increases and log(U) decreases with increasing N2 in both free-Z_* models.

The results from this section provide guidance on which wavelength regimes best constrain different galaxy properties. Supported by other studies (e.g., Topping et al. 2020a), rest-UV spectra are essential for accurately estimating Z_*. Rest-optical spectra, even with the combination of multiple emission-line ratios, cannot constrain the stellar metallicity. At high redshift, we have shown that modeling rest-optical spectra alone will lead to overestimates of stellar metallicity relative to more accurate methods that incorporate rest-UV spectral information. However, rest-optical spectra can be used to constrain 12+log(O/H) and log(U). Because the best-fit values of nebular metallicity and ionization parameter vary based on which rest-optical emission-line diagram is used (see Figure 2.5), the combination of line ratios from multiple diagrams will increase the accuracy of the models. These parameters can even be estimated with reasonable precision without detailed knowledge of

the ionizing spectrum (i.e., the metallicity of the stellar population).

2.4.2.4 The Importance of α-Enhancement

In summary, using rest-optical emission line ratios alone without the constraints from fitting rest-UV spectra, we infer systematically higher Z_* values for both *high* and *low* samples. At the same time, when multiple rest-optical emission lines ratios are measured (N2, S2, O3, and O_{32}), the inferred median nebular parameters (12+log(O/H) and log(U)) and their variation across the BPT diagram, do not depend strongly on the allowed range of Z_*. However, the inclusion of constraints on Z_* from rest-UV fitting is essential for our understanding of the abundance patterns (i.e., α-enhancement) of $z \sim 2.3$ galaxies and we adopt the constrained values of Topping et al. (2020a) for our fiducial modeling procedure (Table 2.2). Because we see variation in Z_*, 12+log(O/H), and log(U) at the median and large- and small-N2 endpoints for the *high* and *low* samples, we conclude that constraints on all three of these physical properties are required for fully understanding the observed distribution of $z \sim 2.3$ star-forming galaxies in the [N II] BPT diagram. The importance of α-enhancement has also been highlighted by Steidel et al. (2016) and Cullen et al. (2019).

It is also important to note that while the *high* sample is more α-enhanced with a harder ionizing spectrum compared to the *low* sample, both populations are α-enhanced and both are characterized by a harder ionizing spectra when compared with their equivalents (i.e., galaxies with similar rest-optical line ratios) at low redshift. Notably, such physical differences apply to the *low* population, even though it overlaps with the local [N II] BPT sequence. Specifically, an overlap in emission-line ratios does not correspond to the same properties for the ionizing radiation field and ionized gas. Therefore, we recommend determining the location of galaxies in multiple rest-optical emission-line diagrams, as well as having some knowledge of the ionizing spectrum, when trying to identify local systems that can be used as true $z \sim 2$ analogs.

In addition, the differences between the *high* and *low* populations found in both this section and in Section 2.3.2.2 suggest that $z \sim 2.3$ galaxies in the *high* sample that generally have a lower Z_* with

higher 12+log(O/H) and log(U) values are also typically smaller with higher sSFR and Σ_{SFR} values. Looking ahead, we must understand why there exists a connection between the local properties of ionized star-forming regions and the overall compactness/intensity of star formation. However, exploring this phenomenon is outside the scope of the current work.

2.4.2.5 Discrepancies Between Data and Models

It is worth noting that in all three diagrams in Figure 2.5, there are galaxies that do not lie within the Cloudy+BPASS grid space. On the [N II] BPT and [S II] BPT diagrams, there are galaxies with O3 values that exceed the extremes of the model grids. Similarly on the O_{32} vs. R_{23} diagram, we observe MOSDEF galaxies with higher R_{23} values than what the Cloudy+BPASS models predict. These offsets are primarily found among the *high* population. Such extreme galaxies are not specific to this study, as Strom et al. (2017) find similar discrepancies between data and models in the corresponding emission-line diagnostic diagrams.

For the Cloudy+BPASS model grids in this study, two possible solutions could be to either elevate n_e or lower Z_*. Increasing n_e has been shown to cause elevated O3 and N2 values (Kewley et al., 2013). Since the *high* population (defined by its elevated O3 and/or N2 values) also has elevated R_{23} values on average, increasing n_e in our Cloudy+PASS models theoretically could push the curves to higher R_{23}. The models in this study, which were constructed by Topping et al. (2020a), set $n_e = 250$ cm^{-3}, which is typical of $z \sim 2.3$ galaxies in both the KBSS sample (Strom et al., 2017) and early MOSDEF work (Sanders et al., 2016). It is also comparable with the median electron densities reported in this work. The models employed in Strom et al. (2017) use $n_e = 300$ cm^{-3}, and similarly cannot reach the highest observed O3 and R_{23} values in the KBSS survey.

Using $Z_* = 0.001$, we explore raising n_e to 1000 cm^{-3} in the Cloudy+BPASS models (right column of Figure 2.7). Comparing the elevated electron density models with the $Z_* = 0.001$, $n_e = 250$ cm^{-3} scenario (left column of Figure 2.5) shows the differences in the predicted emission line ratios caused by isolating variations in n_e on the [N II] BPT, [S II] BPT, and O_{32} vs. R_{23} diagrams. We

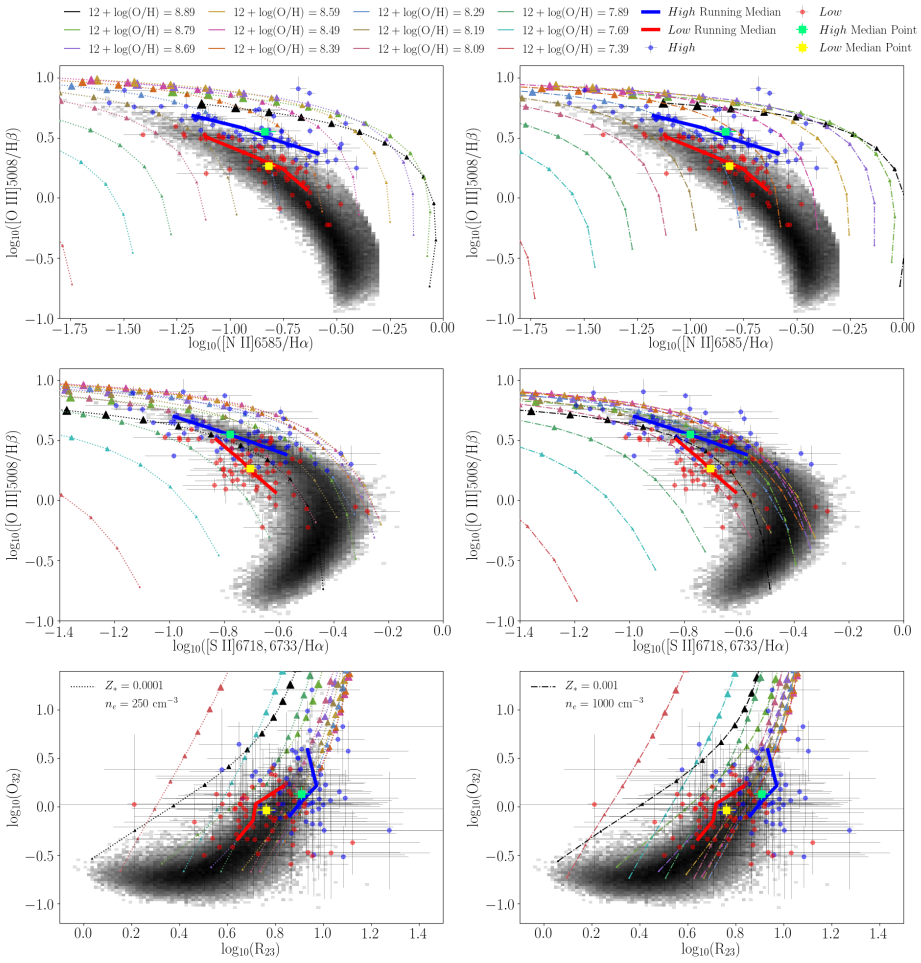

Figure 2.7: Left column: $Z_* = 0.0001$, $n_e = 250$ cm^{-3} (dotted lines). Right column: $Z_* = 0.001$, $n_e = 1000$ cm^{-3} (dot-dashed lines). Cloudy+BPASS model emission-line ratios shown on the [N II] BPT (top row), [S II] BPT (middle row), and O_{32} vs. R_{23} diagrams (bottom row). A comparison of these models with the corresponding panels in Figure 2.5 shows how raising the electron density and lowering stellar metallicity affects the predicted emission-line ratios. The correspondence between colors and symbol size and, respectively, 12+log(O/H) and log(U), matches that in Figure 2.5. Once again, we adopt an age of $10^{8.6}$ yr because it is the approximate median age of the MOSDEF sample (given a constant star-formation history) and include the local SDSS sample (grey 2D histogram), the *high* (blue) sample, and *low* (red) sample with binned medians as shown in Figure 2.3. The green and yellow squares, with associated uncertainties, are the median values of the *high* and *low* populations as shown in Figure 2.5. Aside from at roughly solar and supersolar nebular metallicities, a higher electron density has a minimal affect on the Cloudy+BPASS model grids and cannot reach the elevated O3 and O_{32} galaxies. A lower stellar metallicity is able to reach these values, suggesting that the most offset galaxies have the hardest ionizing spectrum.

find that elevating n_e to such an extreme value has only a small effect on the emission-line ratios, and the models still do not encompass the galaxies observed at the highest N2, S2, O3, and R_{23} values.

A more promising approach is to lower the stellar metallicity. The left column of Figure 2.7 gives the model grids for $Z_* = 0.0001$, which reach the majority of the extreme data points. Therefore, a very low Z_* (i.e., a very hard ionizing spectrum) is the more likely than variations in n_e to be cause for these outliers.

In addition to a low Z_*, other effects may also lead to a harder ionizing spectrum (e.g., variations in the IMF slope and high-mass cutoff or AGN partially contributing to the integrated emission lines). Systematic uncertainties such as the BPASS models under-predicting the hardness of the ionizing spectrum at a given Z_* (particularly at lower values of Z_*), different star-formation histories, or uncertainties in the dust corrections applied to O_{32} and R_{23} could play a role in the observed discrepancies between models and a minority of the sample as well.

2.5 Summary

We present results on the emission-line properties of a sample of 122 star-forming galaxies at $1.9 \leq z \leq 2.7$ from the complete MOSDEF survey with $\geq 3\sigma$ detections for the [O II]$\lambda\lambda$3727,3730, Hβ, [O III]$\lambda\lambda$4960,5008, Hα, [N II]λ6585, and [S II]$\lambda\lambda$6718,6733 emission lines. To investigate the observed systematic offset of $z > 1$ star-forming galaxies on the [N II] BPT diagram relative to local systems, the MOSDEF sample is split into the *high* (offset with elevated O3 and/or N2 values) and *low* (overlapping with the local SDSS sequence) samples. We compare the location of galaxies in both populations on the [S II] BPT and O_{32} vs. R_{23} diagrams. Additionally, we compare physical properties – SFR, M_*, R_e, sSFR, Σ_{SFR}, n_e, and t (i.e., stellar population age) – of the galaxies in both groups using additional CANDELS and 3D-*HST* ancillary data. Finally, we use Cloudy+BPASS photoionization models to investigate potential differences in the stellar metallicity, nebular metallicity, and ionization parameter of the *high* and *low* groups.

The main results are as follows:

1. On the [S II] BPT and O_{32} vs. R_{23} diagrams, the *high* sample is offset on average towards higher S2 at fixed O3 (or vice versa) and higher R_{23} value at fixed O_{32}, respectively, relative to the *low* sample. These results update earlier work from MOSDEF (Sanders et al., 2016) and are consistent with results from Strom et al. (2017), based on the KBSS survey.

2. The *high* sample has a smaller median R_e and M_*, but higher median sSFR and Σ_{SFR} compared to the *low* sample. The observed differences in R_e, sSFR, and Σ_{SFR} are present at fixed stellar mass. The *high* sample is also slightly younger in median age (t); however this age difference is not significant within the uncertainties. There is not a significant variation in SFR or n_e for the two populations. These results imply that the *high* population is associated with more concentrated and intense star formation than the *low* population.

3. Using photoionization models, we find that the *high* population has larger 12+log(O/H) and log(U) values compared to the *low* population. These conclusions hold both when we use the results from Topping et al. (2020a) and assume Z_* values of 0.001 and 0.002 for the *high* and *low* samples, respectively, as well as when we treat Z_* as a free parameter. Also, while the lower Z_*/Z_{neb} ratio of the *high* population implies that this sample is more α-enhanced than the *low* population, both samples are significantly α-enhanced relative to local star-forming galaxies with similar emission-line ratios assuming typical local galaxies have roughly solar α/Fe. These differences in the properties of the ionizing radiation field are critical to include when describing high-redshift galaxies – even those that overlap the local emission-line sequences.

4. Combining the results from the median galaxy properties of the *high* and *low* samples with the Cloudy+BPASS model grids leads to the conclusion that galaxies with a harder ionizing spectrum are associated with smaller sizes and higher sSFR and Σ_{SFR}.

5. A harder ionizing spectrum at fixed nebular metallicity is favored as one of the key drivers

of the [N II] BPT offset. In this study, we find that variation in multiple physical parameters drives the variation in emission-lines in the MOSDEF sample, including Z_*, 12+log(O/H), and log(U). However, even in regions where the $z \sim 2.3$ galaxies overlap local ones in the space of emission-line ratios, the inferred underlying physical parameters for $z \sim 2.3$ galaxies are distinct from those of local galaxies. The full set of these parameters must be understood through modeling both rest-UV and rest-optical spectra, in order to understand the translation between empirical emission-line ratios and key physical quantities such as the gas-phase oxygen abundance.

Understanding the global properties of high-redshift galaxies using large samples at $z \sim 2.3$ is essential when comparing them with local galaxies. The use of large high-redshift samples has enabled us to discover more subtle trends in the MOSDEF data that were not found with more limited data sets (e.g., Shapley et al. 2015; Sanders et al. 2016). The work from this study has shown that galaxies with a harder ionizing spectrum also tend to be smaller in size with more intense and compact star formation. Why these factors are linked is not yet clear, and combining large $z \sim 2.3$ samples of star-forming galaxies with realistic galaxy formation simulations (e.g., FIRE-2; Hopkins et al. 2018) will be important in finding this connection.

It has also been shown in both this work and in Strom et al. (2017) that models are not yet able to reach the highest observed O3 and R_{23} values for $z \sim 2.3$ star-forming galaxies on the [N II] BPT, [S II] BPT, and O_{32} vs. R_{23} diagrams. The local sequence does not reach such elevated O3 and R_{23} values, and unlike their high redshift counterparts, do not greatly exceed the data space covered by the model grids. This discrepancy indicates a need to develop both stellar population and emission-line models that better match the now large data sets of $z \sim 2.3$ star-forming galaxies.

CHAPTER 3

Reconciling the Results of the $z \sim 2$ MOSDEF and KBSS-MOSFIRE Surveys

3.1 Introduction

Rest-frame optical emission-line spectroscopy provides a wealth of information about a galaxy, including its dust extinction, star-formation rate (SFR), virial and non-virial dynamics (e.g., large-scale outflows), active galactic nucleus (AGN) activity, and properties of the ionized interstellar medium (ISM) such as the metallicity, electron density (n_e), ionizing spectrum, and ionization parameter (U; i.e., the ratio of ionizing photon density to hydrogen, and therefore electron, density). Understanding the emission-line properties of star-forming galaxies throughout cosmic history is thus essential for characterizing the formation and evolution of the stellar and gaseous contents of galaxies. One of the most important time periods for studying rest-optical emission-line spectra of galaxies is at $z \sim 2$, which hosts the peak level star formation in the universe (Madau & Dickinson, 2014). During this epoch, the modern Hubble sequence was not yet fully established and many key features of current galaxy patterns were being set, including the bimodal distribution of galaxy colors and correlations between structural parameters and stellar properties.

In the last decade, the commissioning of multi-object near-IR spectrographs on large ground-based telescopes has given us the ability to characterize the rest-optical emission-line properties of these high-redshift galaxies in large statistical samples. Two surveys taking advantage of the MultiObject Spectrometer For Infra-Red Exploration (MOSFIRE; McLean et al. 2012) instrument on the 10 m

Keck I telescope are the MOSFIRE Deep Evolution Field (MOSDEF; Kriek et al. 2015) survey and Keck Baryonic Structure Survey (KBSS; Steidel et al. 2014). Each of the two surveys contains ∼1500 galaxies with deep MOSFIRE observations at $1.4 \lesssim z \lesssim 3.8$, with roughly half the galaxies in each survey at $z \sim 2$.

At $z \sim 2$, Keck/MOSFIRE can observe the full rest-optical wavelength range from 3700 – 7000 Å, including all of the rest-optical emission-lines needed to track the location of $z \sim 2$ galaxies on the "BPT" diagrams. The [O III]λ5008/Hβ vs. [N II]λ6585/Hα diagram (first introduced by Baldwin et al. 1981 and which we refer to hereafter as the "[N II] BPT diagram"), and the [O III]λ5008/Hβ vs. [S II]$\lambda\lambda$6718,6733/Hα diagram (first introduced in Veilleux & Osterbrock 1987 and which we refer to hereafter as the "[S II] BPT diagram") can both be used to distinguish between AGN and star formation activity as the main ionizing source for the ISM of a galaxy. The ionizing spectrum shape as well as the typical ionization parameter are different in gas photoionized by hot stars as opposed to by an AGN. Therefore, star-forming galaxies and AGNs occupy distinct regions within these rest-optical emission-line diagrams.

In early studies with Keck/NIRSPEC, it was found that star-forming galaxies at $z > 1$ show elevated [N II]λ6585/Hα at fixed [O III]λ5008/Hβ (or vice versa; e.g., Shapley et al. 2005; Erb et al. 2006b; Liu et al. 2008) on average compared to local galaxies in the Sloan Digital Sky Survey (SDSS; York et al. 2000), indicating a redshift dependence in the [N II] BPT diagram. Subsequent work based on larger samples collected with MOSFIRE (e.g., Steidel et al. 2014; Shapley et al. 2015), has since confirmed the systematic [N II] BPT offset. There have been numerous explanations that have been proposed for this systematic offset, including variations in the physical properties of galaxies such as H II region ionizing spectra at fixed metallicities, H II region ionization parameter, gas-phase N/O abundance ratio differences, H II region electron densities and density structure, unresolved AGN activity, shocks, and galaxy selection effects (e.g., Liu et al. 2008; Brinchmann et al. 2008; Wright et al. 2010; Kewley et al. 2013; Yeh et al. 2013; Juneau et al. 2014; Masters et al. 2014; Steidel et al. 2014, 2016; Coil et al. 2015; Shapley et al. 2015, 2019; Sanders et al. 2016; Strom

et al. 2017, 2018; Freeman et al. 2019; Kashino et al. 2019; Topping et al. 2020a; Runco et al. 2021b). Results based on both KBSS and recent MOSDEF observations favor the idea that the main driver for the observed offset is a harder ionizing spectrum at fixed nebular oxygen abundance, which arises due to α-enhancement in the massive stars in star-forming galaxies at $z \sim 2$ (Steidel et al., 2014, 2016; Strom et al., 2017; Shapley et al., 2019; Topping et al., 2020a; Reddy et al., 2022; Runco et al., 2021b).

Understanding this offset is vital because rest-optical emission-lines are often used to infer many physical properties of the ISM. Locally, many calibrations exist between rest-optical emission-lines and ISM properties (e.g., gas-phase oxygen abundance; Pettini & Pagel 2004). Without a complete understanding of the [N II] BPT offset, it will remain unclear if these local calibrations can be used in the $z > 1$ universe (Bian et al., 2018; Sanders et al., 2020a).

While the MOSDEF and KBSS studies have converged on the factors physically driving the [N II] BPT offset, there are still differences in key results. Most notable is that the two surveys have found quantitatively different offsets between the emission-line sequences for $z \sim 2$ and local galaxies on the [N II] BPT diagram, with the KBSS sample showing higher emission-line ratios on average (Steidel et al., 2014; Shapley et al., 2015; Strom et al., 2017; Runco et al., 2021b). This discrepancy suggests that there might be fundamental differences between galaxies contained in the two surveys.

To fully understand the driver of the [N II] BPT offset and the correlation between $z \sim 2$ rest-optical emission-lines and galaxy properties (e.g., gas-phase oxygen abundance), a data set of unprecedented size is needed. To achieve such a sample, this study represents the beginning of a collaboration between the MOSDEF and KBSS teams. With over 100 nights of Keck time and ~3000 galaxies observed between $1.4 \lesssim z \lesssim 3.8$ (about half at $z \sim 2$), the combination of these two surveys represents the largest total investment of Keck/MOSFIRE time. Combining the two data sets would yield a sample with a statistical size capable of determining robust trends in galaxy properties and relationships in the $z \sim 2$ universe analogous to what exists locally.

However, because of differences in survey selection methods and results from previous studies (primarily concerning the [N II] BPT diagram), a thorough comparison of the two samples to search for possible biases is necessary before they can be combined. Here we perform a uniform comparison of the two samples to understand if any systematic differences between them exist, and if so, how to merge the samples in a way that mitigates those differences for future work. In this study, we analyze the MOSDEF and KBSS samples using consistent stellar population synthesis modeling assumptions applied to emission-line-corrected photometry, as well as the same methodology for emission-line fitting. This controlled approach eliminates any systematic biases stemming from different analysis methods, and isolates differences between the samples themselves. From the consistent SED fitting, we compare galaxy properties between the two samples. From the consistent emission-line measurements, we compare the locations of MOSDEF and KBSS samples on the [N II] and [S II] BPT diagrams and quantify the differences in their offsets from the local sequence. The combination of these two analyses enables the discovery of any systematic differences between the two samples of galaxies.

In Section 3.2, we present and compare the selection methods for the MOSDEF and KBSS surveys and discuss the $z \sim 2$ samples from each survey that are analyzed in this study. Section 3.3 describes the methodology for the SED and emission-line fitting analyses, and Section 3.4 presents the results from these fitting methods for the $z \sim 2$ spectroscopic samples with multiple emission-line detections that have been analyzed in previous studies. Section 3.5 discusses the results for the $z \sim 2$ spectroscopic samples with multiple emission-line detections and compares their SED properties with those of the larger sample of $z \sim 2$ targeted galaxies from which they are drawn. Section 3.6 presents a summary of key results and looks ahead to future work. Appendix 3A provides SED fitting results for the MOSDEF and KBSS $z \sim 2$ samples assuming constant star formation (CSF) histories instead of the delayed-τ star formation histories described in Section 3.3.1. Finally, Appendix 3B provides examples of spectra to highlight differences between the results of the two emission-line fitting methods discussed in this study. We adopt the following

abbreviations for emission-line ratios used frequently throughout the paper.

$$\text{N2} = [\text{N II}]\lambda 6585/\text{H}\alpha \tag{3.1}$$

$$\text{S2} = [\text{S II}]\lambda\lambda 6718, 6733/\text{H}\alpha \tag{3.2}$$

$$\text{O3} = [\text{O III}]\lambda 5008/\text{H}\beta \tag{3.3}$$

$$\text{O3N2} = \text{O3}/\text{N2} \tag{3.4}$$

$$\text{O3S2} = \text{O3}/\text{S2} \tag{3.5}$$

All emission-line wavelengths are in vacuum. Throughout this paper, we adopt a Λ-CDM cosmology with $H_0 = 70$ km s^{-1} Mpc^{-1}, $\Omega_m = 0.3$, and $\Omega_\Lambda = 0.7$. Also, we assume the solar abundance pattern from Asplund et al. (2009).

3.2 Observations & Sample Selection

Here we provide overviews of the MOSDEF (Section 3.2.1) and KBSS (Section 3.2.2) surveys. We describe the sample selection methods of the surveys and the $z \sim 2$ spectroscopic samples that we adopt from previous studies (KBSS: Strom et al. 2017; MOSDEF: Sanders et al. 2018). In addition, we highlight some of the key differences between the surveys in Section 3.2.3.

Some notable similarities between the two surveys are that they both utilized Keck/MOSFIRE and therefore both obtained moderate spectral resolution (R = 3000-3650) data, both surveys were conducted over roughly the same period (2012-2016), and both contain approximately the same number of galaxies (N~1500).

3.2.1 The MOSDEF Survey

The MOSDEF survey was a 48.5-night Keck/MOSFIRE observing program spanning multiple years (2012-2016). Approximately 1500 galaxies were targeted across three redshift ranges: $1.37 \leq z \leq 1.70$, $2.09 \leq z \leq 2.61$, and $2.95 \leq z \leq 3.80$. These ranges were selected to optimise the

detection of strong rest-optical emission-lines (e.g., [O II]$\lambda\lambda$3727,3730, Hβ, [O III]$\lambda\lambda$4960,5008, Hα, [N II]λ6585, and [S II]$\lambda\lambda$6718,6733) within windows of atmospheric transmission. Roughly half of the galaxies in the survey are in the middle redshift range at $z \sim 2.3$. In this redshift range, ~1/3 of the galaxies were targeted based on existing spectroscopic redshifts, while the remaining ~2/3 were targeted based on photometric redshifts drawn from the 3D-HST survey (Momcheva et al., 2016). The galaxies were selected from five well-studied extragalactic legacy fields covered by the CANDELS and 3D-HST surveys: AEGIS, COSMOS, GOODS-N, GOODS-S, and UDS (Grogin et al., 2011; Koekemoer et al., 2011; Momcheva et al., 2016). The survey is H-band (F160W) magnitude limited, with brightness limits of $H_{\rm AB} = 24.0$, 24.5, and 25.0, respectively, for the lowest, middle and highest redshift ranges. Galaxies were observed for 1.5 hours in each filter (Y, J, and H for a subset) in the lowest redshift bin $z \sim 1.5$. The observing time was increased to 2 hours per filter for the middle ($z \sim 2.3$; J, H, and $K_{\rm s}$ bands) and highest ($z \sim 3.4$; H and $K_{\rm s}$ bands) redshift bins. For a full description of MOSDEF observing details and sample selection, see Kriek et al. (2015).

In this study, we use the MOSDEF subsample from Sanders et al. (2018), which contains 260 star-forming galaxies at $1.9 \leq z \leq 2.7$ ($z_{\rm med} = 2.29$) with S/N of both Hα and H$\beta \geq 3$. Galaxies with sky lines significantly contaminating Hα or Hβ were not included, nor those showing evidence of AGN activity based on their X-ray luminosity, IR colors, or if N2 ≥ 0.5 (Coil et al., 2015; Azadi et al., 2017; Leung et al., 2017). Galaxies with $\log_{10}(M_*/M_\odot) < 9.0$ are rejected due to lack of completeness below that mass cutoff (see Section 3.2.4 for more details).

The current study, which utilizes updated SED and emission-line fitting methods, finds small differences in stellar mass (i.e., M_*) and emission-line S/N from the values used in Sanders et al. (2018). Nine of the 260 galaxies from Sanders et al. (2018) have updated $\log_{10}(M_*/M_\odot) < 9.0$ values, and are removed from this study. Additionally, one galaxy is not in the 3D-HST v4.1 catalog, which is needed for broadband SED fitting, and is also removed from the sample. Hereafter in this work, we define the resulting sample of 250 galaxies as the "MOSDEF $z \sim 2$ spectroscopic

sample."

Figure 3.1 (top left panel) features a redshift histogram of all MOSDEF galaxies at $1.9 \leq z \leq 2.7$, which we refer to hereafter as the "MOSDEF $z \sim 2$ targeted sample". These include galaxies targeted to lie at $2.09 \leq z \leq 2.61$ (Kriek et al., 2015) based on existing photometric or spectroscopic redshifts, and galaxies serendipitously detected on MOSDEF slits with redshifts measured in the range $1.9 \leq z \leq 2.7$. Blue indicates the distribution of the 250 galaxies in the $z \sim 2$ spectroscopic sample that meet the selection criteria from Sanders et al. (2018). Green indicates the 422 galaxies that have a confirmed MOSFIRE redshift, but do not meet all of the selection criteria outlined above (i.e., S/N, AGN, and/or M_* cuts). Purple indicates the 114 galaxies that do not have a confirmed MOSFIRE redshift. The photometric redshift from the 3D-HST catalogs is shown for these galaxies. The median redshift for all MOSDEF galaxies at $1.9 \leq z \leq 2.7$ is the same as that for the 250 galaxy spectroscopic sample (i.e., $z_{\rm med} = 2.29$).

There are 536 galaxies in the MOSDEF $z \sim 2$ targeted sample that were not included in the spectroscopic sample described here. Therefore, there are 786 galaxies in the MOSDEF $z \sim 2$ targeted sample. Galaxies were removed due to several different criteria, as listed above. There were 114 galaxies lacking a robust MOSFIRE redshift. Of the remaining 422 galaxies, 97 galaxies were flagged as AGNs and removed. Of the 325 non-AGNs, 61 galaxies met all of the criteria to make it into the Sanders et al. (2018) sample, but were removed due to sky-line contamination of Hα and/or Hβ. This removal was performed based on visual inspection of the spectra. In addition, 26 galaxies were removed because they have $\log_{10}(M_*/M_\odot) < 9.0$; 98 have S/N$_{\rm H\beta}$ and S/N$_{\rm H\alpha} < 3$, and are not retained; finally, 140 galaxies were removed because they have S/N$_{\rm H\beta} < 3$ and S/N$_{\rm H\alpha}$ ≥ 3. Of the 325 galaxies that have a robust MOSFIRE redshift and are not AGN, 73% are removed due to S/N$_{\rm H\beta} \leq 3$.

3.2.2 The KBSS Survey

The Keck Baryonic Structure Survey (KBSS) began as a redshift survey of star-forming galaxies in 15 independent fields, subtending a total area of 0.25 square degrees. Each KBSS survey region is centered on a bright ($V \sim 16-17$) QSO with $z = 2.7 \pm 0.1$. Galaxies were selected for spectroscopy using photometric pre-selection based on rest-frame far-UV color criteria that had been described and tested in earlier work (Steidel et al., 2003, 2004; Adelberger et al., 2004). The rest-UV spectroscopy was conducted using LRIS-B (Steidel et al., 2004) over the years 2002-2009, deliberately focusing on the redshift range $2 \lesssim z \lesssim 2.7$ to maximize the sensitivity of the background QSO sightline to the IGM and CGM within the survey volume (e.g., Rudie et al. 2012, 2019; Turner et al. 2014). Most of the spectroscopically-observed galaxies satisfied the "BX" or "MD" color selection criteria, yielding galaxy redshifts $\langle z \rangle = 2.17 \pm 0.33$ and $\langle z \rangle = 2.63 \pm 0.28$, respectively. In addition to the UV color criteria, the KBSS UV spectroscopic sample was limited to galaxies with apparent magnitude $\mathcal{R}_{\rm AB}[6830\ \text{Å}] \leq 25.5$ to ensure that the resulting spectra would yield redshifts for galaxies both with and without observed Lyα emission. The full KBSS UV spectroscopic sample consists of 2341 objects (2285 star-forming galaxies and 66 AGN) with $\langle z \rangle = 2.354 \pm 0.432$. Of these, 1435 (61.3%) have $1.9 \leq z \leq 2.7$, and 950 (40.6%) have $2.1 \leq z \leq 2.6$. The latter sub-sample comprised the highest priority targets for near-IR spectroscopy, for the reasons outlined above.

The KBSS-MOSFIRE survey (Steidel et al., 2014; Strom et al., 2017) was initiated soon after MOSFIRE was commissioned in 2012 April. The survey had multiple goals, including obtaining redshifts for galaxies that had failed to yield redshifts from previous LRIS spectroscopy, especially those within a few arc minutes in projection from the central QSO and whose rest-UV colors suggested redshifts in the broader range $1.8 \lesssim z \lesssim 3.5$. Additional photometric selection criteria were imposed to ensure that the targeted sample at $z \sim 2$ would roughly uniformly span the full range of star-forming galaxy properties: first, we used the galaxy $\mathcal{R} - K_{\rm s}$ color (~ 2000 Å $- 6500$ Å in the rest-frame) for galaxies with $z \sim 2.3$, with preference given to those with $\mathcal{R} - K_{\rm s} > 2$.

Also added as potential MOSFIRE targets were galaxies satisfying $\mathcal{R} - K_s > 2$ that were drawn from a region in $U_nG\mathcal{R}$ color space adjacent to the BX and MD region, in an effort to include relatively massive galaxies likely to be more heavily reddened by dust; these were given the name "RK" galaxies (see Strom et al. 2017). None of the RK objects had UV-based redshifts prior to their observation with MOSFIRE.

Unlike MOSDEF, KBSS-MOSFIRE attempted to obtain the complete set of strong nebular lines only for galaxies in the range $z = 2 - 2.7$. However, MOSFIRE slitmasks also included galaxies without previous spectroscopic redshifts, either because they had never been observed with LRIS, or when previous LRIS observations did not result in a secure redshift. For objects without prior redshifts measurements, once a redshift was measured from initial MOSFIRE spectroscopy, the object was retained as a high priority for subsequent MOSFIRE observations only if it fell in the range $2 \leq z \leq 2.7$.

MOSFIRE mask design was done iteratively as the survey progressed. Initially, the highest priority targets were objects with known redshifts $2.1 \leq z \leq 2.6$ drawn from the KBSS rest-UV spectroscopic survey. Any remaining space on each mask was assigned to galaxies in the following order of priority:

1. Galaxies without previous redshifts, drawn from the BX, MD, and RK color selection; BX and MD candidates without known redshifts were favored if they also had $\mathcal{R} - K_s > 2$.

2. Galaxies with UV-based redshifts falling outside the primary $2 \leq z \leq 2.7$ range.

3. Galaxies without UV-based redshifts drawn from color selection windows least likely to fall in the primary redshift range of interest (i.e., "BM", "M", "C" candidates).

The status of all objects in a given survey field was evaluated after each MOSFIRE observing run, and objects were re-prioritized based on the S/N achieved for each emission line of interest; for H- and K_s-band observations these included Hβ, [O III]$\lambda\lambda$4960,5008 in H band, Hα and

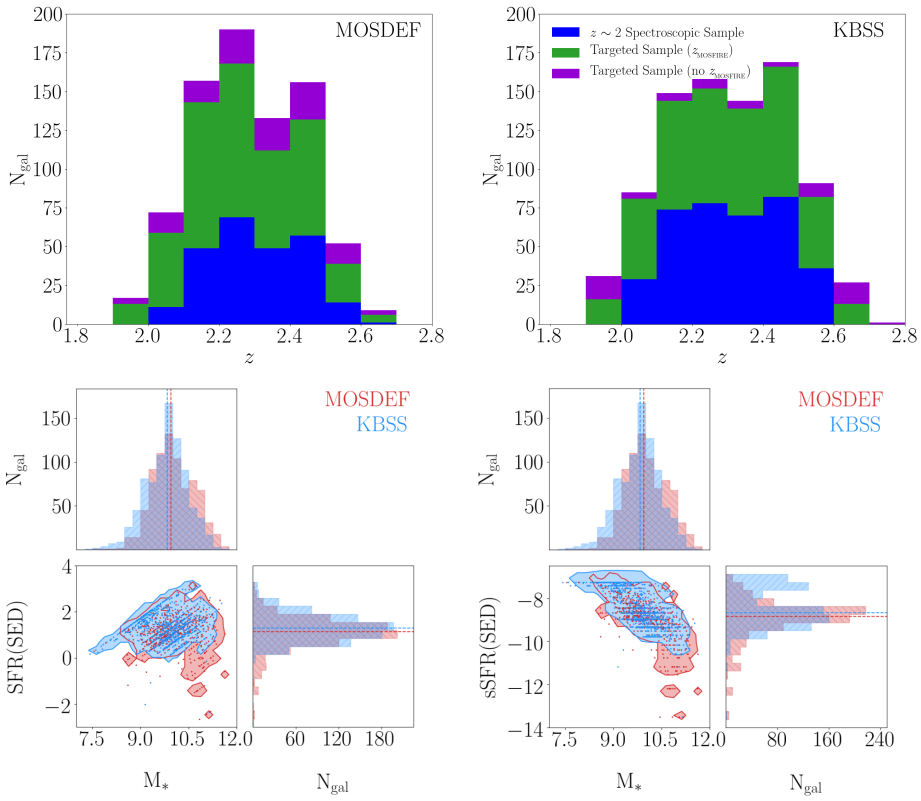

Figure 3.1: Top: Redshift histograms. Shown in these panels are distributions of galaxies at $1.9 \leq z \leq 2.7$ for the MOSDEF (left) and KBSS (right) surveys. Blue indicates the $z \sim 2$ spectrosopic samples discussed in Sections 3.2.1 (MOSDEF) and 3.2.2 (KBSS). Green indicates galaxies that were observed and have a MOSFIRE redshift, but were not included in the $z \sim 2$ spectrosopic samples due to the various sample selection criteria discussed in Sections 3.2.1 and 3.2.2. Purple indicates galaxies that were targeted, but a robust MOSFIRE redshift was not obtained. For MOSDEF, the purple redshifts displayed are photometric redshifts. For KBSS, the purple redshifts displayed were obtained by previous rest-UV observations with Keck/LRIS. The LRIS redshifts were estimated from either Lyα or low-ionization interstellar absorption lines. Bottom: Corner plots comparing SFR(SED) vs. M_* (left) and sSFR(SED) vs. M_* (right) for the MOSDEF (red) and KBSS (blue) $z \sim 2$ targeted samples. The dashed lines on the 1D histograms mark the median values for the distributions, and the contours on the diagonal trace the 3σ regions in 2D space. Individual data points are also shown in the 2D distribution. The range of datapoints is limited by the fact that M_* and SFR(SED) are correlated and are both determined by the normalization of the SPS model to the photometry. In addition, for the 2D panels the data crowd in the upper-left portion of the distribution (left panel) and at high sSFR(SED) (right panel) because of the lower age limit for the stellar populations. In total, there are 786 MOSDEF and 850 KBSS galaxies. Note that two MOSDEF galaxies with $\log_{10}(\mathrm{SFR(SED)}/\mathrm{M}_\odot/\mathrm{yr}^{-1}) < -3.0$ are excluded from the left panel and one MOSDEF galaxy with $\log_{10}(\mathrm{sSFR(SED)}/\mathrm{yr}^{-1}) < -14.0$ is excluded from the right panel to better show the data.

[N II]$\lambda\lambda$6550,6585 in K_s band. High priority targets (based on redshift) were retained for inclusion on new masks until all relevant lines were successfully detected.

For the purposes of comparison with MOSDEF, we consider the KBSS-MOSFIRE $z \sim 2$ targeted sample to include all MOSFIRE-observed galaxies whose redshifts were known from prior rest-UV spectroscopy to be in the range $1.9 \leq z \leq 2.7$ (621 objects in total, of which 558 yielded MOSIFRE redshifts and 63 did not), plus the sample of objects that had not been identified prior to MOSFIRE observation that fall in the primary $1.9 \leq z \leq 2.7$ redshift range (237 objects). The $z \sim 2$ targeted sample thus defined has 858 objects, of which 795 yielded MOSFIRE redshifts[1]. We do not have the broadband photometry required for SED fitting for 8/858 galaxies (seven have a MOSFIRE redshift while one does not). Therefore, the final KBSS $z \sim 2$ targeted sample to be used in this analysis consists of 850 galaxies, 788 of which have a MOSFIRE redshift. In comparison, the MOSDEF $z \sim 2$ targeted sample contains 786 galaxies, of which 672 have a MOSFIRE redshift.

KBSS did not dedicate a specific amount of time to observing each galaxy, instead choosing to stay in a given field until all rest-optical emission-lines were detected in the majority of galaxies in that field. The median observing time for a galaxy in the H-band (covering Hβ and [O III]$\lambda\lambda$4960,5008) was 2.44 hours. The maximum time spent on a galaxy was 10.64 hours. For the K_s-band (covering Hα, [N II]λ6585, and [S II]$\lambda\lambda$6718,6733), the median and maximum observing times were, respectively, 2.78 and 12.13 hours. For full KBSS-MOSFIRE observing details, see Steidel et al. (2014) and Strom et al. (2017).

In this study, we use the KBSS-MOSFIRE sample from Strom et al. (2017), which contains 377 galaxies at $1.9 < z < 2.7$ ($z_{\rm med} = 2.30$) with spectral coverage of the Hβ, [O III]λ5008, Hα, and [N II]λ6585 emission lines (i.e., the four required for the [N II] BPT diagram). To be included in this sample, the S/N of Hα must be ≥ 5, the S/N of Hβ and [O III]λ5008 must be ≥ 3, and

[1]The $z \sim 2$ targeted KBSS-MOSFIRE sample does not include objects without UV redshifts for which no significant emission lines were detected in the MOSFIRE spectra. Many are targets observed in only 1 MOSFIRE atmospheric band as filler, and would be unlikely to be assigned to subsequent masks if initial spectroscopy showed no sign of emission in the desired range.

[N II]λ6585 must simply fall within the wavelength coverage.

Galaxies are identified as having an AGN based on X-ray luminosity, mid-IR photometry, strong UV emission in high-ionization lines (e.g., C IVλ1549, C III]λ1908, and N Vλ1240; Reddy et al. 2008; Hainline et al. 2011), broad emission-line features in the rest-optical spectra, and/or N2 $\geq$ 0.5.

To be consistent with the MOSDEF sample, we remove eight KBSS galaxies from the Strom et al. (2017) sample flagged in the sample as AGN. Hereafter in this work, we define the resulting sample of 369 galaxies as the "KBSS $z \sim 2$ spectroscopic sample."

Figure 3.1 (top right panel) includes a redshift histogram of all KBSS galaxies at $1.9 \leq z \leq 2.7$, which we refer to hereafter as the "KBSS $z \sim 2$ targeted sample". Blue indicates the distribution of the 369 galaxies in the $z \sim 2$ spectroscopic sample that meet the selection criteria from Strom et al. (2017). Green indicates galaxies that have a confirmed MOSFIRE redshift, but do not meet all of the selection criteria (i.e., emission-line S/N and broadband photometry criteria) outlined above. Purple indicates galaxies that do not have a confirmed MOSFIRE redshift. For these galaxies, the redshifts shown are based on Keck/LRIS measurements of either the Lyα or low-ionization interstellar absorption features. The median redshift for all KBSS galaxies at $1.9 \leq z \leq 2.7$ (i.e., $z_{\rm med} = 2.29$) is slightly lower than for the 369 galaxy spectroscopic sample (2.31). Out of these 369 galaxies, 357 (96.7%) are $U_{\rm n}G\mathcal{R}$ color selected and 12 (3.3%) are "RK" galaxies.

3.2.3 MOSDEF & KBSS Sample Comparison

The selection methods for the MOSDEF and KBSS surveys are distinct. MOSDEF is selected based on photometric redshifts (or spectroscopic redshifts when available), with a magnitude limit in the rest-optical (H band), while KBSS-MOSFIRE is a UV-color-selected sample with a magnitude limit in the $\mathcal{R}$ band. As discussed in Shivaei et al. (2015), the MOSDEF magnitude-limited selection method is incomplete in the low-mass regime. At the same time, the KBSS rest-UV sample can be biased against high-mass or dusty galaxies whose $U_{\rm n}G\mathcal{R}$ colors place them outside of the nominal

rest-UV selection windows (e.g., Reddy et al. 2005; Strom et al. 2017). This difference in the M_* regimes probed by the two samples can be seen in the bottom panels of Figure 3.1. This figure contains corner plots showing the 1D histograms and 2D distributions of SFR(SED) vs. M_* (bottom left) and sSFR(SED) vs. M_* (bottom right) for both samples. The sample medians are marked on the 1D histograms and the 3σ regions are traced by contours in the 2D space. It is clear that KBSS more heavily targets the low mass regime while MOSDEF targets span a wider range of stellar populations in the high mass regime. These features of the two samples suggest that they are complementary to one another in the low- and high-mass extremes, and that the combination of the MOSDEF and KBSS $z \sim 2$ surveys would be complete across a wide M_* range of $\sim 10^{8.5} - 10^{11.5}$ $M_\odot$. Additionally, the MOSDEF and KBSS samples are complementary in sSFR(SED) space, as KBSS is better sampled at $\log_{10}(\mathrm{sSFR(SED)/yr^{-1}}) \geq -8.0$ (indicating more intense star formation), especially at the low-mass end, while MOSDEF has more coverage at $\log_{10}(\mathrm{sSFR(SED)/yr^{-1}}) \leq -9.0$ (indicating less intense star formation), especially at the high-mass end. Between the low- and high-mass regimes (i.e., $\sim 10^{9.5} - 10^{10.5} M_\odot$) the contour maps overlap for the two samples. Our methods for measuring these galaxy stellar population properties are presented in Section 3.3.1 and a detailed comparisons of these properties for the two samples are discussed in Sections 3.4.1 and 3.5.2.

Despite the differences in selection of the MOSDEF and KBSS $z \sim 2$ targeted catalogs, there are notable similarities between the two surveys. The surveys have comparable $z \sim 2$ catalog sizes (786 galaxies for MOSDEF and 850 for KBSS) and median redshifts (2.29 for both surveys). Additionally, the majority of galaxies in each survey would meet the selection criteria of the other survey. Most of the KBSS $z \sim 2$ targeted sample (817/850 galaxies or 96.1%) has $H_{\mathrm{AB}} < 24.5$ (i.e., the main MOSDEF selection criterion). Table 3.1 shows the percent of the MOSDEF sample that falls into each region of the $U_{\mathrm{n}}G\mathcal{R}$ diagram as defined in Steidel et al. (2003, 2004); Strom et al. (2017). For MOSDEF galaxies, we passed best-fit stellar population model SEDs (see Section 3.3.1) through the $U_{\mathrm{n}}G\mathcal{R}$ filters to estimate synthetic magnitudes using the IRAF (Tody, 1986, 1993) routine, *sbands*. The statistics for the MOSDEF sample are compared to those of the KBSS sample.

The distribution of MOSDEF and KBSS galaxies in the various regions on the $U_nG\mathcal{R}$ diagram is very similar. Most notable is that MOSDEF has a similar percentage of BX galaxies (82.8%) as KBSS (80.5%). The BX region on the $U_nG\mathcal{R}$ diagram is statistically where $z \sim 2$ galaxies are most likely to be (Steidel et al., 2004). Also, 773/786 galaxies (98.3%) in the MOSDEF $z \sim 2$ targeted sample have $\mathcal{R} < 25.5$ and fall into one of the defined regions of $U_nG\mathcal{R}$ color space. Of the remaining 13 galaxies in the "Other" category, 12 have $\mathcal{R} > 25.5$ while the other one has $\mathcal{R} < 25.5$ but did not fall into any of the defined regions on the $U_nG\mathcal{R}$ diagram. Finally, as we detail in the next section, the spectroscopic incompleteness of the MOSDEF survey leads to an even greater similarity between the distributions of galaxy properties for the MOSDEF and KBSS $z \sim 2$ spectroscopic samples that have been analyzed in, e.g., Sanders et al. (2018) and Strom et al. (2017).

3.2.4 MOSDEF Sample Incompleteness

For MOSDEF, it has been known since the design of the survey that both the number of targets and the success rate drop below $\log_{10}(M_*/M_\odot) = 9.0$ due to the H-band magnitude selection limits (Kriek et al., 2015). Accordingly, Sanders et al. (2018), who analyze a galaxy sample that our current MOSDEF sample is intended to represent, removed any galaxies below a mass limit of $\log_{10}(M_*/M_\odot) = 9.0$. Our new SED fitting methodology utilizing emission-line subtracted photometry resulted in slightly different stellar masses from what was used in Sanders et al. (2018), with a small fraction (3.5%) now below that mass limit. As stated above, we remove these galaxies to be consistent with the well documented MOSDEF incompleteness in this mass regime. KBSS does not have this incompleteness at low mass. Since the goal of this study is to compare MOSDEF and KBSS samples that have been analyzed in previous work (Strom et al., 2017; Sanders et al., 2018), we do not remove the galaxies with $\log_{10}(M_*/M_\odot) < 9.0$ from the KBSS $z \sim 2$ spectroscopic sample.

We note that the MOSDEF survey is also incomplete in the red, massive regime. The success rate of obtaining a $z_{\rm MOSFIRE}$ declines for galaxies with red rest-frame optical/near-IR colors, where rest-

Table 3.1: $U_{\rm n}G\mathcal{R}$ Diagram Statistics

$U_{\rm n}G\mathcal{R}$ Region (1)	N/850 of KBSS (2)	N/786 of MOSDEF (3)
BX	684 (80.5%)	651 (82.8%)
BM	10 (1.2%)	4 (0.5%)
M/MD	97 (11.4%)	75 (9.5%)
C/D	23 (2.7%)	0
RK	28 (3.3%)	43 (5.5%)
Other	8 (0.9%)	13 (1.7%)

Note. — Col. (1): Region of $U_{\rm n}G\mathcal{R}$ space, as defined in Steidel et al. (2003, 2004); Strom et al. (2017). Col. (2): Percent of the KBSS sample in that region of $U_{\rm n}G\mathcal{R}$ space. Col. (3): Percent of the MOSDEF sample in that region of $U_{\rm n}G\mathcal{R}$ space. Note that to fall into one of the regions on the $U_{\rm n}G\mathcal{R}$ diagram, the galaxy must have $\mathcal{R} < 25.5$. Some of the galaxies in the "Other" category fall into one of the defined $U_{\rm n}G\mathcal{R}$ regions, but have $\mathcal{R} > 25.5$.

frame U−V and V−J are both greater than ∼1.25 (we discuss the UVJ diagram and how U−V and V−J colors are estimated in Section 3.3.1). Due to the rest-UV sample selection methods (including the $\mathcal{R} \leq 25.5$ cut off), the KBSS survey does not target galaxies in this regime. Most of the RK galaxies are not in this regime as well. The spectroscopic incompleteness of the MOSDEF survey makes the MOSDEF and KBSS $z \sim 2$ spectroscopic samples more similar than the MOSDEF and KBSS $z \sim 2$ targeted samples are. We explore this topic more in Section 3.5.2.

3.2.5 SDSS Comparison Sample

When discussing the [N II] and [S II] BPT diagrams, we compare the emission lines from our high-redshift MOSDEF and KBSS samples with similar measurements from galaxies in the local universe. We pull archival emission-line measurements from the SDSS Data Release 7 (DR7; Abazajian et al. 2009), specifically from the MPA-JHU DR7 release of spectrum measurements[2]. The SDSS sample is restricted to a redshift range of $0.04 \leq z \leq 0.10$, and AGN are removed using equation 1 from Kauffmann et al. (2003) or if N2 > 0.5. On the [N II] ([S II]) BPT diagrams, a S/N ≥ 3 is required for the Hβ, [O III]λ5008, Hα, and [N II]λ6585 ([S II]$\lambda\lambda$6718,6733) features. These criteria result in comparison samples of 103,422 and 102,543 SDSS galaxies, respectively, on the [N II] and [S II] BPT diagrams.

3.3 Methodology

For this study, it is essential to analyze the MOSDEF and KBSS samples using the same methodology. Doing so eliminates any bias introduced from the analysis process, and can therefore isolate any systematic intrinsic differences between the two samples. Section 3.3.1 introduces how the host galaxy properties are obtained using SED fitting, and Section 3.3.2 describes the emission-line measurements.

[2]https://wwwmpa.mpa-garching.mpg.de/SDSS/DR7/

3.3.1 SED Fitting

Both MOSDEF and KBSS samples are covered by multi-wavelength photometry enabling robust SED fitting; however, the specific sources of the photometry vary between surveys. For MOSDEF, the specific set of ground-based and *HST* optical and near-IR photometric bands varies from field to field (AEGIS, COSMOS, GOODS-N, GOODS-S, and UDS), though all have *Spitzer*/IRAC coverage (Skelton et al., 2014). All KBSS galaxies have U_n, G, $\mathcal{R}$, J, and K_s imaging. Additionally, all 15 fields have *Spitzer*/IRAC coverage (typically two channels per field; Reddy et al. 2012), 10 fields have at least one pointing from *Hubble*/WFC3-IR F160W (Law et al., 2012; Mostardi et al., 2015), and 8 fields have $J1$, $J2$, $J3$, $H1$, $H2$ imaging using *Magellan*-FourStar (Persson et al., 2013). While both MOSDEF and KBSS have broadband photometry spanning a similar wavelength range (rest-UV to rest-IR), we note that MOSDEF has a denser coverage with 15 photometry points on average compared to 7 for KBSS.

In this study, we apply the same SED fitting method to both the MOSDEF and KBSS samples. We use the SED fitting code FAST (Kriek et al., 2009) to obtain many of the key galaxy properties compared between the two galaxy samples. For this modeling, we adopt the Flexible Stellar Population Synthesis (FSPS) library from Conroy & Gunn (2010), assume a Chabrier (2003) stellar initial mass function (IMF), a Calzetti et al. (2000) dust attenuation curve, and delayed-τ star-formation histories where SFR(SED) $\propto t \times e^{-t/\tau}$. Here, t is the time since the onset of star formation, and τ is the characteristic star-formation timescale. Both t and τ are allowed to vary in the FAST modeling. In addition to t and τ, we allow the amount of dust attenuation (A_V) and stellar mass of the galaxy (M_*) to vary and set the metallicity to 0.019, which is defined to be solar metallicity in the Conroy & Gunn (2010) library.

We use emission-line subtracted photometry, where the flux of the strong rest-optical emission lines measured directly from the MOSFIRE spectra (e.g., Hβ, [O III]$\lambda\lambda$4960,5008, and Hα) has been subtracted from the photometric measurements. These strong lines could bias the shape of the SED fit on the red side of the Balmer break, resulting in the fitting code favoring older ages

than it would based solely on the stellar continuum.

From the SED fitting, we compare estimates of M_*, SFR(SED), sSFR(SED), A_V, t/τ for the MOSDEF and KBSS samples. All SFR values are those inferred from the SED fits. These values are listed in Section 3.4.1 for the $z \sim 2$ spectroscopic samples and Section 3.5.2 for the $z \sim 2$ targeted samples.

Using the best-fit SEDs obtained from FAST, we also estimate the rest-frame UVJ colors of the MOSDEF and KBSS samples using the IRAF (Tody, 1986, 1993) function *sbands*. The UVJ diagram is a useful tool because the combination of the U−V and V−J colors breaks the degeneracy for age and reddening (i.e., distinguishing between red quiescent galaxies and dusty star-forming galaxies). Additionally, at red (i.e., high) U−V values, increasing V−J traces increasing sSFR (Williams et al., 2009). In the star-forming track of the UVJ diagram extending from low U−V and V−J up towards higher U−V and V−J, low mass galaxies populate the bottom left region (i.e., blue U−V and V−J colors) while high mass star-forming galaxies occupy the upper right region (i.e., red U−V and V−J colors). Quiescent galaxies lie in the upper left portion of the diagram (Williams et al., 2009).

We note that we experimented with CSF models similar to those utilized in past KBSS studies (e.g., Steidel et al. 2014, 2016; Strom et al. 2017) and some MOSDEF studies (e.g., Du et al. 2018; Reddy et al. 2018). Appendix 3A provides a description of both the CSF models and the results for the $z \sim 2$ spectroscopic and targeted samples. The results from the FAST delayed-τ and CSF models do not perfectly agree with each other; however, the differences are minor (particularly for the spectroscopic samples) and the key takeaways of this study are the same regardless of which SED fitting method we use.

We also experiment with models where star formation increases with time (hereafter referred to as τ-rising models), as this star formation history can provide a better fit to $z \sim 2-3$ galaxies assuming constant star formation (Reddy et al., 2012). Similar to the CSF models, the differences

in results between the delayed-τ and τ-rising models are minor, and the key takeaways of this study would remain unchanged if we used the results from the latter.

3.3.2 Emission-line Measurements

We performed measurements for the MOSDEF and KBSS spectra using a custom emission-line fitting IDL code developed by the MOSDEF team that fits a single Gaussian to each emission-line in the spectra (Reddy et al., 2015). The FWHM estimates are allowed to vary independently for each emission-line, but with the following restrictions. The lower limit for the FWHM is the instrumental resolution, which is determined by sky lines. The upper limit is 0.5 Å larger than the FWHM measured for the line with the highest S/N (usually Hα). The best-fit FAST models obtained through SED fitting were used to correct Hα and Hβ for the underlying contribution of stellar Balmer absorption. Specifically, the continuum under each line was fixed to the best-fit model from FAST. If the best-fit Gaussian model deviates significantly from the data, the emission-line fitting code will pick the integrated bandpass flux as the preferred estimate of the emission-line flux. This custom emission-line fitting code has been used for past MOSDEF studies (e.g., Shapley et al. 2015, 2019; Sanders et al. 2016, 2018); however, it has been since notably updated for more accurate estimates of the contribution of stellar Balmer absorption. For the MOSDEF $z \sim 2$ spectroscopic sample, the median decrease in Balmer absorption correction is 36.4%, when compared with the previous iteration of the MOSDEF code, which results in a 4.1% median decrease in Hβ flux.

The current emission-line fitting code used in this study is different from that used in earlier published work for both MOSDEF and KBSS, which results in small variations in the emission-line S/N compared to past studies. For MOSDEF, updates to the estimates of the stellar Balmer absorption correction result in a Hβ S/N < 3 for three galaxies that previously had a higher S/N and were thus included in the Sanders et al. (2018) sample. For KBSS, the utilization of a different code compared to the one used in Strom et al. (2017) results in 24 galaxies with Hβ S/N < 3, nine galaxies with [O III]λ5008 S/N < 3, and two additional galaxies with Hβ and [O III]λ5008 S/N < 3. Although their S/N falls below the original sample selection criteria, we still include these

galaxies in our study and investigate their SED properties. However, we include only the subset of galaxies with S/N $\geq$ 3 for all relevant emission-lines in our analysis of the [N II] and [S II] BPT diagrams.

We note that one difference between the MOSDEF and KBSS data reduction approaches lies in the 2D to 1D extraction methods. MOSDEF uses an "optimal" (Freeman et al., 2019) extraction while the Strom et al. (2017) catalogs uses a boxcar extraction. We tested how this difference affects the measured emission-line flux by extracting MOSDEF spectra using the boxcar method and refitting the emission lines. For the four emission lines on the [N II] BPT diagram, we find that the boxcar method has a higher median flux of 1-3% compared to the optimal extraction method. For the line ratios (i.e., [O III]λ5008/Hβ and [N II]λ6585/Hα), the difference is less than 1%. Since the difference is negligible, we continue to use the optimal extraction for MOSDEF and boxcar extraction for KBSS, as these are the methods used for the previously published survey results.

3.4 The Physical Properties of the $z \sim 2$ Spectroscopic Samples

In this section, we compare the MOSDEF and KBSS $z \sim 2$ spectroscopic samples introduced in Sections 3.2.1 (MOSDEF) and 3.2.2 (KBSS). Specifically, in Section 3.4.1 we analyze the host galaxy properties of the samples derived from SED fitting. In Sections 3.4.2 and 3.4.3, we investigate the locations of the $z \sim 2$ spectroscopic samples on, respectively, the [N II] and [S II] BPT diagrams.

3.4.1 SED Fitting Properties

Figure 3.2 (panels a-e) displays histograms of the galaxy properties for the MOSDEF and KBSS $z \sim 2$ spectroscopic samples obtained through the FAST SED fitting. The red and blue lines give the distributions for the full MOSDEF (250 galaxies) and KBSS (369 galaxies) $z \sim 2$ spectroscopic samples. The red and blue filled portions of the distributions indicate the subset of galaxies from each sample (143 MOSDEF and 213 KBSS galaxies) that have S/N $\geq$ 3 for Hβ, [O III]λ5008, Hα,

and [N II]λ6585 and are included on the [N II] BPT diagram. Sample medians are displayed as vertical lines for every galaxy property, and we derive 1σ uncertainties on the medians through bootstrap resampling. These medians are estimated using all galaxies in the $z \sim 2$ spectroscopic samples, not only the subsets of galaxies on the [N II] BPT diagram, however the [N II] BPT subsamples yield sample medians that do not significantly change the key results of this study. These values are given in Table 3.2. We also list the probabilities (i.e., p-values), based on the Kolmogorov-Smirnov (K-S) test, of the null hypothesis that the two samples are drawn from the same distribution. The samples are also shown on the UVJ diagram (panel f). We include the Williams et al. (2009) boundary between quiescent and star forming galaxies on the UVJ diagram. Figure 3.3 provides a corner plot of the U−V and V−J colors showing both 1D histograms of each parameter and the distribution of data points in 2D space overlaid with 3σ contours.

Overall, we find that the MOSDEF and KBSS $z \sim 2$ spectroscopic samples have very similar galaxy property distributions and median values. The KBSS sample has a smaller (i.e., younger) median t/τ compared to the MOSDEF sample. The p-value corresponds to an offset of greater than 3σ indicating that this difference is significant. The median values for all other host galaxy properties agree within the uncertainties. We note that despite the sample medians for sSFR(SED) and A_V agreeing within the uncertainties, the p-values correspond to a significance greater than 3σ indicating that the two samples do not appear to occupy the same parameter space for these properties. Of the KBSS sample, 125 galaxies (33.9%) have $\log_{10}(\text{sSFR(SED)/yr}^{-1}) \geq -8.0$ compared to only 27 galaxies (10.8%) of the MOSDEF sample. Also, we find that 50 galaxies (13.6%) in the KBSS sample have stellar population age estimates of $\log_{10}(t/\tau) \leq -2.0$. There is only one MOSDEF galaxy (0.4% of the sample) in this low t/τ regime. The KBSS galaxies with $\log_{10}(t/\tau) \leq -2.0$ are the same galaxies that have $\log_{10}(\text{sSFR(SED)/yr}^{-1}) \geq -8.0$. This correspondence indicates that the KBSS sample has a subset of galaxies that is very young with intense star formation, for which there is no analogous subset of galaxies in the MOSDEF sample. For A_V, we find that 158 MOSDEF galaxies (63.2% of the sample) have $0.5 \leq A_V \leq 1.0$ compared to 161 KBSS galaxies (only 43.6% of the sample). Otherwise, the distributions of galaxy properties

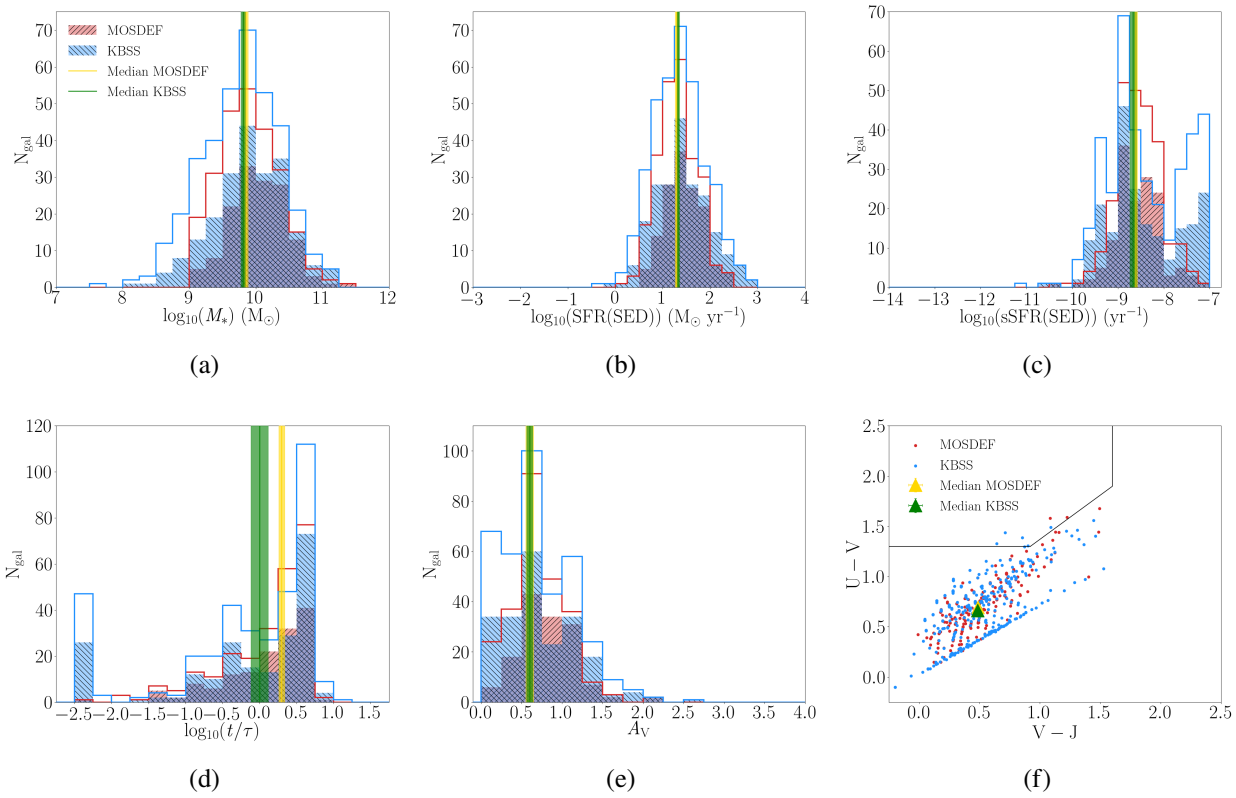

Figure 3.2: Distribution of physical properties for the MOSDEF (red) and KBSS (blue) $z \sim 2$ spectroscopic samples. The red and blue skeletal histograms represent the full spectroscopic samples (i.e., 250 galaxies for MOSDEF and 369 galaxies for KBSS), while the filled regions identify the subset of the spectroscopic samples that are on the [N II] BPT diagram (i.e., 143 galaxies for MOSDEF and 213 galaxies for KBSS). The sample medians, with uncertainties for are shown in yellow (green) for the MOSDEF (KBSS) full spectroscopic samples (i.e., the larger empty histograms), and are given in Table 3.2. The following galaxy properties are shown: (a) M_*, (b) SFR(SED), (c) sSFR(SED), (d) $\log_{10}(t/\tau)$ of the stellar population using a delayed-τ star formation model, (e) A_V, and (f) the UVJ diagram. The quiescent galaxy region in the upper left is enclosed in a solid curve, while star-forming galaxies occupy the bottom half and upper right-hand corner of the diagram. We find that all KBSS and MOSDEF sample median properties agree within the 1σ uncertainty, except for t/τ. The x-axes for panels a-e and both axes for panel f are the same as in Figure 3.7 to show how the distributions of the $z \sim 2$ spectroscopic sample compared to those for the $z \sim 2$ targeted samples.

Table 3.2: Median Values for Physical Properties of the MOSDEF and KBSS $z \sim 2$ Spectroscopic Samples

Physical Property	MOSDEF Median	KBSS Median	p-value	Statistical significance
(1)	(2)	(3)	(4)	(5)
$\log_{10}(M_*/M_\odot)$	9.85 ± 0.03	9.81 ± 0.03	0.0061	2.74σ
$\log_{10}(t/\tau)$	0.30 ± 0.04	0.00 ± 0.12	8.9e−05	3.75σ
$\log_{10}(\mathrm{SFR(SED)}/M_\odot/\mathrm{yr}^{-1})$	1.29 ± 0.04	1.32 ± 0.03	0.064	1.85σ
$\log_{10}(\mathrm{sSFR(SED)}/\mathrm{yr}^{-1})$	-8.61 ± 0.04	-8.67 ± 0.07	8.7e−10	6.13σ
A_V	0.60 ± 0.05	0.60 ± 0.04	5.5e−05	4.03σ
U−V	0.69 ± 0.02	0.66 ± 0.02	0.059	1.89σ
V−J	0.49 ± 0.02	0.48 ± 0.03	0.18	1.34σ

Note. — Col. (1): Physical property of the MOSDEF and KBSS $z \sim 2$ spectroscopic samples (i.e., the skeletal histograms) shown in Figure 3.2. Col. (2): Median value with uncertainty of the MOSDEF $z \sim 2$ spectroscopic sample. Col. (3): Median value with uncertainty of the KBSS $z \sim 2$ spectroscopic sample. Col. (4): Two-tailed p-value, based on the K-S test, estimating the probability that the null hypothesis can be rejected. Col. (5): Statistical significance (i.e., the σ value) corresponding to the p-value.

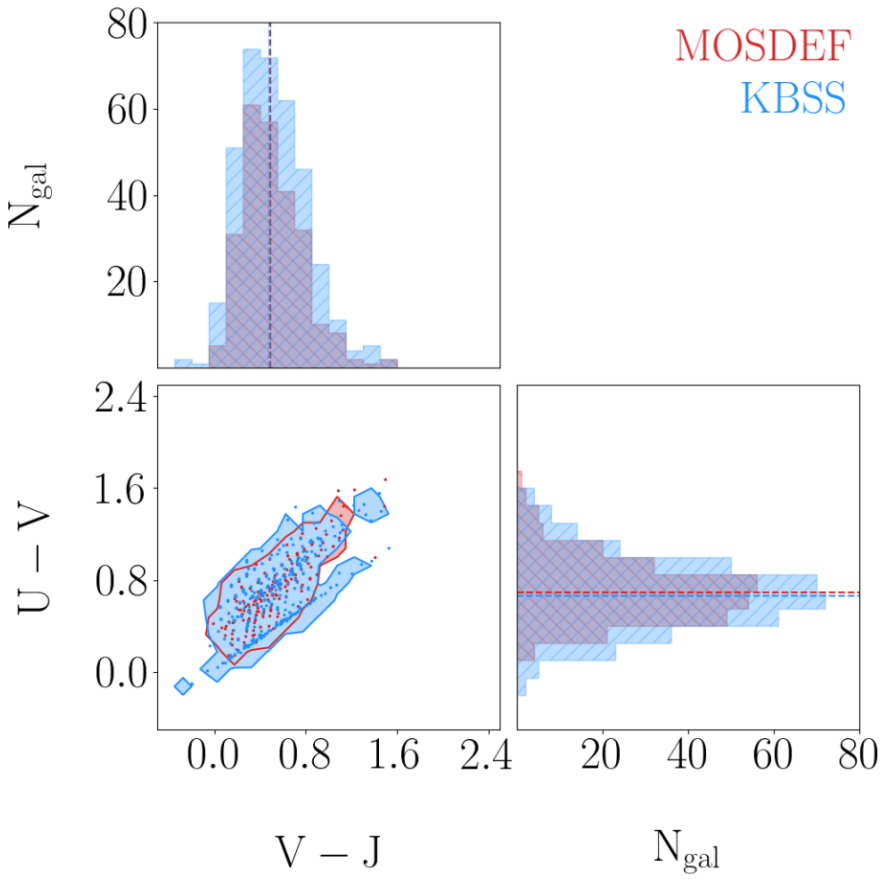

Figure 3.3: Corner plot comparing the distributions of U−V and V−J colors for the MOSDEF (red) and KBSS (blue) $z \sim 2$ spectroscopic samples. The dashed lines on the 1D histograms mark the median values for the distributions of U−V and V−J colors given in Table 3.3, and the contours in the 2D panel trace the 3σ regions in UVJ color-color space. The individual data points are also shown in the 2D UVJ distribution. It is shown here that the MOSDEF and KBSS $z \sim 2$ spectroscopic samples occupy a very similar region of UVJ space, in addition to having sample medians that agree within the uncertainties.

between the two samples are very similar, indicated by p-values at less than 3σ significance.

Figure 3.4 shows corner plots of SFR(SED) vs. M_* (left panel) and sSFR(SED) vs. M_* (right panel) for the MOSDEF and KBSS $z \sim 2$ spectroscopic samples. The sample medians from Table 3.2 are shown on the 1D histogram, and the 3σ contour for each sample is outlined in the 2D distribution. These differences echo those observed for the $z \sim 2$ targeted samples (see Figure 3.1). The difference at low mass is accentuated by the fact that we implemented a mass cut at 10^9 $M_\odot$ for MOSDEF and did not for KBSS. However, the MOSDEF sample cut was implemented because of the known incompleteness at low mass. We emphasize that our goal here is to compare the properties of samples that have been analyzed in previously published work (i.e., Sanders et al., 2018; Strom et al., 2017), and that these different selections at the low-mass end simply reflect what was adopted in these earlier papers. As for the difference in sSFR(SED), the fact that KBSS contains more galaxies at high sSFR(SED) than MOSDEF matches our observation when comparing the distributions in panel (c) of Figure 3.2.

The high M_*, low sSFR(SED) end of the 3σ contours is approximately the same for both samples. This is different from what we find for the $z \sim 2$ targeted samples, where MOSDEF extends to higher mass and lower sSFR(SED) compared to KBSS in Figure 3.1. The difference is due to the MOSDEF sample, where the 3σ contour for the $z \sim 2$ spectroscopic sample does not extend to as high mass and as low sSFR(SED) as the $z \sim 2$ targeted sample. This again points out the MOSDEF incompleteness with respect to the massive, low sSFR(SED) galaxies targeted in the survey (see Section 3.5.2 further discussion on this topic).

Figure 3.5 shows the stacked SEDs of the MOSDEF and KBSS $z \sim 2$ spectroscopic samples. Similar to Figure 13 in Strom et al. (2017), we normalize each spectrum by the flux at 4550 Å , sum the normalized spectra in each sample, then divide by the sample size to account for the uneven sizes of the MOSDEF and KBSS samples. We find that the stacked SEDs of the two samples are nearly identical. It is reasonable that the differences in rest-frame flux of the UV, optical, and near-IR regimes are negligible given that the sample medians for $\log_{10}(t/\tau)$ and UVJ colors agree

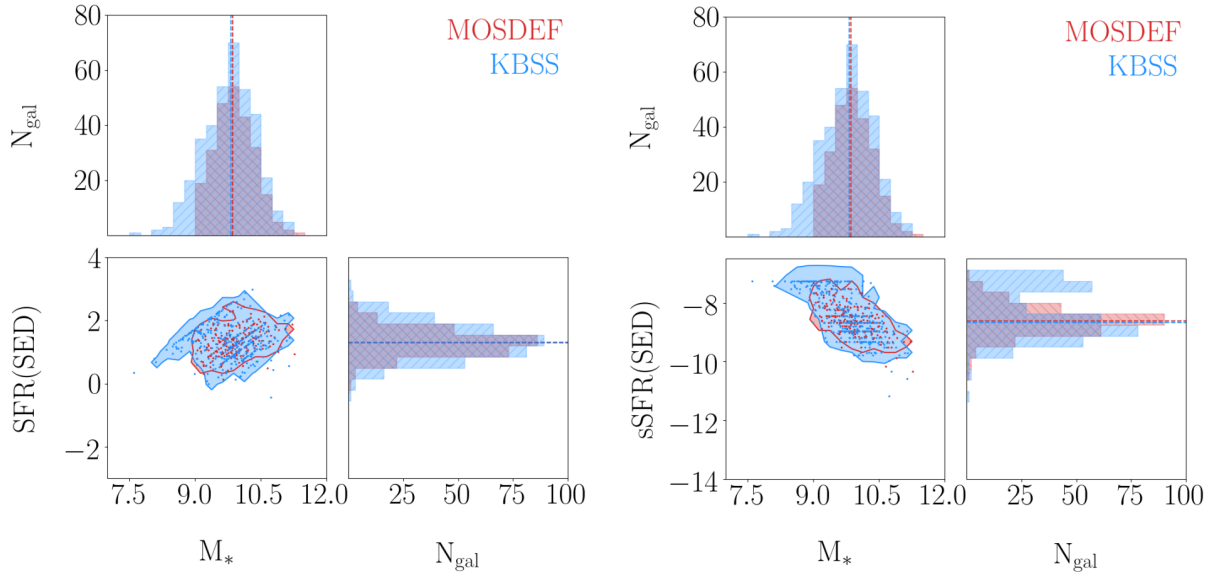

Figure 3.4: Corner plots comparing SFR(SED) vs. M_* (left) and sSFR(SED) vs. M_* (right) for the MOSDEF (red) and KBSS (blue) $z \sim 2$ spectroscopic samples. The dashed lines on the 1D histograms mark the median values for the distributions, and the contours on the diagonal trace the 3σ regions in 2D space. The individual data points are also shown in the 2D distribution. As stated for Figure 3.1, the distribution of datapoints is limited by the fact that both M_* and SFR(SED) are determined by the normalization of the SPS model to the photometry. Additionally, in 2D space the datapoints crowd in the upper-left part of the distribution (left panel) and at high sSFR(SED) (right panel) because of the lower age limit for the stellar populations. We have the same axes limits as the bottom two panels in Figure 3.1 so the distribution of galaxies in the $z \sim 2$ spectroscopic samples can easily be compared with the $z \sim 2$ targeted samples.

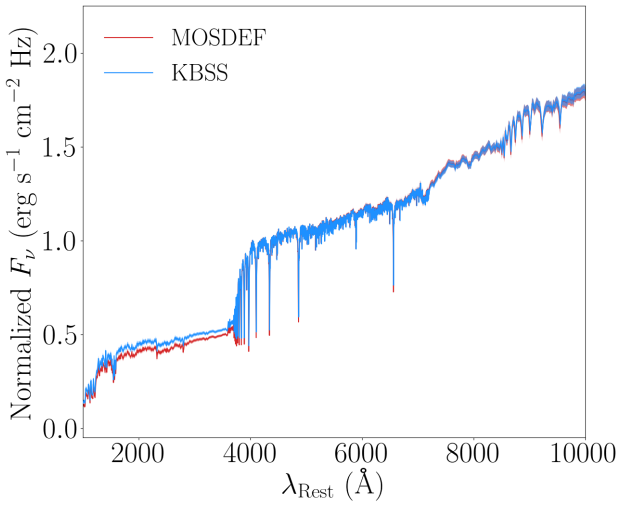

Figure 3.5: Stacked SEDs for the MOSDEF (red) and KBSS (blue) $z \sim 2$ spectroscopic samples. The SEDs are normalized at 4550 Å to show any differences in the global spectral shape. The 1σ scatter of the average SEDs is shown with shaded regions for both samples.

within the uncertainties. The MOSDEF Balmer break is larger compared to KBSS; however, given the separation in median t/τ between the two samples, it is unclear why the difference in the Balmer breaks is not more pronounced.

3.4.2 The [N II] BPT Diagram

The left panel of Figure 3.6 shows the [N II] BPT diagram for the MOSDEF and KBSS samples. We include median lines binned by $\log_{10}$(O3N2) for both samples. There are equal numbers of galaxies in each bin. The binning scheme was adopted because it divides the samples into subgroups segregated roughly along the local star-forming sequence. Only galaxies with S/N $\geq$ 3 for the Hβ, [O III]λ5008, Hα, [N II]λ6585 emission-lines are included on the figure and in the binned medians. There are 143 MOSDEF and 213 KBSS galaxies that meet the S/N requirements to be included in this plot.

We find that the two binned medians for the MOSDEF and KBSS samples have an almost identical offset from the local sequence. When discussing the [N II] BPT diagram, we define the term

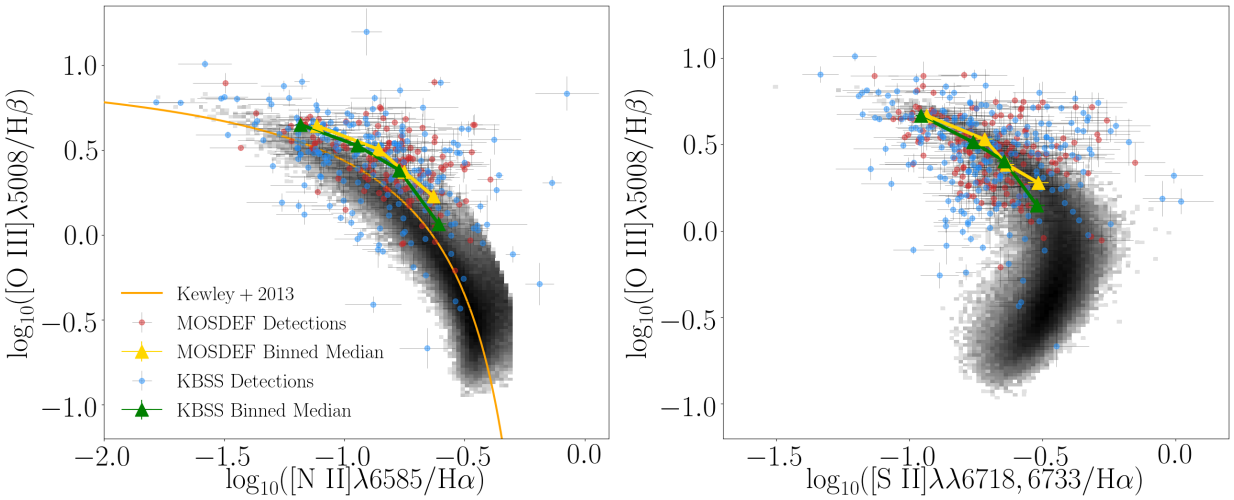

Figure 3.6: The MOSDEF (red) and KBSS (blue) $z \sim 2$ spectroscopic samples on the [N II] BPT (left) and [S II] BPT (right) diagrams. The grayscale 2D histogram indicates local SDSS galaxies. Galaxies must have S/N $\geq$ 3 for the Hβ, [O III]λ5008, Hα, and [N II]λ6585 ([S II]$\lambda\lambda$6718,6733) emission-lines to be included in the [N II] BPT ([S II] BPT) diagram. The yellow and green lines represent binned medians where the sample is binned in $\log_{10}$(O3N2) (left) and $\log_{10}$(O3S2) (right) for the MOSDEF and KBSS samples. The orange curve on the [N II] BPT diagram is a fit to the $z \sim 0$ star-forming locus (Kewley et al., 2013).

"offset" as the orthogonal distance from the Kewley et al. (2013) fit of the local star-forming locus. The MOSDEF and KBSS bins have respectively,a median offset of 0.12 ± 0.02 and 0.10 ± 0.02 dex (0.02 ± 0.02 dex separation) perpendicular to the Kewley et al. (2013) fit. The overlap of the offsets within the uncertainties is very different from those presented in past MOSDEF (Shapley et al., 2015) and KBSS (Steidel et al., 2014; Strom et al., 2017) work. These earlier studies have cited KBSS as having a larger offset from the local sequence than MOSDEF by ∼0.1 dex. We credit the convergence of the [N II] BPT offsets to consistent emission-line fitting between the two samples. Both samples underwent changes to line ratios compared to past measurements.

Here we find that median O3 ratio for the MOSDEF sample is 0.04 dex higher compared to past MOSDEF studies (e.g., Shapley et al., 2015; Sanders et al., 2016). When restricting the $z \sim 2$ spectroscopic sample to galaxies included on the [N II] BPT diagram, the updated (and more robust) methodology for estimating stellar Balmer absorption results in a median decrease of 6.7% in the Hβ fluxes. This updated methodology has a negligible effect on the Hα flux and therefore results in a negligible change to the N2 ratio. The KBSS sample is characterized by a 0.07 dex lower N2 compared to results presented in past KBSS studies. For galaxies with [N II]λ6585 S/N $\geq$ 3.0 in both this study and past KBSS studies (Steidel et al., 2014; Strom et al., 2017), we find a median decrease of 12.8% in [N II]λ6585 flux estimates. In summary, when using a uniform emission-line fitting and Balmer absorption correction methodology we find that both higher O3 for the MOSDEF sample and lower N2 for the KBSS sample combine to erase the apparent differences between the two samples in the [N II] BPT diagram that serve to make the median excitation sequences from each survey indistinguishable within the uncertainties.

3.4.3 The [S II] BPT Diagram

The right panel of Figure 3.6 shows the [S II] BPT diagram for the MOSDEF and KBSS samples. We include median lines binned in $\log_{10}$(O3S2) for both samples. Each bin has an equal number of galaxies. Similar to the case for the [N II] BPT diagram, the binning scheme was adopted because it divides the samples into subgroups segregated roughly along the local star-forming sequence.

Also similar to the [N II] BPT diagram, only galaxies with S/N $\geq$ 3 for the emission-lines relevant to the [S II] BPT diagram (i.e., Hβ, [O III]λ5008, Hα, and [S II]$\lambda\lambda$6718,6733) are included in the figure and the binned medians. There are 156 MOSDEF and 228 KBSS galaxies that meet the S/N requirements to be included in this plot.

Aside from in the bin with the highest S2, the binned medians for the two samples are very similar. Furthermore, the MOSDEF and KBSS median line ratios are more similar than in previous studies (Steidel et al., 2014; Shapley et al., 2015; Strom et al., 2017; Sanders et al., 2018). The MOSDEF sample shows a 0.04 dex increase in O3 (similar to the [N II] BPT diagram), a result of the updated method for estimating stellar Balmer absorption corrections. For KBSS, there is an 0.04 dex decrease in the S2 ratio due to smaller flux estimates by 8.6% on average for the [S II]$\lambda\lambda$6718,6733 doublet than in the methodology from Strom et al. (2017). This change is analogous to the effect we observed with the [N II]λ6585 flux estimates, which will be discussed in Section 3.5.1. Overall, the changes observed in the [S II] BPT diagram reflect similar shifts in MOSDEF and KBSS to those we found in the [N II] BPT diagram.

3.5 Discussion

This section begins with a discussion of the [N II] BPT offset. In Section 3.4.2, we have shown that the median offset from the local sequence for the $z \sim 2$ MOSDEF and KBSS spectroscopic samples agree within the uncertainties when using consistent analysis methods. Section 3.5.1 discusses the significance of this result, compares the results here to previous MOSDEF and KBSS studies, and investigates the bias introduced from utilizing different emission-line fitting methodologies.

We then turn our attention to the MOSDEF and KBSS $z \sim 2$ targeted samples, from which the $z \sim 2$ spectroscopic samples were drawn. Section 3.5.2 compares the host galaxy properties of the $z \sim 2$ targeted samples. Additionally, we discuss differences found between the $z \sim 2$ targeted samples (i.e., the full set of galaxies the MOSDEF and KBSS surveys intended to observe) and the smaller $z \sim 2$ spectroscopic samples (i.e., the subsets of the $z \sim 2$ targeted samples with high S/N

spectra). This comparison is significant because it reveals if the galaxies targeted by the MOSDEF and KBSS surveys are fundamentally different from the subsets of galaxies with high S/N analyzed in past publications (e.g., Steidel et al. 2014; Shapley et al. 2015; Strom et al. 2017; Sanders et al. 2018).

3.5.1 The [N II] BPT Offset

We have shown that, when subject to identical analysis methods, the MOSDEF and KBSS samples are much more similar than reported in previous work. As discussed in Section 3.3.2, we used an updated version of the MOSDEF emission-line fitting code for this study. Using the same code for both samples yielded offsets of 0.12 ± 0.02 and 0.10 ± 0.02 dex from the Kewley et al. (2013) fit (0.02 ± 0.02 dex separation) for, respectively, the MOSDEF and KBSS samples.

As a consistency check, we fit the emission lines of both samples using the same Gaussian fitting assumptions as the `MOSPEC` code that KBSS previously used (Steidel et al., 2014; Strom et al., 2017). `MOSPEC` is a 1D spectral analysis code written in IDL and developed to analyze the MOSFIRE spectra of faint galaxies. Because "`MOSPEC`" and "MOSDEF" are very similar acronyms, we will hereafter refer to the `MOSPEC` code used by the KBSS team as the "KBSS `MOSPEC` code" for clarity. The key difference between the two codes is that the KBSS `MOSPEC` code fixes the centroids of every emission-line in a given band to a single redshift. Also, the velocity widths of all emission-lines are fixed to be the same in each band (i.e., H and K_s). This restriction assigns Hβ and each line in the [O III]$\lambda\lambda$4960,5008 doublet the same velocity widths in the H band, and Hα, [N II]λ6585, and each line in the [S II]$\lambda\lambda$6718,6733 doublet the same velocity width in the K_s-band. As discussed in Section 3.3.2, the centroids and widths are allowed more freedom to vary within the MOSDEF code (Kriek et al., 2015; Reddy et al., 2015). Appendix 3B provides examples of the two codes fitting the same set of spectra to highlight the similarities and differences between them.

It is important to emphasize the motivations that led to the way these two codes were written. For the MOSDEF code, more freedom was allowed in the fitting (e.g., in the centroids and the FWHMs)

to fully marginalize over errors in these parameters for the highest S/N line, given that in some cases these lines were relatively weak and/or did not have a Gaussian shape. For KBSS, which observed the same galaxies many times at different PAs and for a longer period, the line shape can be better quantified. Thus, it is more likely that all lines will provide an accurate probe of the FWHM and redshift.

We find that using the KBSS `MOSPEC` code results in a ~13% median increase in [N II]λ6585 flux estimates for both the MOSDEF and KBSS samples compared to when using the MOSDEF code. This difference corresponds to higher N2 line ratio estimates for both samples as well. A similar effect is observed for the [S II]$\lambda\lambda$6718,6733 doublet.

When using the KBSS `MOSPEC` code, the MOSDEF and KBSS samples, respectively, have a median offset of 0.15 ± 0.02 and 0.12 ± 0.02 dex (0.03 ± 0.02 dex separation) perpendicular to the Kewley et al. (2013) fit. The separation of the two samples with the KBSS `MOSPEC` code is within the uncertainties of that found with the MOSDEF code (i.e., 0.02 ± 0.02 dex). Note that due to the changes to the N2 and O3 flux ratios, both the MOSDEF and KBSS samples are more offset from the local SDSS sequence by 0.03 and 0.02 dex, respectively, when using the KBSS `MOSPEC` code compared to when the MOSDEF code is used. As noted above, this shift arises primarily from the KBSS `MOSPEC` code yielding larger [N II]λ6585 flux estimates compared to the MOSDEF code. There is no significant shift in O3 regardless of which line fitting code is adopted.

When compared to the [N II]λ6585 and [S II]$\lambda\lambda$6718,6733 doublet bandpass integrated line flux, we find that the MOSDEF Gaussian fits generally estimates a lower flux on average while the KBSS Gaussian fits estimates a higher flux on average. In other words, the MOSDEF code underestimates the flux while the KBSS `MOSPEC` code overestimates the flux for these weaker emission-lines compared to their integrated bandpass fluxes. The goal of this paper is not to determine which fitting method is more correct, but instead to show that different assumptions, both reasonable, when implemented into emission-line fitting codes, can lead to different flux measurements resulting in shifts of ~0.02-0.03 dex on the [N II] BPT diagram. These varying assumptions introduce

inherent systematic uncertainty in the flux measurements that are not captured within the statistical uncertainties of the spectra. However, it is important to note that we find nearly identical small relative offsets — 0.02 ± 0.02 dex using the MOSDEF code and 0.03 ± 0.02 dex using the KBSS `MOSPEC` code — between the median MOSDEF and KBSS emission-line sequences on the [N II] BPT diagram when the same line fitting code is used. Therefore, the same conclusions regarding the locus of $z \sim 2$ star-forming galaxies in the [N II] BPT diagram would be reached regardless of which line fitting code is used for analysis.

We note that the ~0.1 dex offset cited in previous MOSDEF (e.g., Shapley et al. 2015) and KBSS (e.g., Steidel et al. 2014; Strom et al. 2017) works is resolved based on updated (smaller) stellar Balmer absorption corrections for the MOSDEF sample as well as consistent emission-line fitting methods.

3.5.2 SED Properties of MOSDEF and KBSS $z \sim 2$ Targeted Samples

In Section 3.4.1, we compared the galaxy properties obtained through SED fitting for the $z \sim 2$ spectroscopic MOSDEF and KBSS samples (i.e., the galaxies shown in blue in Figure 3.1 and analyzed in previous studies Strom et al. 2017; Sanders et al. 2018). Except for t/τ (i.e., age), the sample medians for every other galaxy property investigated agree within the uncertainties. Here, we expand our analysis and examine the SED properties of the full MOSDEF and KBSS $z \sim 2$ targeted survey catalogs (i.e., all galaxies shown in Figure 3.1, including the galaxies where a $z_{\rm MOSFIRE}$ was not measurable). The goal of this analysis is to determine whether the different survey selection methods used by MOSDEF and KBSS resulted in galaxies with systematically different properties targeted in the surveys. As we discuss in Section 3.2.3, most of the MOSDEF $z \sim 2$ galaxies would fall into the KBSS selection criteria (and vice versa). The majority (96.1%) of the KBSS $z \sim 2$ targeted sample satisfies the main selection criterion of the MOSDEF survey (i.e., $H_{\rm AB} < 24.5$), while the distribution of the MOSDEF $z \sim 2$ targeted sample on the $U_{\rm n}G\mathcal{R}$ diagram is very similar to KBSS with 98.5% of MOSDEF galaxies having $\mathcal{R} < 25.5$. This analysis will help to understand the biases of each survey with respect to the other, which is necessary for

future studies using the combined sample.

We consider the same galaxy properties as in Section 3.4.1: M_*, SFR(SED), sSFR(SED), $\log_{10}(t/\tau)$ of the stellar population using a delayed-τ star formation model, A_V, UVJ colors, and stacked SED shapes. The UVJ diagram along with histograms of these properties for MOSDEF and KBSS samples are shown in Figure 3.7. We derive 1σ uncertainties on the medians through bootstrap resampling. Table 3.3 lists the medians with uncertainties, two-tailed p-value based on the K-S test, and the level of significance (the σ value) of the p-value. Additionally, Figure 3.8 explores the UVJ colors in more detail by including both a 2D contour map in UVJ space and 1D histrograms of the U−V and V−J distributions. Finally, the stacked SEDs for the MOSDEF and KBSS $z \sim 2$ targeted samples are shown in Figure 3.9. The stacked SEDs are made using the same methods described in Section 3.4.1 (i.e., the SEDs are normalized at 4550 Å to best show any variations in SED shape between the two samples).

Based on visual inspection of the stacked SEDs, it is clear that on average the MOSDEF $z \sim 2$ targeted sample has a larger Balmer break and higher flux redward of ~5000 Å. These observed differences in SED shapes for the $z \sim 2$ targeted samples are not seen in the stacked SEDs for the $z \sim 2$ spectroscopic samples, indicating that the MOSDEF and KBSS $z \sim 2$ targeted samples are less similar than the $z \sim 2$ spectroscopic samples. Additionally, we find that the MOSDEF $z \sim 2$ targeted sample has a larger median M_*, smaller SFR(SED) and sSFR(SED) medians, and a redder U−V compared to the KBSS $z \sim 2$ targeted sample. The medians for the remaining properties (i.e., t/τ, A_V, and V−J color) all agree within the uncertainties. The p-value from the K-S test for every galaxy property investigated in Figure 3.7 has a significance of at least 4σ, indicating that the shape of the distribution for all galaxy properties considered — even the ones with overlapping sample medians — are significantly different.

Examining the distribution of the galaxies in Figure 3.7, we find clear differences between the two surveys aside from the sample medians. In the KBSS $z \sim 2$ targeted catalog, 281 galaxies (33.1% of the sample) have $\log_{10}(\text{sSFR(SED)}/\text{yr}^{-1}) \geq -8.0$ and 106 galaxies (12.5% of the sample) have

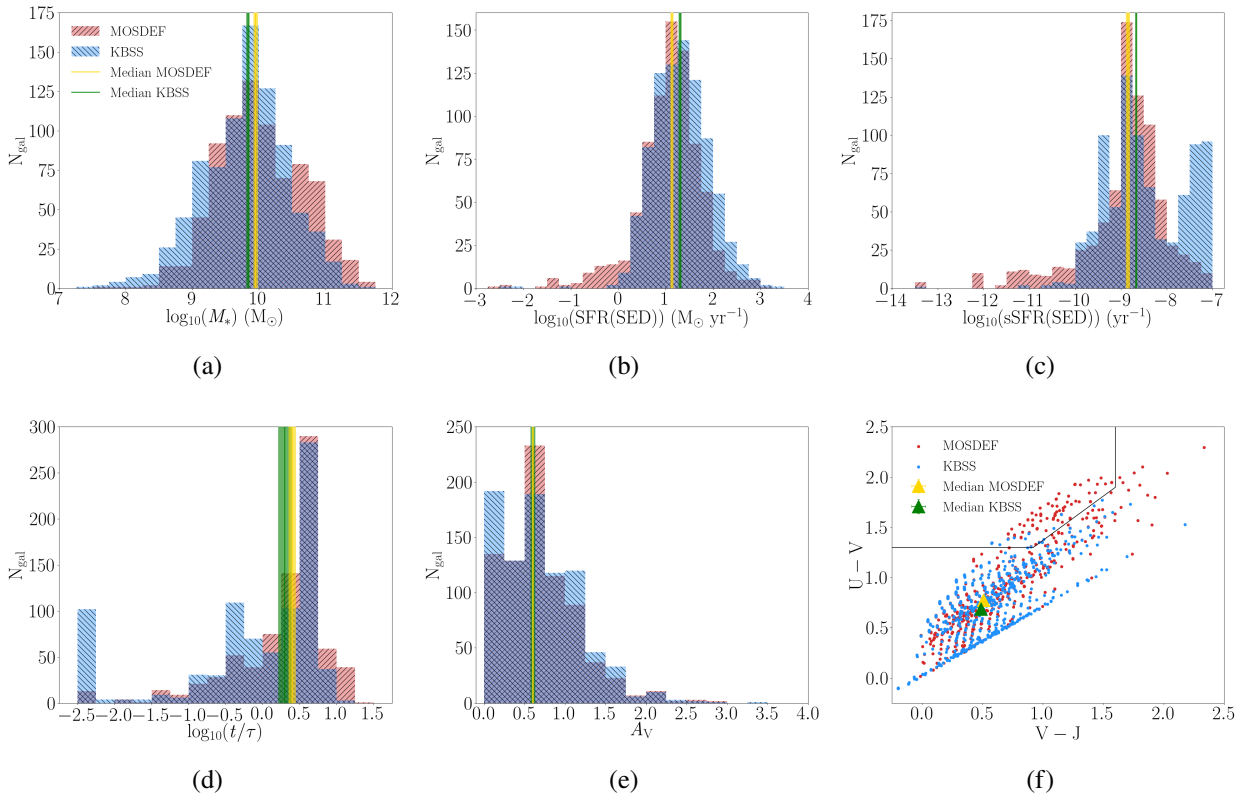

Figure 3.7: Distribution of physical properties for the MOSDEF (red) and KBSS (blue) $z \sim 2$ targeted samples. The sample medians, with uncertainties are shown in yellow (green) for the MOSDEF (KBSS) samples, and are given in Table 3.3. The following galaxy properties are shown: (a) M_*, (b) SFR(SED), (c) sSFR(SED), (d) $\log_{10}(t/\tau)$ of the stellar population using a delayed-τ star formation model, (e) A_V, and (f) the UVJ diagram. We find that the MOSDEF $z \sim 2$ targeted sample has a higher M_*, lower SFR(SED) and sSFR(SED), and a redder U−V color compared to the KBSS $z \sim 2$ targeted sample. Note that two MOSDEF galaxies with $\log_{10}(\mathrm{SFR(SED)/M_\odot/yr^{-1}}) < -3.0$ are excluded from the panel (b), and one MOSDEF galaxy with $\log_{10}(\mathrm{sSFR(SED)/yr^{-1}}) < -14.0$ is excluded from panel (c) to better show the data.

Table 3.3: Median Values for Physical Properties of the MOSDEF and KBSS $z \sim 2$ Targeted Samples

Physical Property	MOSDEF Median	KBSS Median	p-value	Statistical significance
(1)	(2)	(3)	(4)	(5)
$\log_{10}(M_*/M_\odot)$	9.95 ± 0.03	9.84 ± 0.02	1.9e−7	5.21σ
$\log_{10}(t/\tau)$	0.40 ± 0.05	0.30 ± 0.09	7.5e−18	8.61σ
$\log_{10}(\mathrm{SFR(SED)/M_\odot/yr^{-1}})$	1.13 ± 0.02	1.30 ± 0.02	4.2e−9	5.88σ
$\log_{10}(\mathrm{sSFR(SED)/yr^{-1}})$	-8.85 ± 0.04	-8.67 ± 0.01	1.1e−20	9.33σ
A_V	0.60 ± 0.01	0.60 ± 0.03	6.2e−8	5.41σ
U−V	0.78 ± 0.02	0.69 ± 0.01	3.6e−8	5.51σ
V−J	0.51 ± 0.02	0.49 ± 0.01	3.9e−5	4.11σ

Note. — Col. (1): Physical property of the galaxies in the sample shown in Figure 3.7. Col. (2): Median value with uncertainty of the MOSDEF $z \sim 2$ targeted sample. Col. (3): Median value with uncertainty of the KBSS $z \sim 2$ targeted sample. Col. (4): Two-tailed p-value, based on the K-S test, estimating the probability that the null hypothesis can be rejected. Col. (5): Statistical significance (i.e. the σ value) that the p-value corresponds to.

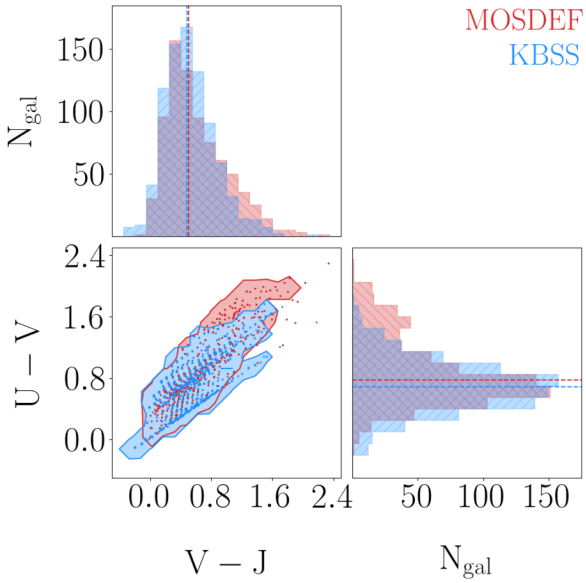

Figure 3.8: Corner plot comparing the distributions of U−V and V−J colors for the MOSDEF (red) and KBSS (blue) $z \sim 2$ targeted samples. The dashed lines on the 1D histograms mark the median values for the distributions of U−V and V−J colors given in Table 3.3, and the contours in the 2D panel trace the 3σ regions in UVJ color-color space. The individual data points are also shown in the 2D UVJ distribution. It is shown here that MOSDEF targeted a population of red galaxies with high U−V color that is not seen in the KBSS $z \sim 2$ targeted sample. Additionally, MOSDEF (KBSS) extends to slightly redder (bluer) regions of V−J color space.

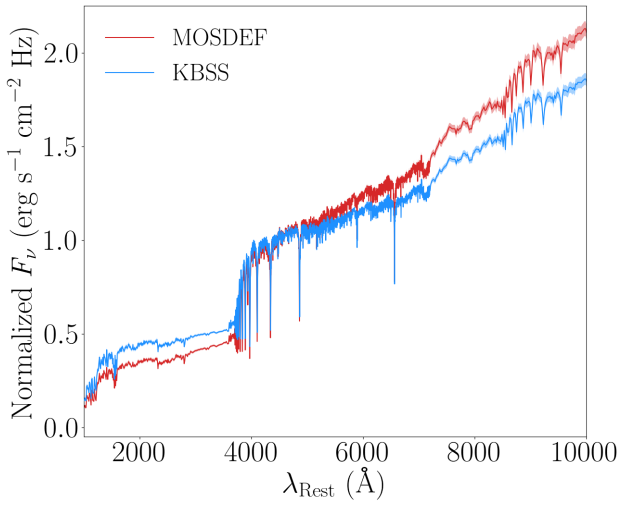

Figure 3.9: Stacked SEDs for the MOSDEF (red) and KBSS (blue) $z \sim 2$ targeted samples. The SEDs are normalized at 4550 Å to show any differences in the global spectral shape. The scatter of the SEDs is shown with shaded regions for both samples.

$\log_{10}(t/\tau) \leq -2.0$. All 106 of the galaxies in this low t/τ regime are in the high sSFR(SED) regime. The MOSDEF $z \sim 2$ targeted catalog is not well represented in these regions of parameter space, with only 77 galaxies (9.8% of the sample) at $\log_{10}(\mathrm{sSFR(SED)/yr^{-1}}) \geq -8.0$ and 14 galaxies (1.8% of the sample) at $\log_{10}(t/\tau) \leq -2.0$. Similar to KBSS, all 14 of the MOSDEF $z \sim 2$ targeted sample galaxies with low t/τ also have a high sSFR(SED). It is apparent that the KBSS $z \sim 2$ sample contains a population of very young galaxies with intense star formation that is mostly absent from the MOSDEF $z \sim 2$ sample. At the same time, MOSDEF contains 59 galaxies (7.5% of the sample) with both U−V and V−J ≥ 1.25, whereas KBSS comparatively only has 18 galaxies (2.1% of the sample) in that area of the UVJ diagram. The 3σ contours in UVJ space in Figure 3.8 also show that the MOSDEF $z \sim 2$ targeted sample probes a more reddened part of UVJ space than KBSS. Galaxies in this regime of the UVJ diagram tend to be more heavily dust obscured or have very low SFR(SED). The distributions of the $z \sim 2$ targeted samples with $A_V \geq 1$ are similar (22.1% and 26.1% of the MOSDEF and KBSS samples), indicating that the reddest galaxies in the MOSDEF $z \sim 2$ targeted sample — i.e., those that are not well represented in the KBSS $z \sim 2$ targeted sample — are not dominated by heavily dust obscured systems but rather those with low sSFR(SED). This difference can be attributed to the original selection method of the KBSS survey (i.e., rest-UV criteria based on $U_nG\mathcal{R}$ colors), and is one of the reasons why the new subset of "RK" galaxies Strom et al. (2017) was added to the survey. However, it is important to note that the "RK" galaxies are a small minority, only 28 galaxies corresponding to 3.3%, of the 850 galaxy KBSS $z \sim 2$ targeted sample.

Some of the results for the $z \sim 2$ targeted samples in Figure 3.7 are different from what we find for the $z \sim 2$ spectroscopic samples in Section 3.4.1. The MOSDEF $z \sim 2$ targeted sample has a higher median M_* and t/τ, a lower median SFR(SED) and sSFR(SED), and redder U−V color compared to the MOSDEF $z \sim 2$ spectroscopic sample. The remaining host galaxy properties (i.e., A_V and V−J) agree within the median uncertainties. Additionally, the subset of the MOSDEF $z \sim 2$ targeted sample with U−V and V−J colors ≥ 1.25 mentioned above are not in the $z \sim 2$ spectroscopic sample (only 2 galaxies, 0.8% of the sample, are in this regime). This indicates

that the population of the MOSDEF survey that is red, old, massive with a relatively low SFR is mostly left out of the $z \sim 2$ spectroscopic sample. For many of these galaxies, a $z_{\rm MOSFIRE}$ was not obtained, indicating that this is an incomplete regime within the MOSDEF survey that will need to be addressed with deeper spectroscopy. This region of UVJ space is mostly absent from the KBSS $z \sim 2$ targeted sample as well.

The KBSS $z \sim 2$ targeted sample has a higher t/τ compared to the KBSS $z \sim 2$ spectroscopic sample analyzed here. The remaining sample properties agree within the median uncertainties, including M_*, SFR(SED), sSFR(SED), $A_{\rm V}$, and UVJ colors. It does not appear that there is an analogous incompleteness within the KBSS catalog to what is observed for massive, low sSFR(SED) galaxies in MOSDEF. However, it is important to note that the KBSS $z \sim 2$ targeted sample does not contain the red population that MOSDEF targeted but was ultimately unsuccessful with. This could be attributed to the differences in the MOSDEF and KBSS observing strategies. MOSDEF observed each object for the equivalent of 2 hours per filter in clear conditions in each band while KBSS retained objects for subsequent observation if all lines had not been detected.

Despite the notable differences in the $z \sim 2$ targeted samples described above, the MOSDEF and KBSS $z \sim 2$ spectroscopic samples analyzed in the BPT diagrams have mostly similar host galaxy property distributions and median values. Because the targeting strategies of the surveys are so different, the similarity of the MOSDEF and KBSS $z \sim 2$ spectroscopic samples reveals the challenges of detecting emission-lines for dusty and/or low sSFR galaxies at $z \sim 2$. As the MOSDEF incompleteness is addressed with deeper spectroscopy for massive galaxies, and therefore a MOSDEF $z \sim 2$ spectroscopic sample that better reflects its $z \sim 2$ targeted sample is assembled, it is unclear how the relative emission-line ratios of the MOSDEF and KBSS $z \sim 2$ spectroscopic samples will change at the massive end.

3.6 Summary

The combination of the MOSDEF and KBSS-MOSFIRE surveys represents the largest investment of Keck/MOSFIRE observing time, with ~3000 galaxies (about half at $z \sim 2$) observed over ~100 nights. The statistical weight of the combined MOSDEF+KBSS sample is capable of determining robust trends in galaxy properties and physical relationships in the $z \sim 2$ universe analogous to what currently exists locally. To understand both how the differences in the survey selection criteria affect the samples and how to account for any biases between the samples when combining them, this study presents a thorough comparison of the $1.9 \leq z \leq 2.7$ MOSDEF and KBSS samples. Using consistent broadband emission-line subtracted SED fitting and emission-line fitting, we compared the physical and emission-line properties of the previously published MOSDEF (Sanders et al., 2018) and KBSS (Strom et al., 2017) samples. In addition, we investigate how well these samples represent the $z \sim 2$ targeted samples from which they are drawn. Applying the same analysis methodology to both samples eliminates biases stemming from the analysis process, meaning any variations found between the samples are due to systematic differences between the samples due to the survey selection method.

The main results are as follows:

1. Despite the differences in galaxy selection methods for the MOSDEF and KBSS surveys, the $z \sim 2$ spectroscopic samples have very similar galaxy properties. KBSS has a lower median t/τ of the stellar population assuming a delayed-τ star formation model compared to MOSDEF, but the medians for all other galaxy properties investigated (M_*, SFR(SED), sSFR(SED), A_V, and UVJ colors) agree within the uncertainties. Additionally, the normalized stacked SEDs are very similar as well. The most notable sample difference is that there are 50 KBSS galaxies (13.6% of the sample) that are very young ($\log_{10}(t/\tau) \leq -2.0$) with intense star formation ($\log_{10}(\text{sSFR(SED)/yr}^{-1}) \geq -8.0$) compared to only 1 such galaxy within the MOSDEF sample.

2. The MOSDEF and KBSS $z \sim 2$ spectroscopic samples have offsets, respectively, of 0.12 ± 0.02 and 0.10 ± 0.02 dex from the local SDSS sequence on the [N II] BPT diagram using the emission-line fitting assumptions from the MOSDEF code. These offsets change to 0.15 ± 0.02 and 0.12 ± 0.02 dex, respectively, from the local SDSS sequence using the emission-line fitting assumptions from the KBSS `MOSPEC` code. The binned medians are also more similar on the [S II] BPT diagram compared to previous MOSDEF and KBSS studies. Because the two samples have similar patterns in their galaxy properties, this agreement on the [N II] BPT diagram can be attributed to the utilization of consistent emission-line fitting. Updated methods for estimating stellar Balmer absorption resulted in smaller Hβ flux estimates (therefore higher O3) for the MOSDEF sample compared to previous studies. Fitting the KBSS sample with the MOSDEF emission-line fitting code resulted in smaller [N II]λ6585 and [S II]$\lambda\lambda$6718,6733 flux estimates (therefore smaller N2 and S2) compared to past KBSS studies that used the KBSS `MOSPEC` code.

3. The MOSDEF $z \sim 2$ targeted sample has a larger median M_*, smaller SFR(SED) and sSFR(SED) medians, and a redder U−V compared to the KBSS $z \sim 2$ targeted sample. These sample differences are highly robust ($> 4\sigma$). Additionally, each survey occupies regions of parameter spaces that are complementary to those spanned by the other survey. In particular, 59 galaxies (7.5%) in the MOSDEF $z \sim 2$ targeted sample are red, displaying U−V and V−J colors ≥ 1.25 while only 18 galaxies (2.1%) in the KBSS $z \sim 2$ targeted sample are in this regime. On the other hand, 106 galaxies (12.5%) in the KBSS $z \sim 2$ targeted sample have $\log_{10}(t/\tau) \leq -2.0$ and $\log_{10}(\mathrm{sSFR(SED)/yr^{-1}}) \geq -8.0$ compared to only 14 galaxies (1.8%) in the MODSEF $z \sim 2$ targeted sample. These differences indicate that the MOSDEF $z \sim 2$ targeted sample contains more massive galaxies with low sSFR(SED) and KBSS includes more young galaxies with intense star formation.

4. While the KBSS $z \sim 2$ spectroscopic sample reflects its $z \sim 2$ targeted sample very well, there are some differences between the MOSDEF $z \sim 2$ spectroscopic sample and its $z \sim 2$

targeted sample. There is a population of the MOSDEF $z \sim 2$ targeted sample that is red, old, massive (i.e., large U−V, V−J, M_*, and t/τ) with a relatively low SFR that is not present in the $z \sim 2$ spectroscopic sample. A $z_{\rm MOSFIRE}$ was not obtained for many of these galaxies, indicating that this is an incomplete regime in the MOSDEF survey. Deeper spectroscopy for these galaxies will be required to fill in this gap.

The results of this study also highlight the systematic uncertainties that arise based on how the measurements are performed on spectroscopic data of faint galaxies. The fact that the previously established difference in [N II] BPT offset between the MOSDEF and KBSS surveys can in large part be attributed to how stellar Balmer absorption corrections and weak emission-line (e.g., [N II]λ6585 and [S II]$\lambda\lambda$6718,6733) fitting are performed, makes this abundantly clear. The different assumptions in the MOSDEF and KBSS fitting codes were both reasonable given the S/N of the spectra for each survey. However, the uncertainty that arises from minor differences in data analysis methods can be extremely difficult to estimate. Until standard methods to analyze basic quantities are adopted and commonly used (if that is even possible given that one's approach to fitting emission-lines depends on the spectral S/N), it is important to consider how minor differences in the data analysis process can affect results from different studies.

With the MOSDEF and KBSS samples now better understood, it is possible to combine them to form a $z \sim 2$ sample of unprecedented size. Future work will involve utilizing this joint sample to construct galaxy scaling relations for the largest rest-optical spectroscopic sample at $z \sim 2$. Currently, there is no consensus on the redshift dependent offset of the mass-metallicity relationship (MZR), or if evolution exists between local and $z \sim 1-3$ galaxies in the "fundamental metallicity relationship" (FMR). In particular, we will investigate the evolution of the mass-metallicity and fundamental metallicity relationships (e.g., Mannucci et al., 2010; Sanders et al., 2021; Strom et al., 2022) using the joint MOSDEF-KBSS sample, enabling the most statistically robust characterization of these relationships at $z \sim 2$.

In this study, we have shown that for large samples spanning multiple orders of magnitude in M_* and

SFR(SED), the median offset of $z \sim 2$ galaxies perpendicular to the local sequence is approximately $0.10 - 0.15$ dex. A challenging systematic uncertainty to quantify and minimize moving forward is that stemming from analysis methods, as discussed above. However, the existence of the offset between $z \sim 2$ and $z \sim 0$ galaxies in the [N II] BPT diagram persists regardless of the analysis method used, and therefore must be reckoned with as we seek to describe the evolution of rest-optical emission properties of galaxies at high redshift.

Appendix

3A CSF Modeling

In this Appendix, we investigate the galaxy properties of the MOSDEF and KBSS $z \sim 2$ spectroscopic and $z \sim 2$ targeted samples assuming a CSF history instead of a delayed-τ star formation history. The SEDs are fit using the stellar population templates from Bruzual & Charlot (2003) assuming a Chabrier (2003) IMF. The Bruzual & Charlot (2003) templates do not account for emission-lines or nebular continuum emission. Following previous studies (Reddy et al., 2018; Du et al., 2018), we adopt two combinations of extinction curves and metallicity: a $1.4Z_{\odot}$ metallicity with the Calzetti et al. (2000) attenuation curve (hereafter referred to as "1.4 $Z_{\odot}$+Calzetti", and a $0.28Z_{\odot}$ metallicity with the Small Magellanic Cloud (SMC) attenuation curve "0.28 $Z_{\odot}$+SMC". Additionally, the code allows stellar population ages between 10 Myr and 5 Gyr and E(B-V) values between 0.0 and 0.6.

We employ several constraints on the models based on past studies of $z \sim 2$ galaxies. Following Du et al. (2018), we use the 1.4 $Z_{\odot}$+Calzetti grid for galaxies with $\log_{10}(M_*/M_{\odot}) \geq 10.45$ and the 0.28 $Z_{\odot}$+SMC grid for galaxies with $\log_{10}(M_*/M_{\odot}) \leq 10.45$. This choice in assumed metallicity based on stellar mass is consistent with the mass-metallicity relationship, MZR, (e.g., Tremonti et al. 2004; Erb et al. 2006a; Andrews & Martini 2013; Steidel et al. 2014; Sanders et al. 2015). We set a minimum stellar population age of 50 Myr, which is based on typical dynamical timescales at $z \sim 2$ (Reddy et al., 2012).

We probe the same set of galaxy properties as with the FAST delayed-τ models: M_*, SFR(SED), sSFR(SED), age of the stellar population (now parameterized by t instead of t/τ), A_V, and UVJ colors. Once again, we used IRAF/*sbands* to estimate the UVJ colors from the best-fit SEDs. Using the M_* from this fitting method, 5/259 galaxies from the MOSDEF $z \sim 2$ spectroscopic sample have $\log_{10}(M_*/M_{\odot}) < 9.0$ and are removed from this sample. This is close to the number of galaxies removed from the MOSDEF $z \sim 2$ spectroscopic sample with the FAST fitting methodology (9

galaxies). Therefore, the MOSDEF $z \sim 2$ spectroscopic sample consists of 254 galaxies using the CSF models. The KBSS $z \sim 2$ spectroscopic sample and both the MOSDEF and KBSS $z \sim 2$ targeted samples have the same number of galaxies as they did in the main analysis.

Figures 3A.1 and 3A.2 show the histograms and UVJ diagram for the galaxy properties of the $z \sim 2$ spectroscopic and $z \sim 2$ targeted samples, respectively. Tables 3A.1 and 3A.2 contain the median values of the distributions for the $z \sim 2$ spectroscopic and $z \sim 2$ targeted samples, respectively. Additionally, Figure 3A.3 gives corner plots showing the 1D histograms and 2D distribution with contour maps of the UVJ colors for the $z \sim 2$ spectroscopic and $z \sim 2$ targeted samples.

We find that the MOSDEF $z \sim 2$ spectroscopic sample has a slightly larger median t (i.e., older) and U−V color (i.e., redder) and slightly smaller median SFR(SED), sSFR(SED), and A_V compared to the KBSS $z \sim 2$ spectroscopic sample. The remaining galaxy properties, M_* and V−J color, agree within the median uncertainties. The p-values estimated from the KS test are greater than 3σ for t, sSFR(SED), and A_V. The result that the KBSS $z \sim 2$ spectroscopic sample is younger than its MOSDEF counterpart is similar to the results using the FAST SED fitting from Section 3.4.1. Also similar is that the 3σ contours occupy similar regions for the UVJ colors in Figure 3A.3. The differences in the median SFR(SED), sSFR(SED), A_V, and U−V color were not seen in Section 3.4.1. Similar to the delayed-τ model results, there is a population (49/369 or 13.3%) of young KBSS galaxies with intense star formation (i.e., $\log_{10}(t/\mathrm{yr}) \leq 8.0$ and $\log_{10}(\mathrm{sSFR(SED)/yr}^{-1}) \geq -8.0$). There are only 3/254 (1.2%) MOSDEF galaxies in this regime.

When looking at the $z \sim 2$ targeted samples, we find that MOSDEF has a larger median M_* and t, a smaller median sSFR(SED), and redder UVJ colors compared to KBSS. The medians for SFR(SED) and A_V agree within the uncertainties. These results are all highly significant, with p-values greater than 4σ for all galaxy properties. The results from the CSF models find differences in the median t and U−V color of MOSDEF and KBSS $z \sim 2$ targeted samples, which was not seen in the FAST fitting. On the other hand, the results from the CSF models find no differences in the median SFR(SED), as found in the results from FAST. Similar to the delayed-τ

models, 124/850 (14.6%) of KBSS galaxies are young ($\log_{10}(t/\mathrm{yr})\leq 8.0$) with intense star formation ($\log_{10}(\mathrm{sSFR(SED)/yr^{-1}})\geq -8.0$) compared to only 12/786 galaxies (1.5%) in the MOSDEF sample. Meanwhile, 134/786 (17.0%) of MOSDEF galaxies are extremely reddened (U−V and V−J ≥ 1.25) compared to 22/850 galaxies (2.6%) in the KBSS sample. Additionally, the 3σ contour map for MOSDEF extends to redder UVJ colors compared to KBSS. We note here that the distribution of inferred U-V and V-J colors for the MOSDEF $z\sim 2$ targeted sample changes when assuming CSF models, relative to the results for the delayed-τ modeling presented in Section 3.5.2. Specifically, the CSF models do not accurately capture the SED shapes of the most massive, low sSFR(SED) galaxies in the MOSDEF $z\sim 2$ targeted sample, and therefore place them (erroneously) outside of the quiescent region of the UVJ diagram.

Figure 3A.4 contains corner plots showing both the 1D histograms and 2D contour mapping for SFR(SED) vs. M_* and sSFR(SED) vs. M_* for the MOSDEF and KBSS spectroscopic (top panels) and targeted (lower panels) samples. We find mostly similar results to the delayed-τ FAST results in the main body of the text (see Figures 3.1 and 3A.4). KBSS extends to lower M_* and higher sSFR(SED) than MOSDEF in both the $z\sim 2$ spectroscopic and $z\sim 2$ targeted samples. The distributions for the KBSS $z\sim 2$ spectroscopic and $z\sim 2$ targeted samples are very similar in both SFR(SED) vs. M_* and sSFR(SED) vs M_* space. Meanwhile, we find the same differences between the MOSDEF $z\sim 2$ spectroscopic and $z\sim 2$ targeted samples. The 3σ contour for the MOSDEF spectroscopic sample reaches a similar upper mass, lower sSFR(SED) limit as the KBSS sample, while the MOSDEF $z\sim 2$ targeted sample extends to higher M_*. This once again shows that MOSDEF is incomplete in this high mass regime. As we discuss previously in the paper, KBSS does not target the high mass galaxies for which MOSDEF is not successful in obtaining high quality S/N spectra.

While the results for the delayed-τ and CSF models do not perfectly align (i.e., the relative median values between the MOSDEF and KBSS $z\sim 2$ spectroscopic and $z\sim 2$ targeted samples sometimes vary based on which fitting method is used, and the rest-frame UVJ colors of the most massive

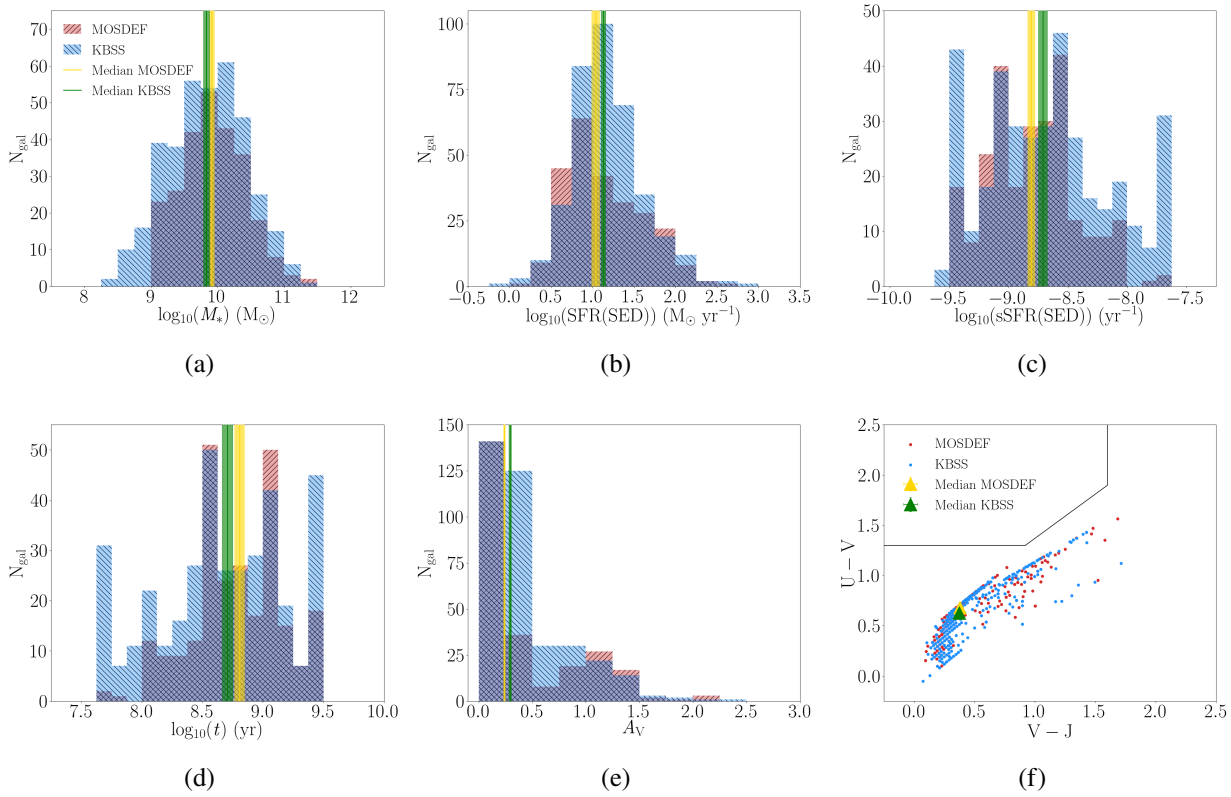

Figure 3A.1: Distribution of physical properties for the MOSDEF (red) and KBSS (blue) $z \sim 2$ spectroscopic samples. The sample medians, with uncertainties are shown in yellow (green) for the MOSDEF (KBSS) samples, and are given in Table 3A.1. The following galaxy properties are shown: (a) M_*, (b) SFR(SED), (c) sSFR(SED), (d) $\log_{10}(t)$ of the stellar population using a constant star formation model, (e) A_V, and (f) the UVJ diagram. We find that the MOSDEF spectroscopic sample has a higher age, lower SFR(SED), lower sSFR(SED), and A_V, and redder U−V color compared to the KBSS spectroscopic sample.

Table 3A.1: Median Values for Physical Properties of the MOSDEF and KBSS $z \sim 2$ Spectroscopic Samples (CSF Models)

Physical Property	MOSDEF Median	KBSS Median	p-value	Statistical significance
(1)	(2)	(3)	(4)	(5)
$\log_{10}(M_*/M_\odot)$	9.91 ± 0.04	9.83 ± 0.05	0.023	2.27σ
$\log_{10}(t/\mathrm{yr})$	8.81 ± 0.04	8.71 ± 0.04	0.00066	3.41σ
$\log_{10}(\mathrm{SFR(SED)/M_\odot/yr^{-1}})$	1.04 ± 0.05	1.13 ± 0.03	0.026	2.23σ
$\log_{10}(\mathrm{sSFR(SED)/yr^{-1}})$	−8.81 ± 0.03	−8.71 ± 0.04	0.00056	3.45σ
A_V	0.24 ± 0.01	0.29 ± 0.01	0.00019	3.73σ
U−V	0.68 ± 0.02	0.63 ± 0.02	0.057	1.90σ
V−J	0.37 ± 0.02	0.37 ± 0.02	0.46	0.74σ

Note. — Col. (1): Physical property of the galaxies in the sample shown in Figure 3A.1. Col. (2): Median value with uncertainty of the MOSDEF $z \sim 2$ spectroscopic sample. Col. (3): Median value with uncertainty of the KBSS $z \sim 2$ spectroscopic sample. Col. (4): Two-tailed p-value, based on the K-S test, estimating the probability that the null hypothesis can be rejected. Col. (5): Statistical significance (i.e. the σ value) that the p-value corresponds to.

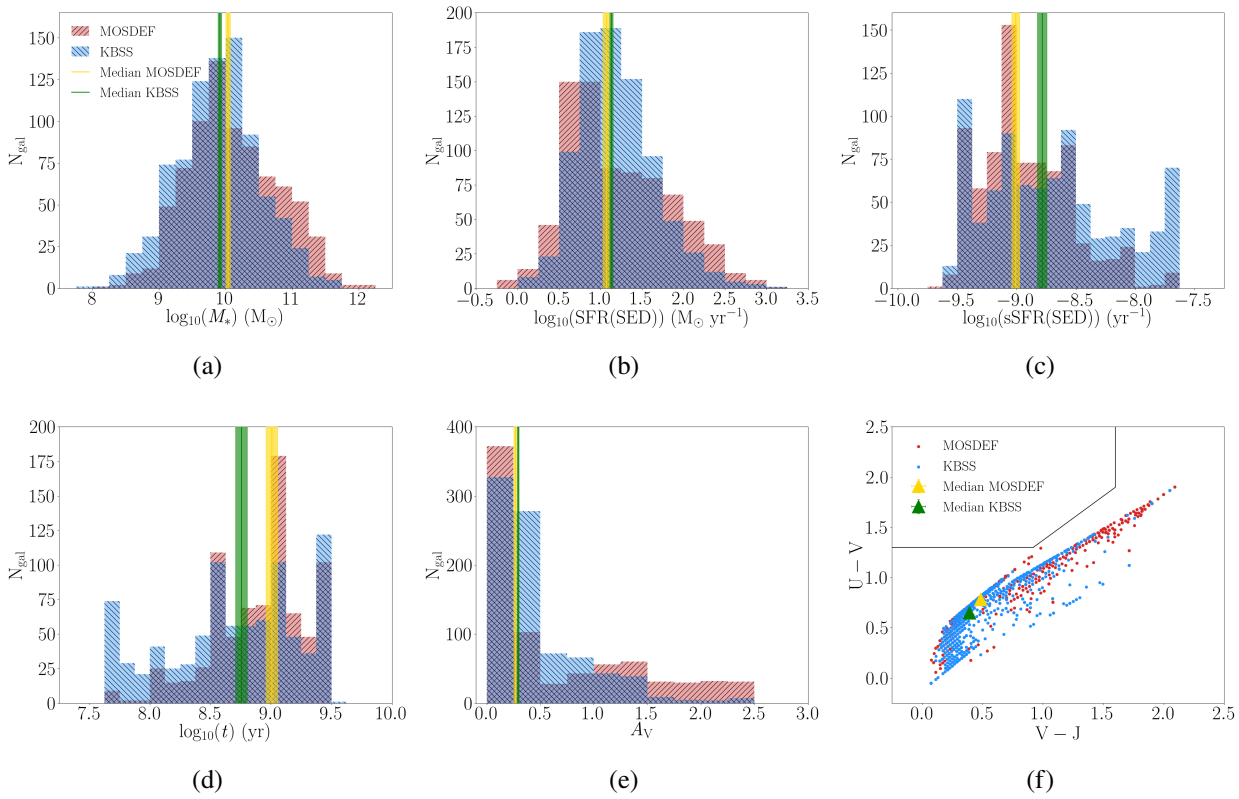

Figure 3A.2: Distribution of physical properties for the MOSDEF (red) and KBSS (blue) $z \sim 2$ targeted samples. The sample medians, with uncertainties are shown in yellow (green) for the MOSDEF (KBSS) samples, and are given in Table 3A.2. The following galaxy properties are shown: (a) M_*, (b) SFR(SED), (c) sSFR(SED), (d) $\log_{10}(t)$ of the stellar population using a constant star formation model, (e) A_V, and (f) the UVJ diagram. We find that the MOSDEF $z \sim 2$ targeted sample has a higher M_* and age, lower SFR(SED) and lower sSFR(SED), and redder UVJ colors compared to the KBSS $z \sim 2$ targeted sample.

Table 3A.2: Median Values for Physical Properties of the MOSDEF and KBSS $z \sim 2$ Targeted Samples (CSF Models)

Physical Property	MOSDEF Median	KBSS Median	p-value	Statistical significance
(1)	(2)	(3)	(4)	(5)
$\log_{10}(M_*/M_\odot)$	10.04 ± 0.04	9.91 ± 0.03	2.5e−7	5.16σ
$\log_{10}(t/\mathrm{yr})$	9.01 ± 0.05	8.76 ± 0.05	7.8e−14	7.47σ
$\log_{10}(\mathrm{SFR(SED)/M_\odot/yr^{-1}})$	1.07 ± 0.04	1.13 ± 0.02	7.2e−6	4.49σ
$\log_{10}(\mathrm{sSFR(SED)/yr^{-1}})$	−9.01 ± 0.03	−8.78 ± 0.04	1.6e−14	7.68σ
A_V	0.27 ± 0.01	0.29 ± 0.01	3.5e−13	7.27σ
U−V	0.78 ± 0.01	0.65 ± 0.02	1.2e−10	6.44σ
V−J	0.48 ± 0.02	0.39 ± 0.01	7.3e−9	5.78σ

Note. — Col. (1): Physical property of the galaxies in the sample shown in Figure 3A.2. Col. (2): Median value with uncertainty of the MOSDEF $z \sim 2$ targeted sample. Col. (3): Median value with uncertainty of the KBSS $z \sim 2$ targeted sample. Col. (4): Two-tailed p-value, based on the K-S test, estimating the probability that the null hypothesis can be rejected. Col. (5): Statistical significance (i.e. the σ value) that the p-value corresponds to.

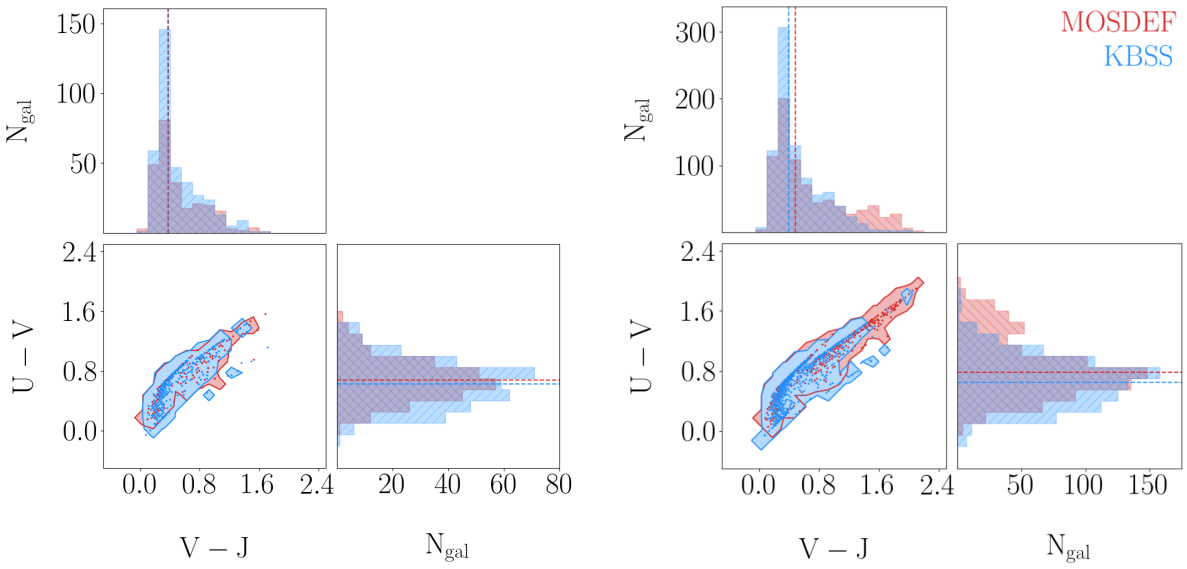

Figure 3A.3: Corner plots comparing the distributions of U−V and V−J colors for the $z \sim 2$ spectroscopic (left) and targeted (right) samples. MOSDEF and KBSS are shown in red and blue, respectively. The dashed lines on the 1D histograms mark the median values for the distributions of U−V and V−J colors given in Tables 3A.1 and 3A.2, and the contours in the 2D panel trace the 3σ regions in UVJ color-color space. The individual data points are also shown in the 2D distribution. Similar to Figure 3.3 and 3.8, it is shown here that while the $z \sim 2$ spectroscopic samples span a similar range in UVJ space, the MOSDEF $z \sim 2$ targeted sample extends to redder UVJ colors than the KBSS $z \sim 2$ targeted sample.

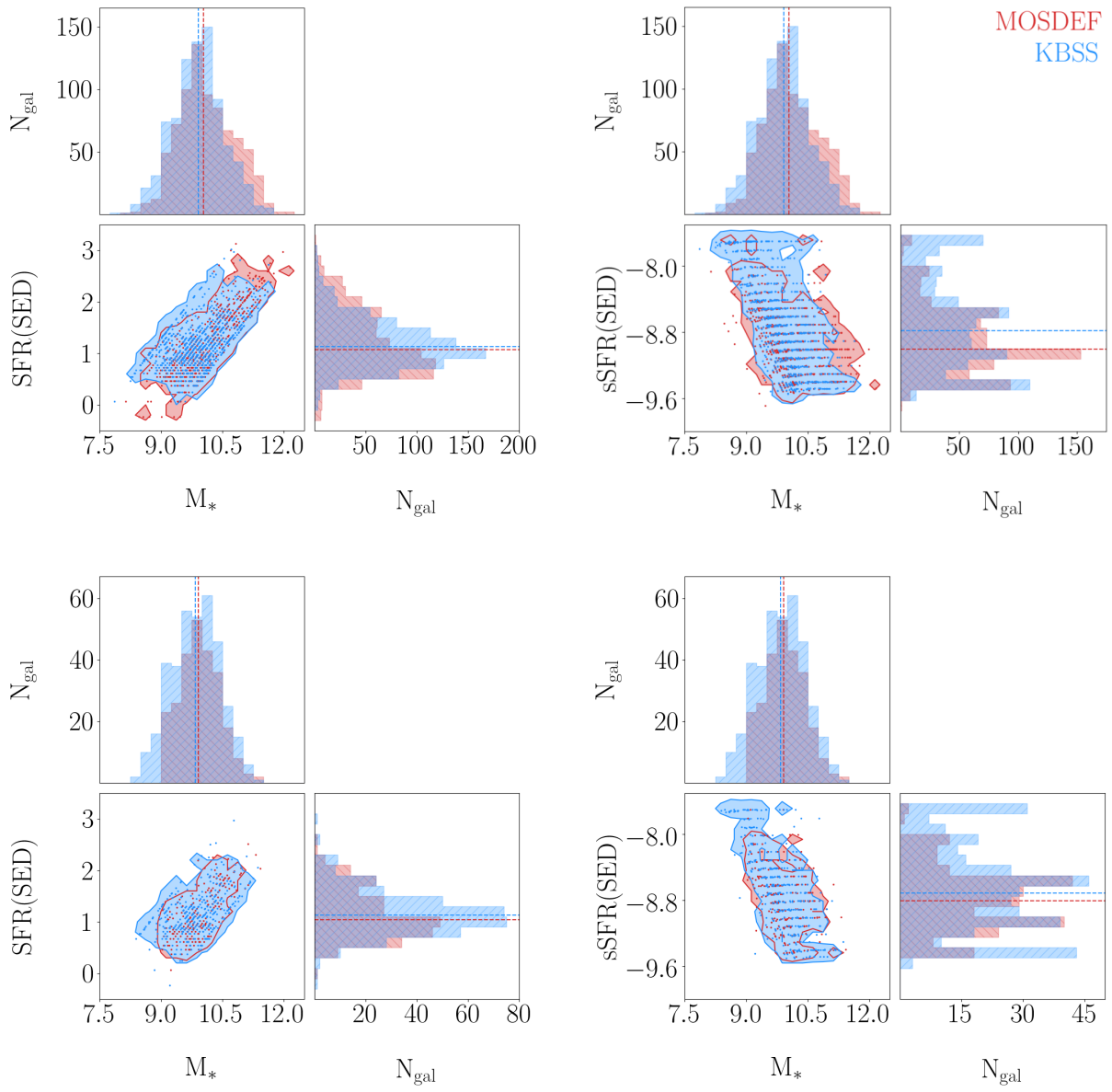

Figure 3A.4: Top: $z \sim 2$ targeted samples. Bottom: $z \sim 2$ spectroscopic samples. The left (right) column contains corner plots comparing SFR(SED) vs. M_* (sSFR(SED) vs. M_*). MOSDEF and KBSS are shown in red and blue, respectively. The dashed lines on the 1D histograms mark the median values for the distributions, and the contours on the diagonal trace the 3σ regions in 2D space. The individual data points are also shown in the 2D distribution. These plots utilize CSF fitting, and are analogous to Figures 3.1 ($z \sim 2$ targeted sample) and 3.4 ($z \sim 2$ spectroscopic sample).

galaxies in the MOSDEF $z \sim 2$ targeted sample are not captured by the CSF models), the key takeaways of the study concerning the galaxy properties are the same for both models.

1. The MOSDEF and KBSS $z \sim 2$ spectroscopic samples are more similar to each other than the $z \sim 2$ targeted galaxy samples.

2. The KBSS spectroscopic and $z \sim 2$ targeted samples have a subset of young galaxies with intense star formation that are mostly absent from the MOSDEF samples.

3. The MOSDEF $z \sim 2$ targeted sample contains extremely red (i.e., high UVJ colors) galaxies that are mostly absent from the KBSS $z \sim 2$ targeted sample.

4. The subset of extremely red MOSDEF galaxies in the $z \sim 2$ targeted sample are not represented in the spectroscopic sample, highlighting that MOSDEF is incomplete in this regime.

As stated in Section 3.3.1, these key takeaways remain unchanged if we use τ-rising models instead of CSF or delayed-τ models.

3B Emission-line Fitting Examples

Here we provide examples of the MOSDEF and KBSS emission-line fitting. In these examples, we focus on the fit of [N II]λ6585 because weaker emission-lines exhibited the most flux variance when one compares the MOSDEF and KBSS `MOSPEC` codes. The fits to Hα and [N II]λ6550 (not relevant to this study) are included in the plots due to their proximity to [N II]λ6585. Figure 3B.1 shows the fits to four example spectra, two from the MOSDEF $z \sim 2$ spectroscopic sample and two from the KBSS $z \sim 2$ spectroscopic sample. Each panel includes the spectra as well as the fits from both the MOSDEF and KBSS `MOSPEC` codes.

As discussed in Section 3.5.1, the MOSDEF Gaussian fit to the [N II]λ6585 line estimates a lower flux on average compared to the integrated bandpass flux. Meanwhile, the KBSS Gaussian fit estimates a higher flux on average compared to the integrated bandpass flux. The assumptions used

by the two methods are both reasonable, given the differences in typical S/N of the MOSDEF and KBSS surveys. The goal of this paper has not been to determine which fitting method is more correct, but instead to show that different assumptions in the emission-line fitting can lead to small systematic variations in measured flux.

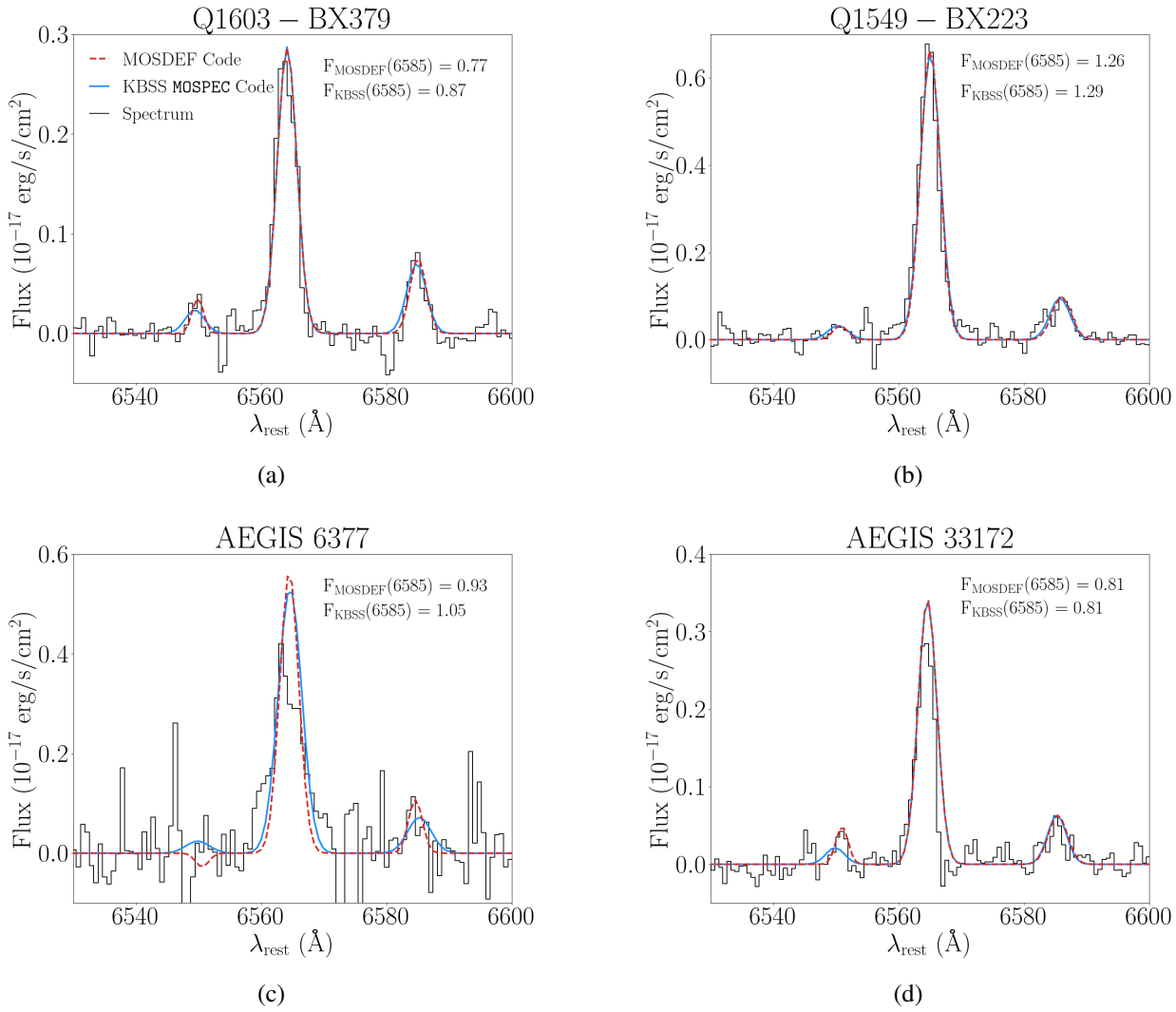

Figure 3B.1: Examples showing how the MOSDEF (red) and KBSS `MOSPEC` (blue) codes fit the Hα and [N II]λ6585 emission-lines. The codes also simultaneously fit the [N II]λ6550; however, we did not use it for this study. We pick the following galaxies to highlight the following details about the code. (a) Q1603-BX379, for which we display the typical [N II]λ6585 offset between the two codes (i.e., the KBSS `MOSPEC` code is ~13% larger). The MOSDEF code uses the Gaussian fit for the preferred flux. (b) Q1549-BX223, for which we display similar [N II]λ6585 fluxes, where the MOSDEF code uses the Gaussian fit for the preferred flux. (c) AEGIS 6377, for which we display the typical [N II]λ6585 offset between the two codes where the MOSDEF code uses the Gaussian fit for the preferred flux. (d) AEGIS 33172, for which we display similar [N II]λ6585 fluxes, where the MOSDEF code uses the Gaussian flux for the preferred flux. Panel (c) shows that the Gaussian peaks for [N II]λ6585 do not always perfectly agree in the two codes.

CHAPTER 4

Towards a Complete Census of the $z \sim 2.3$ Star-forming Galaxy Population

4.1 Introduction

One of the most powerful tools for studying galaxies across time is rest-frame optical emission-line spectroscopy. Such measurements provide much information about the properties of a galaxy, including its active galactic nucleus (AGN) activity, star-formation rate (SFR), virial and non-virial dynamics (e.g., outflows), dust extinction, and properties of the ionized interstellar medium (ISM) such as the electron density (n_e), metallicity, and ionization parameter (U; i.e., the ratio of ionizing photon density to hydrogen, and therefore n_e). Applying this tool to galaxies observed during the peak epoch of star-formation in the universe ($z \sim 2$) is especially effective for understanding the origin of well-known patterns exhibited by galaxies in the universe today.

Over the past decade, the deployment of multi-object near-infrared (IR) spectrographs on large ground-based telescopes — e.g., the MultiObject Spectrometer For Infra-Red Exploration (MOSFIRE; McLean et al. 2012) on the Keck I telescope — has enabled us to collect rest-optical spectra for large statistical samples of high-redshift ($z \sim 1.5 - 3.5$) galaxies. One survey utilizing MOSFIRE is the MOSFIRE Deep Evolution Field (MOSDEF; Kriek et al. 2015) survey, which contains ~1500 galaxies with Keck/MOSFIRE at $1.4 \lesssim z \lesssim 3.8$ with roughly half at $z \sim 2$.

One of the goals of the MOSDEF sample was to target and study a roughly stellar-mass-complete

sample at high redshift. However, there are many stages in which incompleteness can be introduced and thus interfere with this goal. The initial parent catalog of MOSDEF galaxies was composed of galaxies with estimated redshifts within fixed targeted ranges to optimize the detection of strong rest-optical emission lines, and brighter than a fixed $H_{\rm AB}$ magnitude limit. However, there is targeting incompleteness between this parent catalog and the actual sample of MOSDEF galaxies observed. Furthermore, there is spectroscopic incompleteness, between the sample of MOSDEF galaxies observed and the one for which MOSFIRE spectroscopic redshifts were measured. Finally, there is detection incompleteness, between the MOSDEF sample with spectroscopic redshifts, and the sample for which multiple rest-optical emission lines are detected and analyzed in previous works (e.g. Shapley et al., 2015; Sanders et al., 2018; Topping et al., 2020a; Runco et al., 2021b).

Notably, a recent comparison between the MOSDEF and KBSS-MOSFIRE $z \sim 2$ surveys revealed that, for MOSDEF, the subset of star-forming galaxies with S/N $\geq$ 3 for Hβ and Hα display different physical properties from those of the entire catalog of galaxies observed at $z \sim 2$ (Runco et al., 2021a). Specifically, the $z \sim 2$ subsample of galaxies with high S/N spectra have a lower median stellar mass (M_*) and stellar population age, a higher median star formation rate (SFR) and specific star formation rate (sSFR), and a bluer median U$-$V color compared to the $z \sim 2$ observed sample from which it was drawn. Runco et al. (2021a) showed that this high S/N subsample is incomplete with respect to red, massive galaxies targeted by MOSDEF with older and less intense star formation. Accordingly, this subsample does not fully represent the complete demographics of $z \sim 2$ galaxy sample with attempted MOSDEF spectroscopic observations. While the MOSDEF incompleteness appears most severe for galaxies that are not actively forming stars, it is still a matter of concern how representative the $z \sim 2$ subsample of MOSDEF galaxies with high S/N spectra is of the overall $z \sim 2$ star-forming galaxy population.

There has been much previous work investigating the rest-optical emission-line properties of the $z \sim 2$ MOSDEF sample, implementing selection criteria to isolate subsets of the $z \sim 2$ MOSDEF sample with high S/N to obtain clean results unobstructed by low S/N spectra (e.g., Shapley et al.

2015, 2019; Sanders et al. 2016, 2018, 2020a, 2021; Jeong et al. 2020; Topping et al. 2020a,b; Runco et al. 2021b,a). It is important to note that the subsample of MOSDEF galaxies with high S/N analyzed in, e.g., Runco et al. (2021a) and Sanders et al. (2018) comprises only ~32% (250/786 galaxies) of the full $z \sim 2$ sample observed by MOSDEF. Furthermore, even when limited to the set of star-forming galaxies alone — since it is these star-forming galaxies we seek to understand using emission-line diagrams — the high S/N subsample is still only ~41% (250/617 galaxies) of the full $z \sim 2$ observed sample. The question remains if the differences in the physical properties between the galaxies with and without high S/N correspond to a fundamental difference in emission-line properties as well.

Here we aim to investigate this question using spectral stacking. We construct a significantly larger sample of ~ 500 MOSDEF star-forming galaxies, where the only requirement for inclusion is the measurement of a spectroscopic redshift, and rest-frame optical (UVJ) colors corresponding to a star-forming (not quiescent) spectral-energy-distribution (SED). This sample, which we refer to as the "$z \sim 2$ stacked sample" represents a much more complete portion of the star-forming galaxies observed by the MOSDEF survey.

We perform a comparison of the locations of the larger, more complete $z \sim 2$ stacked sample and the previously studied, $z \sim 2$ high-S/N subsample on the [O III]λ5008/Hβ vs. [N II]λ6585/Hα diagram (first introduced by Baldwin et al. 1981 and commonly referred to as the "[N II] BPT diagram"), and the [O III]λ5008/Hβ vs. [S II]$\lambda\lambda$6718,6733/Hα diagram (first introduced in Veilleux & Osterbrock 1987 and commonly referred to as the "[S II] BPT diagram"). These diagrams can be used to infer whether the dominant source of ionizing radiation in an emission-line galaxy is an AGN or star formation, given the distinct regions in emission-line ratio space occupied by AGNs and star-forming galaxies. Another diagram frequently used to characterize emission-line galaxies is the [O III]$\lambda\lambda$4960,5008/[O II]$\lambda\lambda$3727,3730 (O_{32}) vs. ([O III]$\lambda\lambda$4960,5008+[O II]$\lambda\lambda$3727,3730)/Hβ (R_{23}) diagram. O_{32} (R_{23}) roughly probes the ionization parameter (metallicity) of star-forming galaxies (e.g., Lilly et al. 2003; Nakajima et al. 2013). It has been shown that metallicity increases

from high excitation (high O_{32} & R_{23}) to low excitation (low O_{32} & R_{23}) (Andrews & Martini, 2013; Shapley et al., 2015).

Gaining a complete understanding of the [N II] BPT diagram is essential because rest-optical emission-lines are used as calibrations for many physical and chemical galaxy properties not directly observable at high redshift. Many such calibrations exist for star-forming galaxies in the local universe (e.g., strength of emission-line ratios such as [N II]λ6585/Hα correlate with gas-phase oxygen abundance Pettini & Pagel 2004). However, it is well documented that star-forming galaxies at $z > 1$ show elevated [N II]λ6585/Hα at fixed [O III]λ5008/Hβ (or vice versa; e.g. Shapley et al. 2005, 2015; Erb et al. 2006b; Liu et al. 2008; Steidel et al. 2014; Strom et al. 2017; Runco et al. 2021b) on average compared to local $z \sim 0$ galaxies in the Sloan Digital Sky Survey (SDSS; York et al. 2000). Numerous explanations for this systematic offset have been suggested, including galaxy selection effects, shocks, unresolved AGN activity (i.e., galaxies with star-formation and AGN activity is mistaken for only star-formation activity), gas-phase N/O abundance ratio differences, and variations in physical properties of H II regions inside galaxies such as ionization parameter, electron densities, density structure, and the hardness of the ionizing spectra at fixed metallicities (e.g., Liu et al. 2008; Brinchmann et al. 2008; Wright et al. 2010; Kewley et al. 2013; Yeh et al. 2013; Juneau et al. 2014; Masters et al. 2014; Steidel et al. 2014, 2016; Coil et al. 2015; Shapley et al. 2015, 2019; Sanders et al. 2016; Strom et al. 2017, 2018; Freeman et al. 2019; Kashino et al. 2019; Topping et al. 2020a; Runco et al. 2021b).

Current MOSDEF results favor the latter idea (i.e., that $z \sim 2$ star-forming galaxies contain a harder ionizing spectrum at fixed nebular oxygen abundance compared to the population of star-forming galaxies at $z \sim 0$) being the main driver of the observed [N II] BPT offset. This difference in the ionizing spectrum arises due to α-enhancement in the massive stars of $z \sim 2$ star-forming galaxies (Shapley et al., 2019; Topping et al., 2020a; Reddy et al., 2022; Runco et al., 2021b). Studies using the Keck Baryonic Structure Survey (KBSS: Steidel et al. 2014), agree with this interpretation of the offset (e.g., Steidel et al. 2014, 2016; Strom et al. 2017). However, without a complete

understanding of the $z > 1$ [N II] BPT offset, it is unclear if the established local calibrations are valid for high redshift galaxies.

Therefore, this study will also analyze how emission-line ratios commonly used as metallicity calibrators (e.g., [N II]λ6585/Hα; Pettini & Pagel 2004) and dust attenuation tracers (Hα/Hβ; e.g., Kashino et al. 2013; Shapley et al. 2022) correlate with stellar mass. We will investigate potential offsets between the full catalog of MOSDEF $z \sim 2$ star-forming galaxies using spectral stacking with the subset of star-forming galaxies that high S/N $z \sim 2$ spectra. The galaxy properties of these different MOSDEF samples will be estimated using broadband SED fitting to correlate with any offset in the emission-line properties. In addition, we will track the offset between the multiple MOSDEF samples with the local $z \sim 0$ SDSS star-forming sequence to look for evolution in emission-line properties over the past ~10 Gyr.

Finally, the 786 $z \sim 2$ galaxies observed by MOSDEF for spectroscopy do not comprise the full sample satisfying the simple MOSDEF selection criteria — i.e., the parent catalog of 3,780 galaxies in *HST* extragalactic legacy fields with estimated redshifts within the $z \sim 2$ range targeted by MOSDEF and H-band (rest-optical) apparent magnitudes down to a fixed limit ($H_{AB} = 24.5$). Therefore, in this study we also utilize broadband SED fitting compare the full parent catalog of available $z \sim 2$ galaxies with the subset actually observed by MOSDEF. In this part of our analysis, we aim to understand how representative the MOSDEF observed sample is, itself.

Section 4.2 details the MOSDEF survey, defines the multiple MOSDEF samples investigated in this study, and the methodology for the SED modeling used to estimate the physical properties of the galaxies and spectra stacking. Section 4.3 presents the results of the MOSDEF sample comparisons using the spectral stacking and SED fitting techniques, while Section 4.4 provides a discussion on how these results relate to past MOSDEF studies. Finally, Section 4.5 summarizes the key results and looks ahead to future work. We adopt the following abbreviations for emission-line ratios used frequently throughout the paper.

$$\text{N2} = [\text{N II}]\lambda 6585/\text{H}\alpha \tag{4.1}$$

$$\mathrm{S2} = [\mathrm{S\ II}]\lambda\lambda 6718, 6733/\mathrm{H}\alpha \tag{4.2}$$

$$\mathrm{O3} = [\mathrm{O\ III}]\lambda 5008/\mathrm{H}\beta \tag{4.3}$$

$$\mathrm{O3N2} = \mathrm{O3}/\mathrm{N2} \tag{4.4}$$

$$\mathrm{O3S2} = \mathrm{O3}/\mathrm{S2} \tag{4.5}$$

$$\mathrm{O_{32}} = [\mathrm{O\ III}]\lambda\lambda 4960, 5008/[\mathrm{O\ II}]\lambda\lambda 3727, 3730 \tag{4.6}$$

$$\mathrm{R_{23}} = ([\mathrm{O\ III}]\lambda\lambda 4960, 5008 + [\mathrm{O\ II}]\lambda\lambda 3727, 3730)/\mathrm{H}\beta \tag{4.7}$$

Throughout this paper, all emission-line wavelengths are in vacuum, and we adopt a Λ-CDM cosmology with $H_0 = 70$ km s^{-1} Mpc^{-1}, $\Omega_\mathrm{m} = 0.3$, and $\Omega_\Lambda = 0.7$. Also, we assume the solar abundance pattern from Asplund et al. (2009).

4.2 Observations, Sample Selection, & Methods

Here we provide an overview of the MOSDEF survey and describe the selection methods for the various samples used in this study (Section 4.2.1). Additionally, we discuss our approach to SED fitting and estimating key galaxy properties (Section 4.2.2), the methodologies for both emission-line fitting (Section 4.2.3) and stacking spectra (Section 4.2.4), and the selection methods for the local $z \sim 0$ SDSS comparison sample 4.2.5.

4.2.1 The MOSDEF Survey

In the MOSDEF survey, galaxies were targeted within five well-studied *HST* extragalactic legacy fields covered by the CANDELS and 3D-HST surveys: AEGIS, COSMOS, GOODS-N, GOODS-S, and UDS (Grogin et al., 2011; Koekemoer et al., 2011; Momcheva et al., 2016). These fields were selected because of the large amounts of ancillary data available. Multi-wavelength photometric observations enable us to perform robust SED fitting (see below), and observations outside the rest-optical (i.e., X-ray and mid-IR) provide useful information on the incidence of AGN. Within these fields, MOSDEF targets galaxies in three redshift ranges: $1.37 \leq z \leq 1.70$, $2.09 \leq z \leq 2.61$,

and $2.95 \leq z \leq 3.80$. These redshift ranges were selected to optimize the detection of strong rest-frame optical emission-lines (e.g., [O II]$\lambda\lambda$3727,3730, Hβ, [O III]$\lambda\lambda$4960,5008, Hα, [N II]λ6585, and [S II]$\lambda\lambda$6718,6733) within windows of atmospheric transmission. Additionally, galaxies were selected based on H-band (F160W) magnitude, with brightness limits of $H_{\rm AB}$ = 24.0, 24.5, and 25.0, respectively, for the lowest, middle and highest redshift ranges. With these redshift and rest-optical brightness selection cuts, there are 10632 galaxies available for MOSDEF to observe between $z \sim 1.3 - 3.8$, with 3780 galaxies at $z \sim 2$. Hereafter, we refer to these 3780 galaxies at $z \sim 2$ as the MOSDEF "$z \sim 2$ parent sample."

MOSDEF was awarded 48.5 Keck/MOSFIRE nights between 2012-2016. Despite this large allocation, it was not possible to observe the full set of 10632 galaxies that meet the MOSDEF selection criteria. Approximately 1500 galaxies were targeted over the three redshift bins. These galaxies were targeted primarily based on location in the sky for optimization of the MOSFIRE slit masks. About half of the targeted galaxies (786) fall in the middle $z \sim 2$ redshift bin. Of these 786 galaxies, 77 are serendipitous observations and not actually targeted by MOSDEF. For a full description of MOSDEF observing details, see Kriek et al. (2015).

In Runco et al. (2021a), we identified two MOSDEF samples. The MOSDEF "$z \sim 2$ targeted sample" contained all 786 galaxies observed by MOSDEF at $1.9 \leq z \leq 2.7$ (in this study we more accurately refer to it as the "$z \sim 2$ observed sample" because it contains 77 serendipitously observed galaxies), while the MOSDEF "$z \sim 2$ spectroscopic sample" was based on the sample from Sanders et al. (2018). The sample from Sanders et al. (2018) comprised 260 star-forming galaxies (i.e., no AGN) with S/N$_{\rm H\alpha}$ and S/N$_{\rm H\beta} \geq 3$. Additionally, galaxies with $\log_{10}(M_*/M_\odot) < 9.0$ due to the incompleteness of the MOSDEF survey at low mass (see Shivaei et al. 2015 for details). AGN were removed based on X-ray luminosity, IR colors, or if N2 ≥ 0.5 (Coil et al., 2015; Azadi et al., 2017; Leung et al., 2017). In Runco et al. (2021a), we removed 9/260 galaxies due to updated SED fitting yielding a M_* estimate below the 10^9 $M_\odot$ cutoff, and one more additional galaxy due to it not being in the 3D-HST v4.1 catalog which is needed for the SED fitting. Therefore, the final MOSDEF

"$z \sim 2$ spectroscopic sample" from Runco et al. (2021a) contained 250 star-forming galaxies with S/N$_{H\alpha}$ and S/N$_{H\beta} \geq 3$ and $\log_{10}(M_*/M_\odot) \geq 9.0$.

Note that there are 83 galaxies in the $z \sim 2$ observed sample that are not in the $z \sim 2$ parent sample. Of these 83 galaxies, 44 fell serendipitously in MOSDEF slits and were either fainter than the MOSDEF H-band magnitude limit, or else had estimated redshifts slightly outside the MOSDEF target range. The remaining 39 galaxies met the selection criteria in the 3D-HST v2.1 or v4.0 catalogs, which were used to select galaxies for observations during the early stages of the MOSDEF survey, before the finalized 3D-HST v4.1 catalogs were available. However, in the updated v4.1 catalogs used to obtain the $z \sim 2$ parent sample in this study, changes to either the photometry or the redshift caused these galaxies no longer to satisfy the MOSDEF selection criteria. For example, updated photometry measurements could lead to galaxies falling below the $H_{AB} = 24.5$ cut applied to the v4.1 catalog, if they were near that threshold in the v2.1 catalog. In terms of redshift, MOSDEF prioritized different redshift sources in the following order for targeting purposes: previous spectroscopic redshifts, grism redshifts, and then photometric redshifts. It is possible that the most reliable redshift in the v2.1 catalog was in the $z = 2.09 - 2.61$ range, but the updated most reliable redshift in the v4.1 catalog was not (e.g., the most robust redshift in the v2.1 catalog was a photometric redshift at $2.09 \leq z \leq 2.61$, and an updated grism redshift in the v4.1 catalog fell outside of this range).

There is a large difference between the $z \sim 2$ spectroscopic and $z \sim 2$ observed samples, as the former only accounts for ~32% of the sample from which it was drawn. And there is one final layer of incompleteness that must be considered. Specifically, of the 250 galaxies in the $z \sim 2$ spectroscopic sample, only 143, 155, and 181 had S/N ≥ 3 necessary to be analyzed on the [N II] BPT, [S II] BPT, and O_{32} vs. R_{23} diagram, respectively, which is only ~18%, ~20%, and ~23%, respectively, of the $z \sim 2$ observed sample. In this study, we will refer to these 143, 156, and 181 galaxy samples, respectively, as the "$z \sim 2$ N2 BPT detection sample", "$z \sim 2$ S2 BPT detection sample", and "$z \sim 2$ O_{32} detection sample." Note that the $z \sim 2$ O_{32} detection sample requires a

robust detection of Hα, in addition to the lines needed to complete the O_{32} vs. R_{23} diagram, for accurate nebular dust corrections. Dust correcting the emission-lines is required for this diagram because the [O II]$\lambda\lambda$3727,3730 and [O III]$\lambda\lambda$4960,5008 lines are far apart in wavelength. This extra requirement does not remove any additional galaxies from the 181-galaxy sample.

Our goal is to analyze a significantly more complete sample of MOSDEF star-forming galaxies. For this analysis, therefore, we exclude those galaxies identified as quiescent based on UVJ colors, as well as those flagged as AGNs. We also must limit our focus to galaxies with MOSFIRE spectroscopic redshifts, since we need a robust redshift for inclusion in spectral stacking. If we exclude galaxies lacking a robust MOSFIRE redshifts (referred to hereafter as $z_{\rm MOSFIRE}$), those flagged as AGN, or those identified as quiescent galaxies based on UVJ colors, there are 553 *star-forming* galaxies in the $z \sim 2$ observed sample.

To assemble a larger sample of $z \sim 2$ MOSDEF star-forming galaxies, we relax the criteria for individual emission-line detections. However, because this larger sample will be used to create spectral stacks of emission lines in key diagnostic diagrams, we do require *coverage* (if not detection) of all relevant spectral features. Since not all 553 galaxies (based on their redshifts, and locations in MOSFIRE slitmasks) have the required spectral coverage, we remove an additional 75 galaxies that do not have coverage of all four lines (i.e., Hβ, [O III]λ5008, Hα, and [N II]λ6585. Therefore, we have 478 galaxies available for stacking on the [N II] BPT diagram. For the [S II] BPT diagram, we require coverage of [S II]$\lambda\lambda$6717,6730 instead of [N II]λ6585, and find that there are 472 $z \sim 2$ star-forming galaxies with a robust $z_{\rm MOSFIRE}$ and coverage of Hβ, [O III]λ5008, Hα, and [S II]$\lambda\lambda$6717,6730 that are available for stacking. Finally, we require coverage of [O II]$\lambda\lambda$3727,3730, Hβ, [O III]$\lambda\lambda$4960,5008, and Hα for analysis on the O_{32} vs. R_{23} diagram. While Hα is not explicitly included in the line ratios plotted on the O_{32} vs. R_{23} diagram, its detection is required for dust correction, as described above. While Hα is not explicitly included in the line ratios plotted on the O_{32} vs. R_{23} diagram, its detection is required for dust correction, as described above. There are 406 galaxies that meet these criteria.

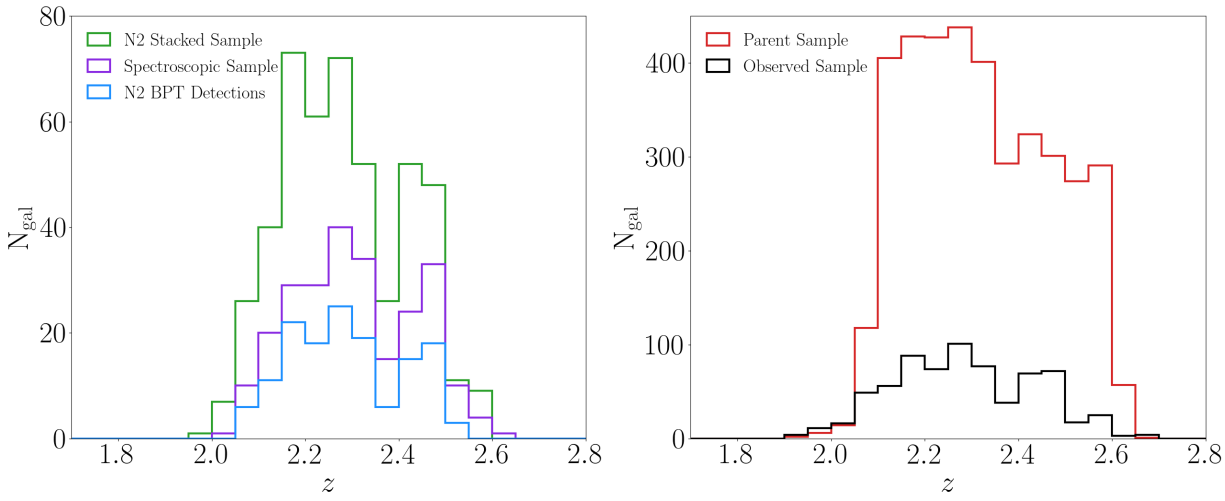

Figure 4.1: Redshift distributions for the different MOSDEF samples analyzed in this study. The left panel shows the MOSDEF $z \sim 2$ N2 stacked sample (green; $z_{\rm med} = 2.28$), $z \sim 2$ spectroscopic sample (purple; $z_{\rm med} = 2.29$), and $z \sim 2$ N2 BPT detection sample (blue; $z_{\rm med} = 2.29$). The right panel shows the MOSDEF $z \sim 2$ observed sample (black; $z_{\rm med} = 2.29$) and $z \sim 2$ parent sample (red; $z_{\rm med} = 2.31$).

The stacked samples more than triple the number of individual galaxies shown on the [N II] and [S II] BPT diagrams in previous MOSDEF studies (e.g., Shapley et al., 2015; Runco et al., 2021b,a). We hereafter refer to these samples as the MOSDEF "$z \sim 2$ N2 stacked sample", MOSDEF "$z \sim 2$ S2 stacked sample", and MOSDEF "$z \sim 2$ O_{32} stacked sample". Table 4.1 summarizes the various MOSDEF samples introduced in this section, providing both the name of each and number of galaxies each contains. The distributions of redshifts for the multiple MOSDEF samples samples are shown in Figure 4.1. The methodology for creating spectral stacks is discussed in Section 4.2.4.

4.2.2 SED Fitting and Derived Properties

The fields targeted by MOSDEF (AEGIS, COSMOS, GOODS-N, GOODS-S, and UDS) are covered by multi-wavelength photometry enabling robust SED fitting. All fields have *Spitzer*/IRAC coverage; however, the specific set of ground-based and *HST* bands from the near-UV to near-IR varies from field to field (Skelton et al., 2014). When available, we use emission-line subtracted photometry for SED fitting, because strong lines (e.g. Hβ, [O III]$\lambda\lambda$4960,5008, and Hα) can bias

Table 4.1: MOSDEF Samples

Sample Name (1)	Number of Galaxies (2)
Parent Sample	3780
Targeted Sample	786
N2 Stacked Sample	478
S2 Stacked Sample	472
O_{32} Stacked Sample	406
Spectroscopic Sample	250
N2 BPT Detection Sample	143
S2 BPT Detection Sample	155
O_{32} Detection Sample	181

Note. — Col. (1): Name of each MOSDEF sample introduced in Section 4.2.1. Col. (2): Number of galaxies in that sample.

the shape of the SED fit redward of the Balmer break. The bias introduced by these emission-lines causes the modeling to favor older stellar population ages than if fitting the stellar continuum alone. The emission-line contribution to the photometry is estimated from the MOSFIRE spectra. Therefore, we use emission-line corrected photometry when there is an available MOSFIRE redshift. Otherwise, we use the raw photometry.

We use the SED-fitting code FAST (Kriek et al., 2009) to model the multi-wavelength photometry of MOSDEF galaxies, adopting the Flexible Stellar Population Synthesis (FSPS) library from Conroy & Gunn (2010) and assuming a Chabrier (2003) stellar initial mass function (IMF) and delayed-τ star-formation histories where SFR(SED) $\propto t \times e^{-t/\tau}$. Here, t represents the time since the beginning of star formation and τ represents the characteristic star-formation timescale. Following previous studies (Du et al., 2018; Reddy et al., 2018), we adopt two combinations of dust attenuation curves and metallicity: one assumes a Calzetti et al. (2000) dust attenuation curve with the the metallicity fixed to the defined solar value in the Conroy & Gunn (2010) library (0.019), and a second assumes a Small Magellanic Cloud (SMC) attenuation curve with the metallicity fixed to 28% solar. We hereafter refer to these grids as the "Calzetti+solar grid" and the "SMC+subsolar grid". In the modeling, we fit for several key galaxy properties, including t, τ, the level of dust attenuation (A_V), M_*, SFR(SED), and sSFR(SED) (i.e., SFR(SED)/M_*).

Following Du et al. (2018), we use the Calzetti+solar grid for galaxies with $\log_{10}(M_*/M_\odot) \geq 10.45$ and the SMC+subsolar grid for galaxies with $\log_{10}(M_*/M_\odot) < 10.45$. This choice in metallicity based on estimated M_* is consistent with past mass-metallicity relationship (MZR) studies (e.g., Tremonti et al. 2004; Erb et al. 2006a; Andrews & Martini 2013; Steidel et al. 2014; Sanders et al. 2015).

While not estimated directly from SED fitting, we can obtain rest-frame UVJ colors by passing the best-fit rest-frame FAST SED through U, V, and J filter bandpasses. We use the IRAF (Tody, 1986, 1993) routine *sbands* to obtain rest-frame UVJ colors. The combination of the U−V and V−J colors can distinguish between red quiescent galaxies and dusty star-forming galaxies by breaking

the degeneracy for age and reddening (Williams et al., 2009). Quiescent galaxies are located in the upper left portion of the U−V vs. V−J diagram. As stated in the Section 4.2.1, we remove galaxies that fall in the quiescent region from this study.

4.2.3 Emission-line Fitting

Emission-line measurements are obtained using a custom IDL code (Reddy et al., 2015), which has been used in many previous MOSDEF studies (e.g., Shapley et al., 2015, 2019, 2022; Sanders et al., 2016, 2018, 2020a, 2021; Runco et al., 2021b,a). A single Gaussian profile is fit to each emission-line in the spectra, where the FWHM and centroid of each Gaussian are allowed to vary for each line. The lower and upper limits for the FWHM estimate are determined by the instrumental resolution estimated by sky lines and highest S/N line (most often Hα or [O III]λ5008). Once the FWHM for the highest S/N line is determined, the FWHM for all other emission lines cannot be 0.5 Å larger than that. The continuum is fixed to the best-fit model from the FAST SED modeling. Additionally, the Balmer lines (Hα and Hβ) are corrected for the underlying contribution of stellar Balmer absorption using the best-fit SED from FAST. As discussed in Runco et al. (2021a), the code has recently been updated to more accurately estimate the magnitude of the stellar Balmer absorption contribution. If the best-fit Gaussian model is not a good fit to the spectrum, the code will choose the integrated bandpass flux as the preferred emission-line flux estimate. Uncertainties on the line fluxes are obtained by perturbing and refitting the spectrum 1000 times. The reported uncertainty is taken from 68th-percentile confidence interval of the distribution of perturbed flux measurements (Reddy et al., 2015). Finally, note that prior to fitting, MOSDEF uses an "optimal" (Freeman et al., 2019) 2D to 1D extraction method and the spectra are slit-loss corrected (see Kriek et al. 2015 for details).

4.2.4 Spectral Stacking

Composite spectra were created using the methodology described in Sanders et al. (2018). To summarize, each galaxy spectrum was shifted into the rest frame and converted from flux density

to luminosity density using $z_{\rm MOSFIRE}$ and resampled onto a uniform wavelength grid. The spacing between each wavelength element is 0.5 Å. In previous work (e.g., Sanders et al., 2018, 2021), the luminosity of a strong emission line (e.g., [O III]λ5008 or Hα) was used to normalize individual galaxy spectra. In this study, we normalized the spectra by SFR(SED) instead of Hα emission-line luminosity because we included galaxies with S/N$_{H\alpha}$ < 3 and only required coverage (not detections) for the rest-optical emission lines we aimed to measure in stacked spectra. The individual spectra were median combined at each wavelength element. As a sanity check, we also tried normalizing the spectra by Hα luminosity before stacking using the subset of galaxies with S/N$_{\rm H\alpha}$ ≥ 3. The emission-line ratios of the Hα and SFR(SED) normalized stacked agreed within the uncertainties of the bins. Therefore, the results and subsequent interpretations do not change based on the method of spectral normalization used.

For all analyses presented in this work, stacked spectra were constructed in bins of M_*. Emission-line luminosities of stacked spectra were measured with the same methodologies used for fitting the individual spectra. Line flux uncertainties were estimated using a Monte Carlo technique where we perturbed the stellar masses of the individual galaxies within the uncertainties, divided the sample into the same M_* bins based on the perturbed stellar masses, and refit the stacked spectra. This process was repeated 100 times, and the 68th-percentile confidence interval of fitted emission-line fluxes was used to estimate the line-flux uncertainty for each emission line. In each bin, the median Balmer absorption luminosity from the individual galaxies was used to correct the Hα and Hβ luminosities for the underlying stellar Balmer absorption.

As stated above, for stacking on the [N II] BPT diagram, we utilized all 480 $z \sim 2$ star-forming galaxies (i.e., no AGN or quiescent galaxies) with a robust $z_{\rm MOSFIRE}$ and coverage of Hβ, [O III]λ5008, Hα, and [N II]λ6585. Of the 480 galaxies, 432 have S/N$_{\rm H\alpha}$ ≥ 3 with coverage of the remaining lines. For the [S II] BPT diagram there are 472 $z \sim 2$ star-forming galaxies with a robust $z_{\rm MOSFIRE}$ and coverage of Hβ, [O III]λ5008, Hα, and [S II]$\lambda\lambda$6718,6733 that are included in the stacking. Lastly, there are 406 galaxies with a robust $z_{\rm MOSFIRE}$ and coverage of [O II]$\lambda\lambda$3727,3730, Hβ,

[O III]$\lambda\lambda$4960,5008, and Hα required for dust-corrected emission-line ratios on the O_{32} vs. R_{23} diagram.

4.2.5 SDSS Comparison Sample

We compare the emission lines of our various $z \sim 2$ MOSDEF samples on the [N II] and [S II] BPT diagrams with similar measurements from galaxies in the local universe. For these comparisons, we utilized archival emission-line measurements from the SDSS Data Release 7 (DR7; Abazajian et al. 2009), specifically from the MPA-JHU DR7 release of spectrum measurements[1]. We restricted the SDSS sample to a redshift range of $0.04 \leq z \leq 0.10$ and removed galaxies with a poor M_* estimate (i.e., $\log_{10}(M_*/M_\odot) < 0$). Additionally, AGN were removed using equation 1 from Kauffmann et al. (2003) or if N2 > 0.5. We employed a S/N cut of 3 to the relevant emission-lines on the [N II], [S II] BPT, and O_{32} vs. R_{23} diagrams. Similar to the MOSDEF sample, we required $S/N_{H\alpha} \geq 3$ for the sample shown on the O_{32} vs. R_{23} diagram to perform the dust corrections. These criteria resulted in SDSS samples of 96,346, 95,132, and 76,810 star-forming galaxies on the [N II] BPT, [S II] BPT, and O_{32} vs. R_{23} diagrams, respectively.

4.3 Results

In this section, we compare the multiple different MOSDEF samples introduced in Section 4.2.1. In Section 4.3.1, we analyze the emission-line properties of the MOSDEF $z \sim 2$ stacked and spectroscopic samples on the [N II] BPT, [S II] BPT, and O_{32} vs. R_{23} diagrams. In Section 4.3.2, we compare the host galaxy properties of the MOSDEF $z \sim 2$ stacked and spectroscopic samples using emission-line corrected photometry in the SED modeling. Additionally, we compare these samples with the MOSDEF $z \sim 2$ samples from Sanders et al. (2021) and Shapley et al. (2022) on diagrams correlating emission-line ratios with M_*. Finally, Section 4.3.3 provides a comparison of the host galaxy properties of the MOSDEF $z \sim 2$ parent and observed samples using emission-line

[1] https://wwwmpa.mpa-garching.mpg.de/SDSS/DR7/

uncorrected photometry in the SED modeling.

4.3.1 Stacking on the BPT diagrams

We show the $z \sim 2$ N2, S2, and O_{32} stacked samples in bins of M_* on the [N II] BPT (top left), [S II] BPT (top right), and O_{32} vs. R_{23} (bottom) diagrams in Figure 4.2. Also included are the $z \sim 2$ N2 BPT and S2 BPT detection samples from Runco et al. (2021a) with galaxies binned according to $\log_{10}$(O3N2) on the N II] BPT diagram and $\log_{10}$(O3S2) on the [S II] BPT diagram. The $z \sim 2$ O_{32} detection sample is included on the O_{32} vs. R_{23} diagram. On the [N II] BPT diagram, the sequence of bins has a similar distribution relative to the local sequence as observed in previous MOSDEF studies (i.e., Equation 1 from Shapley et al. 2015 fitting early MOSDEF data and the O3N2 binned median from Runco et al. 2021a). The bin in the $z \sim 2$ N2 stacked sample with the lowest M_* is located at the upper left (i.e., high O3 and low N2) of the diagram. This bin extends past the region covered by the O3N2 binned median from (Runco et al., 2021a). As bins in the $z \sim 2$ N2 stacked sample increase in M_*, the sequence moves to lower O3 and higher N2. This trend is expected as position on the [N II] BPT diagram is shown to correlate with M_* (e.g., Masters et al. 2016; Runco et al. 2021b). For the N2 $z \sim 2$ stacked sample, the perpendicular offset from the Kewley et al. (2013) fit to the local SDSS sequence is 0.10 ± 0.04 dex. This distance is slightly lower, but agrees within the uncertainties to the smaller $z \sim 2$ N2 BPT detection sample (0.12 ± 0.02).

On the [S II] BPT diagram, the $z \sim 2$ S2 stacked sample has a similar shape to the O3S2 binned median for the $z \sim 2$ S2 BPT detection sample. However, at high S2, the stacks are offset to lower O3 compared to the O3S2 sequence. Similar to what is observed in the [N II] BPT diagram, the bin in the $z \sim 2$ S2 stacked sample with the lowest M_* is located at the upper left part of the diagram (i.e., high O3 and low S2). Both the $z \sim 2$ S2 stacked and S2 BPT detection samples occupy the region of the local SDSS star-forming sequence. However, the lowest-mass bin of the $z \sim 2$ S2 stacked sample does not extend past the $z \sim 2$ S2 BPT detection sample sequence of O3S2 bins to higher O3 and lower S2 (unlike what is found on the [N II] BPT diagram).

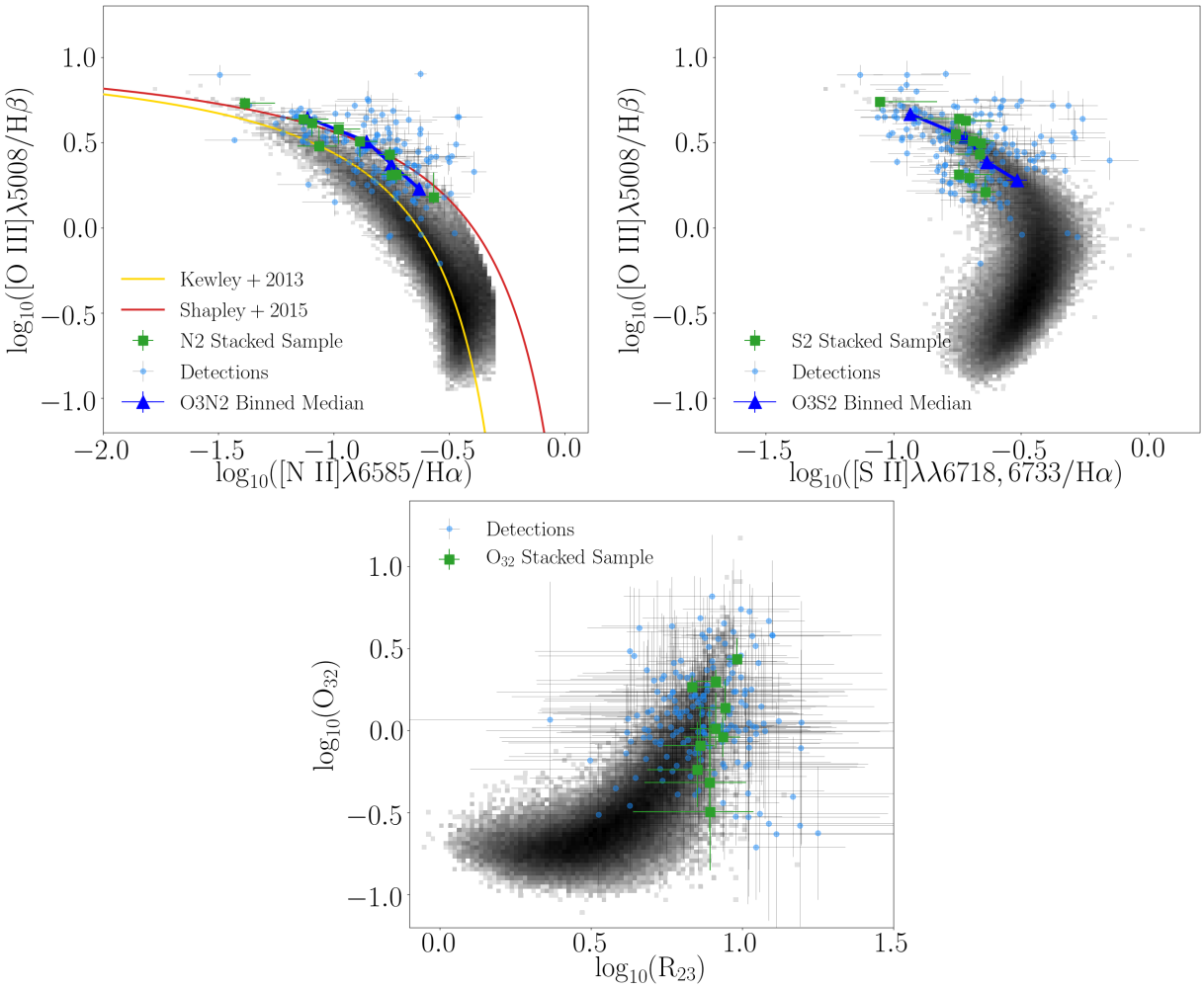

Figure 4.2: The [N II] BPT (top left), [S II] BPT (top right), and O_{32} vs. R_{23} (bottom) diagrams. The N2 and S2 $z \sim 2$ stacked samples are shown with green squares. The grey 2D histograms show the local SDSS $z \sim 0$ star-forming galaxies. The blue points identify the 143, 156, and 181 galaxies with 3σ S/N for all relevant lines on the [N II] BPT, [S II] BPT, and O_{32} vs. R_{23} diagrams, respectively. An additional requirement for a robust Hα detection is needed for dust corrections on the O_{32} vs. R_{23} diagram. The blue triangles are the binned medians from Runco et al. (2021a), binned in O3N2 (O3S2) on the [N II] ([S II]) BPT diagram. The red curve on the [N II] BPT diagram is a fit to early MOSDEF data from Shapley et al. (2015), while the yellow curve is a fit to the SDSS $z \sim 0$ star-forming locus (Kewley et al., 2013).

The $z \sim 2$ O_{32} stacked sample occupies a similar region of O_{32} vs. R_{23} space as the $z \sim 2$ O_{32} detection sample. Both samples are offset to higher R_{23} compared to the local SDSS star-forming sequence. The photoionization models from Runco et al. (2021b) suggest that this offset is caused by the $z \sim 2$ star forming galaxies having a lower stellar metallicity (i.e., a harder ionizing spectra) at fixed gas-phase oxygen abundance than galaxies at $z \sim 0$. Many studies support the idea that $z \sim 2$ star-forming galaxies contain a harder ionizing spectra at fixed gas-phase oxygen abundance (Steidel et al., 2014, 2016; Strom et al., 2017; Shapley et al., 2019; Topping et al., 2020a; Reddy et al., 2022).

Figure 4.2 shows that the median emission-line properties of the $z \sim 2$ N2 BPT, S2 BPT, and O_{32} detection samples are representative of the emission-line properties for the full stacked samples of galaxies with coverage of the emission-lines needed for each diagram. These results indicate that previous MOSDEF studies (e.g., Shapley et al. 2015, 2019, 2022; Sanders et al. 2016, 2018, 2020a, 2021; Runco et al. 2021b; Topping et al. 2020a,b) utilizing high S/N subsets of the $z \sim 2$ MOSDEF survey most likely show little bias in the emission-line properties compared to the full sample. We discuss this topic more in Section 4.4.

4.3.2 Physical Properties of the Stacks

The distributions of galaxy properties for the $z \sim 2$ N2 stacked sample (478 galaxies) are shown in Figure 4.3. We compare this sample with the $z \sim 2$ spectroscopic sample (250 galaxies) and the $z \sim 2$ [N II] BPT sample (143 galaxies). Because the total number of galaxies in each of these three samples is significantly different, we show a probability density where the area under each distribution integrates to 1 instead of raw counts to better compare the distributions of galaxies. Additionally, sample medians with 1σ uncertainties are shown in Figure 4.3 and given in Table 4.2. Median uncertainties are estimated using bootstrap resampling. We use emission-line corrected photometry to estimate these galaxy properties, since all samples in Figure 4.3 have the MOSFIRE spectra required for estimating such corrections. Since the $z \sim 2$ N2, S2, and O_{32} stacked samples contain the same base set of galaxies, median galaxy properties reported for the N2 stacked sample

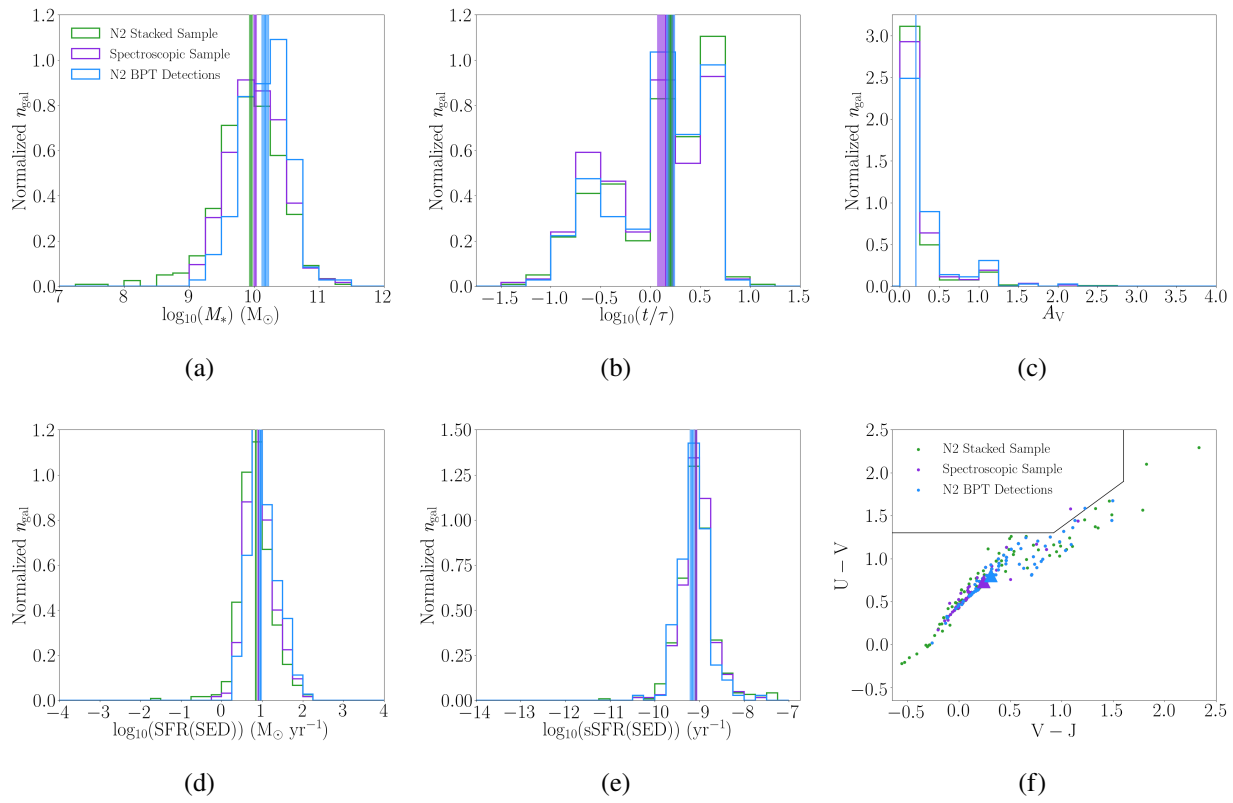

Figure 4.3: Distribution of physical properties and sample medians with 1σ uncertainties for the MOSDEF N2 $z \sim 2$ stacked sample (green), the $z \sim 2$ spectroscopic sample (purple), and the 143 galaxy subset of the $z \sim 2$ spectroscopic sample shown on the [N II] BPT diagram in Figure 4.2 (blue), i.e., the N2 BPT detection sample. The values for the sample medians are given in Table 4.2. For the panels with 1D histograms, the y-axis is normalized so the area under the histogram for each sample adds up to one. Distributions for the following galaxy properties are shown: **(a)** M_*, **(b)** $\log_{10}(t/\tau)$ of the stellar population assuming a delayed-τ star formation model, **(c)** A_V, **(d)** SFR(SED), **(e)** sSFR(SED), **(f)** the UVJ diagram. The box on the UVJ diagram separates the quiescent region (upper left) from the star-forming region (bottom half and upper right). The galaxy properties shown here are estimated using emission-line corrected photometry for all galaxies in the figure.

Table 4.2: Median Values for Physical Properties of the MOSDEF $z \sim 2$ N2 Stacked, Spectroscopic, and N2 BPT Detection Samples

Physical Property	N2 Stacked Median	Spectroscopic Median	N2 BPT Detections Median
(1)	(2)	(3)	(4)
$\log_{10}(M_*/M_\odot)$	9.95 ± 0.03	10.02 ± 0.02	10.17 ± 0.06
$\log_{10}(t/\tau)$	0.20 ± 0.02	0.15 ± 0.08	0.20 ± 0.04
$\log_{10}(\mathrm{SFR(SED)}/M_\odot/\mathrm{yr}^{-1})$	0.84 ± 0.02	0.90 ± 0.02	0.95 ± 0.04
$\log_{10}(\mathrm{sSFR(SED)}/\mathrm{yr}^{-1})$	−9.08 ± 0.02	−9.08 ± 0.03	−9.17 ± 0.05
A_V	0.20 ± 0.001	0.20 ± 0.001	0.20 ± 0.005
U−V	0.74 ± 0.01	0.74 ± 0.01	0.80 ± 0.02
V−J	0.24 ± 0.01	0.24 ± 0.01	0.31 ± 0.02

Note. — Col. (1): Physical property of the multiple MOSDEF samples shown in Figure 4.3. The galaxy properties shown here are estimated using emission-line corrected photometry. Col. (2): Median value with uncertainty of the MOSDEF $z \sim 2$ N2 stacked sample. Col. (3): Median value with uncertainty of the MOSDEF $z \sim 2$ spectroscopic sample. Col. (4): Median value with uncertainty of the MOSDEF $z \sim 2$ N2 BPT detection sample.

are representative for all emission-line-diagram subsets. We also note that the median galaxy properties for the $z \sim 2$ spectroscopic sample are not the identical to those reported in Runco et al. (2021a) because, as discussed in Section 4.2.2, in this study we report galaxy properties for individual galaxies according to either the Calzetti+solar or SMC+subsolar models, based on M_*. In Runco et al. (2021a), all galaxies were fit assuming the Calzetti+solar models.

We find that the $z \sim 2$ N2 stacked sample has a lower median M_* and SFR(SED) compared to both the $z \sim 2$ spectroscopic and N2 BPT detection samples. Additionally, the $z \sim 2$ N2 stacked sample has a lower median sSFR(SED) and bluer UVJ colors compared to the $z \sim 2$ N2 BPT detection sample, but, for these properties, is identical to the $z \sim 2$ spectroscopic sample. All other galaxy properties (i.e., t/τ and A_V) agree within the median uncertainties for the three samples. The bias in M_* is expected, given that galaxies with $\log_{10}(M_*/M_\odot) < 9.0$ were removed from the $z \sim 2$ spectroscopic and N2 BPT detection samples due to the documented MOSDEF incompleteness at this low mass regime. Galaxies in this mass regime were not removed from the stacked samples. Additionally, Figure 4.4 includes corner plots showing the 1D distributions (with uncertainties) and the 2D distributions with 3σ contours for SFR(SED), sSFR(SED), and A_V vs. M_* and also U−V vs. V−J colors. These diagrams show that the $z \sim 2$ N2 stacked sample extends to lower M_*, which as previously stated is expected, but span a similar region in SFR(SED), sSFR(SED), and A_V to that of the $z \sim 2$ spectroscopic and N2 BPT detection samples. The $z \sim 2$ N2 stacked sample occupies a slightly wider range of UVJ colors (to both bluer and redder tails of 2D space) compared to the smaller high S/N samples. Combining these results with the emission-line analysis in Section 4.3.1 reveals that these differences in host galaxy properties between the $z \sim 2$ N2 stacked sample and $z \sim 2$ N2 detection sample do not strongly affect the emission-line ratios.

Figure 4.5 compares the relationships between N2, O3N2, and Balmer decrement (i.e., Hα/Hβ) vs. M_* for different MOSDEF subsamples. These plots include the detections and the $z \sim 2$ N2 stacked sample from the [N II] BPT diagram in the left panel of Figure 4.2. Also included on all three diagrams is the SDSS sample plotted in the [N II] BPT diagram. For the N2 and O3N2 vs. M_*

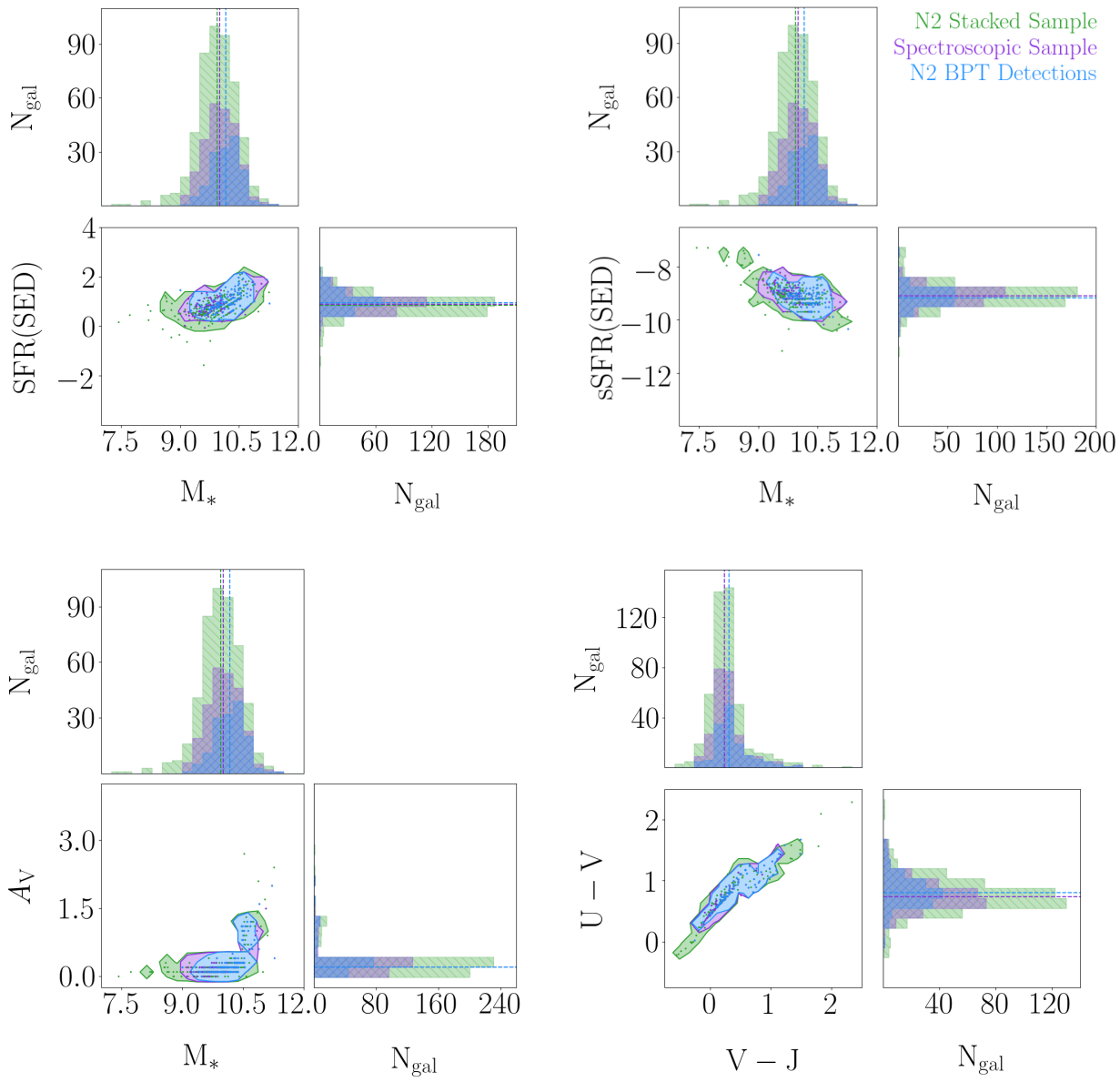

Figure 4.4: Corner plots for SFR(SED) vs. M_* (upper left), sSFR(SED) vs. M_* (upper right), A_V vs. M_* (bottom left), and U−V vs. V−J (bottom right). Shown on these diagrams are the $z \sim 2$ stacked sample (green), $z \sim 2$ spectroscopic sample (purple), and $z \sim 2$ N2 BPT detections (blue). The galaxy properties shown here are estimated using emission-line corrected photometry for all galaxies in the figure.

panels (top right and top left, respectively), we also include a fit to the $z \sim 2$ N2 stacked sample and the $z \sim 2$ MOSDEF stacks (with fit) from Sanders et al. (2021). The stacked sample from Sanders et al. (2021) contains 280 star-forming galaxies at $z \sim 2$ with $S/N_{[O\,III]\lambda5008} \geq 3$ and coverage of [O II]$\lambda\lambda$3727,3730, [Ne II]λ3870, and Hβ. There are four bins with $9.0 \leq \log_{10}(M_*/M_\odot) \leq 10.5$ and one additional bin incorporating galaxies with $\log_{10}(M_*/M_\odot) > 10.5$. Galaxies with $\log_{10}(M_*/M_\odot) < 9.0$ are omitted from the sample. These mass cuts are made because the range of $M_* = 10^{9.0-10.5}$ is where the MOSDEF survey has the highest spectroscopic success rate (Kriek et al., 2015).

In the N2 vs. M_* and O3N2 vs. M_* panels, we find that the linear regressions fit to the $z \sim 2$ N2 stacked sample and Sanders et al. (2021) stacks overlap within the uncertainties, which suggests that the smaller MOSDEF subsample with high S/N is not significantly biased with respect to the full MOSDEF star-forming sample. Line-ratio measurements from both the larger $z \sim 2$ stacked samples constructed here and those presented in Sanders et al. (2021) are offset from the local SDSS star-forming sample, indicating evolution between $z \sim 2$ and $z \sim 0$ in these metallicity-sensitive rest-optical emission-line ratios at fixed M_*.

For the Hα/Hβ vs. M_* diagram, we also include the sliding medians from the $z \sim 2$ MOSDEF sample from Shapley et al. (2022). This sample is very similar to the spectroscopic sample from Sanders et al. (2021), which required $\geq 3\sigma$ detections for [O II]$\lambda\lambda$3727,3730, [Ne II]λ3870, and Hβ, and [O II]λ5008 (i.e., more restrictive than the stacked sample described above). Shapley et al. (2022) adopted this sample from Sanders et al. (2021), with the added requirement of $S/N_{H\alpha} \geq 3$, in order to probe dust attenuation. The $z \sim 2$ N2 stacked sample shows a slightly higher Hα/Hβ ratio on average compared to the Shapley et al. (2022) sliding median bins. This offset is not significant, as the $z \sim 2$ N2 stacked sample bins overlap with the Shapley et al. (2022) sliding median bins within the uncertainties at fixed M_*. Both $z \sim 2$ MOSDEF samples intersect with the running median for the SDSS $z \sim 0$ star-forming sample, indicating that there is no significant evolution in the Balmer decrement at fixed M_*. Many studies have found no evolution in the dust

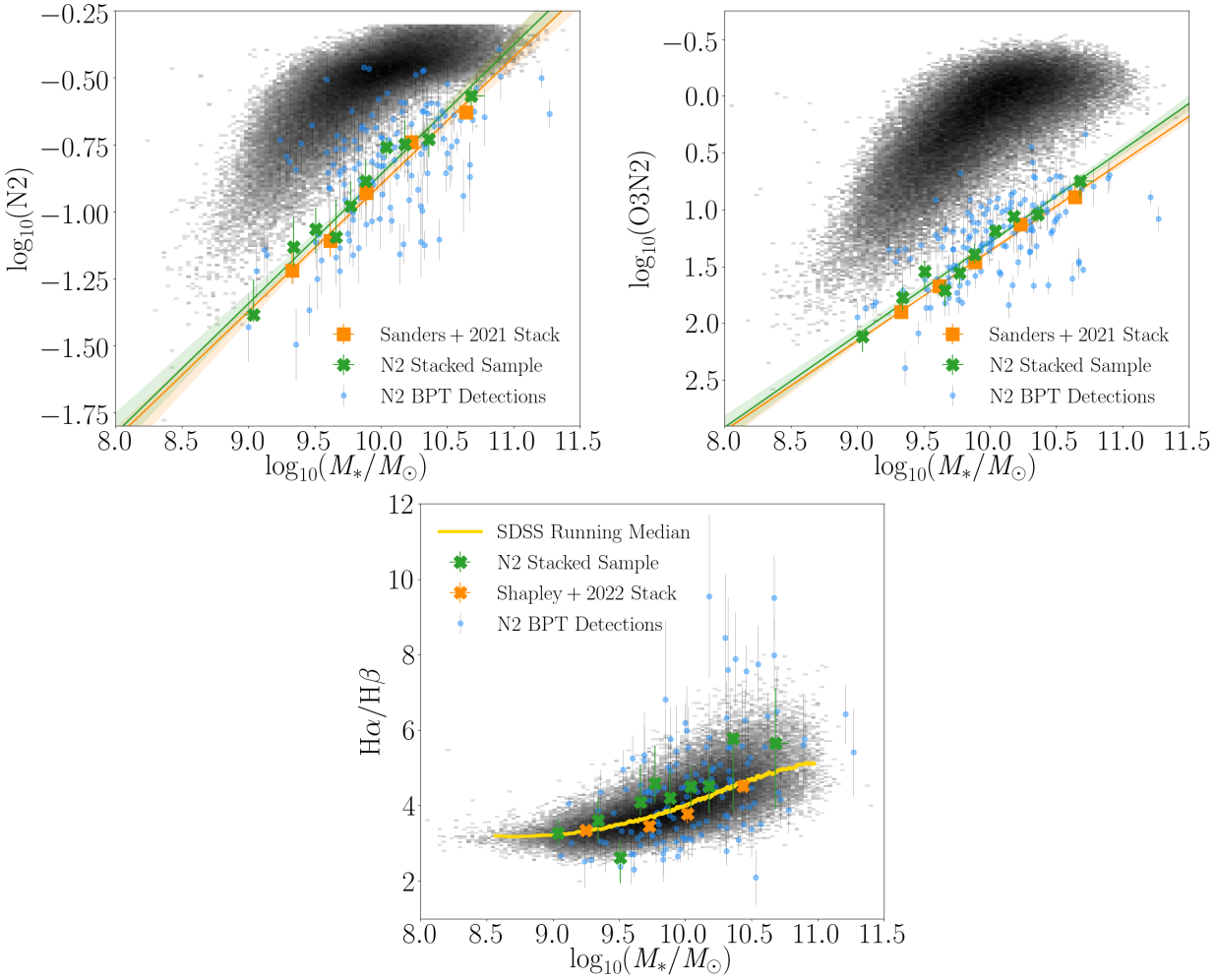

Figure 4.5: $\log_{10}$(N2) vs. M_* (upper left), $\log_{10}$(O3N2) vs. M_* (upper right), and Hα/Hβ vs. M_* (bottom). The blue points identify the 143 galaxies in Figure 4.2 with 3σ S/N for all relevant lines on the [N II] BPT diagram. The green squares show the $z \sim 2$ N2 BPT stacks. Fits to the stacks are included in the $\log_{10}$(N2) vs. M_* and $\log_{10}$(O3N2) vs. M_* panels. Also included are the MOSDEF $z \sim 2$ stacks from Sanders et al. (2021) (upper left and upper right panels) and the sliding median for the MOSDEF $z \sim 2$ sample from Shapley et al. (2022) (bottom panel). The stellar mass values shown here are estimated using emission-line corrected photometry for all galaxies in the figure.

attenuation at fixed M_* between $z \sim 2$ and $z \sim 0$, using a wide variety of methods to trace dust attenuation: the Balmer decrement (e.g., Kashino et al. 2013; Price et al. 2014; Shapley et al. 2022), the magnitude of far-UV 1600 Åattenuation (e.g., Pannella et al. 2015; McLure et al. 2018), the fraction of obscured star formation (e.g., Whitaker et al. 2017), and the ratio of far-IR to UV SFRs (e.g., Meurer et al. 1999; Bouwens et al. 2016).

4.3.3 Comparison of the $z \sim 2$ Parent and Observed Samples

We have shown that the subset of MOSDEF $z \sim 2$ star-forming galaxies with high S/N spectra is representative of the stacked sample of MOSDEF $z \sim 2$ star-forming galaxies with coverage of the [N II] BPT, [S II] BPT, and O_{32} vs. R_{23} diagrams. Now we turn our attention to whether the full sample of $z \sim 2$ galaxies observed in MOSDEF (including both star-forming and non-star-forming targets) is reflective of the complete catalog of galaxies that could have been targeted by MOSDEF. Figure 4.6 shows the 1D distributions of the galaxy properties, with sample medians overlaid, for the $z \sim 2$ parent and observed samples. As in Figure 4.3, we plot the histograms as probability densities instead of raw galaxy counts to best compare the distribution of galaxies. Table 4.3 lists the median galaxy properties of the two samples. Again, the 1σ uncertainties on the medians are estimated using bootstrap resampling. In this comparison of the properties of the $z \sim 2$ parent and observed samples, we use photometry that has not been corrected by emission-lines (unlike what is done in Section 4.3.2) because we do not have a MOSFIRE spectrum for the majority of the $z \sim 2$ parent sample. As we state in Section 4.2.2, emission-lines can bias the modeling to favor older stellar population ages. Therefore, for a uniform analysis, we use uncorrected photometry for all galaxies in the $z \sim 2$ parent and observed samples. We find that the $z \sim 2$ parent sample has a lower median M_*, SFR(SED), sSFR(SED) than the $z \sim 2$ observed sample. However, the difference in the sample medians is only ~0.1 dex. Given that that the majority of galaxies in both samples span ~4 orders of magnitude in each of these parameter spaces (with outlier galaxies extending even farther), the observed median differences are minor. Additionally, the $z \sim 2$ parent sample has a slightly bluer median V−J color compared to the $z \sim 2$ observed sample. All other properties (i.e.,

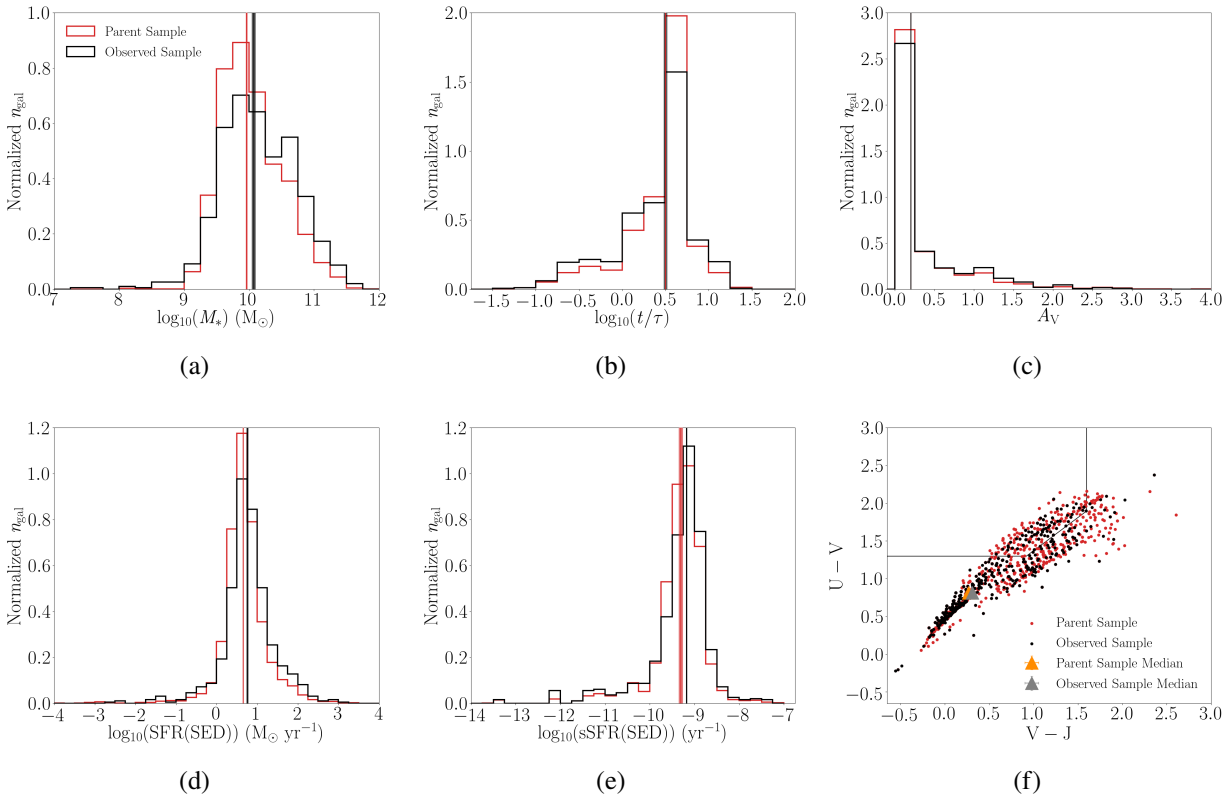

Figure 4.6: Distribution of physical properties and sample medians with 1σ uncertainties for the MOSDEF $z \sim 2$ parent sample (red) and the $z \sim 2$ observed sample (black). The values for the sample medians are given in Table 4.3. For the panels with 1D histograms, the y-axis is normalized so the area under the histogram for each sample adds up to one. The distributions for the following galaxy properties are shown: **(a)** M_*, **(b)** $\log_{10}(t/\tau)$ of the stellar population assuming a delayed-τ star formation model, **(c)** A_V, **(d)** SFR(SED), **(e)** sSFR(SED), **(f)** the UVJ diagram. The box on the UVJ diagram separates the quiescent region (upper left) from the star-forming region (bottom half and upper right). Additionally, the sample medians on the UVJ diagram are orange ($z \sim 2$ parent sample) and grey ($z \sim 2$ observed sample). The galaxy properties shown here are estimated using emission-line uncorrected photometry for all galaxies in the figure.

Table 4.3: Median Values for Physical Properties of the MOSDEF $z \sim 2$ Parent and Observed Samples

Physical Property (1)	Parent Median (2)	Observed Median (3)
$\log_{10}(M_*/M_\odot)$	9.96 ± 0.01	10.07 ± 0.03
$\log_{10}(t/\tau)$	0.50 ± 0.00	0.50 ± 0.02
$\log_{10}(\mathrm{SFR(SED)}/M_\odot/\mathrm{yr}^{-1})$	0.65 ± 0.01	0.76 ± 0.02
$\log_{10}(\mathrm{sSFR(SED)}/\mathrm{yr}^{-1})$	−9.31 ± 0.04	−9.18 ± 0.01
A_V	0.20 ± 0.001	0.20 ± 0.000
U−V	0.81 ± 0.01	0.81 ± 0.01
V−J	0.27 ± 0.01	0.31 ± 0.01

Note. — Col. (1): Physical property of the multiple MOSDEF samples shown in Figure 4.6. The galaxy properties shown here are estimated using emission-line uncorrected photometry. Col. (2): Median value with uncertainty of the MOSDEF $z \sim 2$ parent sample. Col. (3): Median value with uncertainty of the MOSDEF $z \sim 2$ observed sample.

t/τ, A_V, and U−V color) agree within the median uncertainties.

Figure 4.7 includes corner plots of SFR(SED), sSFR(SED), and A_V vs. M_*, which show 1D histograms with sample median of each parameter overlaid, and the 2D distribution of data points outlined by a 3σ contour. The $z \sim 2$ parent and observed samples mostly occupy similar regions in 2D space in all three of these diagrams, with only minor differences at the tails of the distributions (e.g., the $z \sim 2$ parent sample extends to higher A_V and lower SFR(SED) compared to the $z \sim 2$ observed sample).

In summary, Figures 4.6 and 4.7 show that the $z \sim 2$ observed sample is representative of the $z \sim 2$ parent sample from which it was drawn. We discuss the significance of this result in Section 4.4.

4.4 Discussion

In this section, we discuss the completeness of the MOSDEF $z \sim 2$ survey from multiple angles. Section 4.4.1 considers the implications of the completeness of the $z \sim 2$ spectroscopic sample with respect to the larger group of star-forming galaxies in the $z \sim 2$ stacked samples. Section 4.4.2 then compares the completeness of the MOSDEF $z \sim 2$ observed sample (i.e., all galaxies observed by MOSDEF) with the $z \sim 2$ parent sample (i.e., the full sample of galaxies in the AEGIS, COSMOS, GOODS-N, GOODS-S, and UDS fields) that met the MOSDEF selection criteria outlined in Section 4.2.1.

4.4.1 MOSDEF $z \sim 2$ Star-forming Galaxy Completeness

In Sections 4.3.1 and 4.3.2, we show that the emission-line and physical properties of the $z \sim 2$ stacked samples and the subsets of the stacked samples with high S/N spectra are very similar. The small differences in median properties are minor given the large range of values seen in the distributions. The fact that the smaller spectroscopic samples are representative of the full star-forming catalog in the MOSDEF survey is significant, as we can create composite spectra using stacking to increase the available sample size in future studies.

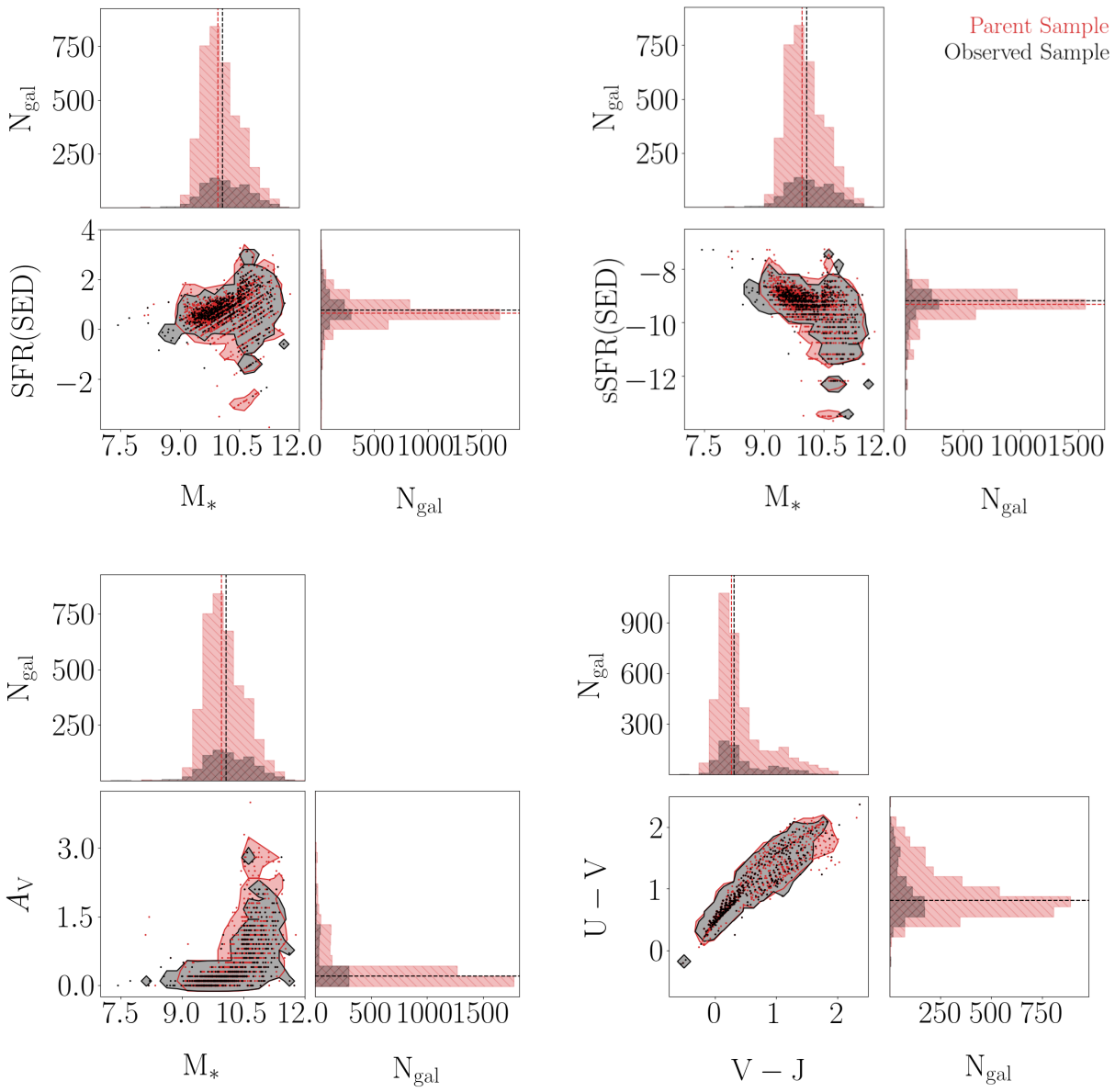

Figure 4.7: Corner plots for SFR(SED) . M_* (upper left), sSFR(SED) vs. M_* (upper right), A_V vs. M_* (bottom left), and U−V vs. V−J (bottom right). Shown on these diagrams are the $z \sim 2$ parent sample (red) and $z \sim 2$ observed sample (black). The galaxy properties shown here are estimated using emission-line uncorrected photometry for all galaxies in the figure.

Additionally, the agreement with the Sanders et al. (2021) sample on the N2 and O3N2 vs. M_* diagrams and with the Shapley et al. (2022) sample on the Hα/Hβ vs. M_* diagram shows that the results and conclusions based on those smaller samples are representative of the larger $z \sim 2$ star-forming population. The offset between local and $z \sim 2$ samples on the N2 and O3N2 vs. M_* diagrams reflects the well-known evolution of the mass-metallicity relation, MZR, (e.g., Andrews & Martini 2013; Steidel et al. 2014; Sanders et al. 2015).

Shapley et al. (2022) discuss that the lack of evolution in dust attenuation at fixed M_* points to an evolution towards increasing patchiness in dust attenuation at higher redshift, given the elevated $M_{\rm dust}/M_*$ ratios inferred at earlier times (e.g., Donevski et al., 2020; Magnelli et al., 2020; Shivaei et al., 2022). Alternatively, this lack of evolution in attenuation could be explained by evolution of the wavelength-dependent dust mass absorption coefficient (κ_λ). This dust cross-section per unit dust mass (κ_λ) has been shown to be inversely correlated with gas surface density, $\Sigma_{\rm gas}$ (Clark et al., 2019), in the local universe. At $z \sim 2$, $\Sigma_{\rm gas}$ is shown to be significantly higher than at $z \sim 0$. If the anticorrelation between κ_λ and gas surface density holds at $z \sim 2$, typical κ_λ values may be lower at high redshift, compared to what is observed in the local universe. Another possibility could be a steeper slope between $M_{\rm dust}/M_*$ and gas-phase oxygen abundance; however, Shapley et al. (2020); Popping et al. (2022) find no evolution in this relationship out to $z \sim 2$. One caveat is that these studies investigated a narrow mass range ($\log_{10}(M_*/M_\odot) \sim 10.5 - 11$). Additional ALMA observations of dust continuum and CO emission from $z \sim 2$ star-forming galaxies spanning a wider range of M_* and metallicity is required for understanding this intriguing lack of evolution in dust attenuation over 10 billion years.

4.4.2 MOSDEF $z \sim 2$ Observed Sample Completeness

In this study we show that the high S/N $z \sim 2$ detection samples analyzed in previous MOSDEF works are representative of the larger $z \sim 2$ stacked samples analyzed for the first time here. Furthermore, the MOSDEF $z \sim 2$ observed sample is representative of the full $z \sim 2$ parent sample. However, in Runco et al. (2021a), we show that the $z \sim 2$ spectroscopic sample containing

only star-forming galaxies suffers from incompleteness in the high-mass, red-UVJ color regime compared to the $z \sim 2$ observed sample. It is not clear if this incompleteness is relevant for our study of $z \sim 2$ *star-forming* galaxies, given that it is dominated by AGN and quiescent galaxies. Therefore, in this section, we investigate if incompleteness also exists between the $z \sim 2$ stacked sample and $z \sim 2$ observed sample, but for star-forming galaxies alone. To do so we look at a new subset of the $z \sim 2$ observed sample, from which all AGN and quiescent galaxies have been removed. Of the 786 galaxies in the MOSDEF $z \sim 2$ observed sample, 171 galaxies are removed for either containing an AGN and/or fall into the quiescent box as defined in Williams et al. (2009). This 615-galaxy sample is less restrictive than the $z \sim 2$ stacked samples in that we do not require coverage of any specific set of emission-lines and also do not require a robust $z_{\rm MOSFIRE}$. We will hereafter refer to this 615 galaxy sample as the "$z \sim 2$ star-forming observed sample."

Figure 4.8 includes corner plots of SFR(SED), sSFR(SED), and $A_{\rm V}$ vs. M_* and also U−V vs. V−J colors. The diagrams feature 1D histograms with sample medians overlaid for each parameter as well as the 2D distribution of data points traced by a 3σ contour. We find that the $z \sim 2$ N2 stacked sample is incomplete with respect to the full $z \sim 2$ observed sample, as the latter extends to higher M_*, lower SFR(SED) and sSFR(SED), and redder UVJ colors. These results reflect what was found in Runco et al. (2021a). On the other hand, the $z \sim 2$ N2 stacked sample is very similar to the $z \sim 2$ star-forming observed sample, with the 3σ contours for both samples covering almost identical ranges in all four diagrams.

This analysis shows that the sample of AGN and quiescent galaxies observed by MOSDEF caused the incompleteness between the $z \sim 2$ spectroscopic and observed samples reported in Runco et al. (2021a). These galaxies make up the population of very red, high mass galaxies with little star formation in the $z \sim 2$ observed sample. This combination of properties is not common for galaxies actively forming stars. In conclusion, the high S/N $z \sim 2$ detection samples of star-forming galaxies used in MOSDEF emission-line studies to date are representative of the full set of $z \sim 2$ star-forming galaxies in the MOSDEF parent catalog, and, therefore, the rest-optical-magnitude-limited

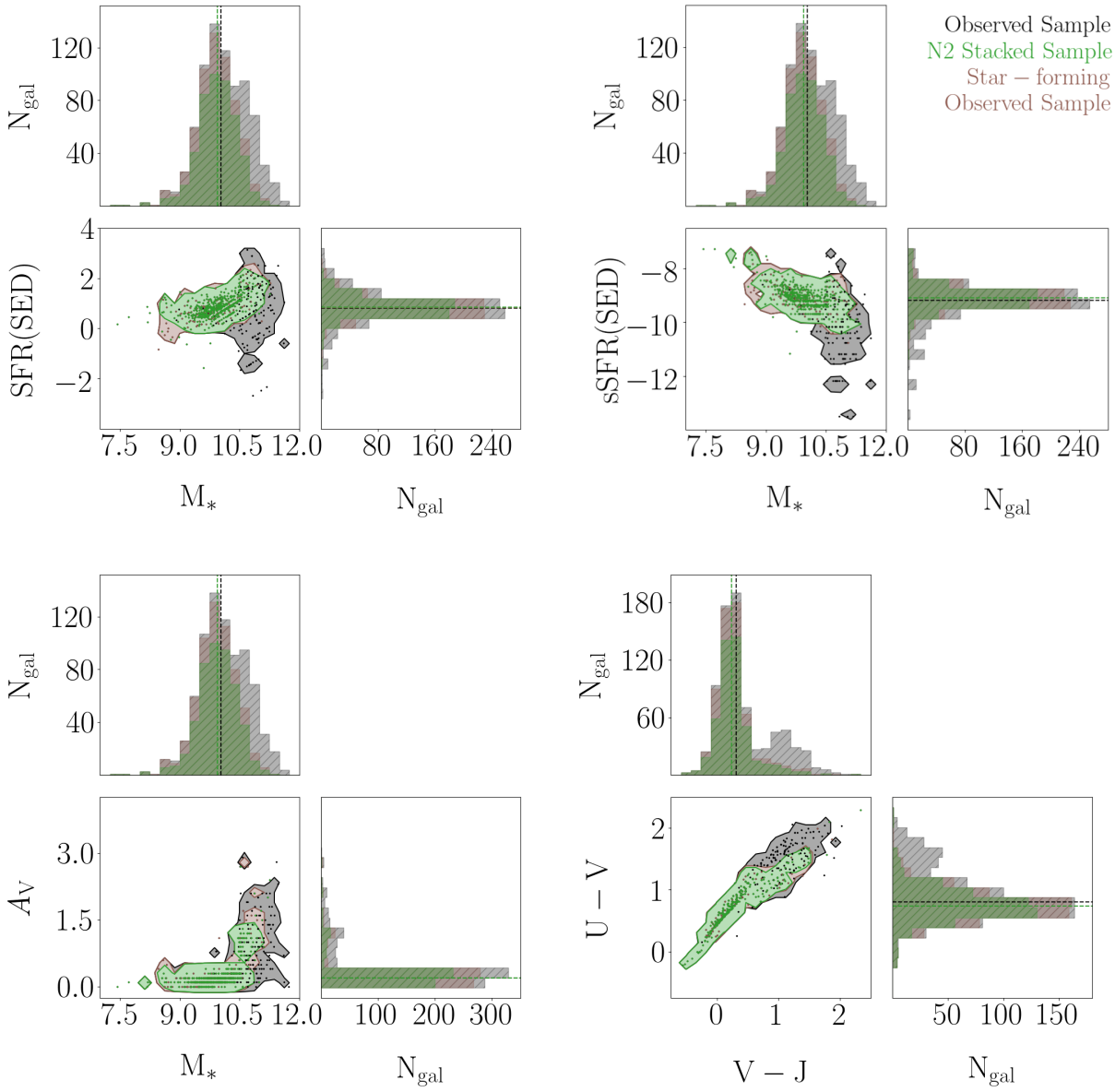

Figure 4.8: Corner plots for SFR(SED) vs. M_* (upper left), sSFR(SED) vs. M_* (upper right), A_V vs. M_* (bottom left), and U−V vs. V−J (bottom right). Shown on these diagrams are the $z \sim 2$ observed sample (black), $z \sim 2$ star-forming observed sample (brown), and the $z \sim 2$ N2 stacked sample (green). The galaxy properties shown here are estimated using emission-line corrected photometry for the majority of the galaxies with a MOSFIRE redshift. Otherwise, emission-line uncorrected photometry is used for the minority of galaxies without the $z_{\rm MOSFIRE}$.

star-forming galaxy population at $z \sim 2$.

4.5 Summary

In this study we investigate the completeness of the $z \sim 2$ MOSDEF survey. We compare the subset of star-forming galaxies with high S/N rest-optical emission-line detections against composite spectra for the full star-forming sample created using spectral stacking. We use a combination of SED and emission-line fitting to test if the high S/N subset typically used in previous MOSDEF studies is representative of the broader population of star-forming galaxies. Additionally, we compare the full $z \sim 2$ sample observed by MOSDEF (including AGN and quiescents) with all galaxies in the five 3D-HST fields targeted by MOSDEF (AEGIS, COSMOS, GOODS-N, GOODS-S, and UDS) at $1.9 \leq z \leq 2.7$ that meet the MOSDEF H-band magnitude selection criteria ($H_{\rm AB}$ = 24.5). In this comparison, we utilize SED fitting to investigate if the properties of the galaxies observed by MOSDEF are representative of the $z \sim 2$ universe.

The main results are as follows:

1. The sequence of bins in the $z \sim 2$ N2, S2, and O_{32} stacked sample occupy similar regions of the [N II] BPT, [S II] BPT, and O_{32} vs. R_{23} diagrams to those of the smaller $z \sim 2$ detection samples with high S/N spectra. Additionally, the bins in the $z \sim 2$ N2 and S2 stacked samples overlap the binned medians for the $z \sim 2$ N2 BPT and S2 BPT detection samples from Runco et al. (2021a). On the [N II] BPT diagram, the lowest-M_* bin in the $z \sim 2$ N2 stacked sample extends the sequence to higher N2 and/or O3. In addition, the $z \sim 2$ N2 stacked sample has the same median offset (within the uncertainties) from the SDSS local sequence as the binned medians from Runco et al. (2021a) (0.10 ± 0.04 dex and 0.12 ± 0.02 dex, respectively). The $z \sim 2$ N2 stacked sample overlaps with the fit to early MOSDEF data from Shapley et al. (2015). This agreement between the high S/N $z \sim 2$ detection samples and the larger stacked samples utilizing all star-forming galaxies at $z \sim 2$ suggests that the emission-lines from smaller high S/N subsets typically used in MOSDEF studies are not biased with respect to

the sample from which they are drawn.

2. We find an offset between the $z \sim 2$ N2 stacked sample and the local star-forming sequence on diagrams using emission-line ratios plotted vs. M_* as proxies for the mass-metallicity relationship. These emission-line ratios include N2 and O3N2. The magnitude of the offset between $z \sim 2$ and $z \sim 0$ line ratio at fixed M_* is similar to that derived from previous studies using high S/N MOSDEF samples. We do not find evolution in dust attenuation (traced by Hα/Hβ) between $z \sim 2$ and local $z \sim 0$ galaxies.

3. The MOSDEF ~ 2 observed sample has a higher median M_*, SFR(SED), and sSFR(SED) and redder median V−J color compared to the $z \sim 2$ parent sample. However, the offset in median M_*, SFR(SED), and sSFR(SED) between the two samples is relatively small (∼0.1 dex) considering that the distributions of these parameters span more than four orders of magnitude. This indicates that the galaxies at $z \sim 2$ observed by the MOSDEF team are not biased from the full galaxy population at this epoch.

4. Removing AGN and quiescent galaxies from the $z \sim 2$ observed sample resolves the issue of incompleteness between the $z \sim 2$ observed sample and the $z \sim 2$ spectroscopic sample reported in Runco et al. (2021a). The $z \sim 2$ spectroscopic sample has very similar galaxy properties to the full catalog of $z \sim 2$ star-forming galaxies in the MOSDEF survey.

The lack of bias between the $z \sim 2$ stacked sample and the smaller high S/N subsets indicate that, moving forward, we can use the latter in future studies as a robust proxy for the $z \sim 2$ star-forming galaxy population. Large statistical samples are needed to better understand the proper utilization of emission-line ratios as calibrations for gas-phase oxygen abundance patters. Such studies are essential and will push us closer to create relationships (e.g., MZR, FMR) in the $z \sim 2$ universe approaching what already exists locally. The construction of composite spectra using spectral stacking has shown to be a valuable tool in assembling these larger samples. Faint and dusty galaxies require longer integration times to capture the full set of rest-optical emission-lines. For

these extreme galaxies it can be difficult to obtain 3σ detections for bright lines (e.g., Hα) on an individual basis. In these situations, measuring weaker lines (e.g., [N II]λ6585) is significantly more challenging. Incorporating these galaxies into composite spectra is essential for creating samples that are more representative of the $z \sim 2$ universe.

CHAPTER 5

A Remarkable $z = 1.89$ Merger

5.1 Introduction

Within the current ΛCDM cosmological framework, galaxies grow in mass through both merging events and the smooth accretion of baryons and dark matter. Mergers are an important component of galaxy formation models (e.g., Hopkins et al. 2010), and obtaining empirical constraints on merger rates as a function of galaxy mass and redshift is a current goal for observational galaxy evolution (e.g., Lotz et al. 2011). Merging systems have been observed out to $z \sim 6$ (Ventou et al., 2017), approximately ∼0.9 Gyr after the big bang.

Locally (i.e., $z \sim 0$), the Sloan Digital Sky Survey (SDSS) has obtained large statistical samples of pre-coalescence galaxy pairs with projected separations of $30 - 80$ kpc and radial velocity differences of $200 - 500$ km s^{-1} (Ellison et al., 2008; Patton et al., 2011, 2013; Scudder et al., 2012, 2015). Compared to isolated galaxies at fixed stellar mass, these systems are identified as having gas-phase metallicity depressed by $\sim 0.02 - 0.05$ dex and star-formation rate (SFR) enhanced by $\sim 60\%$ out to 30 kpc (Scudder et al., 2012). Merging systems at $z > 1$ are identified through a variety of methods including photometric pairs (e.g., Williams et al. 2011; Man et al. 2012, 2016; Mantha et al. 2018), spectroscopic features (e.g., Tasca et al. 2014; Ventou et al. 2017; Dai et al. 2021), and visible morphological features such as tidal tails and double nuclei (e.g., Lofthouse et al. 2017; Kartaltepe et al. 2015).

In the last decade, the commissioning of multi-object near-IR spectrographs on large ground-based

telescopes has enabled us to obtain large samples of high S/N rest-optical emission-line spectra for galaxies at $z \sim 1.5 - 3.5$. Utilizing the MultiObject Spectrometer For Infra-Red Exploration (MOSFIRE; McLean et al. 2012) instrument on the 10 m Keck I telescope, the MOSFIRE Deep Evolution Field (MOSDEF) survey (Kriek et al., 2015) has observed ~1500 galaxies at $1.4 \leq z \leq 3.8$ (roughly half of which are at $z \sim 2$). Previous MOSDEF studies have identified high-redshift mergers using multiple methods. Horstman et al. (2021) identified 55 mergers at $z \sim 2$ using the Cosmic Assembly Near-infrared Dark Energy Legacy Survey (CANDELS) morphology catalog (Kartaltepe et al., 2015), and Wilson et al. (2019) spectroscopically identified 30 galaxy pairs at $1.5 \lesssim z \lesssim 3.5$.

In this study, we present a merger at $z = 1.89$ between the galaxies GOODS-S 43114 and GOODS-S 43683, where galaxy IDs are drawn from the 3D-HST survey catalogs of Skelton et al. (2014). GOODS-S 43114 was targeted by the MOSDEF team, and high-quality J-, H-, and K_s-band Keck/MOSFIRE spectra were obtained. GOODS-S 43683 was not a MOSDEF target; however, it was serendipitously captured in the MOSFIRE slit given the mask position angle. This merger pair has been previously identified by van Dokkum & Brammer (2010) and is in the CANDELS morphology catalog (Kartaltepe et al., 2015), though it has not been highlighted in previous MOSDEF merger analyses (e.g., Wilson et al., 2019; Horstman et al., 2021). In addition, van Dokkum & Brammer (2010) claim that both galaxies contain an active galactic nucleus (AGN) based on X-ray luminosity data from Luo et al. (2008).

The goal of this study is to build on the earlier work of van Dokkum & Brammer (2010) by analyzing the spectroscopic and host-galaxy properties of both galaxies using Keck/MOSFIRE spectra and emission-line corrected SED fitting and comparing with state-of-the-art galaxy merger simulations. Specifically, we aim to better understand the galaxy star formation histories (SFHs) and stellar population properties and the evolutionary stage of the merger, by fitting the Hδ absorption feature following the methodology from Zick et al. (2018) and using it to estimate the velocity dispersion and dynamical mass of the system. Section 5.2 provides an overview of the MOSDEF

survey and presents the observations, the SED fitting methodology, and derived galaxy properties. Section 5.3 presents the results, while Section 5.4 provides a discussion of the key results in the context of current work with galaxy merger simulations. Finally, Section 5.5 summarizes the key results from this study.

All emission-line wavelengths are given in the vacuum frame. Throughout this paper, we adopt a Λ-CDM cosmology with H_0 = 70 km s^{-1} Mpc^{-1}, Ω_m = 0.3, and Ω_Λ = 0.7. Also, we assume the solar abundance pattern from Asplund et al. (2009).

5.2 Observations & Methods

5.2.1 The MOSDEF Survey

Using the MOSFIRE instrument on the 10 m Keck I telescope, the MOSDEF survey has observed ~1500 galaxies throughout its 48.5-night observing program between 2012-2016. MOSDEF galaxies were selected from five well-studied CANDELS and 3D-*HST* legacy fields (Grogin et al., 2011; Koekemoer et al., 2011; Momcheva et al., 2016) – AEGIS, COSMOS, GOODS-N, GOODS-S, and UDS – and were targeted in three distinct redshift ranges: $1.37 \leq z \leq 1.70$, $2.09 \leq z \leq 2.61$, and $2.95 \leq z \leq 3.80$. These redshift bins were selected to optimise the detection of strong rest-optical emission-lines (e.g., [O II]$\lambda\lambda$3727,3730, Hβ, [O III]$\lambda\lambda$4960,5008, Hα, [N II]λ6585, and [S II]$\lambda\lambda$6718,6733) within windows of atmospheric transmission. Moderate spectral resolution (R = 3000-3650) was obtained, and the survey is H-band (rest-optical) magnitude-limited (H_{AB} = 24.0, 24.5, and 25.0, respectively, in the low-, middle-, and high-redshift bins of the MOSDEF sample). We use an ABA'B' (+1."5, 1."2, −1."2, −1."5) dither pattern to account for detector defects, sky variations, and increase the S/N of the final spectra (Kriek et al., 2008). For additional MOSDEF observing details, see Kriek et al. (2015).

5.2.2 GOODS-S 43114 & GOODS-S 43683 Observations

Based on the MOSDEF observing strategy, GOODS-S 43114 was targeted for MOSDEF spectroscopic observations based on a cataloged spectrosopic redshift of $z = 2.6087$ from Balestra et al. (2010). In fact, this cataloged spectroscopic redshift is inconsistent with both the photometric redshift of of $z = 1.9135$ listed in the 3D-HST catalog (see also Schawinski et al., 2011), and the grism spectroscopic redshift presented in van Dokkum & Brammer (2010), the latter of which we were unaware of at the time of observation. The 3D-HST photometric redshift in fact places GOODS-S 43114 outside all of the nominal MOSDEF target ranges. However, within the MOSDEF targeting process, existing spectroscopic redshifts were given priority in the event that a discrepancy arose between spectroscopic and photometric redshift. Using the erroneous spectroscopic redshift for GOODS-S 43114 led to the fortuitous observation of the unique spectra described here.

GOODS-S 43114 was observed across two nights: January 1 and 2 2016. The integration time was 2 hours in each of the J, H, and K_s bands. The spectroscopic redshift derived from our MOSFIRE observations is $z = 1.88694$, which is consistent with the photometric redshift in the 3D-HST catalog (1.9135 ± 0.0395), and slightly lower than the redshift presented in van Dokkum & Brammer (2010) (1.902 ± 0.002). At this redshift, nebular emission lines such as [O II]$\lambda\lambda$3727,3730, Hβ, [O III]$\lambda\lambda$4960,5008, Hα, [N II]λ6585, and [S II]$\lambda\lambda$6718,6733 fall outside of the J, H, and K_s-bands. However, we did observe the Hγ and Hδ Balmer absorption lines in the J band, from which we derived a spectroscopic redshift for GOODS-S 43114. The J-band MOSFIRE spectrum of GOODS-S 43114 is shown in Figure 5.1. No discernible emission- or absorption-line features were captured in the H or K_s-bands.

Figure 5.2 shows the *HST* WFC3 F160W 2D image of GOODS-S 43114 and GOODS-S 43683, including identifications of the centroids of the galaxies and the position of the MOSFIRE slit. We estimate that the centroids of the two galaxies are 2.135 arcseconds (18 kpc) apart, which agrees with van Dokkum & Brammer (2010). As previously stated, GOODS-S 43683 was not specifically targeted as part of the MOSDEF survey; however, as Figure 5.2 shows, it was captured

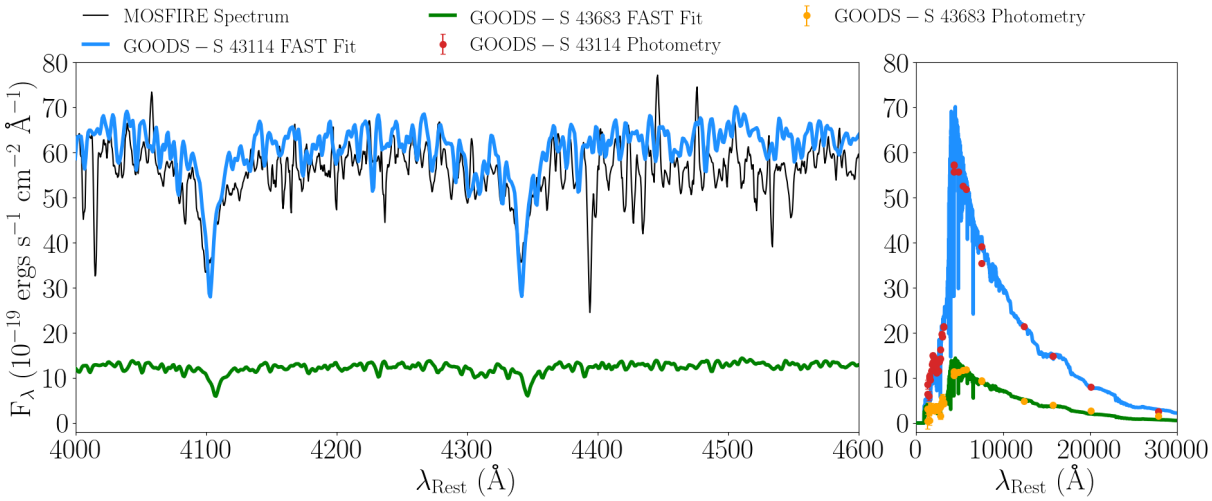

Figure 5.1: Left: MOSFIRE J-band spectrum (black) for GOODS-S 43114 along with the section of the GOODS-S 43114 FAST fit (blue) and GOODS-S 43683 FAST fit (green) that overlaps with the spectra. Here we see the Hγ and Hδ absorption features. Right: The full broadband GOODS-S 43114 FAST fit (blue) with photometry points (red) and full broadband GOODS-S 43683 FAST fit (green) with photometry points (orange).

serendipitously in the MOSDEF slit with GOODS-S 43114 given the slit position angle of −40 degrees E of N. Unfortunately, the adopted ABA'B' dither pattern seems to have washed out the spectrum of GOODS-S 43683, as we do not detect its light in the MOSFIRE slit.

GOODS-S 43114 and GOODS-S 43683 have been identified as a merger pair in van Dokkum & Brammer (2010) and the CANDELS morphology catalog (Kartaltepe et al., 2015). The latter classifies mergers and other galaxy features based on the visual inspection. For GOODS-S 43114 (GOODS-S 43683), 100% (66%) of people classified it as having "any interaction" while 66% (100%) claimed that tidal arms exist. GOODS-S 43114 is a class 4 merger, while GOODS-S 43863 is a class 3 merger, both of which are high confidence merger classifications. van Dokkum & Brammer (2010) also report this galaxy pair as having merger features such as diffuse, tidally-induced spiral arms and tails.

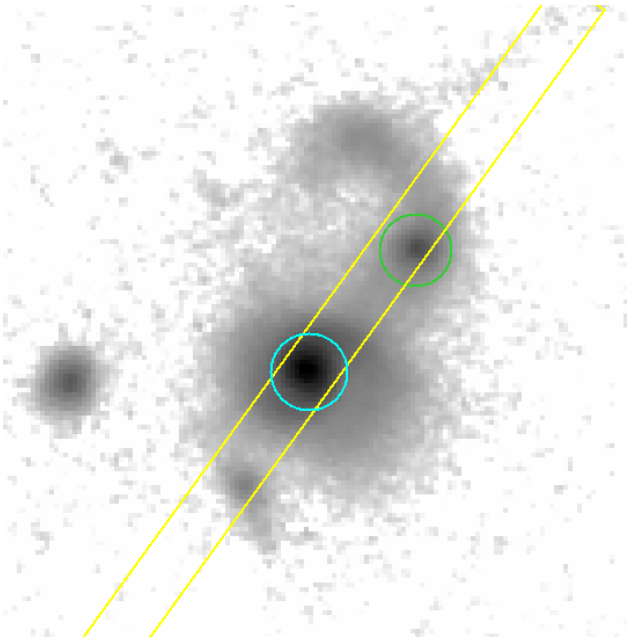

Figure 5.2: The 2D F160W image from the 3D-*HST* catalog with the MOSFIRE slit (yellow), GOODS-S 43114 centroid (blue) and GOODS-S 43683 centroid (green) identified.

5.2.3 SED Fitting & Derived Properties

We use the SED fitting code FAST (Kriek et al., 2009) to obtain best-fit SEDs and estimates of key galaxy properties for GOODS-S 43114 and GOODS-S 43863. With FAST, we adopt the Flexible Stellar Population Synthesis (FSPS) library from (Conroy & Gunn, 2010) and assume a Chabrier (2003) stellar initial mass function (IMF), a Calzetti et al. (2000) dust attenuation curve, and delayed-τ star-formation histories where SFR(SED) $\propto t \times e^{-t/\tau}$ where τ is the characteristic star-formation timescale and t is the time since the onset of star formation. We allow t, τ, the amount of interstellar extinction (A_V), and stellar mass of the galaxy (M_*) to vary within the models, while fixing the metallicity to 0.019 (defined to be solar metallicity in the Conroy & Gunn 2010 library). For the SED fitting, we fix GOODS-S 43114 and GOODS-S 43683 redshifts to the MOSFIRE spectroscopic redshift obtained for GOODS-S 43114. Given that these galaxies are in a merger with the centroids being only ~18 kpc apart, this redshift assumption for GOODS-S 43683 seems reasonable. van Dokkum & Brammer (2010) validate our assumption, reporting

$z = 1.898 \pm 0.003$ for GOODS-S 43683 (they report $z = 1.902 \pm 0.002$ for GOODS-S 43114). In addition, fitting the photometry with the code `EAZY` (Brammer et al., 2008) yields a photometric redshift of 1.899. Along with the best-fit SED and an estimate of M_*, SFR(SED), A_V, and t/τ, we estimate sSFR(SED) from SFR(SED) and M_*. UVJ colors are measured from the best-fit SED using the IRAF (Tody, 1986, 1993) routine *sbands*.

We use broadband photometry drawn from the 3D-*HST* v4.1 catalogs (Skelton et al., 2014) for both GOODS-S 43114 and GOODS-S 43683. For GOODS-S 43114, we fit a combination of the broadband photometry and the J, H, and K_s-band MOSFIRE spectra. Here the MOSFIRE spectra are normalized to match the flux density corresponding to the photometric points in each band. For GOODS-S 43683, we only use the photometry in the fitting process due to no available MOSFIRE spectra.

We estimate the 4000 Å break (D_n4000) and the Hδ absorption-line feature ($H\delta_A$) using the wavelength ranges from, respectively, Worthey & Ottaviani (1997) and Balogh et al. (1999). D_n4000 traces the opacity of stellar atmospheres and increases with metallicity and age. $H\delta_A$ peaks when A-type stars dominate the spectrum, which occurs when a short burst of star formation is followed by rapid quenching. Therefore, the combination of these features can reveal information about the star formation timescale and evolutionary phase of a galaxy, as $H\delta_A$ is sensitive to recently-quenched star formation while D_n4000 is sensitive to age. We utilize the best-fit FAST models to measure both quantities for both GOODS-S 43114 and GOODS-S 43683. For GOODS-S 43114, it is also possible to estimate $H\delta_A$ from the spectra; however, part of the D_n4000 feature is blue-ward of the J-band spectra. The measurement of $H\delta_A$ from the model is consistent with direct integration from the spectrum itself.

We use the Penalized Pixel-Fitting routine (`ppxf`; Cappellari & Emsellem 2004; Cappellari 2017) to estimate the effective velocity dispersion (σ_e) of the GOODS-S 43114. We fit the MOSDFIRE J-band spectrum using the Vazdekis et al. (2010) stellar population library. Since the MOSFIRE spectrum is higher resolution than the stellar templates, we correct the fitted velocity dispersion

upwards by the quadratic differences of the two resolutions. Both the Hγ and Hδ lines are included in the fit. Tanaka et al. (2019) show that the choice of stellar population library and whether or not to mask the Balmer absorption lines does not bias the estimated velocity dispersion.

The velocity dispersion is used to estimate the dynamical mass ($M_{\rm dyn}$) using the following equation:

$$M_{\rm dyn} = \frac{\beta \sigma_{\rm e}^2 R_{\rm e}}{G} \tag{5.1}$$

where β is the virial coefficient and G is the gravitational constant. We adopt a virial coefficient value of 5, corresponding to the case of a sphere of uniform density (Price et al., 2016), and will revisit this assumption in Section 5.4.

5.2.4 SDSS Comparison Sample

In Section 5.3, we compare the D_n4000 and Hδ_A values of GOODS-S 43114 and GOODS-S 43683 with those of local galaxies using archival data from SDSS Data Release 7 (DR7; Abazajian et al. 2009), specifically from the MPA-JHU DR7 release of spectrum measurements[1]. We use the Hδ_A and D_n4000 values from the catalog where the measured continuum indices in the spectra have been corrected for sky-line contamination using the best-fit model spectrum. We restrict the SDSS sample to a redshift range of $0.04 \leq z \leq 0.10$. These criteria give us a final local sample of 305,005 galaxies.

5.3 Results

The host galaxy properties discussed in Section 5.2.3 are shown in Table 5.1. The reported 1σ uncertainties for best-fit galaxy properties (i.e., M_*, SFR(SED), sSFR(SED), τ, t/τ, and A_V) are estimated from Monte Carlo simulations during the FAST SED fitting. Uncertainties for properties obtained from the best-fit SED (i.e., UVJ colors, D_n4000, and Hδ_A) are estimated by perturbing the photometry and MOSFIRE spectra within their uncertainties assuming a normal distribution and

[1] https://wwwmpa.mpa-garching.mpg.de/SDSS/DR7/

Table 5.1: GOODS-S 43114 & GOODS-S 43683 Physical Properties

Physical Property	GOODS-S 43114	GOODS-S 43683
(1)	(2)	(3)
$\log_{10}(M_*/M_\odot)$	$11.63^{+0.06}_{-0.00}$	$11.04^{+0.05}_{-0.00}$
$\log_{10}(t/\tau)$	$1.00^{+0.00}_{-0.00}$	$0.90^{+0.00}_{-0.00}$
$\log_{10}(\tau/\mathrm{Gyr})$	$8.00^{+0.01}_{-0.00}$	$8.20^{+0.02}_{-0.18}$
$\log_{10}(\mathrm{SFR(SED)})$ ($\mathrm{M_\odot\ yr^{-1}}$)	$0.45^{+0.07}_{-0.00}$	$0.46^{+0.05}_{-0.00}$
$\log_{10}(\mathrm{sSFR(SED)})$ ($\mathrm{yr^{-1}}$)	$-11.18^{+0.00}_{-0.00}$	$-10.58^{+0.00}_{-0.00}$
A_V	$0.30^{+0.10}_{-0.01}$	$0.40^{+0.10}_{-0.02}$
U−V	$1.48^{+0.0001}_{-0.00}$	$1.53^{+0.03}_{-0.0001}$
V−J	$0.78^{+0.0001}_{-0.00}$	$0.91^{+0.05}_{-0.00}$
$\mathrm{D_n4000}$	$1.25^{+0.00}_{-0.00}$	$1.26^{+0.00}_{-0.05}$
$\mathrm{H}\delta_\mathrm{A}$	$6.95^{+0.00}_{-0.00}$	$6.06^{+2.7}_{-0.00}$
σ_e ($\mathrm{km\ s^{-1}}$)	121^{+98}_{-75}	N/A
$\log_{10}(M_\mathrm{dyn}/M_\odot)$	$10.72^{+0.51}_{-0.84}$	N/A

Note. — Col. (1): Physical property of the galaxies in the sample. Col. (2): Property value for GOODS-S 43114. Col. (3): Property value for GOODS-S 43683. "N/A" is listed for σ_e and $\log_{10}(M_\mathrm{dyn})$ because we do not have MOSFIRE spectra for this galaxy.

re-fitting the perturbed data in FAST. The best-fit SEDs from the perturbed data are then re-fit, and 1σ uncertainties (16^{th} and 84^{th} percentiles) for the parameters are estimated from the distributions of the fitted, perturbed quantities. Finally, the uncertainties on σ_{e} and M_{dyn} are obtained by perturbing the MOSFIRE spectrum within its uncertainties and re-fitting the perturbed spectra with `ppxf`. Note that many of the reported uncertainties are very small for properties estimated from the SED fitting, which results from both galaxies having a very high number (39) of photometry points.

GOODS-S 43114 is found to be slightly more massive with bluer UVJ colors, a larger $\text{H}\delta_{\text{A}}$, and a smaller sSFR(SED) compared to GOODS-S 43683. The two galaxies have similar values of SFR(SED), t/τ, A_{V}, and $\text{D}_{\text{n}}4000$. The observed difference in sSFR(SED) can be attributed to the difference in M_* since the SFR(SED) values of the two galaxies agree within the uncertainties. According to standard classification (e.g., Cox et al., 2008), the close stellar mass ratio between GOODS-S 43114 and GOODS-S 43683 implies that this system is a “major merger."

Recall from Section 5.2.3 that we fit a combination of the photometry and MOSFIRE spectra of GOODS-S 43114, while we only fit the photometry of GOODS-S 43683. The values presented in Table 5.1 do not change significantly if we fit GOODS-S 43114 using only the photometry, applying the same methodology as for GOODS-S 43683. In addition, the conclusions we derive from these results (see Section 5.4) are not dependent on whether we fit both the photometry and MOSFIRE spectra of GOODS-S 43114, or the photometry alone.

Based on rest-frame UVJ colors, Zick et al. (2018) group galaxies into five bins: quiescent (i), post-starburst (ii), dusty galaxies with lower sSFRs (iii), dust star-forming (iv), and non-dusty star-forming (v). These bins were created based on known correlations between galaxy properties and UVJ colors. For star-forming galaxies, A_{V} increases linearly with increasing U−V and V−J. sSFR(SED) decreases along a direction perpendicular to this A_{V} sequence (i.e., U−V increases and V−J decreases as sSFR(SED) decreases). These relationships motivate the creation of bins (iii), (iv), and (v). Once a galaxy has stopped forming stars its colors will evolve towards the quiescent

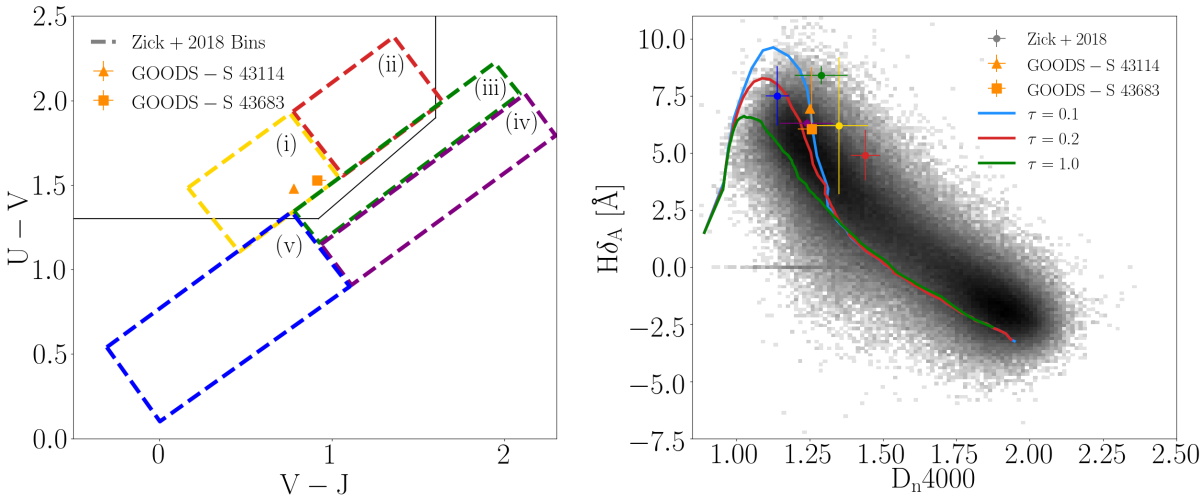

Figure 5.3: Left: UVJ diagram. GOODS-S 43114 and GOODS-S 43683 are shown by the orange triangle and square, respectively. The dashed boxes identify the five bins of galaxies from Zick et al. (2018): quiescent (red), post-starburst (yellow), dusty galaxies with lower sSFRs (green), dust star-forming (purple), and non-dusty star-forming (blue). Both GOODS-S 43114 and GOODS-S 43683 fall into the post-starburst bin. The black line identifies the quiescent box defined in (Williams et al., 2009). Right: $H\delta_A$ vs. D_n4000. The circles are color matched to identify the five bins of galaxies shown in the UVJ diagram. The blue, red, and green lines identify three delayed-τ SFHs, where τ = 0.1, 0.2, and 1.0 Gyr, respectively. The grayscale 2D histogram indicates local SDSS galaxies.

box. As galaxies age away from their star forming epochs, they move along the quiescent sequence in the UVJ diagram (i.e., increasing in U−V and V−J color). Therefore, bins (i) and (ii) comprise an age gradient for galaxies no longer forming stars.

The left panel of Figure 5.3 gives the UVJ diagram with these galaxy bins from Zick et al. (2018) identified. The region occupied by quiescent galaxies following the definition from Williams et al. (2009) is also included. It can be seen that both GOODS-S 43114 and GOODS-S 43683 fall into the post-starburst bin (i.e., bin (ii)). The low SFR(SED) and sSFR(SED) values in both galaxies indicate that these galaxies are not currently forming stars at a rapid rate. In addition, the characteristic shapes of the SEDs in the right panel of Figure 5.1 (specifically, the steep decline in flux density redwards of ~4000 Å) suggests that both galaxies are in a post-starburst phase.

Figure 5.3 shows GOODS-S 43114 and GOODS-S 43683 on the $H\delta_A$ vs. D_n4000 diagram. Also

included are the five datapoints from Zick et al. (2018) representing stacks of galaxies in each of the five UVJ bins, and tracks of SFH with τ = 0.1, 0.2, and 1.0 Gyr. To create these tracks, we use the code `python-FSPS` (Johnson et al., 2021) which generates spectra for synthetic stellar populations using the FSPS library (Conroy & Gunn, 2010). For these models, we make similar assumptions to those in our SED fitting (i.e., a Chabrier 2003 stellar initial mass function (IMF), a Calzetti et al. 2000 dust attenuation curve, and delayed-τ SFHs). Additionally, we incorporate dust emission, nebular continuum and emission lines, stellar remnants, and intergalactic medium (IGM) absorption for a more realistic model.

We find that both GOODS-S 43114 and GOODS-S 43683 fall within the uncertainties of bin (ii) on the H$\delta_{\rm A}$ vs. D_n4000 diagram. Based on the elevated H$\delta_{\rm A}$ value found for both galaxies, it is likely that the spectra are dominated by A-type stars, which implies that star formation shut down in a time frame where the O- and B-type stars no longer exist but the A-type stars still remain. In addition, the fact that the D_n4000 feature and t/τ ratio are very similar for both galaxies indicates that both galaxies have similar stellar population ages, and therefore shut off star formation at roughly the same time. This approximate synchronization is confirmed in Figure 5.4, which shows the estimated SFHs for GOODS-S 43114 and GOODS-S 43683 obtained using the SFR(SED) and τ values from Table 5.1. The bursts of star formation in each galaxy both began and peaked within a few hundred Myrs of each other.

Using `ppxf`, we find $\sigma_{\rm e} = 121^{+98}_{-75}$ km s^{-1} resulting in $\log_{10}(M_{\rm dyn}/M_\odot) = 10.72^{+0.51}_{-0.84}$ for GOODS-S 43114. Figure 5.5 shows the fit to the J-band spectrum with the residuals of the fit. The uncertainty on $\sigma_{\rm e}$ was obtained by perturbing the spectrum within the error spectrum and refitting. The uncertainty on $M_{\rm dyn}$ was obtained by propagating the uncertainty on $\sigma_{\rm e}$ through Equation 5.1. The dynamical mass estimate is approximately one order of magnitude lower than the M_* measurement, which raises concerns about the validity of these values. We discuss the discrepancy between the mass estimates in Section 5.4.2. Since we do not have MOSFIRE spectra of GOODS-S 43683, we cannot estimate $\sigma_{\rm e}$ and subsequently $M_{\rm dyn}$ for this galaxy.

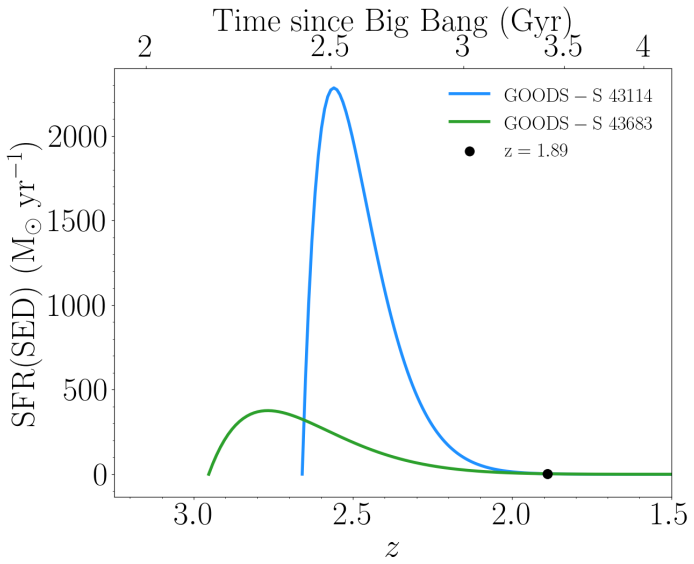

Figure 5.4: SFR(SED) vs. z displaying the SFHs assuming a delayed-τ model for GOODS-S 43114 (blue) and GOODS-S 43683 (green). The black circle identifies the moment of observation (i.e., z = 1.89). The rapid burst of star formation followed by rapid quenching over the course of ~500 Myr or less gives an approximation on when the first pericentric passage took place.

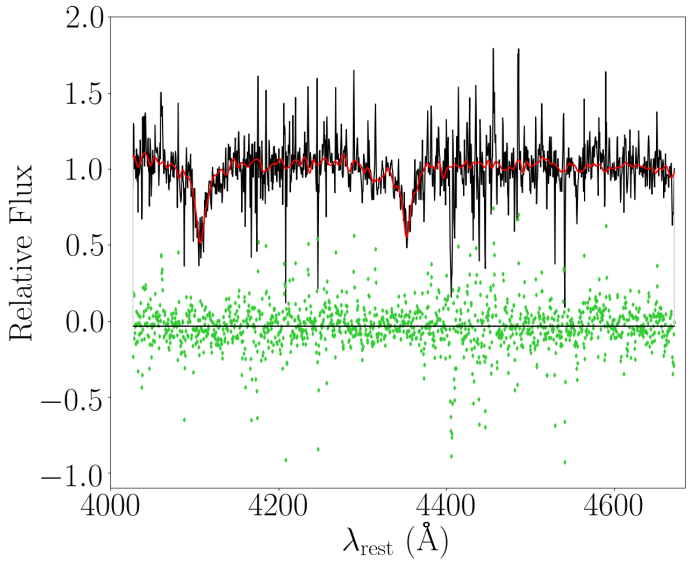

Figure 5.5: Fit to the MOSFIRE J-band spectrum using `ppxf` to estimate σ_e. The MOSFIRE spectrum is shown in black while the fit is shown in red. The residuals to the fit are given as green points. The spectrum and fit are centered at a relative flux of 1, while the residuals are centered at a relative flux of 0.

5.4 Discussion

5.4.1 State of the Merger

Comparing observations to galaxy simulations is important for connecting isolated snapshots of galaxies with the larger evolutionary picture. Numerical simulations help improve our understanding of the both the merger process and the significance of mergers to galaxy formation (e.g., Barnes & Hernquist 1991, 1996; Di Matteo et al. 2007; Cox et al. 2008; Di Matteo et al. 2008; Moreno et al. 2015; Blumenthal & Barnes 2018). State-of-the-art galaxy formation simulations have the resolution to capture feedback-regulated star formation and multi-phase structures within the interstellar medium (ISM; e.g., FIRE-1 and FIRE-2; Hopkins et al. 2011, 2014, 2018), and, therefore, how these galaxy processes and components will respond to a merger event. For example, recent merger modeling with FIRE-2 (Moreno et al., 2019) probes enhanced star formation and ISM gas content during the merger process. In this work, three key stages in a merger are identified: the first pericentric passage, the second pericentric passage, and coalescence. The time between the first and second pericentric passage is ~2-2.5 Gyr (dependent on merger parameters) while the time between the first and second pericentric passage and coalescence is $\lesssim$0.5 Gyr. In addition, this study suggests that SFR spikes at each of these three events with a significant decrease in SFR during the large time gap between the pericentric passages. The SFR stays elevated in the short time between second pericentric passage and coalescence. The timescales between these events and magnitudes of SFR elevation are dependent on the merger parameters, which we discuss below.

For the merger analyzed here, the low SFR(SED) and sSFR(SED) values indicate that GOODS-S 43114 and GOODS-S 43683 are not observed during one of the merger phases corresponding to elevated star formation. Additionally, Figure 5.4 suggests that both galaxies had much higher SFRs in the past. The tidal tail features exhibited by both galaxies suggest that this system has undergone at least one pericentric passage, and that the merger is observed between the first and second pericentric passages. Using the simulations of Moreno et al. (2019) to interpret the distance between the nuclei of GOODS-S 43114 and GOODS-S 43683 (~18 kpc), we infer that it has either

been $\lesssim$0.5 Gyr or ~2-2.5 Gyr after the first pericentric passage

The elevated Hδ_A values and SFHs shown in Figure 5.4 for GOODS-S 43114 and GOODS-S 43683 suggest that both galaxies have recently shut off their star formation. The main sequence lifespan of O-, B- and A-type stars are ~0.01, ~0.1 and ~1 Gyr, respectively. A-type stars will dominate the stellar spectrum during their main sequence lifetime after the main sequence lifetimes of O- and B-type stars have passed. Figure 5.4 indicates that it is roughly $\lesssim$1 Gyr and slightly longer than 1 Gyr between the peak of star formation and epoch of observation for GOODS-S 43114 and GOODS-S 43683, respectively. For both galaxies, the time since peak star formation is longer than the O- and B-star lifetime, and corresponding to a phase when the light from A stars will contribute significantly to the rest-frame optical spectrum. The slightly shorter (longer) time since peak star formation for GOODS-S 43114 (GOODS-S 43683) corresponds to its larger (smaller) Hδ_A.

Combining all of the information gained from the SED fitting with inferences from the models indicates that these galaxies recently underwent their first pericentric passage and are moving away from each other. Detailed velocity mapping would be needed to confirm this theory, and such data currently do exist for this merger. van Dokkum & Brammer (2010) support this claim however, stating that rapid star formation of ~500 $M_\odot$ yr^{-1} could have been ongoing as recently as 150 Myr before observation. The SFH for GOODS-S 43114 in Figure 5.4 suggests that star formation levels of ~500 $M_\odot$ yr^{-1} were ongoing earlier (~500 Myr before observation). This difference in inferred timescale could be due to the SFH assumed: van Dokkum & Brammer (2010) assumed a truncated constant star formation history while a delayed-τ star formation history is assumed in the present analysis.

One important caveat to note is that the Moreno et al. (2019) study simulated mergers for local galaxies. Therefore, while the timescales between pericentric passages and the magnitude of the SFR spikes at these events may be different for the $z \sim 2$ universe, we assume that the basic pattern of galaxies having an elevation in SFR at each pericentric passage with a decrease in-between is still valid (see also, e.g., Cox et al., 2008; Hopkins et al., 2008). Additional caveats

are differences in other merger parameters relative to the Moreno et al. (2019) fiducial model. For example, different orientations and levels of gas content in the galaxies can affect the time between pericentric passages and the elevation in SFR. Fensch et al. (2017) show that mergers with 10% gas fractions characteristic of $z \sim 0$ galaxies undergo a larger increase in SFR compared to mergers of more gas-rich (60% gas fraction) systems characteristic of $z \sim 2$ galaxies. Along the same lines, Scudder et al. (2015) find an anti-correlation between SFR enhancement during the merger and the initial gas fraction. This dependence of SFR enhancement during the merger on gas content can be attributed to a correlation between ISM turbulence and central gas inflow during the merger. In the Fensch et al. (2017) models, both the local-analog gas-poor mergers and $z \sim 2$-analog gas-rich mergers display similar peak gas inflow rates that fuel star formation. The difference in SFR enhancement between the two scenarios is therefore due to the fact that the $z \sim 2$-analog gas-rich galaxies begin the merging process with much higher gas inflow rates.

5.4.2 Implications of the Apparent Mass Discrepancy

The large discrepancy between M_* and $M_{\rm dyn}$ for GOODS-S 43114, in particular with $M_{\rm dyn} < M_*$, raises concerns about the accuracy of these measurements. As stated in Section 5.2.3, our methodology for estimating M_* is robust. The SED is fit assuming a realistic delayed-τ SFH and we use 39 photometry points to constrain the shape of the SED. Additionally, our estimate of M_* agrees within uncertainties with past studies (van Dokkum & Brammer, 2010).

Therefore, it is likely that the $M_{\rm dyn}$ measurement is significantly underestimated. There is a straightforward explanation for how such an underestimate can arise. The axis ratio of the galaxy obtained from the best fit Sérsic model is 0.8651 ± 0.0038. In one plausible scenario, this large axis ratio would result if GOODS-S 43114 is a roughly face-on disk. In such a geometry, the estimate of the velocity dispersion (and subsequent $M_{\rm dyn}$ estimate) is biased low relative to the true value. A more physically-motivated virial coefficient that takes into account the geometry of the galaxy — as well as a correction for its inclination — would be needed to get an accurate dynamical mass. We defer such analysis (e.g., as in Price et al. 2020) to future work.

In other studies of the velocity dispersions and sizes of high-redshift quiescent galaxies, better consistency is obtained between dynamical and stellar masses. For example, van de Sande et al. (2013) find dynamical masses $\sim$ 15% larger than stellar masses for a sample of 5 massive ($\log_{10}(M_*/M_\odot) > 11$) $z \sim 2$ galaxies. Additional studies of high-redshift, massive, quiescent galaxies find that M_* and $M_{\rm dyn}$ are roughly consistent with each other (e.g., Belli et al. 2017; Tanaka et al. 2019; Esdaile et al. 2021). However, the majority of galaxies in these earlier works have structural properties consistent with a spheroidal geometry. In contrast, we infer a face-on disk morphology for GOODS-S 43114, and must take into account rotation (and inclination) as well as dispersion to obtain a robust dynamical mass estimate.

GOODS-S 43114 is not unique for appearing disk-like at $z \sim 2$. For example, Newman et al. (2018a,b) identify four fast-rotating ($v/\sigma \sim 2$), disk-dominated quiescent galaxies at $z \sim 2$ with comparable stellar masses to those presented here (see also Toft et al., 2012, 2017). Newman et al. and Toft et al. argue that merger interactions will cause these massive galaxies evolve into the slow rotating elliptical galaxies observed locally, given their already-extreme masses.

GOODS-S 43114 is undergoing a major merger interaction with GOODS-S 43683, which will likely have a significant impact on its structural properties. Its subsequent star-formation history to the present day will depend on the details of the merger interaction with GOODS-S 43683 as well as the cool gas content in both galaxies. Accordingly, both GOODS-S 43114 and GOODS-S 43683 comprise compelling targets for observations of molecular gas (e.g., CO), in order to understand the fuel available for subsequent star formation.

5.5 Summary

In this study we analyze high-quality Keck/MOSFIRE spectra and multi-wavelength photometry of a merger at $z = 1.89$ between two galaxies that host AGN: GOODS-S 43114 and GOODS-S 43683. Stellar Balmer absorption lines (Hγ and Hδ) fall into the MOSFIRE J-band of GOODS-S 43114. Combining the high S/N spectra and broadband SED-fitting with insights from realistic

galaxy merger simulations enables us to obtain and study the physical properties and SFHs of both galaxies in the merger pair as well as the current phase of the merger process.

The main results are as follows:

1. Both merging galaxies have similar order of magnitude M_*, indicating that this is a major merger. In addition, both galaxies have recently shut off their star formation as shown by their low SFR(SED) and elevated Hδ_A values.

2. The depressed star formation rates combined with the visible tidal tails imply that the galaxies have undergone their first pericentric passage. Modeling the SFHs suggests that the pericentric passage most likely happened less than 1 Gyr ago (approximately around the time of peak star formation of the system), indicating that the galaxies are moving apart from each other.

3. GOODS-S 43114 is likely a face-on disk based on its morphology and smaller than expected velocity dispersion estimate. A more sophisticated dynamical modeling approach incorporating rotation and the inclination of the galaxy will be needed to obtain a reliable dynamical mass estimate. Galaxies that are massive ($\log_{10}(M_*/M_\odot) > 11$), disk-shaped, rotating, and quiescent at $z \sim 2$ are likely the progenitors of the most massive, spheroidal and slow-rotating elliptical galaxies present in the local universe. However, they must undergo significant structural evolution over the intervening $\sim$ 10 Gyr.

Understanding the rapid onset and shut-down of star formation during mergers, especially at $z \sim 2$ (i.e., the peak epoch of star formation), is important for furthering our knowledge of how mergers affect the galactic baryon cycle. Comprehensive studies of individual mergers like the GOODS-S 43114/GOODS-S 43683 system can help further constrain simulations leading to a more accurate galaxy evolution models. For the merger pair analyzed in this work, space-based observations with the James Webb Space Telescope will enable us to observe the full range of rest-optical emission-lines (e.g., Hα, Hβ, [O III]$\lambda\lambda$4960,5008, and [O II]$\lambda\lambda$3727,3730) that are currently

hidden outside the windows of atmospheric transmission. Measurement of these emission-lines will greatly increase our knowledge of the merger, as they contain a wealth of information on AGN activity and gas outflows, as well as the physical properties of the ionized ISM.

CHAPTER 6

Herschel/PACS OH Spectroscopy of Seyfert, LINER, and Starburst Galaxies

6.1 Introduction

The different modes of feedback from active galactic nuclei (AGNs) are thought to play a vital role in the evolution of massive galaxies (Somerville & Davé, 2015), by quenching star formation and the growth of supermassive black holes in their host galaxy (Di Matteo et al., 2005).

Molecular gas is a direct probe of AGN driven outflows (Spoon et al., 2013), which could be capable of displacing a large fraction of the molecular interstellar medium of the host galaxy (Sturm et al., 2011; Veilleux et al., 2013). Among the different molecules that have been used to trace outflows (CO in Feruglio et al. 2010; OH in Fischer et al. 2010; Sturm et al. 2011, HCN, HCO^+, and HNC in Aalto et al. 2012), OH is considered one of the best diagnostic tools due to its large dipole moment (1.67 Debye) and thus its fast radiative rates. The critical densities of the OH transitions are high ($\sim 10^9 cm^{-3}$), which makes them sensitive to radiative pumping (Spoon et al., 2013). There are 14 OH transitions between 34μm and 163μm that arise from the eight lowest energy rotational levels. Those relevant for this study are shown on the OH Grotrian diagram in Figure 6.1. The number of infrared (IR) lines available is another value of OH, as it can probe a broad set of conditions in the molecular gas (Spoon et al., 2013).

The OH doublets can vary widely in their properties. Galaxies have been observed with these

OH doublets primarily in emission (Spinoglio et al., 2005), primarily in absorption (Kegel et al., 1999; González-Alfonso et al., 2004), a combination of the two (Bradford et al., 1999; González-Alfonso et al., 2008), and even P-Cygni features (Fischer et al., 2010). P-Cygni profiles indicate unambiguously the presence of molecular gas outflows.

Dedicated radiative transfer modeling including several OH and H_2O transitions have been performed for a few individual galaxies (e.g., Arp 220 and Mrk 231; González-Alfonso et al. 2004, 2008). These studies have utilized data from the *Infrared Space Observatory* Long Wave Spectrometer (*ISO*/LWS; Clegg et al. 1996; Kessler et al. 1996) and the Photoconductor Array Camera and Spectrometer (PACS; Poglitsch et al. 2010) instrument on the *Herschel Space Observatory* (Pilbratt et al., 2010). The capabilities of the *Herschel*/PACS instrument have led to many studies using the OH line profiles to look for molecular outflow signatures (e.g., Falstad et al. 2015; Fischer et al. 2010; González-Alfonso et al. 2012, 2014, 2015, 2017b; Stone et al. 2016; Sturm et al. 2011; Veilleux et al. 2013).

Some relationships between far-IR OH molecular line properties and host galaxy properties have already been found. Many of these studies have primarily focused on the 119μm OH doublet. This transition has been found to display stronger emission in more luminous AGNs (Veilleux et al., 2013; Stone et al., 2016). More luminous AGNs also tend to have higher terminal outflow velocities for the 79μm (Sturm et al., 2011) and 119μm (Veilleux et al., 2013) OH doublets. Dust has been shown to influence the 119μm OH doublet as well. Using the 9.7μm silicate feature as a tracer for the dust content of the galaxy, Veilleux et al. (2013) and Stone et al. (2016) show that stronger 119μm OH doublet emission is correlated with the 9.7μm silicate feature in either weak absorption or emission, which indicates less dust. A dusty galaxy corresponds to a weak emission or absorption feature for the 119μm OH doublet. The 65μm OH doublet is also shown to show stronger absorption with increasing 9.7μm silicate absorption (González-Alfonso et al., 2015).

The main objective of this paper is to present a large sample of 178 local galaxies, and quantify the emission or absorption of six OH doublets in the far-IR range – 65μm, 71μm, 79μm, 84μm,

119μm, and 163μm – by measuring the equivalent width (EW) of the transitions. We chose to use the EW to quantify the transitions in the sample because the EW measures the relative strength of the OH doublet relative to the continuum emission. There are also nine galaxies in the sample with 53.3μm observations and four with 98.7μm observations; however, due to the combination of a lack of statistics and a lack of resolution to separate the peaks, in particular for the 99μm doublet, we do not include them in this study. We will use our large sample to look for statistical trends in the data, and investigate possible correlations between EW(OH) and host galaxy properties similar to the studies discussed above. However, in our study, we will investigate a more expansive range of galaxy properties and higher number of OH transitions to gain a more complete understanding of OH properties in galaxies. We also span a wide variety of galaxy spectral types, with the goal of obtaining a more complete understanding of the OH spectra. Since we still do not have a full theoretical understanding of the observed OH spectra, here we take an empirical approach to uncover which other observed properties of galaxies may predict the conditions in their molecular gas.

This paper is organized as follows. Section 6.2 describes the sample selection, the observations, the data reduction, and ancillary data collected. Section 6.3 describes the data analysis and the quantities derived from the data. Section 6.4 provides a discussion of the results. Section 6.5 provides a summary of the paper. Finally, the Appendix provides data tables for the sample and statistical information for fits discussed in Section 6.3.

6.2 Observations

This paper investigates six of the 14 OH transitions in the far-IR range: 65μm, 71μm, 79μm, 84μm, 119μm, and 163μm. These six are selected because they lie in the wavelength range covered by PACS and have the best chance of being detected. Hereafter, we refer to these transitions as OH65, OH71, OH79, OH84, OH119, and OH163. All of these transitions are doublets. Table 6.1 shows details of the transitions for these doublets, and Figure 6.1 provides the OH Grotrian diagram. In

Table 6.1: Fine Structure Transitions

Line	Energy Levels	Wavelength (μm)	$\Delta E_{ul}/k$ (K)	A_{ul} (s^{-1})
(1)	(2)	(3)	(4)	(5)
OH65	$^2\Pi_{3/2}$(J = 9/2) $\longleftrightarrow$ $^2\Pi_{3/2}$(J = 7/2)	65.132, 65.279	512.1, 510.9	1.276, 1.267
OH71	$^2\Pi_{1/2}$(J = 7/2) $\longleftrightarrow$ $^2\Pi_{1/2}$(J = 5/2)	71.171, 71.215	617.6, 617.9	1.014, 1.012
OH79	$^2\Pi_{1/2}$(J = 1/2) $\longleftrightarrow$ $^2\Pi_{3/2}$(J = 3/2)	79.116, 79.179	181.9, 181.7	0.03606, 0.03598
OH84	$^2\Pi_{3/2}$(J = 7/2) $\longleftrightarrow$ $^2\Pi_{3/2}$(J = 5/2)	84.420, 84.596	291.2, 290.5	0.5235, 0.5202
OH119	$^2\Pi_{3/2}$(J = 5/2) $\longleftrightarrow$ $^2\Pi_{3/2}$(J = 3/2)	119.234, 119.441	120.7, 120.5	0.1388, 0.1380
OH163	$^2\Pi_{1/2}$(J = 3/2) $\longleftrightarrow$ $^2\Pi_{1/2}$(J = 1/2)	163.015, 163.396	270.2, 269.8	0.06483, 0.06450

Note. — Col. (1): Name of OH doublet. Col. (2): Energy transition for each doublet. Col. (3): Wavelength for both transitions in the doublet. Col. (4): Energy of the upper level for each transition. Col. (5): Einstein A coefficient for each transition. This data is from the LAMBDA database (Schöier et al., 2005).

the next section, we describe the OH measurements obtained from Herschel spectra and additional ancillary measurements of those galaxies, which may be correlated with EW(OH).

6.2.1 *Herschel*/PACS

A sample of 178 local ($z < 0.35$) galaxies were selected from the *Herschel Science Archive*, which were observed with the PACS instrument (Poglitsch et al., 2010) on the *Herschel Space Observatory* (Pilbratt et al., 2010). PACS used an integral field spectrograph with a 5×5 square spaxel detector, which covers a field of view of 47" $\times$ 47". The spectral resolution is wavelength-dependent, with a range of $R = 1000 - 4000$ ($\Delta v = 75 - 300$ km s^{-1}). PACS spans a wavelength range of $51 - 206\mu$m.

To obtain the largest sample for statistical analysis, we follow a similar selection procedure as

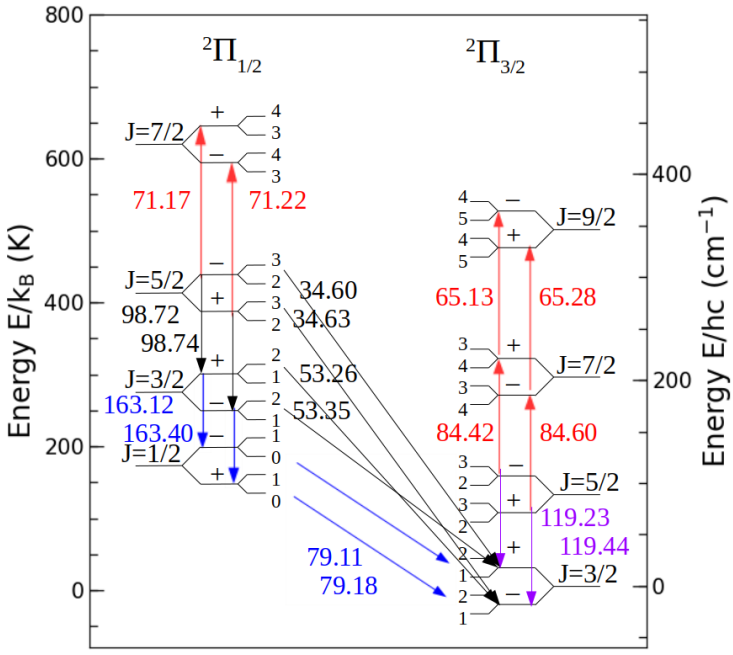

Figure 6.1: OH rotational Grotrian diagram showing the transitions discussed in this paper. Each rotational level is split into two sublevels due to Λ doubling and each sublevel is split again due to the hyperfine structure. The rotational ladder has two branches due to spin splitting (Λ + s, Λ − s) where Λ = 1 and s = 1/2. The integer next to the hyperfine branches of each energy level is the total angular-momentum quantum number, F. The red, blue, purple, and black numbers are the wavelength of the transition in units of μm. Red indicates that the doublet was seen primarily in absorption, blue indicates primarily emission, purple indicates that neither emission or absorption was strongly favored, and black indicates transitions not analyzed in this study but are mentioned in Section 6.4.

that described in Fernández-Ontiveros et al. (2016). In Fernández-Ontiveros et al. (2016), 170 AGN with available mid-IR spectra from *Spitzer*/IRS (Houck et al., 2004; Werner et al., 2004) and far-IR fine structure lines from *Herschel*/PACS were selected from the *Herschel Science Archive*. A comparison sample of 20 starburst galaxies were also selected. In this study, the sample of AGN (163 galaxies) and starbursts (15 galaxies) is slightly smaller. We do not include galaxies from Fernández-Ontiveros et al. (2016) in our sample that do not have observations for at least one of the six OH doublets that we analyze in this paper. However, there are 14 AGN added to this sample that are not in Fernández-Ontiveros et al. (2016) because their selection was based on the detection of fine-structure lines, instead of the OH doublets. Therefore, the samples in this study

and Fernández-Ontiveros et al. (2016) have significant overlap, with only minor differences based on the specific focus of the paper.

The observations originated from many different Herschel proposals. Each project had its own criteria for selecting galaxies, and here are a few of the main reasons why galaxies were targeted:

- Many observed galaxies are very bright, especially in the IR. These objects are ultraluminous infrared galaxies (ULIRGs). The 60μm flux was often chosen for these flux-limited samples. This favors dusty galaxies with high obscuration, included obscured AGN. There were a variety of proposals that targeted these objects (e.g., KPOT_pvanderw_1, OT1_dfarrah_1, OT2_jgracia_1, OT2_larmus_2).

- Previously well-studied galaxies were selected. For example, galaxies were selected from previous surveys (e.g., *Spitzer* Infrared Nearby Galaxy Survey (SINGS; Kennicutt et al. 2003) and Burst Alert Telescope (BAT; Barthelmy et al. 2005)).

- Galaxies were targeted based on their optical spectroscopic classification. This includes Seyferts and starburst galaxies (see Fernández-Ontiveros et al. 2016 and references therein).

Because there is a large variety in the sample selection process for choosing galaxies, we believe that our final sample of 178 galaxies does not have a strong bias towards any particular subset of galaxies. However, there are two exceptions: there are no dwarf galaxies in our sample and galaxies known to be particularly luminous in the far-IR received somewhat more attention. Therefore, the results found in this paper can be considered reflective of how the entire population of low-redshift, non-dwarf, IR-luminous galaxies behave.

Table 6A.1 in Appendix 6A contains the optical spectral type of every galaxy in the sample, which were obtained from the Véron-Cetty & Véron (2010) catalog. Note that while some galaxies have multiple AGN classifications in the catalog, we only include the first one listed. Seyfert types-1, -1.2, -1.5, and -1.8 have both broad Hα and broad Hβ components. To distinguish between them, the

Véron-Cetty & Véron (2010) Catalog used a quantitative method based on the ratio of the Hβ and [O III]λ5007 line fluxes introduced by Winkler (1992). Seyfert-1.9's have a broad Hα component visible but not broad Hβ, and Seyfert-2's have neither broad components (Osterbrock, 1977, 1981). Seyfert-1n are narrow lined Seyfert-1's, which have optical emission spectra similar to Seyfert-1's but have narrower Balmer lines (Osterbrock & Pogge, 1985; Goodrich, 1989). Seyfert-1h's have broad Balmer lines that are only detected in polarized light, indicating that there is a hidden broad-line-region that is completely obscured (Antonucci & Miller, 1985; Miller & Goodrich, 1990; Tran et al., 1992). Seyfert-1i's have a highly reddened broad-line-region which is revealed by a broad Pa β line in the spectra (Goodrich et al., 1994). Low Ionization Nuclear Emission-line Regions (LINERs) have an optical spectrum dominated by low ionization emission lines, which have widths similar to the narrow-line-region of Seyfert galaxies but at a much lower luminosity (Heckman, 1980). If broad Balmer lines are observed, the galaxy is classified as a LINERb (Véron-Cetty & Véron, 2010).

The raw spectra were reduced by Fernández-Ontiveros et al. (2016) using a custom pipeline which is based on standard procedures from HIPE[1] (v13.0.0; Ott 2010), and includes outlier flagging, spectral flat-fielding, regrid of the wavelength sampling, and flux calibration. Following the standard procedure, most of the sources were observed with the chop-node mode and reduced with the background normalization method, using the off-source spectra to perform the background subtraction and also to correct for the spectral response. For more on the data reduction, see Fernández-Ontiveros et al. (2016). A final standard rebinned data cube was produced for each object in the sample.

Table 6A.1 in Appendix 6A contains observational information about the spectra in the sample, including which OH transitions were observed for each galaxy with PACS. Note that not every galaxy in the sample has observations for all six OH doublets discussed in this paper. The transitions with

[1]HIPE is a joint development by the *Herschel* Science Ground Segment Consortium, consisting of ESA, the NASA *Herschel* Science Center, and the HIFI, PACS and SPIRE consortia.

the most observations, which provide the largest statistical samples, are OH79, OH119, and OH163. Figure 6.2 provides a few example spectra from the sample showing the wide variety of OH line profiles observed, and includes absorption, emission, and P-Cygni features.

6.2.2 Galaxy Brightness & IR Line Ratios

To probe the AGN luminosity and strength of the radiation field, we obtain the following luminosities: the intrinsic hard X-ray (2-10 keV) luminosity ($L_{2-10\mathrm{keV}}$), the [O IV] 25.89μm line luminosity ($L_{[\mathrm{O\ IV}]25.89\mu\mathrm{m}}$), and the luminosities of the [Ne V] 14.32μm and 24.32μm emission lines ($L_{[\mathrm{Ne\ V}]14.32\mu\mathrm{m}}$ and $L_{[\mathrm{Ne\ V}]24.32\mu\mathrm{m}}$); and the following IR emission-line ratios: [Ne V] 24.32μm/[Ne II] 12.81μm, [Ne V] 14.32μm/[Ne II] 12.81μm, [Ne III] 15.56μm/[Ne II] 12.81μm, [O IV] 25.89μm/[Ne II] 12.81μm, and [O IV] 25.89μm/[O III] 88.36μm. All of these data were gathered by us in Fernández-Ontiveros et al. (2016). We use redshift-independent distances (see references within Fernández-Ontiveros et al. 2016) whenever possible to convert the [O IV] 25.89μm, [Ne V] 24.32μm, and [Ne V] 14.32μm emission-line fluxes and uncertainties to luminosities. For the rest of the sample, we assume a standard cosmology (H_0 = 70 km s^{-1}, Ω_λ = 0.7, Ω_m = 0.3) to calculate luminosity distances when converting from flux to luminosity.

The highly ionized IR lines ([O IV] 25.89μm, [Ne V] 14.32μm, [Ne V] 24.32μm, and [Ne III] 15.56μm) serve as a tracer of the harder radiation field produced by the AGN. The luminosities of these lines, as well as the intrinsic hard X-rays, probe the strength of the AGN. Comparing the fluxes of these highly ionized lines with the fluxes of lines with lower ionization potential ([Ne II] 12.81μm, [O III] 88.36μm) traces the relative contribution of an AGN compared to an H II or starburst region. Therefore, we expect this ratios will be higher for galaxies with a bright AGNs compared with non-active galaxies (see e.g., Tommasin et al. 2008, 2010).

The X-ray data for $L_{2-10\mathrm{keV}}$ come from a variety of telescopes. Chandra and XMM-Newton were the primary telescopes used, but observations from Suzaku, *Swift*/BAT, ASCA and more were also used. While the observations were not limited to the nuclear region of the galaxies, we assume that

the integrated 2-10 keV flux comes only from this central region because it is too energetic for the star formation in the galaxy to produce in significant amounts.

The [O III] 88.36μm flux is taken from the central spaxel (9.4"×9.4") of the *Herschel*/PACS spectra. EW(OH) for our sample is also measured using only the central spaxel of the *Herschel*/PACS spectra (see Section 6.3.1 for a complete description of how EW(OH) was measured). All of the other IR emission-lines were observed using the high-resolution module of *Spitzer*/IRS. [Ne II] 12.81μm, [Ne V] 14.32μm, and [Ne III] 15.56μm were observed using the short-wavelength arm (4.7" × 11.3"). [Ne V] 24.32μm and [O IV] 25.89μm were observed using the long-wavelength arm (11.1" × 22.3"). For the median redshift in our sample, 0.0164, the spatial sizes for the central spaxel of *Herschel*/PACS, the short-wavelength *Spitzer*/IRS arm, and the long-wavelength *Spitzer*/IRS arm are 3.23×3.23 kpc^2, 1.62×3.89 kpc^2, and 3.82×7.67 kpc^2, respectively.

We assume that the flux for the high-ionization emission-lines ([Ne V] 14.32μm, [Ne III] 15.56μm, [Ne V] 24.32μm, and [O IV] 25.89μm) is primarily from the nucleus rather than star formation. Both the short- and long-wavelength arms of *Spitzer*/IRS capture the entirety of the nucleus, so for these lines it should not matter which arm the fluxes were observed with. Based on the spatial sizes of the *Herschel*/PACS and *Spitzer*/IRS data, we can capture more of the star formation in the galaxy with [O III] 88.36μm compared to [Ne II] 12.81μm. However, both spectra focus on the nucleus and surrounding region of the galaxy and the areas are similar, so the two emission-lines should function as comparable tracers of star formation.

6.2.3 IRAS

To obtain information about the thermal dust continuum emission for each galaxy in the sample, archival data observed by the *Infrared Astronomical Satellite* (IRAS) were obtained in two bandpasses: $19 - 30\mu$m and $40 - 80\mu$m (corresponding to central wavelengths of 25μm and 60μm). Those two bandpasses have an average 10-σ sensitivity of 0.65 Jy and 0.85 Jy respectively.

The ratio of the 25μm and 60μm flux densities, $f_{25\mu\mathrm{m}}$ and $f_{60\mu\mathrm{m}}$ respectively, are used to estimate

the thermal dust continuum emission and act as an IR tracer for AGN strength. The majority of the 25μm flux is from warm dust surrounding the AGN, while the 60μm flux is primarily from cooler dust associated to star formation. Therefore, a stronger AGN that is more “dominant" than the host galaxy should have a larger 25μm/60μm flux density ratio (hereafter referred to as “dust temperature"), since the AGN-heated dust is hotter than that of normal spirals. The ratio for a weak AGN or a non-active galaxy should be much smaller, because the bulk of the IR continuum comes from cooler dust in the host galaxy disk (e.g., Edelson & Malkan 1986; Veilleux et al. 2009; Lee et al. 2011).

The preferred IRAS catalog to use is the Point Source Catalog (PSC) v2.1 (Helou & Walker, 1988). For galaxies that are not in that catalog, data are gathered from other IRAS catalogs: PSC v2.0 (Joint Iras Science, 1994), the Faint Source Catalog (FSC) v2.0 (Moshir et al., 1990), and the Faint Source Reject Catalog (FSRC; Moshir et al. 1992) and other publications (Golombek et al., 1988). It is important to note that for galaxies with large angular sizes, these catalogs can sometimes exclude the outer parts of the disk. Because we are focused on the infrared colors of the nuclear region of these galaxies, this limitation of the catalogs is not a concern in this study. Six galaxies in the sample had no available IRAS data, therefore, data were collected for 172 of the 178 galaxies. The flux density, uncertainty, and corresponding catalog for each object is indicated in Table 6A.2 in Appendix 6A. Some of the data were marked as upper limit measurements in the catalogs. These measurements are identified with a “<" and no uncertainty is reported.

When using dust temperature, there are two main caveats that need to be addressed. First, dwarf galaxies often have high dust temperatures (e.g., Walter et al. 2007). Second, galaxies with extreme dust opacities (e.g., Arp 220 Rangwala et al. 2011) could show lower IRAS $f_{25\mu\mathrm{m}}/f_{60\mu\mathrm{m}}$ values, even if an AGN is present. As previously discussed in Section 6.2.1, our sample does not contain any dwarf galaxies and, while slightly favoring IR-luminous galaxies, is very diverse. Therefore, we are not concerned with the bias of dwarf galaxies, and do not expect galaxies with extreme dust opacities to significantly affect our findings.

6.2.4 Obscuration Tracers

Because we expect that the warm molecular gas traced by the OH doublets should be associated with dusty embedded regions, we include in our study the observations for the following dust absorption tracers: the 9.7μm silicate line and the Balmer decrement. The observations for the silicate, Hα, and Hβ lines come from a variety of sources in the literature. The 9.7μm silicate line was always measured using the low-resolution module of *Spitzer*/IRS with an aperture of ~3.6", while the optical Balmer lines come from a variety of sources, most of which are ground-based slit spectroscopy (typically ~1" and limited by seeing).

The strength of the silicate feature is quantified using the method derived by Spoon et al. (2007):

$$S_{\rm sil} = \ln \frac{f_{\rm obs}(9.7\mu{\rm m})}{f_{\rm cont}(9.7\mu{\rm m})} \tag{6.1}$$

Where $f_{\rm obs}$ is the observed flux density of the 9.7μm silicate line and $f_{\rm cont}$ is the continuum flux density at 9.7μm. $S_{\rm sil}$ can be interpreted as an estimate of the optical depth for silicate absorption features.

Table 6A.3 in Appendix 6A gives the strength of the silicate absorption feature, the Balmer fluxes, and the sources that these measurements come from. There is some overlap between our sample and those from Spoon et al. (2013), Veilleux et al. (2013), and Stone et al. (2016) (OH119) and González-Alfonso et al. (2015) (OH65), which find correlations between the silicate feature and these doublets. We will test if this relationship exists with our sample for OH65 and OH119, and if the other OH doublets follow a similar trend.

6.3 Analysis & Results

In this section, we first describe how we obtained our EW measurements from the archival PACS datacubes. Then, to uncover which observed galaxy properties may predict emission/absorption for the OH doublets in our sample, we investigate possible correlations between these EW values and

galaxy observables such as AGN luminosity, radiation field hardness, dust temperature traced by the IRAS $f_{25\mu m}/f_{60\mu m}$ ratio, and dust extinction. A positive EW value indicates that the transition is in emission while a negative value indicates absorption.

6.3.1 Measuring EW

From the reduced data cubes, spectra from the central spaxel (9.4" × 9.4" or 3.23 × 3.23 kpc^2 at the median redshift of our sample, 0.0164) were extracted. Focusing on the central spaxel will magnify the effects of a possible AGN component on the OH transitions. We used Python scripts developed by us in Fernández-Ontiveros et al. (2016) to measure the flux, estimate the continuum level for each OH transition, and obtain the EWs. The continuum was estimated using a 1-D polynomial fit to the spectral channels located in the red and blue wings next to the OH line. The integrated flux values with uncertainties are shown in Table 6A.4 in Appendix 6A.

We do see complex kinematics of the OH gas for some of the galaxies in the sample. Typical cases include the doublets that display P-Cygni profiles, which have both positive and negative components (see Figure 6.2). Other line profiles have prominent broad wings, which could be signatures of outflows. Also, some measurements are blended with weak neighboring spectral lines. The only case that the numerical integration method gives an unreliable EW measurement is with P-Cygni features, therefore, we remove these observations when looking for for correlations between EW(OH) and galaxy observables. We only observe P-Cygni profiles in a minority of galaxies (see Section 6.3.2.5 below for more details), so this does not notably reduce our sample size.

The EW and the uncertainty of these OH transitions are derived, and Table 6A.5 in Appendix 6A shows the EW measurements with uncertainties for each object. For some galaxies, only the continuum was detected, with no OH emission or absorption above or below the noise level, respectively. In this case, the continuum flux density (C) was used to estimate an upper limit for the EW as $3\sigma/C$. σ corresponds to the RMS of the continuum emission along the spectral range

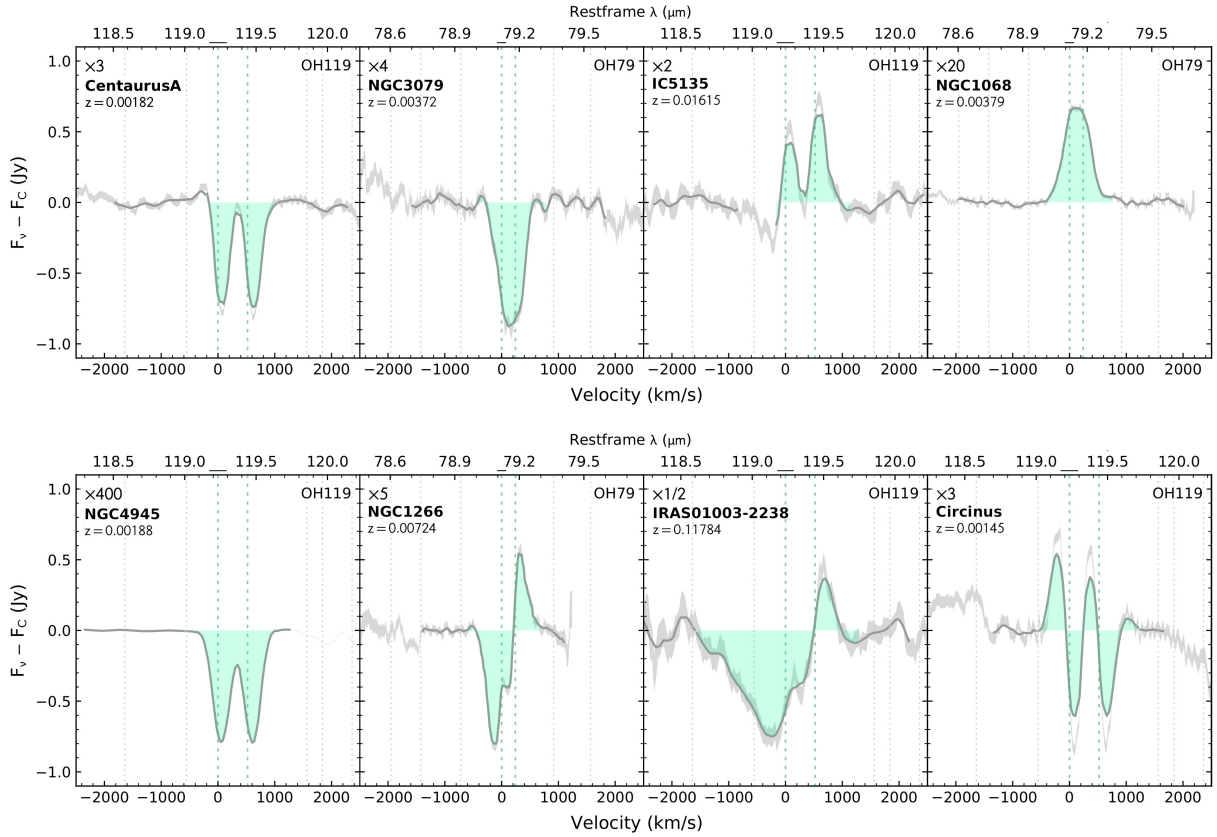

Figure 6.2: Examples of the variety of spectra observed with PACS. These spectra are the central spaxel of the observations of the 5×5 array. From left to right: Top: doublet absorption (Centaurus A: Seyfert-2); absorption where the doublet is blended into one line (NGC 3079: LINER); doublet emission (IC 5135: Seyfert-1.9); emission where the doublet is blended into one line (NGC 1068: Seyfert-1h). Bottom: doublet absorption (NGC 4945: Seyfert-2); P-Cygni profile with the emission and absorption components approximately equal in strength (NGC 1266: LINER); P-Cygni profile with a stronger absorption component than emission (IRAS 01003-2238: Seyfert-2); reverse P-Cygni profile with emission and absorption components approximately equal in strength (Circinus: Seyfert-1h). The top axis is the restframe wavelength, the bottom axis the velocity centered in the middle of the OH doublet, and the y-axis is the difference between the flux of the OH doublet and the flux of the continuum, normalized by the factor indicated in the upper-left corner of each panel. The gray line is the data. The green shaded region is the integrated line flux used to estimate the EW of the transition. The velocities are given relative to the blue peak of the doublet, that is v = 0 km/s coincides with the left peak of the doublet when no redshift or blueshift are detected. The two vertical dashed lines show the galaxy rest wavelength of the doublet.

observed. The upper limit EW(OH) measurements are identified with a "<" in Table 6A.5 in Appendix 6A.

6.3.1.1 Caveat on EW(OH) Emission & Absorption

In this paper, we focus on the study of the most fundamental observed properties of OH spectra in galaxies. The first most basic measurement is whether an OH doublet is mostly in emission or absorption (i.e. is the sign of EW(OH) positive or negative). This simple observable is expected to indicate the importance of a) excitation of higher energy levels in the OH molecules versus b) higher column densities of molecules in their lower energy states. Galaxies in which a) is more important should show more OH emission lines, whereas those in which b) is more important should show stronger absorption.

Once the sign of the EW(OH) is measured, the second most important quantity is its strength. We therefore search for statistical trends in the sign and strength of EW(OH) with other galaxy properties, which correlate with molecular excitation or optical depth. We now consider both of these correlations in turn.

Even though absorption and emission of a spectral line have different physical origins, we intentionally include the two different types of OH line profiles in the same analysis when looking for trends in the sample. This is because our goal is to find global trends with observables that could affect EW(OH) (e.g., total luminosity, hardness of the radiation field, and extinction) that all galaxies in the local universe follow, including if EW(OH) changes from tending to be in emission to absorption (or vice versa).

6.3.2 Comments on the Sample

In this section, we identify some trends observed for EW(OH) in the sample data. As noted in Section 6.3.1, the EW(OH) values can be found in Table 6A.5 in Appendix 6A.

6.3.2.1 Doublets Favoring Absorption

While it has only ten detections, OH65 is found almost exclusively in absorption, with only one detection (10% of the sample) showing emission. The galaxy with EW(OH65) emission is NGC 2146, which is a non-active galaxy, but is a bright LIRG. For OH71, all five detections are seen in absorption. This could be due to the fact that these transitions originate at the highest energies (the lower energy levels of both transitions are between 300-400 K) on the OH Grotrian diagram.

Although not to the same degree as the OH65 and OH71 doublets, OH84 is also primarily seen in absorption (85% of detections). The two galaxies seen in emission are ESO 103-G35 and NGC 1068, which are both optically classified as Sefyert-2 galaxies.

6.3.2.2 OH163 in Emission

One important finding is that OH163 is always detected in emission (25 galaxies). No other OH doublet in this study is found exclusively in emission. OH79 strongly favors emission (89% of detections), but unlike OH163, it can also be found in absorption.

6.3.2.3 OH119

OH119 is the most diverse doublet in the sample, showing the largest variety in profiles, and unlike the other doublets discussed previously, the number of galaxies seen in emission and absorption is approximately equal. When we investigate possible correlations between EW(OH) and various galaxy observables in the rest of this study, the OH119 doublet is the most discussed transition from the sample because it has the highest number of detections, which makes the results the most statistically significant.

6.3.2.4 Relative EW Strengths between Transitions

Not including upper limits, for the doublets that are found primarily in absorption − OH65, OH71, and OH84 − OH65 and OH71 have the weakest detected EW values (strongest EW absorption =

-0.028μm and -0.017μm respectively) with OH84 (strongest EW absorption = -0.056μm) being two or three times stronger. For galaxies with measurements of both OH65 and OH84, the EW of the latter is also about twice as large. However, this is based only on 7 galaxies that have detections for both doublets. These relative strengths of the observed OH doublets could be explained by the OH Grotrian diagram shown in Figure 6.1. OH65 and OH71 are the highest energy transitions in the sample, making it harder for the lower levels to be populated. OH84 is the level immediately below OH65, so OH84 could be stronger because the lower energy level corresponds to a lower excitation temperature and therefore is easier to populate than OH65 and OH71.

OH119, which is observed in both emission and absorption with regularity, has maximum absorption and emission values of -0.163μm and 0.103μm respectively. This maximum absorption for OH119 is about an order of magnitude stronger than OH65 and OH71, and about twice as strong as OH84. For OH79, which favors emission, the maximum absorption is very weak (-0.027μm) and is about even strength with OH65 and OH71. The emission for OH79 is much stronger (max EW emission = 0.242μm), which is about twice as strong as OH119. OH163, which is only seen in emission, has comparable emission strength to that of OH119.

6.3.2.5 P-Cygni Features

Some of our galaxies contain one or more OH transitions with a P-Cygni profile, a clear indication that the galaxy has a molecular outflow moving out from the AGN component. The P-Cygni features are identified by eye, and it was found that 19 galaxies in the sample show P-Cygni features in one or more OH transitions. Out of these 19 galaxies, five (IRAS 01003-2238, IRAS 17208-0014, IRAS 23365+3604, Mrk 273, and NGC 6240) have two OH transitions that show a P-Cygni feature and one (Mrk 231) contains three transitions that display it. Many of these P-Cygni features have been published in previous studies, with about half of them having been identified in Veilleux et al. (2013). Table 6.2 shows which OH transitions for which galaxies display a P-Cygni feature. Table 6.3 shows the percentage of observations that show a P-Cygni feature for each OH transition.

Table 6.2: List of Objects Showing P-Cygni Features

Object Name	OH Transitions with P-Cygni Feature (μm)
(1)	(2)
Circinus	119*
IRAS 01003-2238	79, 119
IRAS 05189-2524	119
IRAS 12071-0444	119
IRAS 13120-5453	79
IRAS 14394+5332	119
IRAS 15462-0450	119
IRAS 17208-0014	79
IRAS 19254-7245	119
IRAS 23365+3604	79, 119
Mrk 231	71, 79, 119
Mrk 273	79, 119
Mrk 848B	79
NGC 253	79
NGC 1266	79
NGC 3079	119
NGC 5728	119
NGC 6240	84, 119
NGC 7674	79

Note. — Col. (1): Name of the object. Col. (2): OH transitions that show a P-Cygni feature for the object. Note that a * indicates that it is a reverse P-Cygni feature.

Table 6.3: Percent of P-Cygni Features Found for each OH Transition

OH Transition (μm) (1)	Number of P-Cygni Features Observed (2)	Percent that show a P-Cygni Feature (3)
65	0 out of 23	0%
71	1 out of 13	7.7%
79	10 out of 152	6.6%
84	1 out of 20	5.0%
119	13 out of 86	15.1%
163	0 out of 29	0%

Note. — Col. (1): OH transition. Col. (2): Number of galaxies with P-Cygni features observed. Col. (3): Percent of observations that displayed a P-Cygni or reverse P-Cygni feature.

The two tables show that OH79 and OH119 have the highest number of P-Cygni observations as well as the highest percentage. We find one P-Cygni feature in the OH71 and OH84 doublets (Mrk 231 and NGC 6240 respectively). OH65 and OH163 do not show any P-Cygni features.

Circinus is a unique galaxy in our sample, because it is the only one to show a reverse P-Cygni profile in the nuclear spectrum. A reverse P-Cygni profile indicates that there is an inflow instead of an outflow of molecular gas.

We note that González-Alfonso et al. (2017b) identifies the PACS observation for OH84 in IRAS 23365+3604 as a P-Cygni feature, but we do not. The key reason for this difference is that González-

Alfonso et al. (2017b) uses a 3×3 spaxel area for their spectra, while we only use the central spaxel. This means that if the P-Cygni feature is tracing a molecular outflow in the galaxy, it has left the central region of the galaxy.

As discussed above in Section 6.3.1, the EW measurements for P-Cygni features are unreliable. Therefore, we will not include the P-Cygni lines reported in Table 6.2 in the rest of this section when we investigate correlations between EW(OH) and galaxy observables.

6.3.3 EW(OH) vs. AGN Luminosity and Radiation Field Hardness

The far-IR continuum is typically dominated by thermal emission from dust grains, which can be heated either by absorbing UV/optical emission from young stars or an AGN. In this paper, we use several observables to quantify the relative importance of star formation and non-stellar nuclear activity. Both the column density and temperature of the dust may differ depending on the strength of these mechanisms in the central region of the host galaxy. We now investigate which of the observables introduced in Sections 6.2.2, 6.2.3, and 6.2.4 may correlate with EW(OH). A positive correlation mainly tells us that increasing a physical parameter makes the corresponding OH doublet more likely to appear in emission.

For the rest of Section 6.3, we use the following guidelines when investigating possible correlations between EW(OH) and the galaxy observables. We only consider detections for both EW(OH) and the host galaxy properties we look to correlate EW(OH) with. Upper limit observations are excluded when looking for trends between EW(OH) and these observables so that the limits do not hide any correlations. Also, a minimum threshold of 8 galaxies is adopted when looking for correlations between EW(OH) and the galaxy observables. We use the Spearman rank-order correlation coefficient, r, and p-value to judge the strength of possible relationships. A "significant correlation" is identified as having $|r| \geq 0.5$ and $p < 0.01$ and a "weak correlation" is identified as having $|r| \geq 0.5$ and $0.01 < p < 0.05$. When $p < 0.05$ but $|r| < 0.5$, this indicates that there is a lot of scatter in the relationship, and we therefore deem these observables to be uncertain predictors

of EW(OH).

6.3.3.1 Line Ratios

Optical emission may be heavily absorbed by dust, therefore, we turn to IR tracers. Mid- and far-IR spectroscopy provides measures of the emission produced by accretion onto a supermassive black hole in AGNs and the emission produced by star-formation (e.g., Spinoglio & Malkan 1992). Using ratios of a high-ionization potential emission-line (AGN-dominated) to a low-ionized emission-line (H II region or starburst-dominated) can probe the relative contribution of both sources in a galaxy (e.g., Tommasin et al. 2008, 2010; Spinoglio et al. 2015; Fernández-Ontiveros et al. 2016). The larger the ratio means that a galaxy has a larger AGN contribution, while a smaller ratio would indicate that there is little or no AGN activity (starburst-dominated galaxy).

We investigate the following emission-line ratios against EW(OH): [Ne V]24.32μm/[Ne II]12.81μm, [Ne V]14.32μm/[Ne II]12.81μm, [Ne III] 15.56μm/[Ne II] 12.81μm, [O IV] 25.89μm/[Ne II] 12.81μm, and [O IV] 25.89μm/[O III] 88.36μm. These ratios are set up so that the emission-line in the numerator is more highly ionized, indicating that it arises in a warmer (AGN) environment. The emission-line in the denominator has lower ionization potential. Therefore, we expect AGN dominated galaxies to have higher IR emission-line ratios compared to obscured AGNs and non-active galaxies.

An orthogonal distance regression using a modified trust-region Levenberg-Marquardt-type algorithm was used to obtain a first degree polynomial fit for the data of each OH doublet. The fit is weighted using the uncertainties from both EW(OH) and the emission-line ratios. To obtain the uncertainty for the line ratios, we add the uncertainties of the emission-lines in quadrature. As mentioned above, we exclude any galaxies for which either EW(OH) or the emission-line ratio is an upper limit observation. We estimated a fit for each EW(OH) against each emission-line ratio individually. Table 6B.6 in the Appendix gives the results for the log-linear fits. Plots for EW(OH) vs. [Ne V] 14.32μm/[Ne II] 12.81μm and [O IV] 25.89μm/[O III] 88.36μm are shown in Figures

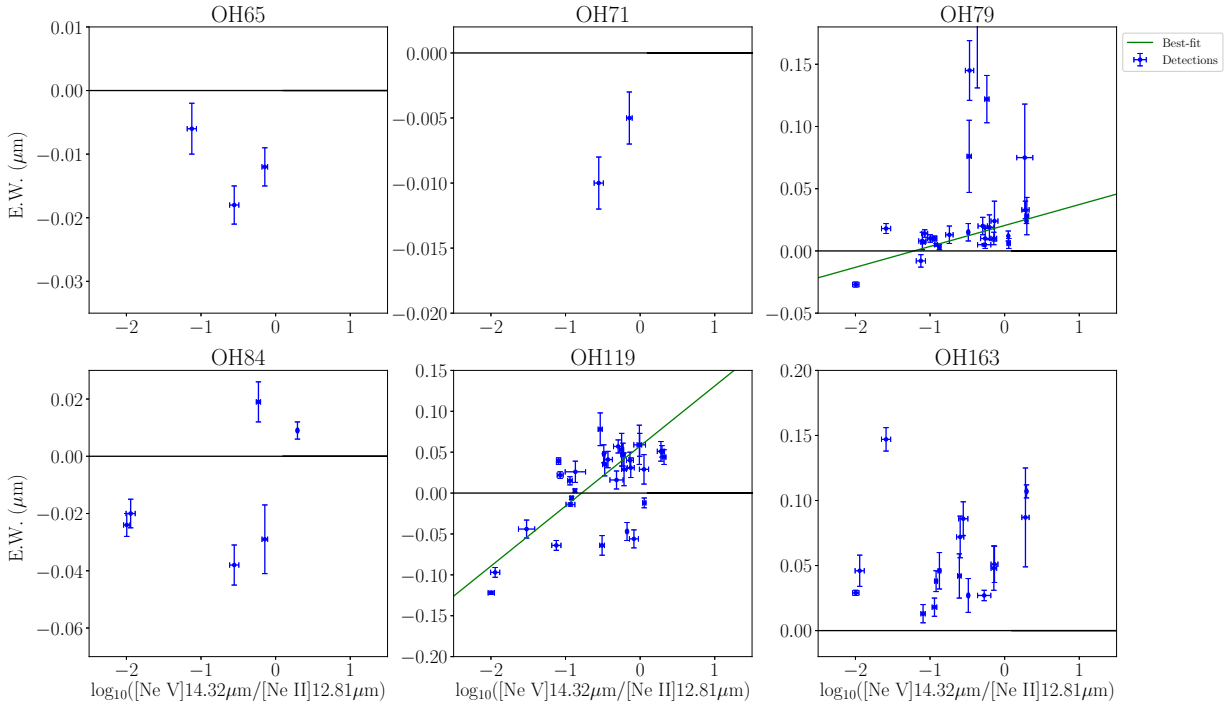

Figure 6.3: EW of the OH doublet vs. the logarithm of the [Ne V] 14.32μm/[Ne II] 12.81μm emission-line ratio. Galaxies must have detections in EW(OH), [Ne V] 14.32μm, and [Ne II] 12.81μm to be included in the plot and fits. The weighted log-linear fits, using the parameters given in Table 6B.6, are shown for fits with p < 0.05. We do not show the fit for slopes with a p-value > 0.05. For OH79, MCG-01-24-012 is an outlier (EW = 0.242μm), and is cut off to better show the rest of the data.

6.3 and 6.4 respectively. There is one panel for each OH doublet, and the fits from Table 6B.6 that have p < 0.05 are show in the Figures as a solid green line. Figures for EW(OH) vs. the other three line ratios ([Ne V] 24.32μm/[Ne II] 12.81μm, [O IV] 25.89μm/[Ne II] 12.81μm, and [Ne III] 15.56μm/[Ne II] 12.81μm) are available as supplementary figures in the Appendix.

We find that the OH119 doublet is the most significantly affected by changes to the emission-line ratios. Table 6B.6 shows that EW(OH119) has a significant correlation ($r \geq 0.5$ and p < 0.01) with log([Ne V] 14.32μm/[Ne II] 12.81μm), log([Ne III] 15.56μm/[Ne II] 12.81μm), and log([O IV] 25.89μm/[O III] 88.36μm). The latter two line ratios are the strongest predictors of EW(OH119), with $r > 0.60$. Due to the large amount of scatter ($r = 0.45$, p = 0.005), log([O IV] 25.89μm/[Ne II]

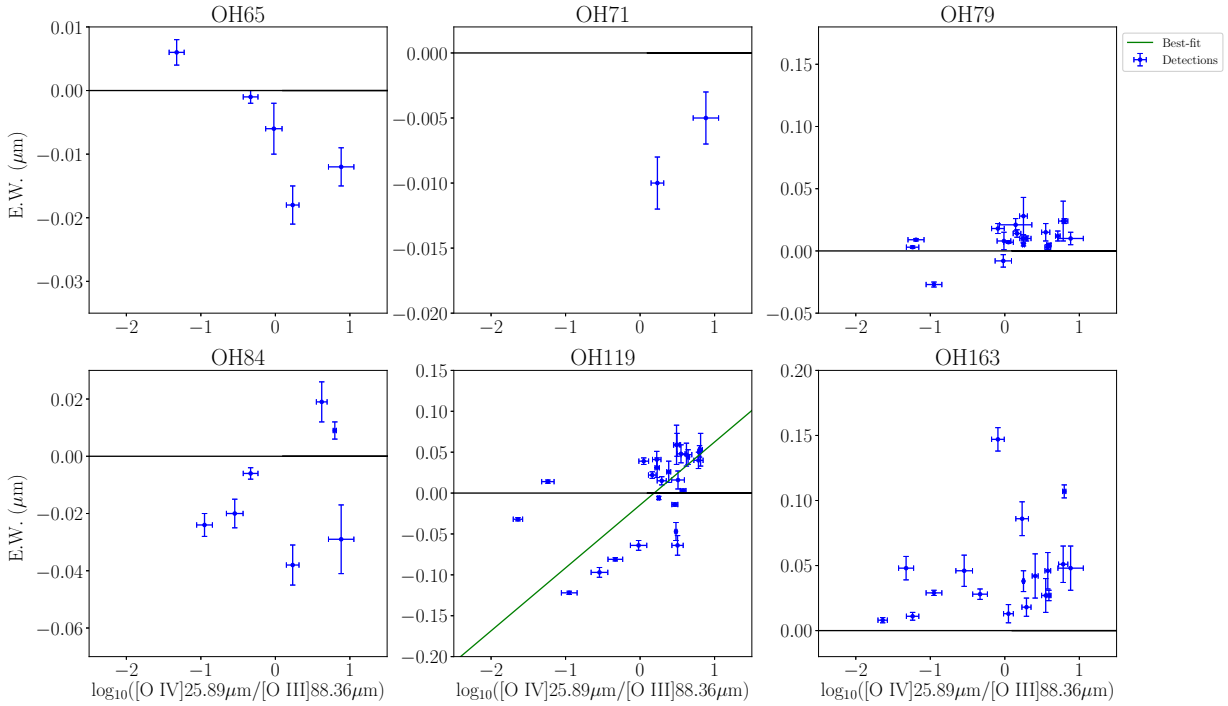

Figure 6.4: EW of the OH doublet vs. the logarithm of the [O IV] 25.89μm/[O III] 88.36μm emission-line ratio. Galaxies must have detections in EW(OH), [O IV] 25.89μm, and [O III] 88.36μm to be included in the plot and fits. The weighted log-linear fits, using the parameters given in Table 6B.6, are shown for fits with p < 0.05. We do not show the fit for slopes with a p-value > 0.05.

12.81μm) is shown to be an uncertain predictor of EW(OH119). OH119 is more likely to be in absorption for low emission-line ratios, and transitions to emission as the high-ionization IR lines become stronger. Since high-ionization lines are dominated by the AGN emission, we can associate an enhanced OH119 emission with the presence of an AGN.

While already significant ($r = 0.52$, p = 0.0025), it is worth noting that the strength of the correlation between EW(OH119) and log([Ne V] 14.32μm/[Ne II] 12.81μm) greatly increases in strength (r = 0.71, p = 0.00003) when we remove IRAS 12514+1027, NGC 5506, PKS 2048-57, and NGC 7172 from the fit. These four galaxies are identified as outliers because EW(OH119) is in absorption, while the rest of the sample is in emission at log([Ne V] 14.32μm/[Ne II] 12.81μm) $\gtrsim -0.5$. Removing the same four galaxies also makes log([O IV] 25.89μm/[Ne II] 12.81μm) a much better

predictor of EW(OH119) as well (r = 0.58, p = 0.0004). Based on our methodology outlined in Section 6.3.3, without these outliers, EW(OH119) vs. log([O IV] 25.89μm/[Ne II] 12.81μm) displays a significant correlation. One explanation for these four outlier galaxies could be that the molecular gas seen in OH does not react instantaneously to the AGN activity, so these few cases out of the correlation might be recent AGN sources that need some Myrs to drive OH119 into emission (i.e. into the correlation).

While to a lesser degree, EW(OH79) and EW(OH163) are also correlated with the IR emission-lines ratios. EW(OH79) shows a significant correlation (r = 0.50, p = 0.007) with log([Ne V] 14.32μm/[Ne II] 12.81μm). Due to low p-values but r values of 0.46 and 0.37, respectively, log([Ne III] 15.56μm/[Ne II] 12.81μm) and log([O IV] 25.89μm/[Ne II] 12.81μm) are found to be uncertain predictors of EW(OH79). The r value for the EW(OH79) relationships is always smaller compared to that of EW(OH119), indicating that while the IR line ratios can predict EW(OH79), it is not as strong. Despite the increase in scatter, this doublet displays strong emission when the ratio of the high ionization to low ionization lines is largest, which indicates that a more highly ionized galaxy (due to the presence of an AGN) will contain OH79 emission, similar to OH119. At lower flux ratio values, OH79 primarily shows weak emission, with only a few galaxies in absorption. This is different from OH119, which displayed deep absorption when the low ionization line was significantly stronger. There are four galaxies, IC 1816, MCG-01-24-012, Mrk 705, Mrk 883, with extreme OH79 emission (EW $>$ +0.10) compared to the rest of the sample; however, removing these objects does not significantly improve the strength of any of the three fits.

EW(OH163) displays a weak correlation (r = 0.69, p = 0.02) with log([Ne V] 24.32μm/[Ne II] 12.81μm). Also, log([Ne III] 15.56μm/[Ne II] 12.81μm) is found to be an uncertain predictor of the doublet (r = 0.43, p = 0.03). In both of these relationships, stronger OH163 emission is found in the more ionized galaxies, similar to both OH119 and OH79. OH163 is more likely to display weaker emission at lower flux ratio values. There are no obvious outliers in the relationship with log([Ne III] 15.56μm/[Ne II] 12.81μm); therefore, log([Ne V] 24.32μm/[Ne II] 12.81μm) is the

better predictor of EW(OH163).

Based on the criteria outlined in Section 6.3.3, no correlations are found between EW(OH65), EW(OH71), and EW(OH84) with any of the emission-line ratios. This is primarily due to a lack of observations. There could be possible correlations between EW(OH65) and both log([O IV] 25.89μm/[Ne II] 12.81μm) and log([O IV] 25.89μm/[O III] 88.36μm) as $r = -0.90$ and p = 0.04 for both relationships. However, there are only five galaxies in both of these samples, which are too few to conclude if these correlations exist. If the EW(OH65) correlations are real, this would imply that a warm gas with a significant fraction of molecules at ~300 K (see Figure 6.1) is needed to drive OH65 absorption. A relatively luminous source and/or a strong radiation field is needed to achieve temperatures this high.

It is important to note that the normal spiral galaxy M83, which has no indications of AGN activity any of these observables, shows OH79 and OH119 weakly in emission. As discussed, none of the correlations are perfect, and the occasional outlier is expected. Therefore, we caution that some of the generalizations that we draw from the full sample may not necessarily apply to every galaxy. Our physical interpretation of the OH transitions may not fully explain the observed OH doublets in every galaxy.

6.3.3.2 AGN Luminosity

To probe the brightness of the AGN, we convert the most highly ionized line fluxes from Section 6.3.3.1, [O IV] 25.89μm, [Ne V] 14.32μm, and [Ne V] 24.32μm, to luminosities. As outlined in Section 6.2.2, we will refer to these as $L_{[\mathrm{O\ IV}]25.89\mu\mathrm{m}}$, $L_{[\mathrm{Ne\ V}]14.32\mu\mathrm{m}}$, and $L_{[\mathrm{Ne\ V}]24.32\mu\mathrm{m}}$, respectively. We will also investigate possible correlations with the intrinsic hard X-ray (2-10 keV) luminosity, $L_{2-10\mathrm{keV}}$. These luminosities should all increase with increasing AGN activity in the host galaxy (e.g., Tommasin et al. 2008, 2010; also Diamond-Stanic et al. 2009 for $L_{[\mathrm{O\ IV}]25.89\mu\mathrm{m}}$).

We use the same fitting method as Section 6.3.3.1. Unlike the IR luminosities, the $L_{2-10\mathrm{keV}}$ data was published without estimated uncertainties. Therefore, in this scenario, only the uncertainty on

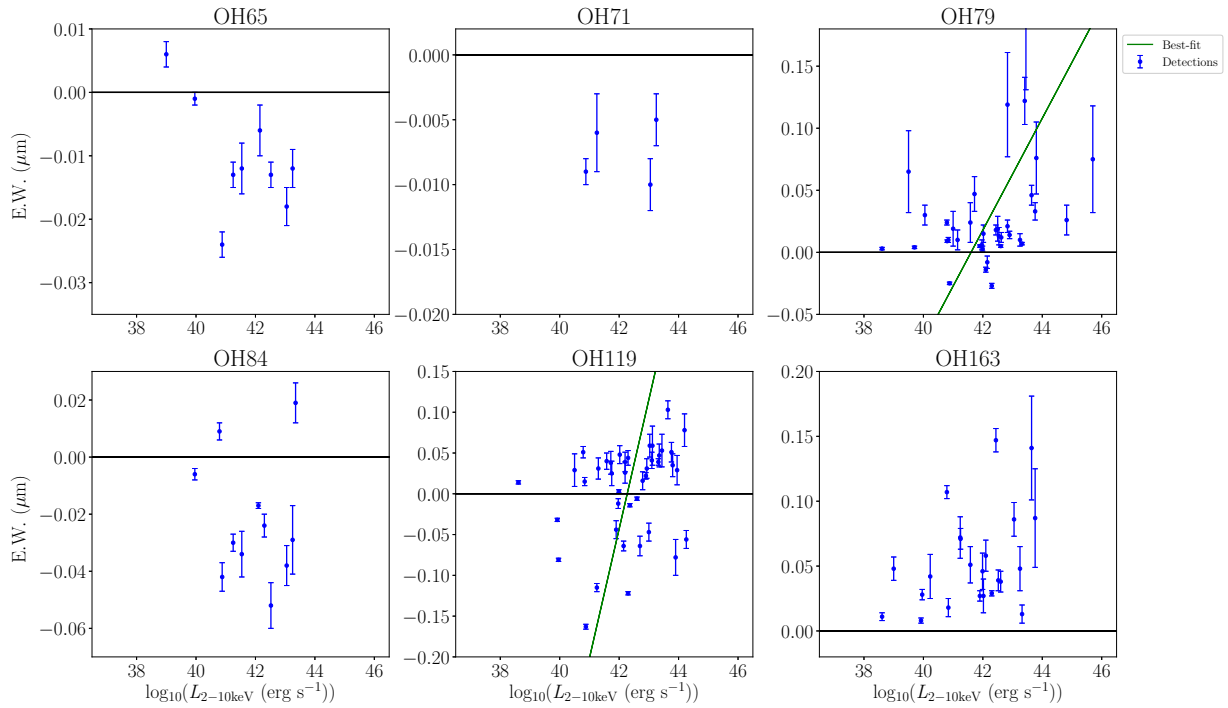

Figure 6.5: EW of the OH doublet vs. log($L_{2-10\mathrm{keV}}$ (erg/s)). Galaxies must have detections in EW(OH) and $L_{2-10\mathrm{keV}}$ to be included in the plot and fits. The weighted log-linear fits, using the parameters given in Table 6B.7, are shown for fits with p < 0.05. For both EW(OH79) and EW(OH119), $|r| \leq 0.5$, which indicates that $L_{2-10\mathrm{keV}}$ is an uncertain predictor of these doublets. We do not show the fit for slopes with a p-value > 0.05. For OH79, MCG-01-24-012 is an outlier (EW = 0.242μm), and is cut off to better show the rest of the data.

EW(OH) is incorporated into the fits. Table 6B.7 in the Appendix gives the results for the log-linear fits. We include plots for EW(OH) vs. log($L_{2-10\mathrm{keV}}$) (Figure 6.5) and log($L_{[\mathrm{O\ IV}]25.89\mu\mathrm{m}}$) (Figure 6.6), with one panel for each OH line in this section. Figures for EW(OH) vs. the other two line ratios ($L_{[\mathrm{Ne\ V}]14.32\mu\mathrm{m}}$ and $L_{[\mathrm{Ne\ V}]24.32\mu\mathrm{m}}$) are available as supplementary figures in the Appendix. The fits from Table 6B.7 with p < 0.05 are shown in the Figures as a solid green line.

We find very few correlations between the OH doublets and the IR and X-ray luminosities. EW(OH163) displays a significant correlation (r = 0.56, p = 0.007) with log($L_{[\mathrm{O\ IV}]25.89\mu\mathrm{m}}$). This is the strongest correlation found between an OH doublet and a luminosity observable. Due to low p-values (0.03 and 0.014) but large scatter in the data (r = 0.35 and 0.41), log($L_{2-10\mathrm{keV}}$) is an

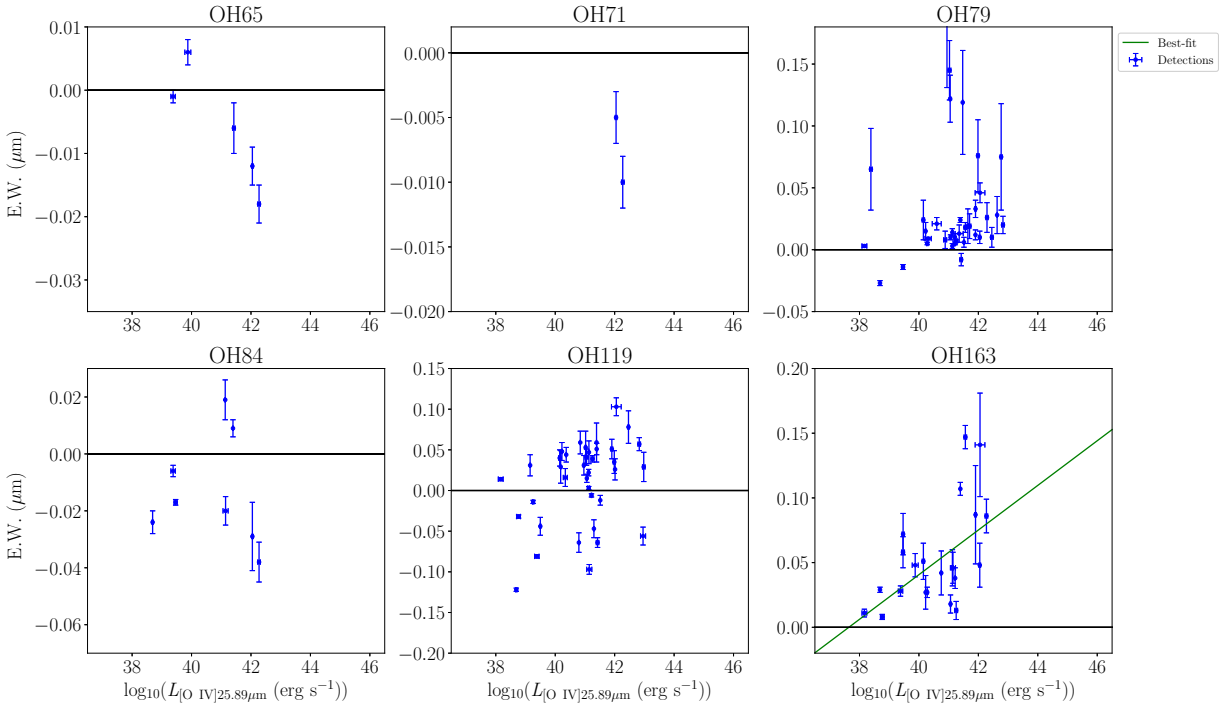

Figure 6.6: EW of the OH doublet vs. $\log(L_{[\mathrm{O\ IV}]25.89\mu\mathrm{m}}$ (erg/s)). Galaxies must have detections in EW(OH) and $L_{[\mathrm{O\ IV}]25.89\mu\mathrm{m}}$ to be included in the plot and fits. The weighted log-linear fits, using the parameters given in Table 6B.7, are shown for fits with $p < 0.05$. We do not show the fit for slopes with a p-value > 0.05. For OH79, MCG-01-24-012 is an outlier (EW = 0.242μm), and is cut off to better show the rest of the data.

uncertain predictor of EW(OH119) and EW(OH79), respectively. Despite the scatter for OH79 and OH119, these relationships indicate that these three OH doublets all display the strong emission in the most luminous AGN. At lower luminosities, which indicate either weak or no AGN activity, we see deep absorption (OH119), weak emission (OH163), and a mixture of weak emission and weak absorption (OH79).

Similar to Section 6.3.3.1, no correlations are found for OH65, OH71, and OH84. Low statistics once again are a factor in this. It is possible that a relationship between EW(OH65) and $\log(L_{[\mathrm{O\ IV}]25.89\mu\mathrm{m}})$ could exist ($r = -0.90$, p = 0.04), but this is based on only five galaxies. However, if this correlation exists, it suggests that a luminous source would be needed to create gas temperature warm enough to drive OH65 into absorption.

6.3.3.3 Comparison Between the Luminosity and IR Emission-Line Tracers

The IR emission-line ratios in Section 6.3.3.1 and luminosities in Section 6.3.3.2 both trace the strength of the AGN to probe the spectral type of the galaxy. When OH79, OH119, and OH163 correlate with one of these AGN tracers (luminosity or emission-line ratio), it is always positive. This means that these doublets display the strongest emission when the emission-line ratios and luminosities suggest that the galaxy contains a dominant AGN feature. When the tracers suggest that the galaxy has either a weak or no AGN, we observe deep absorption (OH119), weak emission (OH163), and a mixture of weak emission and weak absorption (OH79). The slopes of the fits are generally largest for EW(OH119) meaning that this doublet is the most affected by the AGN tracers. Because we observe EW(OH119) with deep absorption and strong emission, and do not for EW(OH79) and EW(OH163), this is reasonable. For OH119, the results that emission is stronger in more luminous AGN aligns with previous studies (Veilleux et al., 2013; Stone et al., 2016).

OH79, OH119, and OH163 all correlate with a higher percentage of the emission line ratios than the X-ray and IR luminosities. Also, the relationships with the IR emission-line flux ratios are generally at a higher significance with less scatter. These two results suggest that comparing the relative contributions of AGN activity and star formation is a better predictor of EW(OH) than the AGN luminosity. In other words, EW(OH) cares more about the relative contribution of the AGN to the total power (the line ratios), and less about the total power of the AGN (the luminosities). This result is in line with Fluetsch et al. (2019), who find that the mass loading factor (which measures how fast the outflow ejects the gas from the galaxy compared to the gas consumption by star formation) depends on the relative contribution of the AGN to the bolometric luminosity.

While not significant due to samples of only five galaxies, EW(OH65) is also found to anti-correlate with both IR emission-line ratio and IR luminosity tracers. As discussed above, this suggests that an AGN is needed to elevate the temperature of gas high enough (~300 K), to drive OH65 into absorption.

6.3.4 EW(OH) vs. 25-60 Color Temperature

In this section, we estimate the thermal dust continuum emission to use as another IR probe of AGN strength. As stated in Section 6.2.3, to investigate the dominance of the AGN component in the host galaxy, we use the $f_{25\mu m}/f_{60\mu m}$ ratio (referred to as “dust temperature") from IRAS. The ratio of these flux densities can be used as a proxy of the strength of the AGN because the majority of the 25μm flux originates from warm dust surrounding the AGN while most of the 60μm flux is from cooler dust in star formation. Therefore, we expect the galaxies with luminous AGN to have a higher dust temperature than less luminous AGN and non-active galaxies (e.g., Edelson & Malkan 1986; Spinoglio et al. 1995; Veilleux et al. 2009; Lee et al. 2011).

We fit the data using the same method described in the previous section, using uncertainties for both EW(OH) and dust temperature. Table 6B.8 provides the parameters of the best-fit lines and Spearman rank-order correlation statistics, and a plot of EW(OH) vs. the logarithm of the dust temperature traced by the IRAS $f_{25\mu m}/f_{60\mu m}$ ratio is shown in Figure 6.7.

We find a highly significant ($r \geq 0.5$, $p < 0.01$) positive relationship between dust temperature and both EW(OH79) and EW(OH119). These correlations show that the two OH doublets are more likely to be in strong emission when surrounded by warmer dust, which indicates that the AGN component has a relatively high luminosity output. For galaxies with cooler dust, indicating a galaxy with either a weak or no AGN component, we find OH119 primarily in deep absorption. OH79 is shown to be in either weak absorption, compared to OH119, or weak emission when surrounded by cooler dust temperatures.

The other four OH doublets show no correlation with dust temperature. For OH65, González-Alfonso et al. (2015) did not find a significant relationship between EW and dust temperature as well. The samples are similar in size: there are 23 galaxies (10 detections) in this sample and 29 (25 detections) in González-Alfonso et al. (2015). This study contains 9 galaxies (~39%) not included in González-Alfonso et al. (2015); however, 8/10 detections in this study are also in

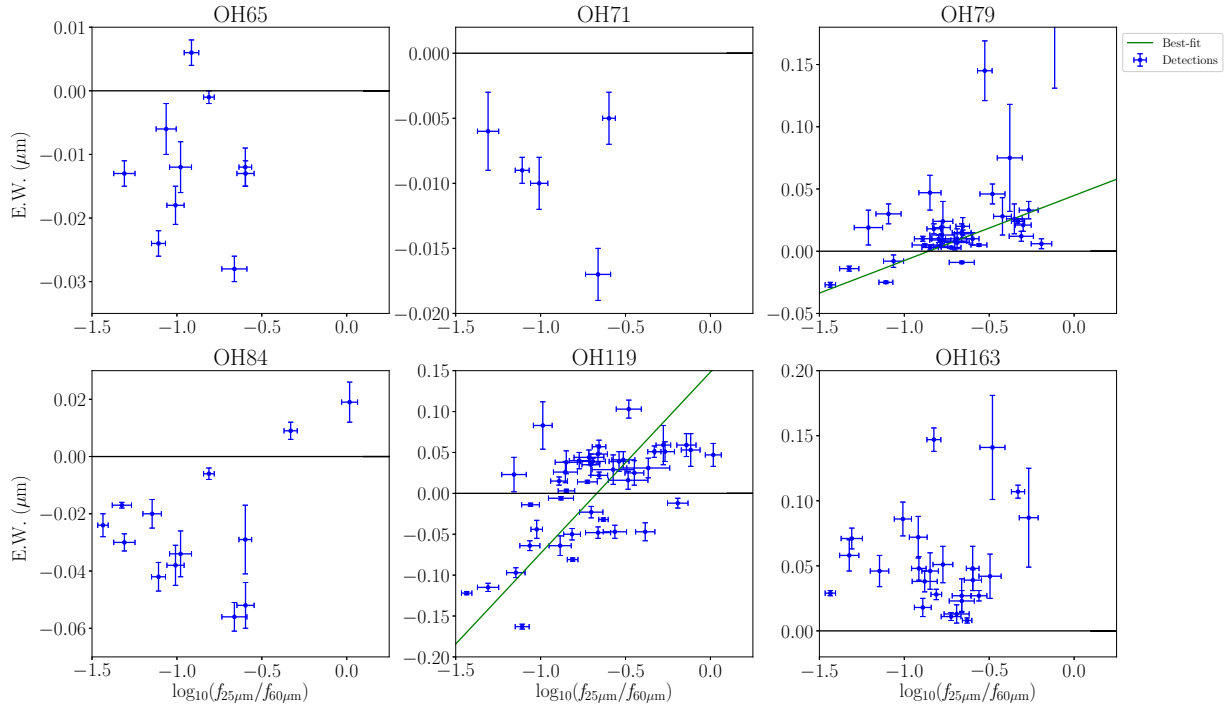

Figure 6.7: EW of the OH doublet vs. the logarithm of the dust temperature traced by the IRAS $f_{25\mu m}/f_{60\mu m}$ ratio. Galaxies must have detections in EW(OH), IRAS 25μm flux, and IRAS 60μm flux to be included in the plot and fits. The weighted linear fits, using the parameters given in Table 6B.8, are shown for fits with p < 0.05. We do not show the fit for slopes with a p-value > 0.05. For OH79, MCG-01-24-012 is an outlier (EW = 0.242μm), and is cut off to better show the rest of the data.

González-Alfonso et al. (2015).

6.3.5 EW vs. Dust Obscuration

This section investigates possible effects of dust reddening and extinction on the sample using one IR and one optical dust tracer.

6.3.5.1 IR Silicate Absorption

The OH doublets we observe are produced by warm/dense molecular gas, which is expected to be associated with dust. We therefore, compared our OH measurements with the 9.7μm silicate dust

feature in those same galaxies. Recall from Section 6.2.4 that the measurements were compiled from a variety of sources (Alonso-Herrero et al. 2016; Farrah et al. 2013; González-Martín et al. 2015; Hernán-Caballero et al. 2015; Wu et al. 2009) (see Table 6A.3 in Appendix 6A) and the strength of the silicate feature is quantified using the method derived by Spoon et al. (2007). Figure 6.8 shows the EW plotted against the strength of the silicate feature, and Table 6B.9 contains the fitting parameters and correlation statistics to the data.

We find a highly significant correlation (r = 0.59, p = 0.001) for EW(OH119). The relationship is positive, meaning that as $S_{\rm sil}$ increases (silicate absorption weakens), this doublet is more likely to display stronger emission. It is important to note that this relationship can be strengthened by removing one outlier, IRAS 11095-0238. We identify this galaxy as an outlier because OH119 is in emission even though it has the fourth strongest silicate absorption in the sample ($S_{\rm sil} = -3.28$). Except for Mrk 1066 ($S_{\rm sil} = -1.01$) no other galaxy shows EW(OH119) past a silicate strength of -1.00. Excluding IRAS 11095-0238, increases the strength of the fit: r = 0.65, p = 0.00003.

The results for OH119 agree with Stone et al. (2016) (which expand on/confirm the results of Spoon et al. 2013 and Veilleux et al. 2013). For OH119, these studies find that a stronger silicate absorption feature (more dust extinction), leads to weaker OH119 emission and stronger OH119 absorption. Spoon et al. (2013) and Veilleux et al. (2013) find this correlation using samples of local ULIRGs. Stone et al. (2016) combines the sample of ULIRGs from Veilleux et al. (2013) and incorporates their BAT AGNs to create a more expansive sample. Our sample size is comparable in size to Stone et al. (2016), with some overlap in the selected galaxies, allowing us to confirm this relationship.

We find $S_{\rm sil}$ to be a uncertain predictor (r = 0.42, p = 0.02) of EW(OH79). However, removing the two largest outliers, IRAS 11095-0238 (similar reasons as for OH119) and MCG-01-24-012 (due to extreme EW emission, +0.242), increases the strength of the relationship, and we now find a significant correlation (r = 0.54, p = 0.002) between the two observables. Similar to OH119, the relationship between EW(OH79) and $S_{\rm sil}$ is positive; however, the r value for OH79 is lower

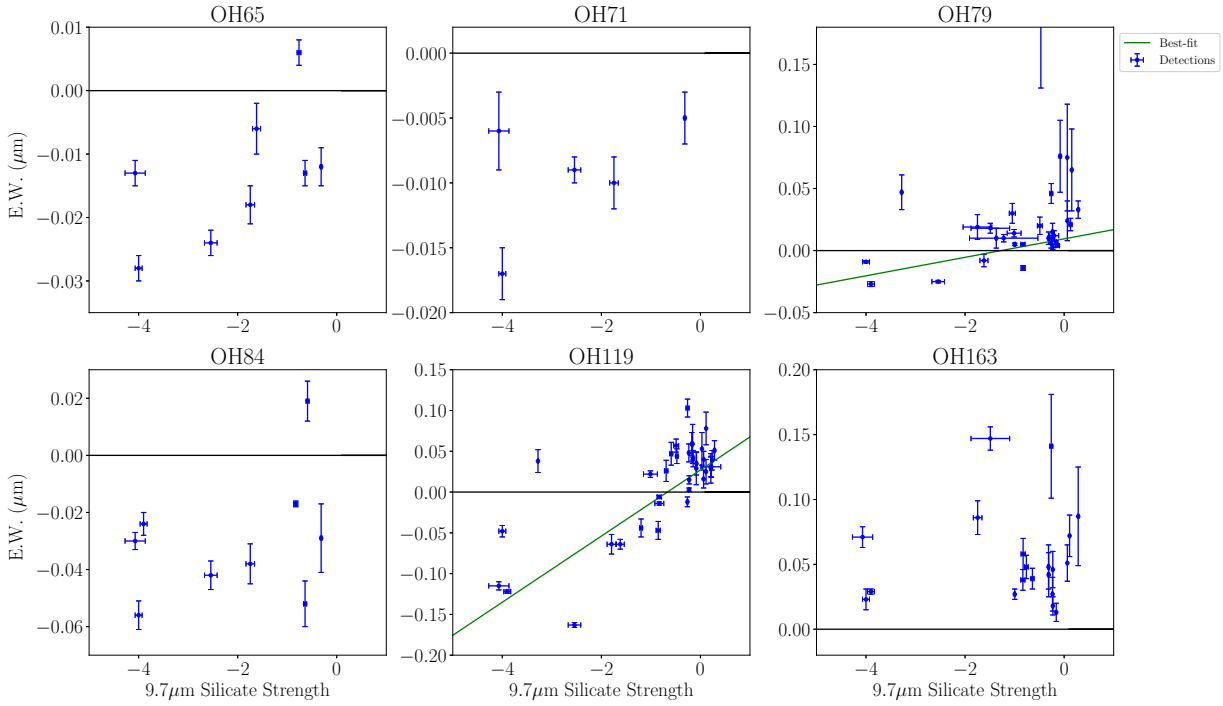

Figure 6.8: EW of the OH doublet vs. the strength of the 9.7μm silicate feature. Galaxies must have detections in EW(OH) and $S_{\rm sil}$ to be included in the plot and fits. The weighted log-linear fits, using the parameters given in Table 6B.9, are shown for fits with p < 0.05. We do not show the fit for slopes with a p-value > 0.05. For OH79, MCG-01-24-012 is an outlier (EW = 0.242μm), and is cut off to better show the rest of the data.

than that of OH119. This comparison exists both with and without the outlier galaxies in the two samples, meaning that the strength of the 9.7μm silicate feature is more predictive of EW(OH119).

The other four OH doublets show no correlation with $S_{\rm sil}$, based on their p-values. Our results for EW(OH65) do show a high correlation coefficient (r = 0.60); however, this does not translate to a small p-value (p = 0.12) because there are only eight galaxies in the sample. González-Alfonso et al. (2015) had almost three times the number of detections as this study, with six of our eight detections in their sample, and they do find a correlation between EW(OH65) and silicate strength. They claim that while deep OH65 absorption does not guarantee deep silicate absorption, a trend between the two exists. González-Alfonso et al. (2015) also claim that the two quantities are produced from the same material. Our sample does not contradict this, but is too small to be conclusive.

6.3.5.2 Balmer Decrement

An additional optical tracer for the extinction affecting the ionized gas is the Hα/Hβ ratio. Hβ is more obscured by dust, so it is expected that a larger Balmer ratio will be observed in dustier galaxies. The line fluxes were collected from published measurements in the literature, and Table 6A.3 in Appendix 6A provides the data measurements along with the citations.

The results of the linear regression analysis are given in Table 6B.9 in the Appendix, and a figure for EW(OH) vs. Hα/Hβ is available as a supplementary figure in the Appendix. EW(OH79) has the strongest correlation with the Balmer decrement in the sample. The correlation is significant (r = −0.63, p = 0.002), and reveals that a larger Hα/Hβ ratio (i.e. more dust obscuration) results in either weak emission or weak absorption. The galaxies with the strongest EW(OH79) emission have small Balmer ratios.

Similar to OH79, OH119 tends to have the strongest emission at low Hα/Hβ, and emission gets weaker and absorption becomes more prevalent at high Hα/Hβ. The relationship between EW(OH119) and Hα/Hβ has a low p-value (0.014) but also a low r value (−0.47), which indicates that the Balmer decrement is an uncertain predictor of the doublet. However, the correlation greatly improves when removing two outliers, NGC 253 and NGC 7172. These two galaxies can be identified as outliers in the sample because they have deep absorption (−0.081μm and −0.064μm) at low Hα/Hβ ratios (2.84 and 3.00). All other galaxies in the sample show strong emission (EW $\sim$ +0.05μm) in this Balmer decrement range. Without NGC 253 and NGC 7172, EW(OH119) has a significant relationship (r = −0.72 and p = 0.00005) with the Balmer decrement. NGC 7172 was identified in Section 6.3.3.1 as a galaxy with a recent AGN source that needs some Myrs to drive OH119 into emission. This means that even though this galaxy has low dust extinction, the nuclear source was not powerful enough to create OH119 emission until just recently and the doublet needs more time to reach equilibrium in emission.

While both the silicate feature and Balmer decrement show that a higher dust concentration leads

to weaker emission and deeper absorption for the OH79 and OH119 doublets, it is shown that $S_{\rm sil}$ is the better extinction predictor for EW(OH119) and the Balmer decrement is the better predictor for EW(OH79).

No correlation is found for the other four OH transitions in the sample. For these doublets, OH163 was the only one to meet the eight galaxies threshold; however, even with small statistics, the other three galaxies show no indication of a possible relationship with the Balmer decrement.

6.3.6 Bivariate Linear Regression Test for EW(OH)

In Sections 6.3.3.1, 6.3.3.2, and 6.3.5, we found correlations between the EW of OH doublets and: 1) IR and X-ray luminosities of the galaxy; 2) IR emission-line ratios; and 3) dust extinction tracers. In those sections we found many correlations of varying strength between EW(OH) and the many observables. Here we use a bivariate linear regression to see if EW(OH) is correlated with multiple observables. We chose one observable from each section: 1) the $L_{2-10\rm keV}$ to probe the brightness of the AGN using X-rays; 2) the log([O IV] 25.89μm/[Ne II] 12.81μm) IR emission-line ratio because this is a tracer of the relative AGN/star-formation contribution; and 3) the strength of the silicate feature for the dust extinction tracer because this traces the obscuration. The dependent variable in the bivariate linear regression, EW(OH), is weighted using its uncertainties. Due to limited sample size, we do not include OH65, OH71, and OH84 in these bivariate relationships. Table 6B.10 gives the coefficient of each independent parameter ($L_{2-10\rm keV}$, log([O IV] 25.89μm/[Ne II] 12.81μm), and $S_{\rm sil}$), the y-intercept of the regression, and the R^2 value evaluating the strength of the correlation.

There is a very strong correlation between EW(OH119) and the bivariate linear regression (R^2 = 0.91). This makes sense because this doublet has a relationship with all three observables individually. While not as strong as the OH119 doublet, EW(OH79) is correlated with this bivariate linear regression ($R^2 = 0.61$). OH79 also displayed a relationship with all three observables individually; however, these were generally not as strong as those for EW(OH119). This could

explain why the bivariate correlation for EW(OH79) is weaker. The bivariate regression shows no correlation with EW(OH163), which can be expected since this doublet displayed no correlation with any of the three observables individually.

6.3.7 OH79 vs. OH119

The OH79 and OH119 doublets show the most significant correlations in Sections 6.3.3, 6.3.4, and 6.3.5. Also, the transitions share the same lower energy level, suggesting a tight relationship between both OH doublets. To test this, we compared the EW for the 20 galaxies that have detections for both transitions (this excludes galaxies with P-Cygni features and upper limit observations). Figure 6.9 displays the plot comparing the EW of the OH79 and OH119.

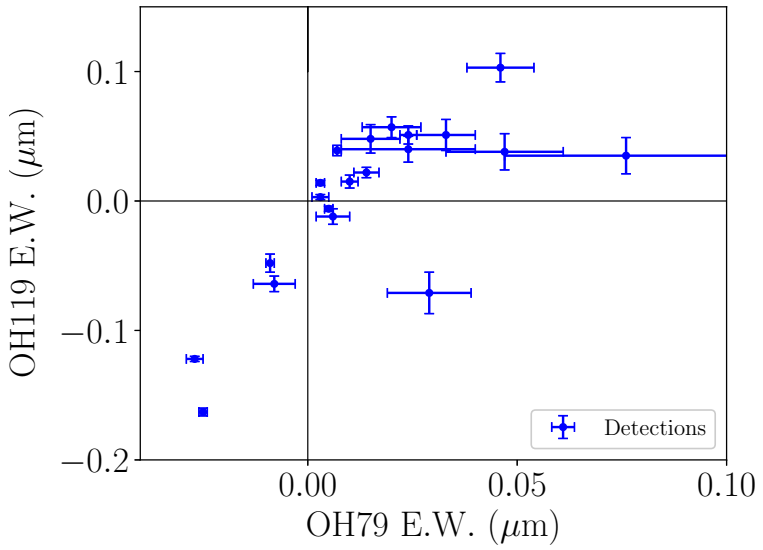

Figure 6.9: EW(OH119) vs. EW(OH79). Only galaxies with detections for both doublets are shown. The error bars for Mrk 478 is cut off to better show the rest of the data.

Figure 6.9 reveals that for most galaxies, the doublets are either both in emission or both in absorption, and a larger EW for one transition generally indicates a larger EW for the other. This positive trend between the two doublets is very strong with high significance, as indicated by r = 0.71 and p = 0.0005. There does seem to be a saturation at EW(OH79) $\gtrsim 0.03\mu$m, where OH119 seems to flatten around EW(OH119) $\sim 0.05\mu$m. In the sample, there are three objects that have an

emission profile for OH79 and an absorption profile for OH119: IRAS 20037-1547, PKS 2048-57, and NGC 7582. Two of them, PKS 2048-57 and NGC 7582, have small EW(OH79) emission, small EW(OH119) absorption, and appear to follow the trend with the rest of the sample. The third galaxy, IRAS 20037-1547, however, is a noticeable outlier. There are no galaxies that have an absorption profile for OH79 and an emission profile for OH119.

6.3.8 OH79 vs. OH163

OH79 and OH163 are the two doublets most likely to be seen in emission in the sample. They also are connected in the OH Grotrian diagram, as the upper level of the OH79 doublet is the lower level of the OH163 doublet. To test if there is a relationship between EW(OH79) and EW(OH163), we look at the 16 galaxies (excluding galaxies with P-Cygni features and upper limit observations) that have detections for both transitions. Figure 6.10 shows the plot comparing the EWs.

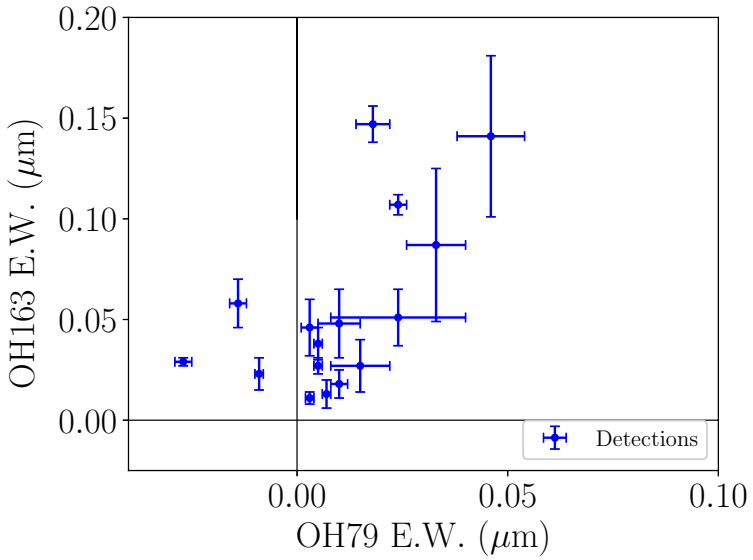

Figure 6.10: EW(OH163) vs. EW(OH79). Only galaxies with detections for both doublets are shown.

Figure 6.10 shows that there is weak correlation (r = 0.54, p = 0.03) between EW(OH79) and EW(OH163). The trend is positive, meaning that stronger emission for one of the doublets implies stronger emission for the other. This relationship could explain why we only observe OH163 in emission in the complete sample. The lower level of the OH163 doublet could be depopulated by

the OH79 transition, which would prevent OH163 absorption from occurring.

There are three objects where OH79 shows absorption while OH163 shows emission: NGC 3079, NGC 4418, and NGC 4945. All three of these galaxies have buried nuclei, indicated by their deep 9.7μm silicate absorption. NGC 4418 and NGC 4945 have the second and third strongest silicate absorption in the entire 178 galaxy sample. Removing these three galaxies reveals a significant correlation (r = 0.73, p = 0.004) between the OH163 and OH79 doublets.

6.4 Discussion and Interpretations

To gain a deeper understanding of the correlations that we found in Section 6.3, we look to compare our results with various models of OH transitions from the literature. We can interpret the results described above in terms of OH level populations because we combine several transitions measured simultaneously.

6.4.1 OH Level Populations & the Mechanisms which Control them

OH emission can arise from two mechanisms: radiative pumping and collisional excitation. Collisions with the surrounding medium are dependent on the temperature of the region. The nuclear region of an active galaxy is warmer than that of a star-forming galaxy, therefore the former will have more energetic collisions. The correlations of EW(OH) with the galaxy properties that we analyzed in Section 6.3 are probably driven by the nuclear region of the galaxies, where the impact of the AGN is dominant.

To estimate the energy of possible collisions, we reference the results of models from González-Alfonso et al. (2004, 2008, 2012, 2014, 2017b) and Falstad et al. (2015) that generate the observed OH transitions to learn about properties of the environment that they were created in. The models in these studies have multiple components; they start with a hot inner region and cooler extended region, and then add one or two extra components if necessary to better fit the observed spectra. One example of an extra component added to the two-region model is the addition of a more extended

halo component with a lower temperature to Arp220 (González-Alfonso et al., 2004). For most of the galaxies modeled in these studies, the dust temperature of the far-IR continuum source ranges from about 90−150 K for the inner nuclear region, while the cooler extended region is roughly 40−90 K.

For the OH transitions in this sample, radiative excitation primarily comes from far-IR photons, which can originate from either AGN activity or star formation. We will discuss the method of excitation for the OH transitions in our sample one at a time. We refer to the OH Grotrian diagram, Figure 6.1 in Section 6.2.1, throughout this section.

6.4.1.1 OH119

Sections 6.3.3.1, 6.3.3.2, and 6.3.4 probe the AGN luminosity, radiation field hardness, and dust temperature of a galaxy. The results in these Sections show that EW(OH119) has a significant correlation ($r \geq 0.5$, $p < 0.01$) with 3/5 IR emission-line ratios and the IRAS $f_{25\mu m}/f_{60\mu m}$ dust temperature. An additional IR line ratio and the intrinsic 2-10 keV X-ray luminosity are also uncertain predictors of EW(OH119). Therefore, 6/10 observables tracing the strength of an AGN have some level of predictive power for EW(OH119). The relationships are positive, meaning that when these observables are large (luminous AGN, hard radiation field, and warm dust), OH119 is very likely to be in emission, and the opposite (dim/no AGN, soft radiation field, cooler dust), tends to bring OH119 into deep absorption. These results indicate that OH119 emission is dependent on the conditions created by an AGN, which suggests that OH119 emission is created through collisional excitation. If OH119 emission were generated primarily by radiative pumping of far-IR photons, we would expect to find the doublet in emission for galaxies with a weak or no AGN, which we do not find. However, a possible contribution to the OH119 emission from radiative pumping by far-IR photons cannot be disregarded.

This idea agrees with Spinoglio et al. (2005) and Stone et al. (2016), which both claim that OH119 emission is generated through collisions. The argument from Spinoglio et al. (2005) comes from

the relative strengths of the OH transitions they observed and the Einstein-A coefficients. Table 6.1 in Section 6.1 gives the Einstein-A coefficients of the OH transitions in this study, which were gathered from the LAMBDA database (Schöier et al., 2005). As discussed in Spinoglio et al. (2005), if the OH119 transitions were excited exclusively via radiative pumping, there would be two paths it could take: absorption of either the 34.6μm or 53.3μm ground-state OH transitions. If the radiative pumping happened through the 34.6μm transition, then the 98.7μm OH transition would be about five times stronger than OH119. If OH119 were excited by the 53.3μm path, then OH163 would be about five times stronger than OH119. The estimate of the relative strengths between the OH transitions come from the Einstein-A coefficients. In their study, Spinoglio et al. (2005) could not detect the 98.7μm doublet, and OH163 was not five times stronger than OH119, so they concluded that OH119 must be a result of collisional excitation, and not radiative pumping.

Our results agree with the claims made by Spinoglio et al. (2005) on how the OH119 comes into emission. When comparing galaxies that have detections showing emission for both OH119 and OH163, we find median fluxes of 4.44×10^{-14} erg s^{-1} cm^{-2} and 2.62×10^{-14} erg s^{-1} cm^{-2} for the sample. This shows that the OH119 doublet is actually stronger on average than the OH163 doublet when comparing the emission detections in the same galaxy (the average OH163/OH119 flux ratio is 0.59). The only galaxy where the OH163 doublet is stronger is NGC 1365. Because we do not see a flux ratio of $\sim$5 for OH163/OH119, it seems unlikely that the 53.3μm path dominates the OH119 emission via radiative pumping. Unfortunately, we do not have any OH 98.7μm detections, similar to Spinoglio et al. (2005), to confirm or rule out the 34.6μm path as a possible source of OH119 emission from radiative pumping; however, based on the results with our AGN tracers radiative pumping through the 34.6μm path seems unlikely.

In Stone et al. (2016), they use their correlation between EW(OH119) and the silicate feature to conclude that OH119 emission comes from a circumnuclear region where the temperature, OH abundance, and number density favors collisional excitation over radiative pumping. We find a similar relationship between EW(OH119) and the silicate feature, and therefore also support the

idea that OH119 emission originates from collisions.

These correlations, which indicate the importance of collisional excitation of OH119, are nonetheless imperfect, and some of the observed scatter could be attributed to other factors. In particular, high obscuration is correlated with absorption in this transition. Therefore, where that additional affect is strong, i.e. in a heavily obscured AGN, the OH doublet may not be strongly in emission.

6.4.1.2 OH163

As stated in Section 6.3.2.2, all detections for the OH163 doublet are in emission. Because the sample spans all Seyfert types and includes LINERs and non-active galaxies, this means that an AGN is not needed to generate OH163 emission. In fact, we do not find a correlation between EW(OH163) and the majority of the AGN and dust temperature tracers discussed in Section 6.3. Therefore, OH163 emission should arise primarily from radiative pumping of the far-IR background, which as discussed above can come from either AGN activity or star formation.

Once again, this idea agrees with Spinoglio et al. (2005), who also claim that OH163 emission arises primarily from radiative pumping. For this doublet, the upper level of the transition is 270 K above the ground state. Spinoglio et al. (2005) argue is too high for collisional excitation to be effective; however, cascading down from absorption of a 34.6μm or 53.3μm photon can lead to OH163 emission. This is a reasonable assumption given the ranges of T_{dust} in the models referenced at the beginning of this section.

The correlations between EW(OH163) and a few of the AGN tracers – log([Ne V] 24.32μm/[Ne II] 12.81μm), log([Ne III] 15.56μm/[Ne II] 12.81μm), and log($L_{[\mathrm{O\ IV}]25.89\mu\mathrm{m}}$) – could suggest that the inclusion of an AGN creating higher luminosities could lead to more far-IR photons available to pump OH163 into stronger emission. Without an AGN, there will still be far-IR photons for radiative pumping – albeit there will be fewer – which is why we see OH163 in weaker emission, but still emission nonetheless. No correlation is found between EW(OH163) and the majority of the AGN tracers however, which could be due to the fact that star formation can also affect the

strength of the far-IR background.

6.4.1.3 OH79

The results in Sections 6.3.3.1, 6.3.3.2, and 6.3.4 show that EW(OH79) has a significant correlation with one of the IR emission-line ratios, [Ne V] 14.32μm/[Ne II] 12.81μm, and the IRAS $f_{25\mu m}/f_{60\mu m}$ dust temperature. Two more IR line ratios and the intrinsic 2-10 keV X-ray luminosity are also uncertain predictors of the doublet. These relationships are all positive, so EW(OH79) emission is strongest when these observables are large (luminous AGN with warm surrounding dust), similar to OH119 and OH163. When we observe the opposite (dim/no AGN with cooler surrounding dust) some galaxies show OH79 in weak emission (similar to OH163) and other galaxies show OH79 in weak absorption (compared to OH119). One possible explanation for this difference could be that emission for the OH79 doublet arises from a mix of collisional excitation and radiative pumping. The effects of the latter could prevent OH79 from being observed in deep absorption when an AGN is not present (similar to OH119), and instead keeping the doublet in either weak emission or weak absorption.

This is supported when comparing EW(OH79) and EW(OH119) in Section 6.3.7. In this smaller subsample of galaxies that have detections of both doublets, there are seven galaxies where OH119 is in absorption, and OH79 is in absorption in four of them. Also, while the peak emission for both doublets is similar (~0.10), but the deepest absorption is about an order of magnitude different (~ -0.15 for EW(OH119) and ~ -0.03 for EW(OH79)). This suggests that while the presence of a dominant AGN affects both doublets similarly, radiative pumping from a far-IR background can keep OH79 in weak emission when there is either a weak or no AGN present.

This argument that OH79 emission arises from a mix of radiative pumping and collisions was first made by Spinoglio et al. (2005). The upper level of the OH79 transition is only 182 K above the ground state, which Spinoglio et al. (2005) argue is a low enough temperature for a warm dense region (AGN) to excite it, at least partially, through collisional excitation. Also, OH79 could be

excited through the same far-IR radiative pumping mechanism as OH163 (i.e. cascading down from absorption of a 34.6μm or 53.3μm photon).

6.4.1.4 OH65

For OH65, we make an argument based on energy levels to rule out collisions as the primary form of excitation. The temperatures derived from the literature models are much lower than what would be needed to collisionally excite OH65 (the upper level of the transition is ~500 K) in any significant amount. While AGNs cannot create warm enough environments to generate OH65 emission, the results from correlating EW(OH65) with log([O IV] 25.89μm/[Ne II] 12.81μm), log([O IV] 25.89μm/[O III] 88.36μm) and log($L_{[\mathrm{O\ IV}]25.89\mu\mathrm{m}}$) suggest that AGNs could drive OH65 absorption. The sample sizes for these correlations are very small (only 5 galaxies); however, there is a strong (r = −0.90, p = 0.04) negative relationship between EW(OH65) and each of these observables. These results suggest that a warm AGN region is needed to populate the lower energy level (~300 K) of the OH65 doublet. In a weak radiation field (i.e. a non-active galaxy), the population of OH molecules in the lower level of the 65μm transition could be scarce, thus suppressing the absorption in this doublet. The one galaxy in the sample with OH65 in emission is NGC 2146, which is a starburst galaxy, supports this idea. Based on the temperatures from the literature, the emission in NGC 2146 is likely not a result of collisional excitation. Radiative pumping is therefore the more likely method.

6.4.1.5 OH71

OH71 is the highest energy transition in the sample, with the upper level of the transition ~600 K. Therefore, this temperature is too high for significant amounts of collisionally excited OH71 emission, similar to OH65. It is possible that we only observe OH71 exclusively in absorption because it is such a high energy transition. OH71 has the smallest number of detections in the sample, so it is possible that more observations could reveal rare cases of emission. When investigating possible correlations with AGN tracers, the statistics were too small (three or fewer

galaxies) for the OH71 doublet to investigate if a similar phenomenon to OH65 is observed. More data are needed to see if AGNs drive OH71 absorption, similar to OH65.

6.4.1.6 OH84

For OH84, it is difficult to strongly support either collisional excitation or radiative pumping as the main mode of excitation. On the energy diagram, OH84 does not lie significantly above the temperature that the nuclear region is thought to have, so at least a small amount of collisional excitation could be possible in the warmest galaxies. We did not find a relationship with any of the AGN, radiation field hardness, and dust temperature tracers; however, small sample sizes for many of these test make it difficult to draw conclusions. More data are needed to make a strong argument about whether OH84 emission arises from collisional excitation or radiative pumping.

6.4.2 Interpretation of the Obscuration & Column density

A high column density of gas and dust might be expected to enhance both the absorption strength of OH and the dust obscuration. We used two observables as proxies for the column density of interstellar matter along our line-of-sight to the center of the galaxy. The Hα/Hβ ratio measures dust extinction since it increases from its intrinsic ratio (which may range from ~3 in low-density ionized gas to values greater than 4 in the BLR of a Seyfert 1 nucleus (Lacy et al., 1982; Malkan et al., 2017). The brighter the AGN, the more concentrated this line emission should be in the nucleus. For extremely dusty galaxies (e.g., ULIRGs), the optical line ratios could substantially under-estimate the dust column density to the galaxy center.

At high extinctions, a reliable tracer in the mid-IR range is the depth of the silicate absorption at 9.7μm. In Seyfert 1's silicates are often seen in emission (Hatziminaoglou et al., 2015). We find that the silicate feature has a more significant impact on EW(OH119) than the Balmer decrement. A relationship between EW(OH65) and $S_{\rm sil}$ has also been shown in González-Alfonso et al. (2015). As discussed in Section 6.3.5.1, we find a high correlation coefficient (r = 0.60) but a p-value greater than 0.05. The high p-value in this situation could be partially attributed to the low sample

size (eight galaxies). Therefore, our sample does not contradict the correlation between EW(OH65) and $S_{\rm sil}$ found in González-Alfonso et al. (2015), but is too small to be conclusive. With only a small sample (four galaxies), this study finds no correlation between EW(OH65) and the Balmer decrement as well. The results for EW(OH79) oppose the idea that a IR dust tracer is preferable as that doublet shows a stronger correlation with the optical Balmer decrement.

There appears to be some connection between the strength of the CO(16-15) line and how obscured the galaxy is. The spectral separation between OH163 and the CO(16-15) transition is small enough that CO(16-15) is within the spectral range of the OH163 observations. CO(16-15) is too weak to be detected in the majority of the sample; however, some examples of galaxies where the transition is clearly visible are NGC 253, NGC 1068, NGC 3079, NGC 4418, and NGC 4945. The transition is very prominent in NGC 4418, which has a deeply buried Seyfert 2 nucleus and the second deepest silicate absorption in the sample ($S_{\rm sil} = -4.00$), while it is not so strong in NGC 253, which is a starburst. The upper level of CO(16-15) is ~750 K, so a very warm and dense region is needed to produce this emission. In our sample, CO(16-15) is much more likely to be observed in the most obscured galaxies; however, it is not guaranteed to find the transition in these galaxies. IRAS 17208-0014 has the strongest silicate absorption ($S_{\rm sil} = -4.07$); however, CO(16-15) is not visible in the spectrum.

6.5 Summary

In this paper, we investigate possible relationships between the strength of an AGN/starburst component in the host galaxy with the EW values from a series of six OH doublets (OH65, OH71, OH79, OH84, OH119, OH163) in a sample of 178 galaxies. The sample contains a wide range of optical spectral classifications − a complete range of Seyfert-types, LINERs, and non-active star-forming galaxies. The sample was observed using the PACS instrument on the *Herschel Space Observatory* and collected from *Hershel Science Archive* and the optical spectral classifications come from the Véron-Cetty & Véron (2010) catalog.

We look for trends within the OH data itself, and with galaxy observables. To probe the spectral type of the galaxy, brightness of an AGN/starburst component, and radiation field of the galaxy, we use many observables. These include various IR emission-line ratios, various IR emission-line luminosities, the intrinsic 2-10 keV X-ray luminosity, and the 25μm/60μm IRAS flux density ratio as a proxy for dust temperature. We use the strength of the silicate 9.7μm feature and the Balmer decrement to probe dust extinction.

The main results of this study are as follows:

1. In our sample, we find OH71 to be always in absorption, OH65 and OH84 to be primarily in absorption, OH119 to have a comparable number of both emission and absorption observations, OH79 to be primarily in emission, and OH163 to be always in emission.

2. For OH79, OH119, and OH163, we find that galaxies containing a bright AGN creating a warm, dense environment are more likely to drive these three lines into strong emission. For galaxies that have an obscured AGN or no AGN, these show strong absorption (OH119), weak emission (OH163), and a mixture of weak absorption and weak emission (OH79). These differences could be explained by their method of excitation: collisional excitation (OH119), radiative pumping (OH163), and a mix of both processes (OH79).

3. The results for EW(OH65) suggest that there is a possibility that absorption becomes stronger with increasing AGN strength. This could mean that a warm (~300 K), dense environment is required to populate the ground levels to enable these transitions, and a less extreme environment (e.g., star-forming galaxies) may not be able to excite a significant number of OH molecules to generate the OH65 transition. However, this is only based on samples of five galaxies, so more data are needed to confirm this relationship.

4. We find a relationship between dust extinction and the OH79 and OH119 doublets. This relationship is seen with both the silicate feature and Balmer decrement for OH79 and OH119. EW(OH79) has a better correlation with the Balmer decrement, while EW(OH119)

has a stronger relationship with $S_{\rm sil}$. For these doublets, we see emission weaken/absorption strengthen as the dust extinction becomes stronger, suggesting that the warm and dense molecular gas producing the OH emission/absorption is associated with a dusty environment.

5. No correlations are found between either EW(OH71) or EW(OH84) with any of the AGN, radiation field hardness, dust temperature, and dust extinction tracers.

6. P-Cygni features are observed in ~10% of the galaxies in our sample. We find that one galaxy (Circinus) has a reverse P-Cygni feature, which indicates a molecular inflow.

This work is based on observations made with the *Herschel* and the *Spitzer* IR space observatories, whose observations are at the base of the present study. Future missions SPICA (e.g., González-Alfonso et al. 2017a; Spinoglio et al. 2017; Roelfsema et al. 2018) and NASA Origins (e.g., Meixner et al. 2018) will be able to extend this work to even larger samples of galaxies, both in the local and distant Universe.

Appendix

6A Data Tables

Table 6A.1: The Sample

Object Name	R.A. (J2000)	Dec. (J2000)	z	Optical Spectral Classification	Transitions Observed (μm)
(1)	(2)	(3)	(4)	(5)	(6)
Mrk334	00 03 09.6038	+21 57 36.8064	0.021945	Seyfert-1.8	79
IRAS00182-7112	00 20 34.7210	−70 55 26.2488	0.326999	Seyfert-2	79,84,119
IRAS00198-7926	00 21 53.6141	−79 10 07.9572	0.0728	Seyfert-2	79
NGC253	00 47 33.0727	−25 17 18.9960	0.000811	Starburt	65,71,79,84,119,163
Mrk348	00 48 47.1468	+31 57 25.1280	0.015034	Seyfert-1	84
IZw1	00 53 34.9236	+12 41 35.9232	0.0612	Seyfert-1n	65,79,119,163
IRAS00521-7054	00 53 56.2310	−70 38 04.2216	0.0689	Seyfert-1	79
ESO541-IG12	01 02 17.3818	−19 40 08.6556	0.056552	Seyfert-2	79
IRAS01003-2238	01 02 49.9894	−22 21 57.2616	0.117835	Seyfert-2	79,119
NGC454E	01 14 24.9300	−55 23 49.2936	0.012158	Seyfert-2	79
M74	01 36 41.7384	+15 47 00.8592	0.002192	Starburt	79
IRAS01364-1042	01 38 52.8629	−10 27 11.5848	0.048247	LINER	79
IIIZw35	01 44 30.5400	+17 06 08.8056	0.027436	Seyfert-2	79
Mrk1014	01 59 50.2483	+00 23 40.7436	0.16311	Seyfert-1.5	79,119
NGC788	02 01 06.4567	−06 48 57.1284	0.013603	Seyfert-1	79
Mrk590	02 14 33.5640	−00 46 00.2568	0.026385	Seyfert-1	79
IC1816	02 31 50.9863	−36 40 19.5312	0.016945	Seyfert-2	79
NGC973	02 34 20.1233	+32 30 20.4912	0.016195	Seyfert-2	79
NGC1068	02 42 40.7071	−00 00 48.0204	0.003793	Seyfert-1	65,71,79,84,119,163
Mrk1066	02 59 58.5960	+36 49 13.7172	0.012025	Seyfert-2	79,119
NGC1222	03 08 56.7413	−02 57 18.5688	0.008079	Starburt	79
Mrk1073	03 15 01.4347	+42 02 08.9124	0.023343	Seyfert-2	79
NGC1266	03 16 00.7435	−02 25 38.6292	0.007238	LINER	79
NGC1275	03 19 48.1524	+41 30 42.1452	0.017559	Seyfert-1.5	79

Continued on next page

Table 6A.1 – *Continued from previous page*

Object Name	R.A. (J2000)	Dec. (J2000)	z	Optical Spectral Classification	Transitions Observed (μm)
(1)	(2)	(3)	(4)	(5)	(6)
Mrk609	03 25 25.3747	−06 08 37.9932	0.034488	Seyfert-1.8	79
NGC1365	03 33 36.3828	−36 08 25.7136	0.005457	Seyfert-1.8	65,79,119,163
NGC1386	03 36 46.2043	−35 59 57.2964	0.002895	Seyfert-1i	79
IRAS03450+0055	03 47 40.1952	+01 05 13.9992	0.031	Seyfert-1.5	79
IRAS04103-2838	04 12 19.4510	−28 30 24.9876	0.117464	LINER	79
ESO420-G13	04 13 49.6872	−32 00 25.0884	0.011908	Seyfert-2	79
NGC1566	04 20 00.4058	−54 56 16.6056	0.005017	Seyfert-1.5	119
3C120	04 33 11.0940	+05 21 15.7104	0.03301	Seyfert-1.5	79,119
MCG-05-12-006	04 52 04.9634	−32 59 25.7352	0.018753	LINER	79
NGC1808	05 07 42.3377	−37 30 45.9216	0.003319	Starburt	79
Zw468.002NED01	05 08 19.6894	+17 21 48.1356	0.017505	Seyfert-2	79
Zw468.002NED02	05 08 21.2146	+17 22 08.0400	0.016842	Seyfert-2	79
IRAS05189-2524	05 21 01.3966	−25 21 45.2772	0.042563	Seyfert-1	65,71,79,84,119,163
NGC1961	05 42 04.6459	+69 22 42.4704	0.013122	LINER	79
UGC3351	05 45 47.8942	+58 42 03.9312	0.01486	Seyfert-2	79
NGC2110	05 52 11.3803	−07 27 22.4532	0.007789	Seyfert-1	119
ESO005-G04	06 05 41.3597	−86 37 54.1956	0.006228	Seyfert-2	119
Mrk3	06 15 36.4104	+71 02 14.9388	0.013509	Seyfert-1	79
NGC2146	06 18 37.7933	+78 21 24.6024	0.002979	Starburt	65,163
Mrk620	06 50 08.6539	+60 50 44.7936	0.006138	Seyfert-1	79
IRAS07027-6011	07 03 24.2563	−60 15 22.4136	0.031322	Seyfert-2	79
AM0702-601NED02	07 03 28.6291	−60 16 44.3568	0.031105	Seyfert-2	79
Mrk9	07 36 57.0348	+58 46 13.4724	0.039874	Seyfert-1.5	79
IRAS07598+6508	08 04 30.4843	+64 59 52.6668	0.1483	Seyfert-1	79,119
Mrk622	08 07 41.0030	+39 00 15.2424	0.023229	Seyfert-2	79
IRAS08311-2459	08 33 20.5961	−25 09 33.8220	0.100449	Seyfert-1i	79,119
3C218	09 18 05.6477	−12 05 43.5552	0.053841	LINER	79
MCG-01-24-012	09 20 46.2653	−08 03 21.9564	0.019644	Seyfert-2	79

Continued on next page

Table 6A.1 – *Continued from previous page*

Object Name	R.A. (J2000)	Dec. (J2000)	z	Optical Spectral Classification	Transitions Observed (μm)
(1)	(2)	(3)	(4)	(5)	(6)
NGC2841	09 22 02.6906	+50 58 35.6232	0.002128	LINER	79
Mrk705	09 26 03.2729	+12 44 03.8616	0.029151	Seyfert-1.2	79
UGC5101	09 35 51.5976	+61 21 11.7072	0.039367	Seyfert-1	65,79,119
IRAS09413+4843	09 44 42.2263	+48 29 16.6308	0.055303	Seyfert-2	79
NGC2992	09 45 41.9443	−14 19 34.7592	0.00771	Seyfert-1	119
ESO434-G40	09 47 40.1434	−30 56 55.9320	0.008486	Seyfert-1i	119
M82	09 55 52.1724	+69 40 47.6148	0.000677	Starburt	65,119,163
NGC3081	09 59 29.5414	−22 49 34.5900	0.007976	Seyfert-1	119
3C234	10 01 49.5324	+28 47 08.8836	0.184925	Seyfert-1.9	79
NGC3079	10 01 57.8491	+55 40 47.5752	0.003723	LINER	65,79,84,119,163
3C236	10 06 01.7378	+34 54 10.4832	0.1005	LINER	79
NGC3184	10 18 16.9380	+41 25 27.4008	0.001975	Starburt	79
NGC3198	10 19 55.0022	+45 32 59.3376	0.002202	Starburt	79
NGC3227	10 23 30.5710	+19 51 54.2952	0.003859	Seyfert-1.5	79,119,163
NGC3256	10 27 51.2376	−43 54 13.9176	0.009354	Starburt	79
M95	10 43 57.7049	+11 42 13.2192	0.002595	Starburt	79
NGC3393	10 48 23.4595	−25 09 43.4160	0.012509	Seyfert-2	79
NGC3516	11 06 47.4667	+72 34 07.1364	0.008836	Seyfert-1.5	79,119
IRAS11095-0238	11 12 03.3701	−02 54 22.7232	0.106634	LINER	79,119
NGC3621	11 18 15.8839	−32 48 46.0584	0.002435	Seyfert-2	79
Mrk1298	11 29 16.7186	−04 24 07.2684	0.06196	Seyfert-1	119
NGC3783	11 39 01.7114	−37 44 18.9780	0.00973	Seyfert-1.5	79,119
NGC3938	11 52 49.4218	+44 07 14.6316	0.002699	Starburt	79
NGC3982	11 56 28.1167	+55 07 30.9756	0.003699	Seyfert-1.9	79,119,163
NGC4051	12 03 09.6017	+44 31 52.7484	0.002336	Seyfert-1n	79,119,163
IRAS12018+1941	12 04 24.5484	+19 25 10.0236	0.168	Seyfert-2	79
UGC7064	12 04 43.3190	+31 10 37.8804	0.024997	Seyfert-1.9	79
NGC4138	12 09 29.7782	+43 41 07.0620	0.002962	Seyfert-1.9	119

Continued on next page

Table 6A.1 – *Continued from previous page*

Object Name	R.A. (J2000)	Dec. (J2000)	z	Optical Spectral Classification	Transitions Observed (μm)
(1)	(2)	(3)	(4)	(5)	(6)
IRAS12071-0444	12 09 45.1171	−05 01 13.9728	0.128355	Seyfert-2	79,119
NGC4151	12 10 32.5812	+39 24 21.0564	0.003319	Seyfert-1.5	79,119
NGC4388	12 25 46.7693	+12 39 43.2396	0.008419	Seyfert-1	79,84,119,163
NGC4395	12 25 48.8592	+33 32 48.6672	0.001064	Seyfert-1.8	119
NGC4418	12 26 54.6206	−00 52 39.4500	0.007268	Seyfert-2	65,71,79,84,119,163
3C273	12 29 06.6953	+02 03 08.5932	0.158339	Seyfert-1	79,119
NGC4536	12 34 27.0715	+02 11 17.4768	0.006031	Starburt	79
NGC4507	12 35 36.6329	−39 54 33.5556	0.011801	Seyfert-1	79,119
NGC4559	12 35 57.6502	+27 57 35.9064	0.002692	Starburt	79
NGC4569	12 36 49.7950	+13 09 46.5588	0.000784	LINER	79
NGC4579	12 37 43.5170	+11 49 05.7180	0.00506	LINERb	79,119
NGC4593	12 39 39.4550	−05 20 39.0156	0.0091	Seyfert-1	79,119
NGC4594	12 39 59.4331	−11 37 22.6020	0.003416	LINER	79
IC3639	12 40 52.8415	−36 45 21.0672	0.010924	Seyfert-1	79,119,163
NGC4631	12 42 07.7616	+32 32 34.6308	0.002021	Starburt	79
NGC4725	12 50 26.5766	+25 30 02.8908	0.004023	Seyfert-2	79
NGC4736	12 50 53.0830	+41 07 12.7236	0.001027	LINER	79
IRAS12514+1027	12 54 00.8126	+10 11 12.3936	0.319	Seyfert-2	119
Mrk231	12 56 14.2291	+56 52 25.2192	0.042171	Seyfert-1	65,71,79,84,119,163
NGC4922	13 01 24.4958	+29 18 30.1284	0.023586	Seyfert-2	79
NGC4941	13 04 13.1066	−05 33 05.6700	0.003696	Seyfert-2	79,119
NGC4945	13 05 27.2633	−49 28 03.9972	0.001878	Seyfert-2	65,71,79,84,119,163
ESO323-G77	13 06 26.1154	−40 24 52.6284	0.015014	Seyfert-1.2	79
NGC5033	13 13 27.4738	+36 35 38.1192	0.002919	Seyfert-1.8	79,119
IRAS13120-5453	13 15 06.3348	−55 09 22.7736	0.030761	Seyfert-2	65,71,79,84,119,163
MCG-03-34-064	13 22 24.4668	−16 43 42.4488	0.016541	Seyfert-1	79
CentauruA	13 25 27.6499	−43 01 09.2424	0.001825	Seyfert-2	65,71,79,84,119,163
MCG-06-30-015	13 35 53.7667	−34 17 44.2320	0.007749	Seyfert-1.5	79,119

Continued on next page

Table 6A.1 – *Continued from previous page*

Object Name	R.A. (J2000)	Dec. (J2000)	z	Optical Spectral Classification	Transitions Observed (μm)
(1)	(2)	(3)	(4)	(5)	(6)
M83	13 37 00.8647	−29 51 55.9152	0.001711	Starburt	65,79,119,163
IRAS13349+2438	13 37 18.7135	+24 23 03.1776	0.107641	Seyfert-1n	79
Mrk266SW	13 38 17.2342	+48 16 32.0232	0.0276	Seyfert-2	79,119
NGC5273	13 42 08.3774	+35 39 15.4836	0.003619	Seyfert-1.9	119
Mrk273	13 44 42.0850	+55 53 13.0236	0.03778	Seyfert-2	65,71,79,84,119,163
PKS1345+12	13 47 33.4116	+12 17 24.0828	0.12174	Seyfert-2	79,119,163
IC4329A	13 49 19.2478	−30 18 34.0812	0.016054	Seyfert-1.2	79
NGC5347	13 53 17.8054	+33 29 26.9160	0.007789	Seyfert-1	79
Mrk463E	13 56 02.8855	+18 22 18.1884	0.05	Seyfert-1	79,119
Circinu	14 13 09.8640	−65 20 20.4180	0.001448	Seyfert-1	65,79,119,163
NGC5506	14 13 14.8757	−03 12 27.6984	0.006181	Seyfert-1	79,119
NGC5548	14 17 59.5536	+25 08 12.6348	0.017175	Seyfert-1.5	79
Mrk1383	14 29 06.5710	+01 17 06.2196	0.08657	Seyfert-1	79
IRAS14394+5332	14 41 04.4220	+53 20 09.0456	0.104542	Seyfert-2	119
Mrk478	14 42 07.4724	+35 26 22.9236	0.079055	Seyfert-1n	79,119
NGC5728	14 42 23.8990	−17 15 10.7820	0.009353	Seyfert-1.9	79,119
3C305	14 49 21.5957	+63 16 13.9512	0.041639	Seyfert-2	79
IC4518A	14 57 41.1614	−43 07 55.2540	0.016261	Seyfert-2	79
NGC5793	14 59 24.7471	−16 41 36.4236	0.011645	Seyfert-2	79
NGC5899	15 15 03.2662	+42 02 59.5716	0.008546	Seyfert-2	119
3C317	15 16 44.4874	+07 01 17.7420	0.034457	Seyfert-2	79
Mrk848B	15 18 06.1210	+42 44 44.8116	0.040191	LINER	79
IRAS15206+3342	15 22 38.0904	+33 31 36.1164	0.124409	Seyfert-2	119
Arp220	15 34 57.2443	+23 30 11.4048	0.018126	Seyfert-2	65,71,79,84,119,163
NGC5990	15 46 16.3632	+02 24 55.5840	0.012806	Seyfert-2	79
IRAS15462-0450	15 48 56.8114	−04 59 33.5292	0.099792	Seyfert-1n	79,119
PKS1549-79	15 56 58.8979	−79 14 04.2180	0.1522	Seyfert-1	79
Mrk876	16 13 57.1718	+65 43 09.9444	0.129	Seyfert-1	79,119

Continued on next page

Table 6A.1 – *Continued from previous page*

Object Name	R.A. (J2000)	Dec. (J2000)	z	Optical Spectral Classification	Transitions Observed (μm)
(1)	(2)	(3)	(4)	(5)	(6)
NGC6166	16 28 38.2543	+39 33 04.1436	0.030354	Seyfert-1-Q	79
Mrk883	16 29 52.8703	+24 26 38.0976	0.037496	Seyfert-1.9	79
ESO137-G34	16 35 13.9807	−58 04 47.9388	0.009144	Seyfert-2	119
NGC6221	16 52 46.3414	−59 13 00.8112	0.004999	Seyfert-2	119
NGC6240	16 52 58.8862	+02 24 03.6288	0.02448	LINER	65,71,79,84,119,163
NGC6300	17 16 59.5411	−62 49 13.9224	0.003699	Seyfert-2	119
IRAS17208-0014	17 23 21.9626	−00 17 00.8088	0.04281	LINER	65,71,79,84,119,163
IRAS18216+6418	18 21 57.2215	+64 20 36.0708	0.297	Seyfert-1.2	79,119
Fairall49	18 36 58.2146	−59 24 08.2332	0.020021	Seyfert-1	79
ESO103-G35	18 38 20.3078	−65 25 39.2412	0.013286	Seyfert-2	79,84,119
ESO140-G043	18 44 53.9914	−62 21 52.8264	0.014178	Seyfert-1.5	79,119
NGC6786	19 10 53.9232	+73 24 36.6444	0.025017	Seyfert-2	79
ESO141-G55	19 21 14.1430	−58 40 12.9828	0.037109	Seyfert-1.2	79
IRAS19254-7245	19 31 21.4243	−72 39 21.4848	0.061709	Seyfert-1	79,119
NGC6814	19 42 40.5804	−10 19 25.2192	0.005214	Seyfert-1.5	119
ESO339-G11	19 57 37.5576	−37 56 08.3112	0.019199	Seyfert-2	79
3C405	19 59 28.3490	+40 44 02.0616	0.056075	Seyfert-1.9	65,79,119
IRAS20037-1547	20 06 31.8302	−15 39 06.8184	0.191899	Seyfert-1	79,119
NGC6860	20 08 46.8727	−61 05 59.7336	0.014884	Seyfert-1.5	79
MCG+04-48-002	20 28 35.0647	+25 43 59.9340	0.01391	Seyfert-1	79
NGC6926	20 33 06.1092	−02 01 38.4960	0.019613	Seyfert-2	79
Mrk509	20 44 09.7555	−10 43 24.6864	0.034397	Seyfert-1.5	79,119
PKS2048-57	20 52 02.3414	−57 04 07.4928	0.011348	Seyfert-1	79,119
UGC11763	21 32 27.8167	+10 08 19.2768	0.062977	Seyfert-1.5	119
IC5135	21 48 19.5166	−34 57 04.6728	0.016151	Seyfert-1.9	79,119,163
NGC7172	22 02 01.8792	−31 52 10.7796	0.008683	Seyfert-2	79,119,163
IRAS22017+0319	22 04 19.1628	+03 33 51.1164	0.0611	Seyfert-1	79
NGC7213	22 09 16.2394	−47 09 59.9508	0.005839	LINERb	79,119

Continued on next page

Table 6A.1 – *Continued from previous page*

Object Name	R.A. (J2000)	Dec. (J2000)	z	Optical Spectral Classification	Transitions Observed (μm)
(1)	(2)	(3)	(4)	(5)	(6)
3C445	22 23 49.5487	−02 06 12.8880	0.055879	Seyfert-1.5	79
ESO602-G25	22 31 25.4808	−19 02 04.2540	0.025041	LINER	79
NGC7314	22 35 46.2106	−26 03 01.5840	0.004763	Seyfert-1	79,119
UGC12138	22 40 17.0690	+08 03 13.4964	0.024974	Seyfert-1.8	79
NGC7469	23 03 15.6154	+08 52 25.8888	0.016317	Seyfert-1.5	65,71,79,84,119,163
NGC7479	23 04 56.6462	+12 19 22.5012	0.007942	Seyfert-1.9	119
IC5298	23 16 00.6881	+25 33 23.9472	0.027422	Seyfert-2	79
NGC7591	23 18 16.2811	+06 35 08.9196	0.0165312	LINER	79
NGC7592W	23 18 21.7963	−04 24 57.0528	0.024183	Seyfert-2	79
NGC7582	23 18 23.6107	−42 22 13.6020	0.005254	Seyfert-1	79,84,119,163
NGC7603	23 18 56.6530	+00 14 37.8600	0.029524	Seyfert-1.5	79
NGC7674	23 27 56.7070	+08 46 44.3856	0.028924	Seyfert-1	79
NGC7679	23 28 46.6524	+03 30 41.0760	0.017139	Seyfert-1.9	79
IRAS23365+3604	23 39 01.2696	+36 21 08.5896	0.06448	LINER	65,79,84,119

Note. — Col. (1): Target name. Col. (2): Right ascension (collected from the 2MASS Point Source Catalog). Col. (3): Declination (collected from the 2MASS Point Source Catalog). Col. (4): Redshifts gathered from the NASA/IPAC Extragalactic Database (NED). Col. (5): Optical spectral type taken from the Véron-Cetty & Véron (2010) Catalog. Col. (6): The OH doublets that were observed for each object.

Table 6A.2: IRAS Data

Object Name	IRAS Catalog	$f_{25\mu m}$ Flux (Jy)	$f_{60\mu m}$ Flux (Jy)
(1)	(2)	(3)	(4)
Mrk334	PSC v2.1	1.054 ± 0.116	4.255 ± 0.511
IRAS00182-7112	PSC v2.0	< 0.250	1.300 ± 0.130
IRAS00198-7926	PSC v2.1	1.210 ± 0.097	3.196 ± 0.288
NGC253	PSC v2.1	117.100 ± 4.684	758.700 ± 45.522
Mrk348	PSC v2.0	0.773 ± 0.062	1.440 ± 0.115
IZw1	FSC v2.0	1.210 ± 0.121	2.240 ± 0.179
IRAS00521-7054	PSC v2.1	0.837 ± 0.059	1.107 ± 0.077
ESO541-IG12	PSC v2.1	0.294 ± 0.047	0.718 ± 0.072
IRAS01003-2238	PSC v2.0	0.555 ± 0.044	2.240 ± 0.179
NGC454E	FSC v2.0	0.417 ± 0.033	1.480 ± 0.118
M74	PSC v2.0	< 0.399	3.010 ± 0.241
IRAS01364-1042	PSC v2.1	0.415 ± 0.062	6.745 ± 0.809
IIIZw35	PSC v2.1	1.074 ± 0.118	13.300 ± 1.729
Mrk1014	PSC v2.1	0.626 ± 0.163	2.338 ± 0.281
NGC788	FSC v2.0	< 0.515	0.511 ± 0.041
Mrk590	PSC v2.0	< 0.379	0.533 ± 0.043
IC1816	PSC v2.1	0.423 ± 0.030	1.420 ± 0.099
NGC973	PSC v2.1	0.313 ± 0.050	1.683 ± 0.151
NGC1068	PSC v2.1	86.83 ± 3.473	185.800 ± 14.864
Mrk1066	PSC v2.1	2.313 ± 0.162	10.450 ± 0.941
NGC1222	PSC v2.0	2.380 ± 0.190	12.800 ± 1.024

Continued on next page

Table 6A.2 – *Continued from previous page*

Object Name	IRAS Catalog	$f_{25\mu m}$ Flux (Jy)	$f_{60\mu m}$ Flux (Jy)
(1)	(2)	(3)	(4)
Mrk1073	PSC v2.1	1.425 ± 0.100	8.250 ± 0.743
NGC1266	PSC v2.0	1.160 ± 0.093	11.100 ± 0.888
NGC1275	PSC v2.1	3.618 ± 0.217	7.220 ± 0.650
Mrk609	PSC v2.0	0.430 ± 0.034	2.580 ± 0.206
NGC1365	PSC v2.1	11.090 ± 0.555	78.150 ± 7.815
NGC1386	PSC v2.1	1.441 ± 0.086	5.886 ± 0.471
IRAS03450+0055	PSC v2.0	0.584 ± 0.047	0.501 ± 0.040
IRAS04103-2838	PSC v2.1	0.575 ± 0.046	1.766 ± 0.141
ESO420-G13	PSC v2.1	2.191 ± 0.131	13.740 ± 0.962
NGC1566	PSC v2.1	0.885 ± 0.124	12.700 ± 1.143
3C120	PSC v2.1	0.708 ± 0.064	1.315 ± 0.092
MCG-05-12-006	PSC v2.1	1.300 ± 0.104	7.857 ± 0.707
NGC1808	PSC v2.1	15.870 ± 0.635	97.120 ± 8.741
Zw468.002NED01			
Zw468.002NED02	FSC v2.0	1.094 ± 0.066	10.210 ± 0.511
IRAS05189-2524	PSC v2.1	3.523 ± 0.176	13.940 ± 0.976
NGC1961	PSC v2.0	0.475 ± 0.038	6.600 ± 0.528
UGC3351	PSC v2.1	0.807 ± 0.073	14.240 ± 1.282
NGC2110	PSC v2.1	0.881 ± 0.070	4.459 ± 0.401
ESO005-G04	PSC v2.1	0.730 ± 0.036	7.694 ± 0.462
Mrk3	PSC v2.1	2.841 ± 0.170	3.914 ± 0.313

Continued on next page

Table 6A.2 – *Continued from previous page*

Object Name	IRAS Catalog	$f_{25\mu m}$ Flux (Jy)	$f_{60\mu m}$ Flux (Jy)
(1)	(2)	(3)	(4)
NGC2146	PSC v2.1	17.260 ± 0.690	141.700 ± 12.753
Mrk620	PSC v2.1	1.364 ± 0.095	6.328 ± 0.570
IRAS07027-6011	PSC v2.0	0.840 ± 0.084	4.900 ± 0.686
AM0702-601NED02			
Mrk9	PSC v2.1	0.525 ± 0.053	0.878 ± 0.079
IRAS07598+6508	PSC v2.0	0.624 ± 0.050	1.750 ± 0.140
Mrk622	PSC v2.0	0.445 ± 0.036	1.380 ± 0.110
IRAS08311-2459	PSC v2.1	1.095 ± 0.066	4.959 ± 0.347
3C218	Golombek et al. 1988	< 0.035	0.115 ± 0.017
MCG-01-24-012	PSC v2.0	0.477 ± 0.038	0.621 ± 0.050
NGC2841	PSC v2.1	< 0.250	2.430 ± 0.267
Mrk705	PSC v2.1	< 0.302	0.687 ± 0.055
UGC5101	PSC v2.1	1.045 ± 0.084	12.090 ± 1.330
IRAS09413+4843	FSC v2.0	0.188 ± 0.030	0.556 ± 0.044
NGC2992	PSC v2.1	1.365 ± 0.123	6.872 ± 0.893
ESO434-G40			
M82	PSC v2.1	274.300 ± 10.972	1170.000 ± 58.500
NGC3081			
3C234	FSC v2.0	0.324 ± 0.026	0.113 ± 0.009
NGC3079	PSC v2.1	2.032 ± 0.142	42.860 ± 4.714
3C236	Golombek et al. 1988	< 0.020	0.072 ± 0.011

Continued on next page

Table 6A.2 – *Continued from previous page*

Object Name	IRAS Catalog	$f_{25\mu m}$ Flux (Jy)	$f_{60\mu m}$ Flux (Jy)
(1)	(2)	(3)	(4)
NGC3184	PSC v2.0	< 0.544	2.350 ± 0.188
NGC3198	PSC v2.1	0.458 ± 0.041	3.703 ± 0.296
NGC3227	PSC v2.1	1.737 ± 0.139	7.980 ± 0.798
NGC3256	PSC v2.1	15.430 ± 0.926	94.630 ± 12.302
M95	PSC v2.1	1.915 ± 0.230	17.370 ± 2.606
NGC3393	PSC v2.1	0.711 ± 0.078	2.376 ± 0.285
NGC3516	PSC v2.1	0.919 ± 0.064	1.739 ± 0.122
IRAS11095-0238	PSC v2.1	0.457 ± 0.055	3.226 ± 0.290
NGC3621	PSC v2.0	0.704 ± 0.056	13.900 ± 1.112
Mrk1298	FSRC	0.335 ± 0.027	0.603 ± 0.048
NGC3783	PSC v2.1	2.435 ± 0.170	3.372 ± 0.371
NGC3938	PSC v2.1	0.224 ± 0.031	4.927 ± 0.443
NGC3982	PSC v2.1	0.836 ± 0.067	6.918 ± 0.623
NGC4051	PSC v2.1	1.398 ± 0.126	8.282 ± 0.828
IRAS12018+1941	PSC v2.0	0.272 ± 0.022	1.640 ± 0.131
UGC7064	PSC v2.0	0.384 ± 0.031	2.860 ± 0.229
NGC4138			
IRAS12071-0444	PSC v2.0	0.528 ± 0.042	2.580 ± 0.206
NGC4151	FSRC	4.833 ± 0.387	6.315 ± 0.505
NGC4388	PSC v2.1	3.553 ± 0.249	10.900 ± 1.199
NGC4395	FSC v2.0	0.205 ± 0.043	2.375 ± 0.190

Continued on next page

Table 6A.2 – *Continued from previous page*

Object Name	IRAS Catalog	$f_{25\mu m}$ Flux (Jy)	$f_{60\mu m}$ Flux (Jy)
(1)	(2)	(3)	(4)
NGC4418	PSC v2.0	9.570 ± 0.766	43.900 ± 3.512
3C273	PSC v2.0	0.928 ± 0.074	2.220 ± 0.178
NGC4536	PSC v2.0	3.470 ± 0.278	30.300 ± 2.424
NGC4507	PSC v2.1	1.407 ± 0.141	4.583 ± 0.550
NGC4559	PSC v2.1	0.400 ± 0.052	5.332 ± 0.533
NGC4569	PSC v2.1	0.880 ± 0.097	7.211 ± 0.865
NGC4579	PSC v2.1	< 0.332	4.537 ± 0.635
NGC4593	PSC v2.1	0.921 ± 0.221	2.809 ± 0.337
NGC4594	FSC v2.0	0.497 ± 0.040	3.110 ± 0.249
IC3639	PSC v2.1	2.304 ± 0.207	7.205 ± 0.865
NGC4631	PSC v2.0	2.990 ± 0.239	51.500 ± 4.120
NGC4725	PSC v2.0	< 0.250	0.718 ± 0.057
NGC4736	PSC v2.1	3.476 ± 0.278	56.070 ± 8.411
IRAS12514+1027	PSC v2.1	< 0.474	0.744 ± 0.074
Mrk231	PSC v2.1	8.517 ± 0.511	33.600 ± 3.360
NGC4922	PSC v2.0	1.310 ± 0.105	6.610 ± 0.529
NGC4941	PSC v2.1	< 0.575	1.335 ± 0.147
NGC4945	PSC v2.1	14.240 ± 0.712	388.100 ± 19.405
ESO323-G77	PSC v2.1	1.244 ± 0.100	5.514 ± 0.496
NGC5033	PSC v2.0	1.050 ± 0.084	13.300 ± 1.064
IRAS13120-5453	PSC v2.1	2.965 ± 0.178	41.490 ± 4.564

Continued on next page

Table 6A.2 – *Continued from previous page*

Object Name	IRAS Catalog	$f_{25\mu m}$ Flux (Jy)	$f_{60\mu m}$ Flux (Jy)
(1)	(2)	(3)	(4)
MCG-03-34-064	PSC v2.0	2.790 ± 0.223	5.710 ± 0.457
CentaurusA	PSC v2.0	15.000 ± 1.200	172.000 ± 13.760
MCG-06-30-015	PSC v2.0	0.805 ± 0.064	1.120 ± 0.090
M83	PSC v2.1	19.560 ± 1.174	103.700 ± 12.444
IRAS13349+2438	PSC v2.1	0.874 ± 0.096	0.692 ± 0.090
Mrk266SW	PSC v2.1	1.021 ± 0.123	7.291 ± 0.802
NGC5273	PSC v2.0	< 0.504	1.200 ± 0.096
Mrk273	PSC v2.1	2.325 ± 0.140	23.700 ± 2.370
PKS1345+12	PSC v2.1	0.665 ± 0.080	2.011 ± 0.241
IC4329A	PSC v2.0	2.250 ± 0.180	2.040 ± 0.163
NGC5347	PSC v2.1	0.922 ± 0.083	1.443 ± 0.130
Mrk463E	PSC v2.1	1.614 ± 0.129	2.184 ± 0.197
Circinus	PSC v2.1	68.440 ± 2.738	248.700 ± 24.870
NGC5506	PSC v2.1	3.642 ± 0.255	8.814 ± 0.970
NGC5548	PSC v2.0	0.760 ± 0.061	1.040 ± 0.083
Mrk1383	FSC v2.0	0.208 ± 0.017	0.236 ± 0.019
IRAS14394+5332	PSC v2.1	0.335 ± 0.037	2.076 ± 0.166
Mrk478	PSC v2.1	< 0.250	0.593 ± 0.053
NGC5728	PSC v2.0	0.812 ± 0.065	8.400 ± 0.672
3C305	FSC v2.0	< 0.096	0.204 ± 0.016
IC4518A			

Continued on next page

Table 6A.2 – *Continued from previous page*

Object Name	IRAS Catalog	$f_{25\mu m}$ Flux (Jy)	$f_{60\mu m}$ Flux (Jy)
(1)	(2)	(3)	(4)
NGC5793	PSC v2.0	< 0.788	6.330 ± 0.506
NGC5899	PSC v2.1	0.363 ± 0.040	3.202 ± 0.256
3C317	Golombek et al. 1988	< 0.085	< 0.115
Mrk848B	PSC v2.1	1.525 ± 0.107	9.385 ± 0.657
IRAS15206+3342	PSC v2.1	0.389 ± 0.031	1.743 ± 0.139
Arp220	PSC v2.1	8.110 ± 0.406	104.100 ± 8.328
NGC5990	PSC v2.1	1.692 ± 0.135	9.938 ± 0.994
IRAS15462-0450	PSC v2.1	0.478 ± 0.048	3.235 ± 0.324
PKS1549-79	PSC v2.1	0.497 ± 0.035	1.117 ± 0.089
Mrk876	PSC v2.1	< 0.250	0.628 ± 0.075
NGC6166	Golombek et al. 1988	< 0.020	< 0.100
Mrk883	PSC v2.1	< 0.305	1.110 ± 0.089
ESO137-G34	PSC v2.1	0.743 ± 0.037	2.277 ± 0.114
NGC6221	PSC v2.1	5.267 ± 0.316	36.320 ± 4.722
NGC6240	PSC v2.1	3.505 ± 0.175	23.470 ± 1.878
NGC6300	PSC v2.1	2.152 ± 0.151	14.050 ± 1.265
IRAS17208-0014	PSC v2.1	1.672 ± 0.134	34.090 ± 4.091
IRAS18216+6418	PSC v2.0	0.395 ± 0.032	1.130 ± 0.090
Fairall49	PSC v2.1	1.373 ± 0.110	3.206 ± 0.289
ESO103-G35	PSC v2.1	2.357 ± 0.141	2.267 ± 0.204
ESO140-G043	PSC v2.0	0.861 ± 0.069	2.000 ± 0.160

Continued on next page

Table 6A.2 – *Continued from previous page*

Object Name	IRAS Catalog	$f_{25\mu m}$ Flux (Jy)	$f_{60\mu m}$ Flux (Jy)
(1)	(2)	(3)	(4)
NGC6786	PSC v2.0	< 0.250	< 0.400
ESO141-G55	PSC v2.1	0.354 ± 0.032	0.618 ± 0.043
IRAS19254-7245	PSC v2.1	1.424 ± 0.014	5.236 ± 0.419
NGC6814	PSC v2.1	0.586 ± 0.053	5.693 ± 0.512
ESO339-G11	PSC v2.0	1.290 ± 0.103	6.360 ± 0.509
3C405	PSC v2.1	1.062 ± 0.255	2.329 ± 0.163
IRAS20037-1547	PSC v2.1	< 0.283	1.713 ± 0.154
NGC6860	PSC v2.0	0.354 ± 0.028	1.050 ± 0.084
MCG+04-48-002	PSC v2.0	1.060 ± 0.085	11.200 ± 1.008
NGC6926	PSC v2.1	0.450 ± 0.068	5.956 ± 0.596
Mrk509	PSC v2.1	0.744 ± 0.060	1.425 ± 0.114
PKS2048-57	PSC v2.1	3.838 ± 0.269	5.976 ± 0.717
UGC11763	PSC v2.0	0.317 ± 0.025	0.524 ± 0.042
IC5135	PSC v2.1	2.142 ± 0.150	16.670 ± 1.500
NGC7172	PSC v2.1	0.777 ± 0.070	5.958 ± 0.715
IRAS22017+0319	PSC v2.1	0.741 ± 0.089	1.134 ± 0.125
NGC7213	PSC v2.1	0.743 ± 0.067	2.564 ± 0.256
3C445	FSC v2.0	0.264 ± 0.021	0.306 ± 0.024
ESO602-G25	PSC v2.1	0.745 ± 0.067	5.844 ± 0.584
NGC7314	PSC v2.1	0.652 ± 0.111	3.386 ± 0.372
UGC12138	PSC v2.1	0.414 ± 0.050	0.858 ± 0.077

Continued on next page

Table 6A.2 – *Continued from previous page*

Object Name	IRAS Catalog	$f_{25\mu m}$ Flux (Jy)	$f_{60\mu m}$ Flux (Jy)
(1)	(2)	(3)	(4)
NGC7469	PSC v2.1	5.479 ± 0.438	26.950 ± 4.043
NGC7479	PSC v2.1	3.318 ± 0.299	12.120 ± 1.576
IC5298	PSC v2.0	1.720 ± 0.138	9.630 ± 0.770
NGC7591	PSC v2.1	0.787 ± 0.165	7.646 ± 0.918
NGC7592W	PSC v2.1	1.098 ± 0.231	8.074 ± 0.969
NGC7582	PSC v2.1	6.329 ± 0.506	48.010 ± 7.202
NGC7603	PSC v2.0	< 0.475	0.831 ± 0.066
NGC7674	PSC v2.1	1.921 ± 0.211	5.571 ± 0.669
NGC7679	PSC v2.1	1.149 ± 0.126	7.412 ± 0.889
IRAS23365+3604	PSC v2.0	0.808 ± 0.065	7.690 ± 0.615

Note. — Col. (1): Target name. Col. (2): IRAS Catalog used. Col. (3) & (4): Flux density and uncertainty of the 25μm and 60μm lines (Jy).

Table 6A.3: 9.7μm Silicate & Balmer Data

Object Name	Silicate Strength	Ref.	Hα (10^{-14}erg/s/cm^2)	Hβ (10^{-14}erg/s/cm^2)	Ref.
(1)	(2)	(3)	(4)	(5)	(6)
Mrk334			28.35	4.48	MAL17,OST93
IRAS00182-7112					
IRAS00198-7926					
NGC253					
Mrk348	-0.333 ± 0.017	WU09	11.96	2.80	MAL86,KOS78
IZw1	0.284 ± 0.014	WU09	74.80	31.00	MAL17,OKE79,VER04
IRAS00521-7054					
ESO541-IG12			1.38	0.32	MAL17
IRAS01003-2238	-0.77 ± 0.08	FAR13			
NGC454E	-0.38 ± 0.16	HER15			
M74					
IRAS01364-1042					
IIIZw35	-1.046 ± 0.061	GM15	3.55	0.45	KOS78
Mrk1014	0.21 ± 0.02	FAR13			
NGC788	-0.19 ± 0.09	HER15	3.78	1.35	VAC97
Mrk590				6.02	MAL17
IC1816			18.20	5.00	WIN92
NGC973					
NGC1068			773.75	178.48	MAL17,KOS78
Mrk1066	-1.01 ± 0.14	ALO16	55.80	7.13	GOO83
NGC1222					
Mrk1073	-0.76 ± 0.12	ALO16			
NGC1266			0.60		MOU10
NGC1275	0.13 ± 0.03	ALO16	217.46	74.73	HO93,HO97
Mrk609			8.62	1.39	OST81
NGC1365	-0.229 ± 0.011	WU09	143.1	6.0	MAL17
NGC1386	-0.542 ± 0.027	WU09	25.57	5.25	PHI83

Continued on next page

Table 6A.3 – *Continued from previous page*

Object Name	Silicate Strength	Ref.	Hα (10^{-14}erg/s/cm^2)	Hβ (10^{-14}erg/s/cm^2)	Ref.
(1)	(2)	(3)	(4)	(5)	(6)
IRAS03450+0055	0.027 ± 0.001	WU09			
IRAS04103-2838					
ESO420-G13	−1.22 ± 0.69	HER15	16.1		MAL17
NGC1566					
3C120	0.130 ± 0.007	WU09	208.9	30.4	DUR88,MAL17
MCG-05-12-006					
NGC1808	−0.132 ± 0.037	GM15	81.5	5.75	MAL17
Zw468.002NED01					
Zw468.002NED02					
IRAS05189-2524	−0.315 ± 0.016	WU09			
NGC1961			1.91	0.32	HO97
UGC3351					
NGC2110					
ESO005-G04	−1.199 ± 0.031	GM15			
Mrk3	−0.43 ± 0.06	ALO16	111.51	21.00	KOS78
NGC2146	−0.762 ± 0.038	GM15	16.22	1.46	HO97
Mrk620			26.30	4.73	HO97
IRAS07027-6011					
AM0702-601NED02					
Mrk9	0.050 ± 0.003	WU09	51.86	25.80	ERK97
IRAS07598+6508	0.113 ± 0.006	WU09			
Mrk622			5.45	0.46	SHU81
IRAS08311-2459	−0.49 ± 0.05	FAR13			
3C218	−1.064 ± 0.053	GM15			
MCG-01-24-012	−0.47 ± 0.14	HER15			
NGC2841	0.154 ± 0.008	GM15	2.14	0.26	HO93
Mrk705			53.66	19.80	ERK97
UGC5101	−1.619 ± 0.081	WU09	3.87	0.2	MAL17

Continued on next page

Table 6A.3 – *Continued from previous page*

Object Name	Silicate Strength	Ref.	Hα (10^{-14}erg/s/cm^2)	Hβ (10^{-14}erg/s/cm^2)	Ref.
(1)	(2)	(3)	(4)	(5)	(6)
IRAS09413+4843					
NGC2992					
ESO434-G40					
M82			158.49	6.34	HO97,MOU10
NGC3081					
3C234	−0.007 ± 0.001	WU09		2.12	MAL17
NGC3079	−0.828 ± 0.041	WU09	1.17	0.05	HO97
3C236					
NGC3184	−1.220 ± 0.061	GM15	7.59	1.74	HO97,MOU10
NGC3198	−1.623 ± 0.008	GM15	1.66	0.27	HO97,MOU10
NGC3227	−0.234 ± 0.012	WU09	46.77	15.90	MAL17,HO97
NGC3256	−0.233 ± 0.035	GM15			
M95			5.62	1.29	HO97,MOU10
NGC3393	−0.40 ± 0.07	HER15	39.39	9.56	DIA88,GIL10
NGC3516	−0.158 ± 0.008	WU09	264.45	87.33	MAL17,HO97
IRAS11095-0238	−3.28 ± 0.01	FAR13			
NGC3621	−0.004 ± 0.011	GM15	0.76	0.09	MOU10
Mrk1298					
NGC3783	−0.175 ± 0.009	GM15	447.12	131.80	WIN92
NGC3938			0.09		HO97,MOU10
NGC3982	0.110 ± 0.006	WU09	4.30	1.25	MAL17,PHI83,HO97
NGC4051	0.065 ± 0.003	WU09	77.78	26.10	ERK97
IRAS12018+1941					
UGC7064	−0.031 ± 0.002	WU09	4.31	1.11	MAL17
NGC4138					
IRAS12071-0444	−1.37 ± 0.01	FAR13			
NGC4151	0.030 ± 0.002	WU09	1384.70	502.90	MAL17,HO97
NGC4388	−0.699 ± 0.035	WU09	19.47	4.06	MAL17,PHI83

Continued on next page

Table 6A.3 – *Continued from previous page*

Object Name	Silicate Strength	Ref.	Hα (10^{-14}erg/s/cm^2)	Hβ (10^{-14}erg/s/cm^2)	Ref.
(1)	(2)	(3)	(4)	(5)	(6)
NGC4395					
NGC4418	−4.00 ± 0.07	HER15			
3C273	0.064 ± 0.003	WU09	649.00	197.00	MOR88
NGC4536			11.48	2.18	HO97,MOU10
NGC4507	−0.148 ± 0.007	GM15	59.56	11.54	PHI83
NGC4559			1.00	0.27	HO97,MOU10
NGC4569	0.53 ± 0.07	ALO16	23.99	4.80	HO97,MOU10
NGC4579	0.218 ± 0.011	WU09	5.56	0.91	MAL17,HO97,MOU10
NGC4593	0.063 ± 0.003	WU09	297.00	50.90	MOR88,MAL17
NGC4594	−0.036 ± 0.002	WU09	10.47	3.04	MAL17,HO97
IC3639	−0.312 ± 0.016	WU09	37.80	13.50	MAL17,VAC97
NGC4631			0.47	0.15	HO97
NGC4725	3.452 ± 0.173	GM15	0.85	0.26	HO97,MOU10
NGC4736	0.359 ± 0.018	GM15	2.51		HO97,MOU10
IRAS12514+1027					
Mrk231	−0.640 ± 0.032	WU09		45.0	MAL17
NGC4922			8.1	1.22	MAL17
NGC4941	−0.084 ± 0.004	WU09	9.49	2.0	MAL17
NGC4945	−3.90 ± 0.07	HER15			
ESO323-G77	0.10 ± 0.25	HER15	263.53	52.60	WIN92
NGC5033	−0.116 ± 0.006	WU09	5.01	1.10	MAL17,HO97
IRAS13120-5453					
MCG-03-34-064	−0.20 ± 0.09	HER15			
CentaurusA	−0.83 ± 0.09	HER15			
MCG-06-30-015	−0.108 ± 0.005	WU09	68.12	13.0	MOR88,WIN92
M83					
IRAS13349+2438	0.038 ± 0.002	WU09			
Mrk266SW	−0.692 ± 0.035	WU09	16.84	2.83	OST83,VEI95

Continued on next page

Table 6A.3 – *Continued from previous page*

Object Name	Silicate Strength	Ref.	Hα (10^{-14}erg/s/cm^2)	Hβ (10^{-14}erg/s/cm^2)	Ref.
(1)	(2)	(3)	(4)	(5)	(6)
NGC5273					
Mrk273	−1.746 ± 0.087	WU09	28.20	3.06	MAL17
PKS1345+12	−0.26 ± 0.03	FAR13			
IC4329A	−0.077 ± 0.004	WU09	469.56	36.40	WIN92
NGC5347	−0.251 ± 0.013	WU09	3.19	0.36	MAL17
Mrk463E	−0.464 ± 0.023	WU09	35.87	9.12	MAL86
Circinus	−0.997 ± 0.012	GM15			
NGC5506	−0.852 ± 0.043	WU09	45.53	5.09	MAL17,SHU80,DUR88
NGC5548	0.040 ± 0.002	WU09	9.33	7.28	MAL17,HO97
Mrk1383	−0.07 ± 0.02	ALO16	153.00	29.80	MOR88
IRAS14394+5332					
Mrk478	−0.08 ± 0.02	ALO16			
NGC5728	−0.784 ± 0.051	GM15	34.40	5.76	PHI83
3C305					
IC4518A	−1.75 ± 0.29	HER15			
NGC5793	−0.39 ± 0.02	ALO16			
NGC5899					
3C317			0.43	0.05	COH81
Mrk848B					
IRAS15206+3342					
Arp220	−2.543 ± 0.127	WU09			
NGC5990					
IRAS15462-0450	−0.38 ± 0.04	FAR13			
PKS1549-79					
Mrk876	0.114 ± 0.006	GM15			
NGC6166					
Mrk883					
ESO137-G34					

Continued on next page

Table 6A.3 – *Continued from previous page*

Object Name	Silicate Strength	Ref.	Hα (10^{-14}erg/s/cm^2)	Hβ (10^{-14}erg/s/cm^2)	Ref.
(1)	(2)	(3)	(4)	(5)	(6)
NGC6221					
NGC6240	−1.49 ± 0.39	ALO16	8.5	0.53	MAL17,CON12
NGC6300					
IRAS17208-0014	−4.07 ± 0.204	ALO16			
IRAS18216+6418					
Fairall49	−0.14 ± 0.15	HER15			
ESO103-G35	−0.590 ± 0.029	GM15	19.30	1.85	MOR88
ESO140-G043	0.21 ± 0.20	HER15	93.34	26.90	MOR88,WIN92
NGC6786					
ESO141-G55	0.27 ± 0.22	HER15	381.88	79.13	MOR88,WIN92
IRAS19254-7245	−1.345 ± 0.067	WU09			
NGC6814					
ESO339-G11					
3C405	−0.60 ± 0.07	HER15	7.93	1.20	OST75
IRAS20037-1547					
NGC6860	0.005 ± 0.001	WU09	73.65	14.30	WIN92
MCG+04-48-002					
NGC6926					
Mrk509	−0.002 ± 0.001	WU09	248.90	134.57	WIN92,MAL17
PKS2048-57	−0.263 ± 0.013	WU09	79.36	14.30	PHI83
UGC11763					
IC5135	−0.227 ± 0.011	WU09	117.76	19.40	PHI83,VAC97
NGC7172	−1.795 ± 0.09	WU09	1.11	0.37	MAL17,VAC97
IRAS22017+0319					
NGC7213	0.236 ± 0.012	WU09	210.03	27.10	WIN92
3C445	0.25 ± 0.20	HER15	24.20	9.20	ERK97,MOR88
ESO602-G25	−2.03 ± 1.10	HER15			
NGC7314	−0.476 ± 0.024	WU09	18.00	3.77	MOR88,MAL17

Continued on next page

Table 6A.3 – *Continued from previous page*

Object Name	Silicate Strength	Ref.	Hα (10^{-14}erg/s/cm^2)	Hβ (10^{-14}erg/s/cm^2)	Ref.
(1)	(2)	(3)	(4)	(5)	(6)
UGC12138			28.19	4.84	MAL17
NGC7469	−0.159 ± 0.008	WU09	249.00	102.45	MAL17,MOR88
NGC7479					
IC5298			6.37	1.47	MAL17
NGC7591					
NGC7592W					
NGC7582	−0.833 ± 0.042	WU09	105.65	15.17	MAL17
NGC7603	0.211 ± 0.011	WU09		7.87	MAL17
NGC7674	−0.215 ± 0.011	WU09	24.95	5.40	KRA94
NGC7679	−0.06 ± 0.37	HER15			
IRAS23365+3604					

Note. — Col. (1): Target name. Col. (2): Strength of the silicate absorption feature where a negative value indicates an absorption feature, and a positive value indicates emission (as defined in Spoon et al. (2007)). Col. (3): Reference for the 9.7μm silicate data. ALO16: Alonso-Herrero et al. (2016), FAR13: Farrah et al. (2013), GM15: González-Martín et al. (2015), HER15: Hernán-Caballero et al. (2015), WU09: Wu et al. (2009). Col. (4): Line flux of the Hα line (in units of 10^{-14}erg/s/cm^2). Col. (5): Line flux of the Hβ line (in units of 10^{-14} erg/s/cm^2). Col. (6): References for the Hα and Hβ data. COH81: Cohen & Osterbrock (1981), CON12: Contini (2012), DIA88: Diaz et al. (1988), DUR88: Durret & Bergeron (1988), ERK97: Erkens et al. (1997), GIL10: Gilli et al. (2010), GOO83: Goodrich & Osterbrock (1983), HO93: Ho et al. (1993), HO97: Ho et al. (1997), KOS78: Koski (1978), KRA94: Kraemer et al. (1994), MAL86: Malkan (1986), MAL17: Malkan et al. (2017), MOR88: Morris & Ward (1988), MOU10: Moustakas et al. (2010), OKE79: Oke & Lauer (1979), OST75: Osterbrock & Miller (1975), OST81: Osterbrock (1981), OST83: Osterbrock & Dahari (1983), OST93: Osterbrock & Martel (1993), PHI83: Phillips et al. (1983),SHU80: Shuder (1980), SHU81: Shuder & Osterbrock (1981), VAC97: Vaceli et al. (1997), VEI95: Veilleux et al. (1995), VER04: Véron-Cetty et al. (2004), WIN92: Winkler (1992).

Table 6A.4: Derived OH Integrated Flux Values

Object Name	OH65	OH71	OH79	OH84	OH119	OH163
	(10^{-14}erg/s/cm^2)	(10^{-14}erg/s/cm^2)	(10^{-14}erg/s/cm^2)	(10^{-14}erg/s/cm^2)	(10^{-14}erg/s/cm^2)	(10^{-14}erg/s/cm^2)
(1)	(2)	(3)	(4)	(5)	(6)	(7)
Mrk334			< -4.78			
IRAS00182-7112			< -1.01	< -1.43	-1.09 ± 0.31	
IRAS00198-7926			3.41 ± 1.90			
NGC253	-49.08 ± 28.76	< -250.82	-102.72 ± 79.66	-168.79 ± 69.64	-1193.81 ± 21.93	125.40 ± 18.35
Mrk348				< -0.94		
IZw1	< -21.64		3.57 ± 0.72		2.02 ± 0.46	1.31 ± 0.57
IRAS00521-7054			< -5.29			
ESO541-IG12			< -2.32			
IRAS01003-2238			< -3.38		-3.15 ± 1.06	
NGC454E			< -3.13			
M74			< -9.53			
IRAS01364-1042			6.76 ± 5.00			
IIIZw35			16.11 ± 4.26			
Mrk1014			< -2.98		0.88 ± 0.56	
NGC788			< -3.67			
Mrk590			< -4.86			
IC1816			8.09 ± 1.22			
NGC973			< -2.90			
NGC1068	< -37.15	< -19.13	96.02 ± 8.34	32.31 ± 9.89	63.99 ± 8.94	50.93 ± 2.43
Mrk1066			8.32 ± 2.01		4.96 ± 1.00	
NGC1222			< -4.61			
Mrk1073			< -6.75			
NGC1266			-9.33 ± 1.72			
NGC1275			6.20 ± 1.44			
Mrk609			1.97 ± 1.02			
NGC1365	< -19.10		5.87 ± 2.89		2.78 ± 1.69	11.68 ± 3.60
NGC1386			< -2.69			
IRAS03450+0055			< -3.31			
IRAS04103-2838			< -4.05			
ESO420-G13			8.89 ± 2.70			
NGC1566					2.20 ± 2.06	
3C120			< -8.50		< -2.21	
MCG-05-12-006			9.48 ± 2.67			
NGC1808			10.66 ± 3.97			
Zw468.002NED01			< -4.87			

Continued on next page

Table 6A.4 – *Continued from previous page*

Object Name	OH65	OH71	OH79	OH84	OH119	OH163
	(10^{-14}erg/s/cm^2)	(10^{-14}erg/s/cm^2)	(10^{-14}erg/s/cm^2)	(10^{-14}erg/s/cm^2)	(10^{-14}erg/s/cm^2)	(10^{-14}erg/s/cm^2)
(1)	(2)	(3)	(4)	(5)	(6)	(7)
Zw468.002NED02			< -10.81			
IRAS05189-2524	-11.32 ± 2.70	-4.61 ± 1.99	6.06 ± 2.60	-16.46 ± 6.59	3.32 ± 2.66	2.92 ± 1.03
NGC1961			< -4.57			
UGC3351			< -11.52			
NGC2110					3.34 ± 1.21	
ESO005-G04					-3.90 ± 0.99	
Mrk3			< -1.70			
NGC2146	27.10 ± 11.47					24.19 ± 4.76
Mrk620			< -4.98			
IRAS07027-6011			< -4.14			
AM0702-601NED02			< -8.93			
Mrk9			< -2.42			
IRAS07598+6508					0.74 ± 0.44	
Mrk622			< -3.80			
IRAS08311-2459			5.51 ± 1.83		5.67 ± 0.80	
3C218			< -2.57			
MCG-01-24-012			4.64 ± 1.65			
NGC2841			4.32 ± 2.14			
Mrk705			4.32 ± 0.61			
UGC5101	-4.65 ± 3.23		-5.94 ± 3.39		-21.73 ± 2.12	
IRAS09413+4843			< -3.67			
NGC2992					-3.85 ± 1.12	
ESO434-G40					0.29 ± 0.14	
M82	< -54.16				-166.42 ± 8.93	14.79 ± 3.89
NGC3081					1.01 ± 0.56	
3C234			< -2.18			
NGC3079	< -10.52		-21.18 ± 2.80	-24.26 ± 1.93	-70.35 ± 2.10	20.07 ± 3.96
3C236			< -1.51			
NGC3184			< -6.85			
NGC3198			< -10.22			
NGC3227			4.49 ± 2.12		7.34 ± 1.75	1.78 ± 0.82
NGC3256			28.99 ± 3.68			
M95			< -7.84			
NGC3393			< -3.94			
NGC3516			< -3.63		1.49 ± 0.60	
IRAS11095-0238			5.98 ± 1.74		1.35 ± 0.50	

Continued on next page

Table 6A.4 – *Continued from previous page*

Object Name	OH65	OH71	OH79	OH84	OH119	OH163
	(10^{-14}erg/s/cm^2)	(10^{-14}erg/s/cm^2)	(10^{-14}erg/s/cm^2)	(10^{-14}erg/s/cm^2)	(10^{-14}erg/s/cm^2)	(10^{-14}erg/s/cm^2)
(1)	(2)	(3)	(4)	(5)	(6)	(7)
NGC3621			< -13.25			
Mrk1298					< 0.36	
NGC3783					1.04 ± 0.25	
NGC3938			< -10.02			
NGC3982			< -2.32		< -1.98	1.25 ± 0.27
NGC4051			3.05 ± 1.97		2.73 ± 0.71	1.43 ± 0.38
IRAS12018+1941			< -5.15			
UGC7064			< -2.56			
NGC4138					< -0.61	
IRAS12071-0444			1.17 ± 0.91		-0.99 ± 0.69	
NGC4151			< -1.76		2.34 ± 0.86	
NGC4388			< -3.74	< -5.95	< -4.61	< -1.48
NGC4395					< -0.96	
NGC4418	-82.05 ± 5.58	-38.28 ± 5.77	-16.14 ± 2.66	-82.69 ± 7.63	-24.86 ± 3.42	3.71 ± 1.27
3C273			1.21 ± 0.67		< -0.50	
NGC4536			< -13.21			
NGC4507			< -3.28		2.54 ± 0.65	
NGC4559			< -3.91			
NGC4569			< -9.24			
NGC4579			< -6.64		1.31 ± 0.54	
NGC4593			< -3.60		1.08 ± 0.73	
NGC4594			< -10.65			
IC3639			< -4.67		< -2.00	0.72 ± 0.28
NGC4631			< -11.73			
NGC4725			< -7.11			
NGC4736			< -7.03			
IRAS12514+1027					-0.69 ± 0.14	
Mrk231	-29.85 ± 3.70	-7.05 ± 6.85	-12.93 ± 7.52	-62.74 ± 9.56	-38.59 ± 4.11	5.76 ± 1.17
NGC4922			2.78 ± 2.32			
NGC4941			< -2.43		0.63 ± 0.43	
NGC4945	< -203.16	< -445.03	-789.55 ± 72.08	-640.58 ± 102.19	-1908.92 ± 24.39	155.29 ± 10.94
ESO323-G77			< -7.93			
NGC5033			< -2.90		< -3.42	
IRAS13120-5453	< -16.82	< -19.12	-15.67 ± 5.70	-45.68 ± 12.25	-91.21 ± 5.98	15.57 ± 4.08
MCG-03-34-064			2.68 ± 0.92			
CentaurusA	< -10.14	< -12.51	< -10.08	< -12.57	-9.95 ± 1.31	< -3.26

Continued on next page

Table 6A.4 – *Continued from previous page*

Object Name	OH65	OH71	OH79	OH84	OH119	OH163
	(10^{-14}erg/s/cm^2)	(10^{-14}erg/s/cm^2)	(10^{-14}erg/s/cm^2)	(10^{-14}erg/s/cm^2)	(10^{-14}erg/s/cm^2)	(10^{-14}erg/s/cm^2)
(1)	(2)	(3)	(4)	(5)	(6)	(7)
MCG-06-30-015			< 3.24		< −0.92	
M83	< −31.57		7.46 ± 3.37		11.75 ± 1.48	4.02 ± 0.93
IRAS13349+2438			< −2.38			
Mrk266SW			< −8.84		2.35 ± 1.22	
NGC5273					< −0.78	
Mrk273	−28.71 ± 4.31	−13.72 ± 3.15	< −11.59	−32.66 ± 5.96	−10.00 ± 2.74	9.23 ± 1.34
PKS1345+12			4.45 ± 0.75		3.28 ± 0.35	1.26 ± 0.35
IC4329A			< −2.32			
NGC5347			< −2.19			
Mrk463E			< −3.08		< −0.76	
Circinus	< −39.97		39.10 ± 8.09		−1.99 ± 1.61	23.19 ± 3.64
NGC5506			< −4.02		−6.74 ± 1.59	
NGC5548			< −3.22			
Mrk1383			< −3.18			
IRAS14394+5332					−1.45 ± 1.03	
Mrk478			3.21 ± 1.18		0.57 ± 0.23	
NGC5728			< −6.32		−2.11 ± 1.19	
3C305			< −1.01			
IC4518A			4.35 ± 2.30			
NGC5793			< −6.82			
NGC5899					< −1.96	
3C317			< −3.81			
Mrk848B			< −10.01			
IRAS15206+3342					< −0.89	
Arp220	−234.74 ± 17.43	−72.85 ± 6.51	−168.00 ± 9.45	−206.26 ± 25.75	−395.26 ± 6.12	
NGC5990			< −8.39			
IRAS15462-0450			< −3.53		−1.59 ± 0.59	
PKS1549-79			1.12 ± 0.53			
Mrk876			< −5.99		1.18 ± 0.31	
NGC6166			< −0.57			
Mrk883			5.95 ± 1.90			
ESO137-G34					< −1.03	
NGC6221					< −6.89	
NGC6240	< −4.30	< −15.18	19.75 ± 4.49	−6.78 ± 5.03	−29.00 ± 4.38	19.87 ± 1.16
NGC6300					−7.86 ± 1.03	
IRAS17208-0014	−34.76 ± 4.50	−15.33 ± 7.23	−2.90 ± 1.71	−51.39 ± 5.08	−76.09 ± 2.97	14.88 ± 1.74

Continued on next page

Table 6A.4 – *Continued from previous page*

Object Name	OH65	OH71	OH79	OH84	OH119	OH163
	(10^{-14}erg/s/cm^2)	(10^{-14}erg/s/cm^2)	(10^{-14}erg/s/cm^2)	(10^{-14}erg/s/cm^2)	(10^{-14}erg/s/cm^2)	(10^{-14}erg/s/cm^2)
(1)	(2)	(3)	(4)	(5)	(6)	(7)
IRAS18216+6418					< -0.91	
Fairall49			< -2.33			
ESO103-G35			< -5.50	1.04 ± 0.40	0.73 ± 0.21	
ESO140-G043			< -4.24		1.18 ± 0.47	
NGC6786			< -3.65			
ESO141-G55			< -2.58			
IRAS19254-7245			< -2.68		-1.56 ± 0.66	
NGC6814					1.28 ± 0.45	
ESO339-G11			< -4.92			
3C405	< -12.86		< -1.61		< -1.50	
IRAS20037-1547			2.43 ± 0.87		-2.41 ± 0.53	
NGC6860			< -4.55			
MCG+04-48-002			< -7.55			
NGC6926			< -2.92			
Mrk509			< -3.51		< -1.44	
PKS2048-57			0.98 ± 0.76		-0.60 ± 0.31	
UGC11763					< -0.29	
IC5135			8.28 ± 1.93		5.56 ± 1.88	2.54 ± 0.94
NGC7172			< -3.63		-7.25 ± 1.37	< -3.73
IRAS22017+0319			< -6.01			
NGC7213			< -2.98		0.95 ± 0.30	
3C445			< -3.39			
ESO602-G25			< -5.81			
NGC7314			< -1.77		1.17 ± 0.25	
UGC12138			< -6.49			
NGC7469	< -17.87	< -17.51	9.02 ± 1.87	< -7.79	21.77 ± 2.17	2.70 ± 1.49
NGC7479					-8.71 ± 1.53	
IC5298			< -10.65			
NGC7591			< -11.13			
NGC7592W			< -4.41			
NGC7582			13.06 ± 2.21	< -17.07	-6.82 ± 2.17	6.75 ± 1.39
NGC7603			< -3.39			
NGC7674			< -4.88			
NGC7679			< -7.59			
IRAS23365+3604	-7.31 ± 2.11		< -5.63	-11.42 ± 2.52	-11.12 ± 1.64	

Continued on next page

Table 6A.4 – *Continued from previous page*

Object Name	OH65	OH71	OH79	OH84	OH119	OH163
	(10^{-14}erg/s/cm^2)	(10^{-14}erg/s/cm^2)	(10^{-14}erg/s/cm^2)	(10^{-14}erg/s/cm^2)	(10^{-14}erg/s/cm^2)	(10^{-14}erg/s/cm^2)
(1)	(2)	(3)	(4)	(5)	(6)	(7)

Note. — Col. (1): Target name. Col. (2): Integrated flux value and uncertainty of the OH65 doublet. Col. (3): Integrated flux value and uncertainty of the OH71 doublet. Col. (4): Integrated flux value and uncertainty of the OH79 doublet. Col. (5): Integrated flux value and uncertainty of the OH84 doublet. Col. (6): Integrated flux value and uncertainty of the OH119 doublet. Col. (7): Integrated flux value and uncertainty of the OH163 doublet. Note that if an integrated flux measurement does not have an uncertainty value, it is an upper limit observation. If there is an uncertainty, it is a detection.

Table 6A.5: Derived EW(OH) Values

Object Name	Classification	OH65 (μm)	OH71 (μm)	OH79 (μm)	OH84 (μm)	OH119 (μm)	OH163 (μm)
(1)	(2)	(3)	(4)	(5)	(6)	(7)	(8)
Mrk334	Seyfert-1.8			< 0.022			
IRAS00182-7112	Seyfert-2			< 0.016	< 0.030	−0.078 ± 0.022	
IRAS00198-7926	Seyfert-2			0.028 ± 0.015			
NGC253	Starburst	−0.001 ± 0.00	< 0.006	−0.003 ± 0.002	−0.006 ± 0.002	−0.081 ± 0.002	0.028 ± 0.004
Mrk348	Seyfert-1h				< 0.045		
IZw1	Seyfert-1n	< 0.190		0.033 ± 0.007		0.051 ± 0.012	0.087 ± 0.038
IRAS00521-7054	Seyfert-1h			< 0.131			
ESO541-IG12	Seyfert-2			< 0.079			
IRAS01003-2238	Seyfert-2			< 0.042		−0.154 ± 0.052	
NGC454E	Seyfert-2			< 0.109			
M74	Starburst			< 0.000			
IRAS01364-1042	LINER			0.019 ± 0.014			
IIIZw35	Seyfert-2			0.030 ± 0.008			
Mrk1014	Seyfert-1.5			< 0.033		0.029 ± 0.018	
NGC788	Seyfert-1h			< 0.154			
Mrk590	Seyfert-1			< 0.460			
IC1816	Seyfert-2			0.145 ± 0.024			
NGC973	Seyfert-2			< 0.044			
NGC1068	Seyfert-1h	< 0.007	< 0.004	0.024 ± 0.002	0.009 ± 0.003	0.051 ± 0.007	0.170 ± 0.005
Mrk1066	Seyfert-2			0.014 ± 0.003		0.022 ± 0.004	
NGC1222	Starburst			< 0.013			
Mrk1073	Seyfert-2			< 0.021			
NGC1266	LINER			−0.011 ± 0.002			
NGC1275	Seyfert-1.5			0.021 ± 0.005			
Mrk609	Seyfert-1.8			0.013 ± 0.007			
NGC1365	Seyfert-1.8	< 0.025		0.003 ± 0.002		0.003 ± 0.002	0.046 ± 0.014
NGC1386	Seyfert-1i			< 0.011			
IRAS03450+0055	Seyfert-1.5			< 0.179			
IRAS04103-2838	LINER			< 0.046			
ESO420-G13	Seyfert-2			0.010 ± 0.003			
NGC1566	Seyfert-1.5					0.023 ± 0.021	
3C120	Seyfert-1.5			< 0.139		< 0.074	
MCG-05-12-006	LINER			0.019 ± 0.005			
NGC1808	Starburst			0.004 ± 0.001			
Zw468.002NED01	Seyfert-2			< 0.044			

Continued on next page

Table 6A.5 – *Continued from previous page*

Object Name	Classification	OH65 (μm)	OH71 (μm)	OH79 (μm)	OH84 (μm)	OH119 (μm)	OH163 (μm)
(1)	(2)	(3)	(4)	(5)	(6)	(7)	(8)
Zw468.002NED02	Seyfert-2			< 0.023			
IRAS05189-2524	Seyfert-1h	−0.012 ± 0.00	−0.005 ± 0.002	0.010 ± 0.005	−0.029 ± 0.012	0.018 ± 0.015	0.048 ± 0.017
NGC1961	LINER			< 0.171			
UGC3351	Seyfert-2			< 0.012			
NGC2110	Seyfert-1h					0.035 ± 0.013	
ESO005-G04	Seyfert-2					−0.044 ± 0.011	
Mrk3	Seyfert-1h			< 0.018			
NGC2146	Starburst	0.006 ± 0.00					0.048 ± 0.009
Mrk620	Seyfert-1h			< 0.016			
IRAS07027-6011	Seyfert-2			< 0.039			
AM0702-601NED02	Seyfert-2			< 0.033			
Mrk9	Seyfert-1.5			< 0.055			
IRAS07598+6508	Seyfert-1					0.025 ± 0.015	
Mrk622	Seyfert-2			< 0.064			
IRAS08311-2459	Seyfert-1i			0.020 ± 0.007		0.057 ± 0.008	
3C218	LINER			< 0.636			
MCG-01-24-012	Seyfert-2			0.242 ± 0.111			
NGC2841	LINER			0.065 ± 0.033			
Mrk705	Seyfert-1.2			0.122 ± 0.019			
UGC5101	Seyfert-1	−0.006 ± 0.00		−0.008 ± 0.005		−0.064 ± 0.006	
IRAS09413+4843	Seyfert-2			< 0.127			
NGC2992	Seyfert-1h					−0.023 ± 0.007	
ESO434-G40	Seyfert-1i					0.018 ± 0.009	
M82	Starburst	< 0.002				−0.032 ± 0.002	0.008 ± 0.002
NGC3081	Seyfert-1h					0.022 ± 0.012	
3C234	Seyfert-1.9			< 0.516			
NGC3079	LINER	< 0.005		−0.014 ± 0.002	−0.017 ± 0.001	−0.087 ± 0.003	0.058 ± 0.012
3C236	LINER			< 0.280			
NGC3184	Starburst			< 0.000			
NGC3198	Starburst			< 0.000			
NGC3227	Seyfert-1.5			0.015 ± 0.007		0.048 ± 0.011	0.027 ± 0.013
NGC3256	Starburst			0.009 ± 0.001			
M95	Starburst			< 0.010			
NGC3393	Seyfert-2			< 0.054			
NGC3516	Seyfert-1.5			< 0.043		0.059 ± 0.024	
IRAS11095-0238	LINER			0.047 ± 0.014		0.038 ± 0.014	

Continued on next page

Table 6A.5 – *Continued from previous page*

Object Name	Classification	OH65 (μm)	OH71 (μm)	OH79 (μm)	OH84 (μm)	OH119 (μm)	OH163 (μm)
(1)	(2)	(3)	(4)	(5)	(6)	(7)	(8)
NGC3621	Seyfert-2			< 0.000			
Mrk1298	Seyfert-1					< 0.048	
NGC3783	Seyfert-1.5					0.059 ± 0.014	
NGC3938	Starburst			< 0.031			
NGC3982	Seyfert-1.9			< 0.049		< 0.064	0.072 ± 0.016
NGC4051	Seyfert-1n			0.024 ± 0.016		0.040 ± 0.010	0.051 ± 0.014
IRAS12018+1941	Seyfert-2			< 0.068			
UGC7064	Seyfert-1.9			< 0.046			
NGC4138	Seyfert-1.9					< 0.068	
IRAS12071-0444	Seyfert-2			0.010 ± 0.008		−0.028 ± 0.019	
NGC4151	Seyfert-1.5			< 0.011		0.053 ± 0.020	
NGC4388	Seyfert-1h			< 0.022	< 0.037	< 0.070	< 0.039
NGC4395	Seyfert-1.8					< 0.377	
NGC4418	Seyfert-2	−0.028 ± 0.00	−0.017 ± 0.002	−0.009 ± 0.001	−0.056 ± 0.005	−0.048 ± 0.007	0.023 ± 0.008
3C273	Seyfert-1			0.075 ± 0.043		< 0.058	
NGC4536	Starburst			< 0.010			
NGC4507	Seyfert-1h			< 0.019		0.041 ± 0.010	
NGC4559	Starburst			< 0.000			
NGC4569	LINER			< 0.047			
NGC4579	LINERb			< 0.000		0.031 ± 0.013	
NGC4593	Seyfert-1			< 0.036		0.016 ± 0.011	
NGC4594	LINER			< 0.000			
IC3639	Seyfert-1h			< 0.056		< 0.059	0.042 ± 0.017
NGC4631	Starburst			< 0.127			
NGC4725	Seyfert-2			< 0.074			
NGC4736	LINER			< 0.000			
IRAS12514+1027	Seyfert-2					−0.056 ± 0.011	
Mrk231	Seyfert-1	−0.013 ± 0.00	−0.004 ± 0.004	−0.009 ± 0.005	−0.052 ± 0.008	−0.085 ± 0.009	0.039 ± 0.008
NGC4922	Seyfert-2			0.008 ± 0.007			
NGC4941	Seyfert-2			< 0.054		0.029 ± 0.020	
NGC4945	Seyfert-2	< 0.006	< 0.014	−0.027 ± 0.002	−0.024 ± 0.004	−0.122 ± 0.002	0.029 ± 0.002
ESO323-G77	Seyfert-1.2			< 0.026			
NGC5033	Seyfert-1.8			< 0.017		< 0.025	
IRAS13120-5453	Seyfert-2	< 0.005	< 0.007	−0.007 ± 0.002	−0.020 ± 0.005	−0.097 ± 0.006	0.046 ± 0.012
MCG-03-34-064	Seyfert-1h			0.012 ± 0.004			
CentaurusA	Seyfert-2	< 0.006	< 0.009	< 0.008	< 0.011	−0.014 ± 0.002	< 0.011

Continued on next page

Table 6A.5 – *Continued from previous page*

Object Name	Classification	OH65 (μm)	OH71 (μm)	OH79 (μm)	OH84 (μm)	OH119 (μm)	OH163 (μm)
(1)	(2)	(3)	(4)	(5)	(6)	(7)	(8)
MCG-06-30-015	Seyfert-1.5			< 0.000		< 0.046	
M83	Starburst	< 0.012		0.003 ± 0.001		0.014 ± 0.002	0.011 ± 0.003
IRAS13349+2438	Seyfert-1n			< 0.073			
Mrk266SW	Seyfert-2			< 0.034		0.026 ± 0.013	
NGC5273	Seyfert-1.9					< 0.045	
Mrk273	Seyfert-2	−0.018 ± 0.00	−0.010 ± 0.002	< 0.012	−0.038 ± 0.007	−0.032 ± 0.009	0.086 ± 0.013
PKS1345+12	Seyfert-2			0.046 ± 0.008		0.103 ± 0.011	0.141 ± 0.040
IC4329A	Seyfert-1.2			< 0.032			
NGC5347	Seyfert-1h			< 0.038			
Mrk463E	Seyfert-1h			< 0.042		< 0.029	
Circinus	Seyfert-1h	< 0.003		0.005 ± 0.001		−0.001 ± 0.001	0.027 ± 0.004
NGC5506	Seyfert-1h			< 0.015		−0.047 ± 0.011	
NGC5548	Seyfert-1.5			< 0.074			
Mrk1383	Seyfert-1			< 0.210			
IRAS14394+5332	Seyfert-2					−0.039 ± 0.028	
Mrk478	Seyfert-1n			0.076 ± 0.029		0.035 ± 0.014	
NGC5728	Seyfert-1.9			< 0.018		−0.012 ± 0.007	
3C305	Seyfert-2			< 0.076			
IC4518A	Seyfert-2			0.019 ± 0.010			
NGC5793	Seyfert-2			< 0.016			
NGC5899	Seyfert-2					< 0.072	
3C317	Seyfert-2			< 0.000			
Mrk848B	LINER			< 0.023			
IRAS15206+3342	Seyfert-2					< 0.037	
Arp220	Seyfert-2	−0.024 ± 0.00	−0.009 ± 0.001	−0.025 ± 0.001	−0.042 ± 0.005	−0.163 ± 0.003	
NGC5990	Seyfert-2			< 0.024			
IRAS15462-0450	Seyfert-1n			< 0.032		−0.046 ± 0.017	
PKS1549-79	Seyfert-1h			0.026 ± 0.012			
Mrk876	Seyfert-1			< 0.000		0.078 ± 0.020	
NGC6166	Seyfert-1-Q			< 0.442			
Mrk883	Seyfert-1.9			0.119 ± 0.042			
ESO137-G34	Seyfert-2					< 0.040	
NGC6221	Seyfert-2					< 0.021	
NGC6240	LINER	< 0.003	< 0.011	0.018 ± 0.004	−0.007 ± 0.005	−0.058 ± 0.009	0.147 ± 0.009
NGC6300	Seyfert-2					−0.050 ± 0.007	
IRAS17208-0014	LINER	−0.013 ± 0.00	−0.006 ± 0.003	−0.002 ± 0.001	−0.030 ± 0.003	−0.115 ± 0.005	0.071 ± 0.008

Continued on next page

Table 6A.5 – *Continued from previous page*

Object Name	Classification	OH65 (μm)	OH71 (μm)	OH79 (μm)	OH84 (μm)	OH119 (μm)	OH163 (μm)
(1)	(2)	(3)	(4)	(5)	(6)	(7)	(8)
IRAS18216+6418	Seyfert-1.2					< 0.116	
Fairall49	Seyfert-1h			< 0.019			
ESO103-G35	Seyfert-2			< 0.082	0.019 ± 0.007	0.047 ± 0.014	
ESO140-G043	Seyfert-1.5			< 0.050		0.031 ± 0.012	
NGC6786	Seyfert-2			< 0.021			
ESO141-G55	Seyfert-1.2			< 0.094			
IRAS19254-7245	Seyfert-1h			< 0.027		−0.032 ± 0.014	
NGC6814	Seyfert-1.5					0.083 ± 0.029	
ESO339-G11	Seyfert-2			< 0.020			
3C405	Seyfert-1.9	< 0.076		< 0.014		< 0.041	
IRAS20037-1547	Seyfert-1			0.029 ± 0.010		−0.071 ± 0.016	
NGC6860	Seyfert-1.5			< 0.161			
MCG+04-48-002	Seyfert-1			< 0.018			
NGC6926	Seyfert-2			< 0.044			
Mrk509	Seyfert-1.5			< 0.048		< 0.051	
PKS2048-57	Seyfert-1h			0.006 ± 0.004		−0.012 ± 0.006	
UGC11763	Seyfert-1.5					< 0.034	
IC5135	Seyfert-1.9			0.010 ± 0.002		0.015 ± 0.005	0.018 ± 0.007
NGC7172	Seyfert-2			< 0.022		−0.064 ± 0.012	< 0.060
IRAS22017+0319	Seyfert-1h			< 0.156			
NGC7213	LINERb			< 0.066		0.039 ± 0.012	
3C445	Seyfert-1.5			< 0.295			
ESO602-G25	LINER			< 0.018			
NGC7314	Seyfert-1h			< 0.031		0.044 ± 0.009	
UGC12138	Seyfert-1.8			< 0.190			
NGC7469	Seyfert-1.5	< 0.009	< 0.012	0.007 ± 0.001	< 0.006	0.039 ± 0.004	0.013 ± 0.007
NGC7479	Seyfert-1.9					−0.047 ± 0.008	
IC5298	Seyfert-2			< 0.020			
NGC7591	LINER			< 0.028			
NGC7592W	Seyfert-2			< 0.037			
NGC7582	Seyfert-1h			0.005 ± 0.001	< 0.032	−0.006 ± 0.002	0.038 ± 0.008
NGC7603	Seyfert-1.5			< 0.058			
NGC7674	Seyfert-1h			< 0.031			
NGC7679	Seyfert-1.9			< 0.028			
IRAS23365+3604	LINER	−0.012 ± 0.00		< 0.014	−0.034 ± 0.008	−0.078 ± 0.012	

Continued on next page

Table 6A.5 – *Continued from previous page*

Object Name	Classification	OH65 (μm)	OH71 (μm)	OH79 (μm)	OH84 (μm)	OH119 (μm)	OH163 (μm)
(1)	(2)	(3)	(4)	(5)	(6)	(7)	(8)

Note. — Col. (1): Target name. Col. (2): Integrated flux value and uncertainty of the OH65 doublet. Col. (3): Integrated flux value and uncertainty of the OH71 doublet. Col. (4): Integrated flux value and uncertainty of the OH79 doublet. Col. (5): Integrated flux value and uncertainty of the OH84 doublet. Col. (6): Integrated flux value and uncertainty of the OH119 doublet. Col. (7): Integrated flux value and uncertainty of the OH163 doublet. Note that if an integrated flux measurement does not have an uncertainty value, it is an upper limit observation. If there is an uncertainty, it is a detection.

6B Fitting Statistics

Table 6B.6: Best-fit Parameters for EW(OH) vs. Emission-Line Ratio Fluxes

Parameters	OH65	OH71	OH79	OH84	OH119	OH163
(1)	(2)	(3)	(4)	(5)	(6)	(7)
$\log\left(\frac{[\text{Ne V}]14.32\mu\text{m}}{[\text{Ne II}]12.81\mu\text{m}}\right)$						
slope			0.017 ± 0.003		0.07 ± 0.01	0.019 ± 0.009
Y-intercept			0.020 ± 0.003		0.06 ± 0.01	0.06 ± 0.01
Correlation Coefficient			0.50		0.52	0.39
p-value			0.007***		0.0025***	0.14
$\log\left(\frac{[\text{Ne V}]24.32\mu\text{m}}{[\text{Ne II}]12.81\mu\text{m}}\right)$						
slope			0.006 ± 0.004		0.05 ± 0.02	0.059 ± 0.008
Y-intercept			0.013 ± 0.003		0.03 ± 0.01	0.087 ± 0.06
Correlation Coefficient			0.18		0.10	0.69
p-value			0.43		0.61	0.02**
$\log\left(\frac{[\text{Ne III}]15.56\mu\text{m}}{[\text{Ne II}]12.81\mu\text{m}}\right)$						
slope	−0.016 ± 0.009		0.021 ± 0.004	0.014 ± 0.008	0.10 ± 0.02	0.05 ± 0.01
Y-intercept	−0.021 ± 0.008		0.018 ± 0.003	−0.005 ± 0.006	0.05 ± 0.01	0.07 ± 0.01
Correlation Coefficient	−0.24		0.46	0.28	0.61	0.43
p-value	0.54		0.002*	0.38	9.4e-06***	0.03*
$\log\left(\frac{[\text{O IV}]25.89\mu\text{m}}{[\text{Ne II}]12.81\mu\text{m}}\right)$						
slope			0.004 ± 0.002	0.012 ± 0.005	0.07 ± 0.01	0.026 ± 0.008
Y-intercept			0.008 ± 0.002	−0.001 ± 0.006	0.010 ± 0.008	0.06 ± 0.01
Correlation Coefficient			0.37	0.07	0.45	0.39
p-value			0.02*	0.87	0.005*	0.08
$\log\left(\frac{[\text{O IV}]25.89\mu\text{m}}{[\text{O III}]88.36\mu\text{m}}\right)$						
slope			0.005 ± 0.003		0.08 ± 0.02	0.022 ± 0.007
Y-intercept			0.006 ± 0.002		−0.01 ± 0.01	0.043 ± 0.007
Correlation Coefficient			0.40		0.63	0.36
p-value			0.08		0.0006***	0.14

Note. — Col. (1): Linear fitting parameters. Col. (2)−(7): Results from the linear fit for each OH transition, and the Spearman rank-order correlation coefficient and the p-value to test for non-correlation. *: indicates $p < 0.05$; however, the observable is an uncertain predictor of EW(OH) due to $r < 0.5$. **: indicates a weak correlation with $r \geq 0.5$ and $0.01 < p < 0.05$. ***: indicates a significant correlation with $r \geq 0.5$ and $p < 0.01$. Blank spaces in the table indicate that there is less than 8 galaxies so no fit was made.

Table 6B.7: Best-fit Parameters for EW(OH) vs. the X-ray and IR Emission-Line Luminosities

Parameters	OH65	OH71	OH79	OH84	OH119	OH163
(1)	(2)	(3)	(4)	(5)	(6)	(7)
$\log(L_{2-10\mathrm{keV}})$						
Slope	−0.009 ± 0.004		0.05 ± 0.002	−0.2 ± 0.6	0.16 ± 0.08	0.06 ± 0.03
Y-intercept	0.38 ± 0.18		−1.88 ± 0.65	7.89 ± 25.42	−6.70 ± 3.55	−2.48 ± 1.13
Correlation Coefficient	−0.39		0.41	−0.07	0.35	0.36
p-value	0.30		0.014*	0.83	0.03*	0.09
$\log(L_{[\mathrm{O\ IV}]25.89\mu\mathrm{m}})$						
Slope			0.005 ± 0.001	0.006 ± 0.005	0.035 ± 0.007	0.017 ± 0.004
Y-intercept			−0.18 ± 0.06	−0.24 ± 0.19	−1.44 ± 0.27	−0.65 ± 0.17
Correlation Coefficient			0.31	−0.38	0.31	0.56
p-value			0.06	0.35	0.06	0.007***
$\log(L_{[\mathrm{Ne\ V}]14.32\mu\mathrm{m}})$						
Slope			0.010 ± 0.002		0.039 ± 0.007	0.013 ± 0.005
Y-intercept			−0.41 ± 0.08		−1.56 ± 0.27	−0.47 ± 0.22
Correlation Coefficient			0.33		0.27	0.35
p-value			0.09		0.13	0.19
$\log(L_{[\mathrm{Ne\ V}]24.32\mu\mathrm{m}})$						
Slope			0.009 ± 0.006		0.009 ± 0.005	0.04 ± 0.02
Y-intercept			−0.35 ± 0.24		−0.35 ± 0.19	−1.51 ± 0.82
Correlation Coefficient			−0.13		−0.002	0.17
p-value			0.56		0.99	0.61

Note. — Col. (1): Linear fitting parameters. Col. (2)–(7): Results from the linear fit for each OH transition, and the Spearman rank-order correlation coefficient and the p-value to test for non-correlation. *: indicates p < 0.05; however, the observable is an uncertain predictor of EW(OH) due to $r < 0.5$. **: indicates a weak correlation with $r \geq 0.5$ and 0.01 < p < 0.05. ***: indicates a significant correlation with $r \geq 0.5$ and p < 0.01. Blank spaces in the table indicate that there is less than 8 galaxies so no fit was made.

Table 6B.8: Best-fit Parameters for Figure 6.7 (EW(OH) vs. IRAS $f_{25\mu m}/f_{60\mu m}$ Dust Temperature Tracer)

OH Doublet	Slope (m)	Y-intercept (b)	Correlation Coefficient	p-value
(1)	(2)	(3)	(4)	(5)
OH65	0.08 ± 0.05	0.06 ± 0.06	0.11	0.76
OH71				
OH79	0.052 ± 0.006	0.045 ± 0.006	0.50	0.001***
OH84	0.03 ± 0.01	0.02 ± 0.01	0.12	0.71
OH119	0.22 ± 0.03	0.15 ± 0.02	0.57	0.00005***
OH163	−0.004 ± 0.015	0.024 ± 0.014	−0.03	0.89

Note. — Col. (1): OH doublet. Col. (2): Slope of the best-fit line. Col. (3): Y-intercept of the best-fit line. Col. (4): The Spearman rank-order correlation coefficient. Col. (5): The p-value to test for non-correlation. *: indicates $p < 0.05$; however, the observable is an uncertain predictor of EW(OH) due to $r < 0.5$. **: indicates a weak correlation with $r \geq 0.5$ and $0.01 < p < 0.05$. ***: indicates a significant correlation with $r \geq 0.5$ and $p < 0.01$. For columns (2)-(5), blank rows in the table indicate that there is less than 8 galaxies so no fit was made.

Table 6B.9: Best-fit Parameters for EW(OH) vs. Dust Extinction

Parameters	OH65	OH71	OH79	OH84	OH119	OH163
(1)	(2)	(3)	(4)	(5)	(6)	(7)
S_{sil}						
Slope	0.005 ± 0.003		0.007 ± 0.001	0.006 ± 0.003	0.041 ± 0.004	0.002 ± 0.003
Y-intercept	−0.002 ± 0.006		0.009 ± 0.002	−0.013 ± 0.005	0.027 ± 0.006	0.04 ± 0.01
Correlation Coefficient	0.60		0.42	0.38	0.59	0.02
p-value	0.12		0.02*	0.31	0.0001***	0.92
Balmer Decrement						
Slope			−0.0011 ± 0.0003		−0.010 ± 0.004	−0.0021 ± 0.0009
Y-intercept			0.018 ± 0.004		0.09 ± 0.03	0.06 ± 0.02
Correlation Coefficient			−0.63		−0.47	0.07
p-value			0.002***		0.014*	0.80

Note. — Col. (1): Linear fitting parameters. Col. (2)−(7): Results from the linear fit for each OH transition, and the Spearman rank-order correlation coefficient and the p-value to test for non-correlation. *: indicates $p < 0.05$; however, the observable is an uncertain predictor of EW(OH) due to $r < 0.5$. **: indicates a weak correlation with $r \geq 0.5$ and $0.01 < p < 0.05$. ***: indicates a significant correlation with $r \geq 0.5$ and $p < 0.01$. Blank spaces in the table indicate that there is less than 8 galaxies so no fit was made.

Table 6B.10: Bivariate Regression Results

OH Doublet	log([O IV] 25.89μm/[Ne II] 12.81μm) Coeff.	log($L_{2-10keV}$) Coeff.	S_{sil} Coeff.	Y-Intercept	R^2
(1)	(2)	(3)	(4)		
OH65					
OH71					
OH79	0.0026	−0.0007	0.0088	0.0437	0.61
OH84					
OH119	−0.005	0.018	0.039	−0.755	0.91
OH163	−0.005	0.003	0.005	−0.070	0.04

Note. — Col. (1): OH doublet. Col. (2)-(4): Coefficients for the log([O IV] 25.89μm/[Ne II] 12.81μm), log($L_{2-10keV}$), and S_{sil} fits. Col. (5): Y-intercept for the bivariate fit. Col. (4): R^2 for the bivariate fit. Blank spaces in the table indicate that there is less than 8 galaxies so no fit was made.

6C Supplemental Figures

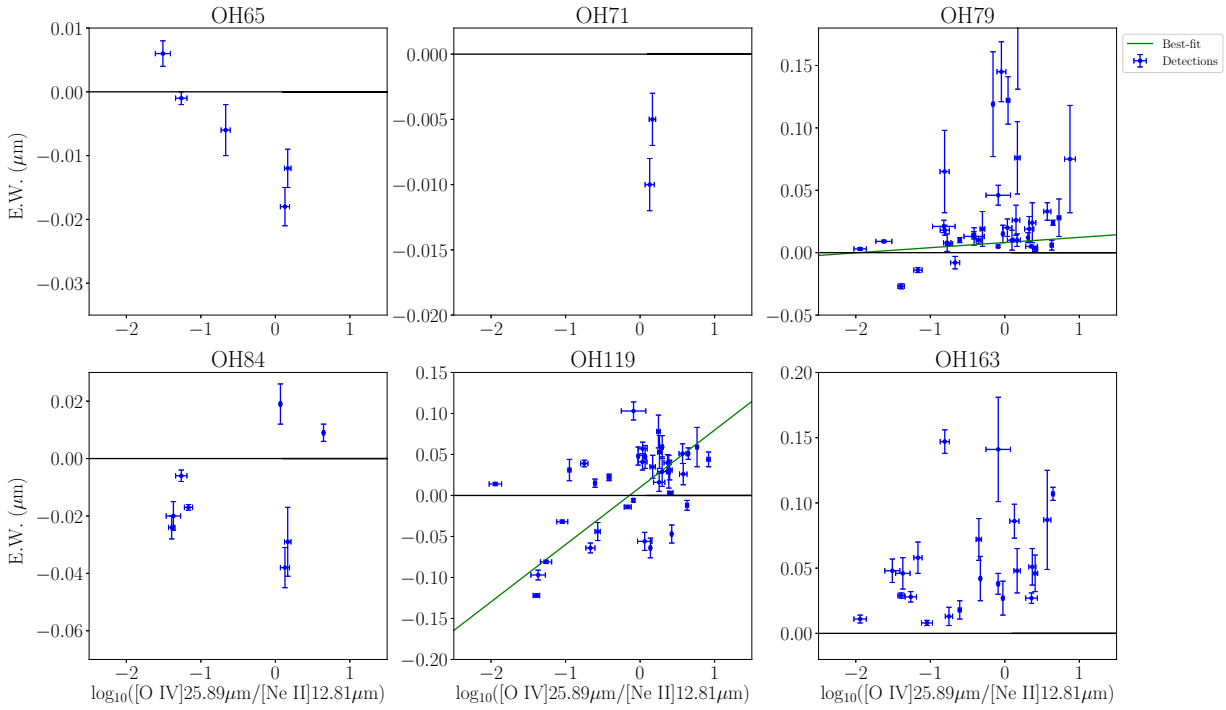

Figure 6C.1: EW of the OH doublet vs. the logarithm of the [O IV] 25.89μm/[Ne II] 12.81μm emission-line ratio. Galaxies must have detections in EW(OH), [O IV] 25.89μm, and [Ne II] 12.81μm to be included in the plot and fits. The weighted log-linear fits, using the parameters given in Table 6B.6, are shown for fits with p < 0.05. We do not show the fit for slopes with a p-value > 0.05. For OH79, MCG-01-24-012 is an outlier (EW = 0.242μm), and is cut off to better show the rest of the data.

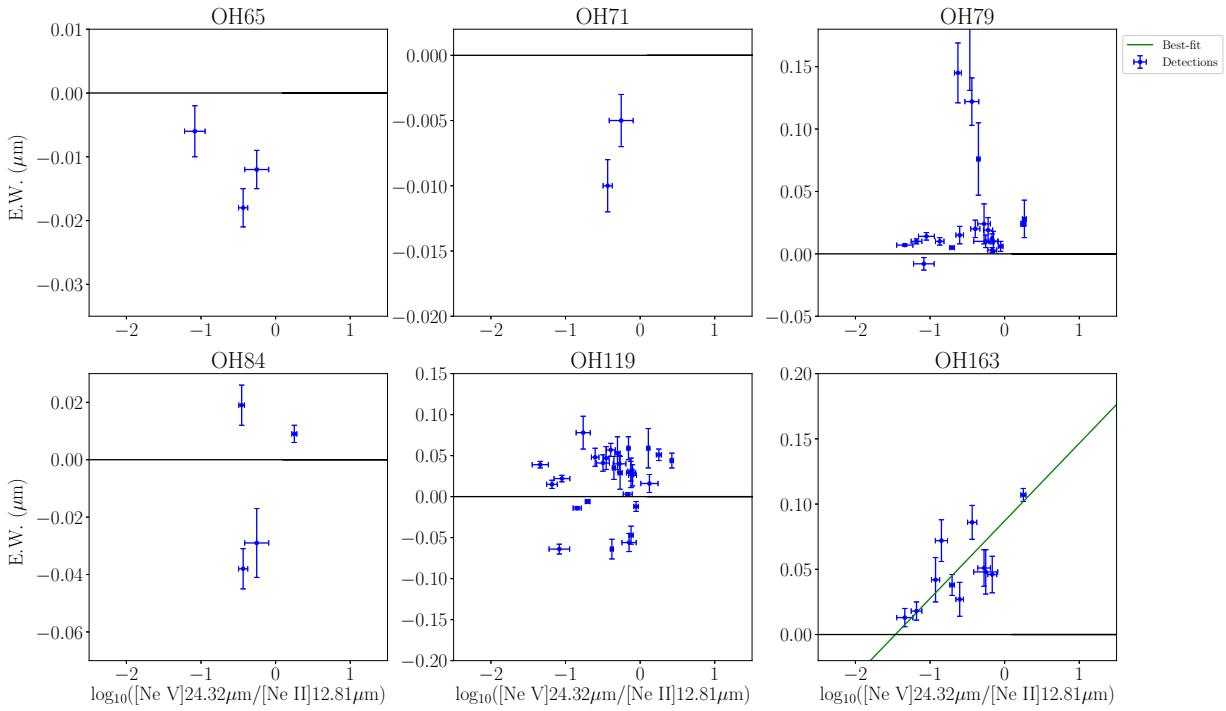

Figure 6C.2: Same as Figure 6C.1 for the [Ne V] 24.32μm/[Ne II] 12.81μm emission-line ratio.

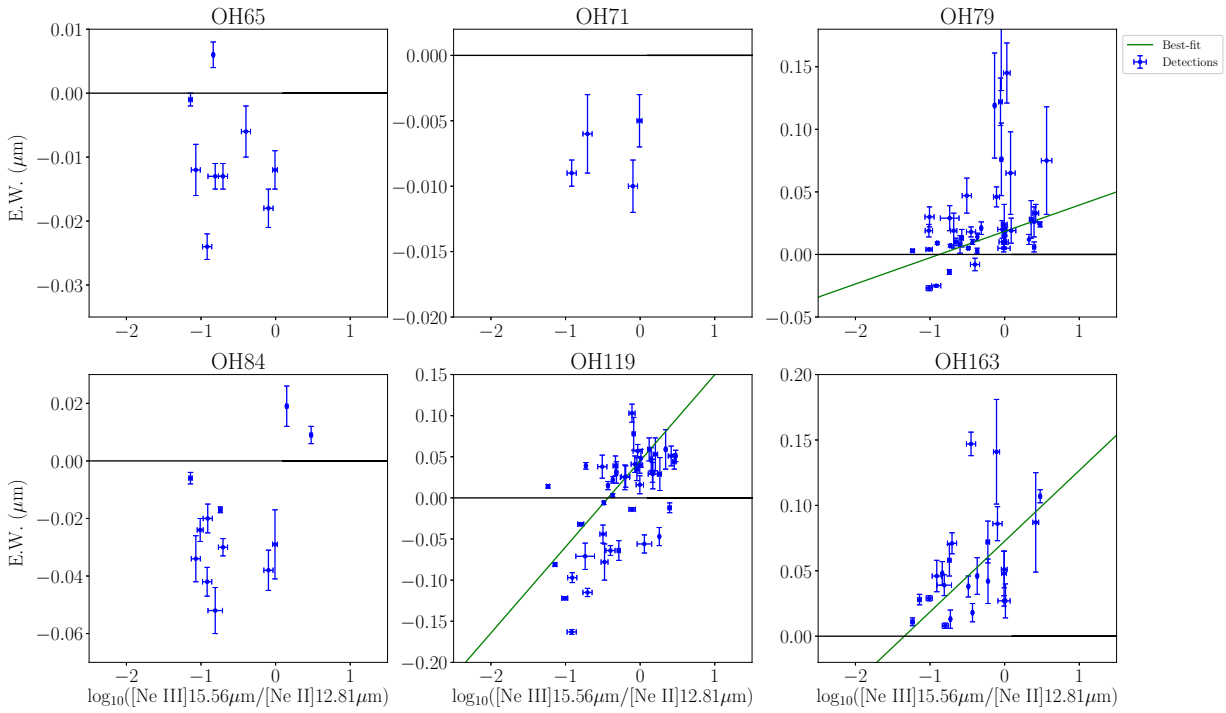

Figure 6C.3: Same as Figure 6C.1 for the [Ne III] 15.56μm/[Ne II] 12.81μm emission-line ratio.

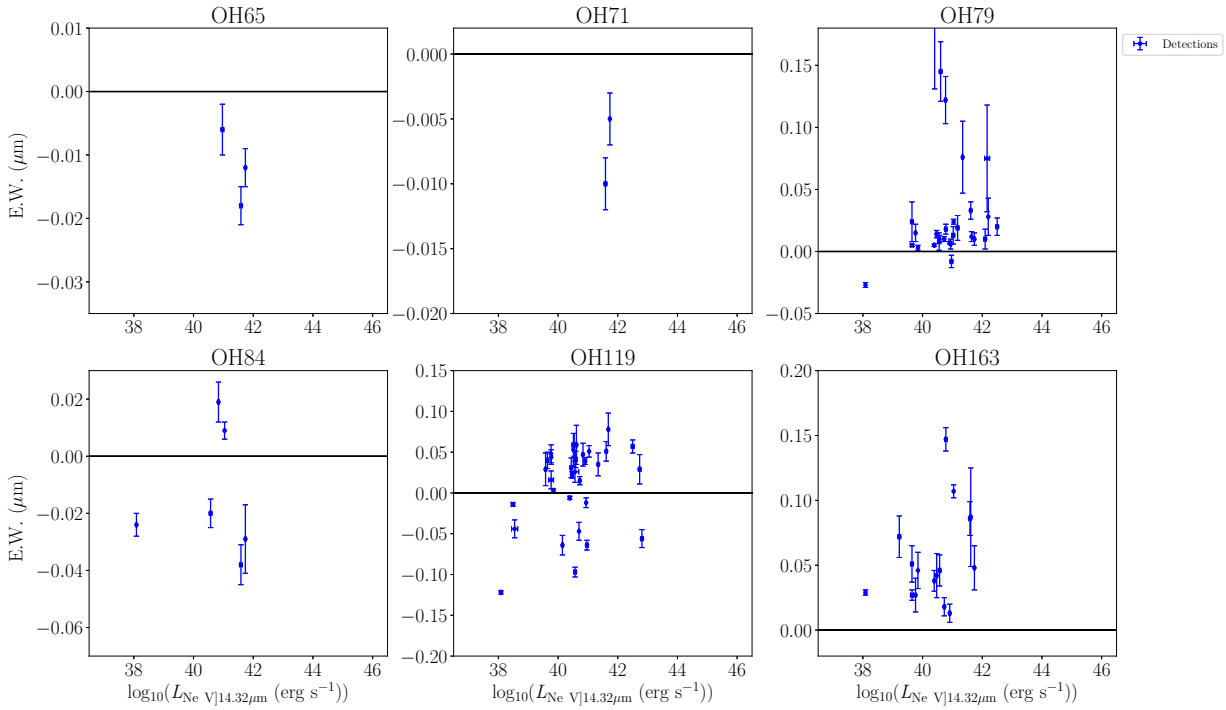

Figure 6C.4: EW of the OH doublet vs. $\log(L_{[\text{Ne V}]14.32\mu\text{m}}$ (erg/s)). Galaxies must have detections in EW(OH) and $L_{[\text{Ne V}]14.32\mu\text{m}}$ to be included in the plot and fits. The weighted log-linear fits, using the parameters given in Table 6B.7, are shown for fits with p < 0.05. We do not show the fit for slopes with a p-value > 0.05. For OH79, MCG-01-24-012 is an outlier (EW = 0.242μm), and is cut off to better show the rest of the data.

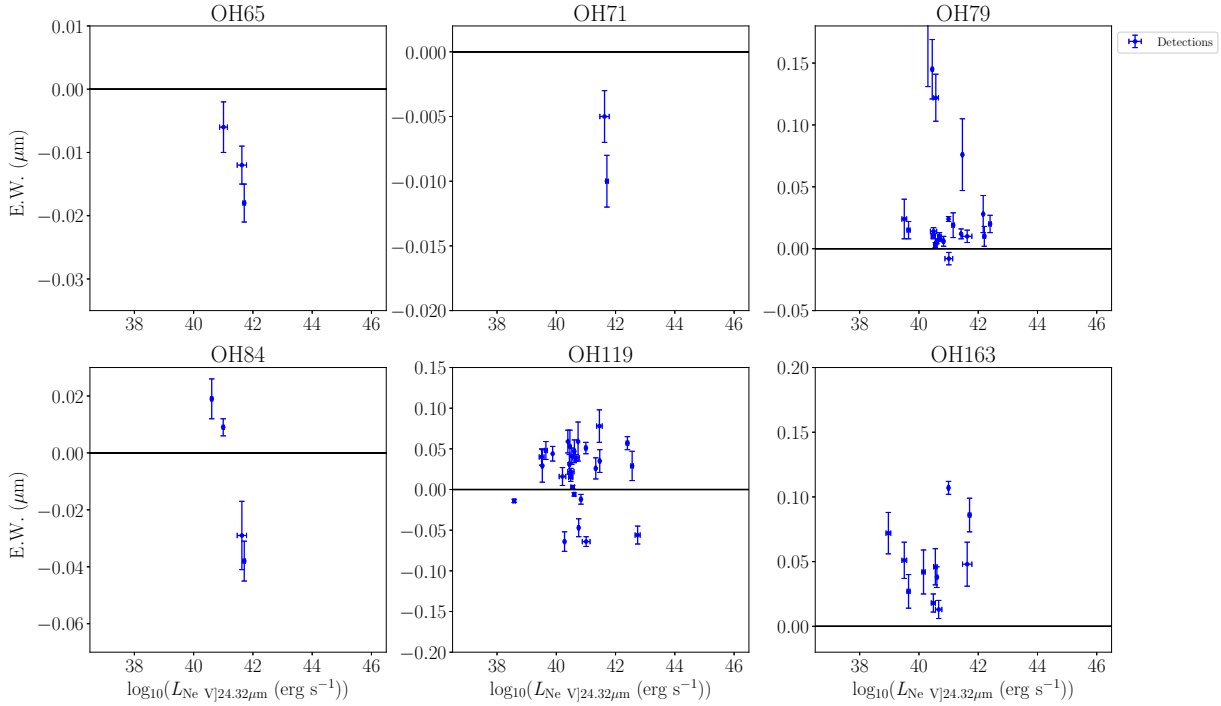

Figure 6C.5: Same as Figure 6C.4 for the [Ne V] 24.32μm emission-line luminosity.

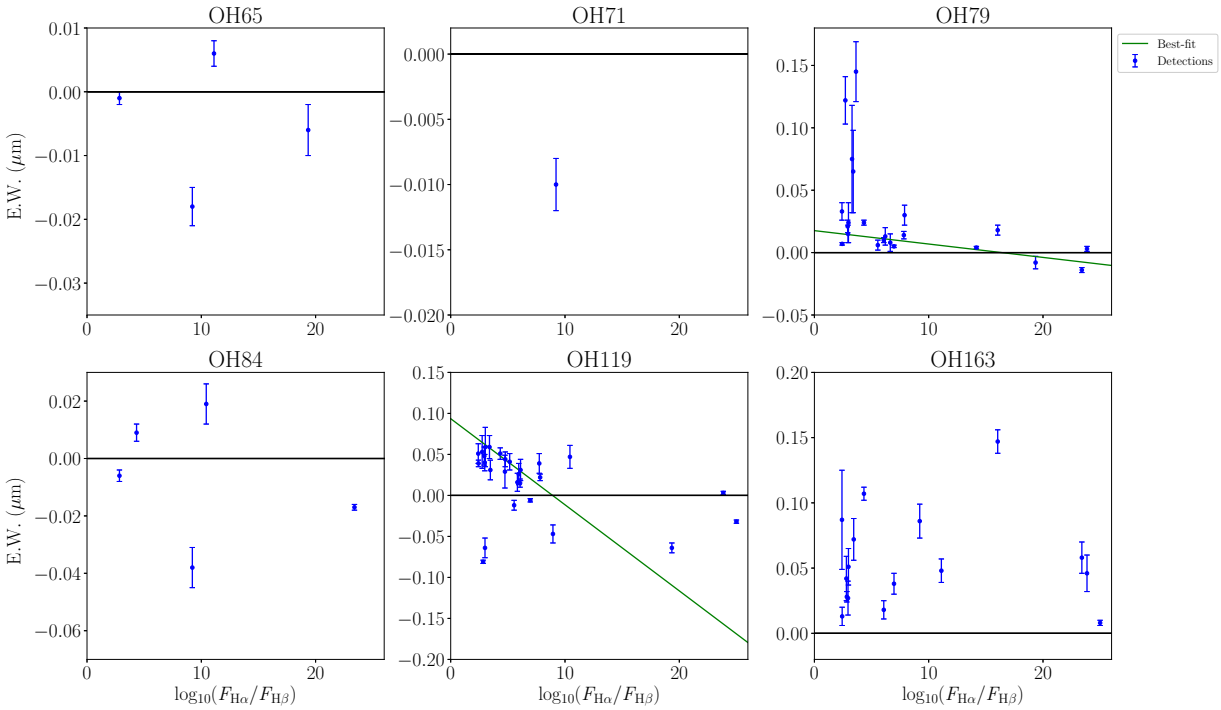

Figure 6C.6: EW of the OH doublet vs. the ratio of Hα to Hβ. Galaxies must have detections in EW(OH), Hα, and Hβ to be included in the plot and fits. The weighted log-linear fits, using the parameters given in Table 6B.9, are shown for fits with p < 0.05. We do not show the fit for slopes with a p-value > 0.05.

CHAPTER 7

Conclusions

To understand the evolution of the universe, it is essential to study galaxies across multiple cosmic epochs. In this thesis, I have presented a comprehensive study of both rest-optical emission-line spectra in the $z \sim 2$ universe and far-IR OH spectroscopy in the local $z \sim 0$ universe. I analyze the rest-optical emission-line properties of the star-forming galaxies in the now complete MOSDEF survey, both the subset of galaxies with high S/N in all relevant emission-lines, and the larger sample of lower S/N stacked galaxies with BPT coverage. I also compare the MOSDEF and KBSS-MOSFIRE surveys to gain a full understanding of the well cited differences found between the two samples in previous studies. I identify and analyze a unique galaxy in the MOSDEF survey at $z = 1.89$ that is part of a major merger and investigate the physical properties and SFH of this system. Finally, I present a study on the affects host galaxy observables have on far-IR OH doublet transitions in the local $z \sim 0$ universe.

In Chapter 2, I analyze the sample of 122 star-forming galaxies at $z \sim 2$ in the MOSDEF survey with S/N $\geq$ 3 for the [O II]$\lambda\lambda$3727,3730, Hβ, [O III]$\lambda\lambda$4960,5008, Hα, [N II]λ6585, and [S II]$\lambda\lambda$6718,6733 emission lines. I split the sample into two groups, galaxies offset from the local $z \sim 0$ SDSS sequence (*high* sample) and galaxies overlapping with the local sequence (*low* sample). I find that the galaxies more offset on the [N II] BPT diagram have a harder ionizing spectrum with a more intense and compact distribution of star formation compared to the $z \sim 2$ galaxies overlapping with the local emission-line sequence. In addition, galaxies in the *high* sample are more α-enhanced (i.e., having super-solar O/Fe values); however, both the *high* and *low* samples

are significantly α-enhanced relative to local $z \sim 0$ star-forming galaxies (assuming approximately solar α/Fe metallicity for the SDSS galaxies) at similar locations on the [N II] BPT diagram. Such α-enhancement is due to the typical star-formation histories of $z \sim 2$ star-forming galaxies and the different timescales and chemical yields of Type Ia and Type II supernovae. Type Ia (II) supernovae events produce large amounts of iron (α elements such as oxygen) and occur on timescales of ~ 1 Gyr (~ 0.1 Gyr) after the onset of star formation in a galaxy. Galaxies at $z \sim 2$ are too young to have significant numbers of Type Ia supernova events (with high Fe yields), leading to these galaxies being chemically "young" with a much lower α/Fe ratio compared to galaxies today.

With the physical and emission-line properties of the MOSDEF $z \sim 2$ sample better understood, in Chapter 3 I compare the MOSDEF $z \sim 2$ sample with the KBSS-MOSFIRE $z \sim 2$ sample. In particular, I analyze both the high S/N samples from previously published works (Sanders et al. 2018 for MOSDEF and Strom et al. 2017 for KBSS) as well as the larger samples targeted by both surveys using consistent SED and emission-line fitting techniques. I find that the $z \sim 2$ targeted samples have differences in the median values of the physical properties investigated, which is expected due to the different methods used to construct the surveys (i.e., rest-optical limited for MOSDEF and primarily rest-UV selected for KBSS). However, the $z \sim 2$ spectroscopic samples with high S/N emission-lines are actually much more similar. Aside from the stellar population age, the median values for the remaining host galaxy properties investigated in this study agree within the uncertainties. Even more significant is that the magnitudes of the perpendicular offsets of the MOSDEF and KBSS $z \sim 2$ spectroscopic samples relative to the local SDSS sequence agree within the uncertainties. The previously cited differences in the magnitudes of this offset have been resolved by an updated (smaller) estimate of the stellar Balmer absorption corrections for the MOSDEF sample as well as utilizing consistent emission-line fitting techniques. This result is found when fitting both samples with either the MOSDEF or KBSS `MOSPEC` emission-line fitting code. Both sets of emission-line fitting assumptions were reasonable, revealing that even simple analysis processes can introduce noticeable uncertainties in the results. The line fluxes of weaker emission lines (e.g. [N II]λ6585) were most affected by the differences in the line fitting methodologies.

Finally, it was revealed that while the KBSS $z \sim 2$ spectroscopic sample reflected the targeted sample from which it was drawn, the MOSDEF $z \sim 2$ spectroscopic sample was incomplete with respect to the population of high mass, red galaxies it targeted.

The results from this comparison reveal notable differences between the high S/N $z \sim 2$ spectroscopic sample and the complete $z \sim 2$ sample observed by MOSDEF. As previously stated, the full $z \sim 2$ targeted sample is redder and more massive on average; however, this sample contains both AGN and quiescent galaxies. In order to gain a more complete census of star-forming galaxies *alone*, in Chapter 4 I remove all non-star-forming galaxies (i.e., AGN and quiescents) as well as galaxies that do not have a robust redshift from the observed spectrum, and utilize spectral stacking to investigate the properties of all $z \sim 2$ MOSDEF star-forming galaxies with coverage of all rest-optical emissions-lines necessary for the [N II] BPT diagram. This $z \sim 2$ stacked sample is over three times larger than the $z \sim 2$ spectroscopic sample with high S/N BPT detections. The galaxies in the $z \sim 2$ stacked sample are slightly more massive with lower rates of star formation (only ~ 0.1 dex for each property). In addition, I find that the $z \sim 2$ stacked sample has a similar perpendicular offset to the SDSS local sequence on the [N II] BPT diagram, and the correlations between these rest-optical line ratios and M_* for the $z \sim 2$ stacked sample agree with other recent MOSDEF studies using smaller high S/N samples. These findings indicate that such high S/N subsets of the MOSDEF $z \sim 2$ targeted sample frequently used are representative of all star-forming galaxies observed by MOSDEF. The MOSDEF $z \sim 2$ targeted sample is also similar to the $z \sim 2$ parent sample from which it was drawn. There are minor differences between the sample medians for M_*, SFR(SED), and sSFR(SED); however, overall the distributions are very similar. These findings are significant, as they show that the galaxies targeted by MOSDEF are representative of the $z \sim 2$ galaxy population.

In Chapter 5, I investigate a unique galaxy in the MOSDEF sample, GOODS-S 43114. This galaxy is currently undergoing a major merger with the neighboring galaxy, GOODS-S 43683, at $z = 1.89$. X-ray luminosity measurements show that both galaxies contain an AGN, and UVJ

colors and SED shape indicate that both are in a post-starburst phase. Modeling the SFHs reveals that the bursts of star formation in GOODS-S 43114 and GOODS-S 43683 both began and peaked within a few hundred Myrs of each other. The t/τ values found from SED fitting agree within the uncertainties, confirming the similarities in the SFHs for the two galaxies. Connecting this information with realistic galaxy simulations suggests that the merging pair has completed the first pericentric passage, which likely triggered the star formation bursts in both galaxies. Furthermore, GOODS-S 43114 is probably a face-on disk as estimates of the velocity dispersion and dynamical mass underestimate the true values.

Shifting focus to the local $z \sim 0$ universe, in Chapter 6 I search for correlations between far-IR OH doublet transitions with a variety of host galaxy observables. I find that equivalent width (EW) for the lower energy level transitions (i.e., OH79, OH119, and OH163) strongly correlate with the presence and strength of an AGN. EW(OH79) and EW(OH119) are also found to be influenced by the amount of dust extinction in the host galaxy. The relationship between these transitions and the host galaxy observables are different for each line due to the differences in how they are excited into emission (collisionally for OH119, radiation pumping for OH163, and a mix of both processes for OH79). Larger sample sizes are needed to confirm any possible correlations between EW(OH) and AGN strength or dust extinction for the higher energy level transtions (i.e., OH65, OH71, and OH84). Predicting the shape of OH line profiles based on these more widely available galaxy observables will help realistic galaxy simulations (e.g. FIRE-2; Hopkins et al. 2018) constrain outflow properties, thus more accurately predicting the impact of outflows on galaxy evolution.

As we look ahead, the future is bright for extragalactic astronomy, as the field will be transformed by both new observatories and new instruments upgrading existing observatories in the near future. The James Webb Space Telescope (JWST) has recently launched, and has improved sensitivity and a wider wavelength range compared to *Keck*/MOSFIRE. JWST can obtain both rest-optical spectra at $z \sim 2$ as well as expanding the rest-optical emission-line analysis shown in this thesis out to to the reionization epoch ($z > 6$), which *Keck*/MOSFIRE is not capable of doing. Analyzing the

rest-optical emission-line properties of star-forming galaxies at the end of the epoch of reionization (approximately 1 Gyr after the Big Bang) will transform our understanding of galaxies in the early universe. Data acquisition for JWST is scheduled to begin within the next year. Additionally, there are new instruments to upgrade the W.M. Keck observatory. One notable instruments is Liger, which is a near-IR integral field spectrograph (IFS) with better sensitivity than its predecessor the OH-Suppressing Infrared Integral Field Spectrograph (OSIRIS), allowing for better mapping of galaxy kinematics, morphology, and emission-line strength at $z \sim 2$. Liger is not yet complete and still being designed. Finally, the next generation of ground-based telescopes are in various stages of development. The European Extremely Large Telescope (E-ELT) and the Giant Magellan Telescope (GMT) are under construction with planned first light by 2027 and 2029, respectively. Construction for the Thirty Meter Telescope (TMT) has not yet begun. These telescopes will have much larger primary mirrors than existing ones (e.g., Keck), which means we will be able to obtain higher quality rest-optical and rest-UV spectra for $z \sim 2$ galaxies in a fraction of the observing time.

When all of these planned projects are complete, there is significant discovery space related to galaxy formation and evolution. Higher resolution rest-optical spectra will lead to the detection of fainter emission-lines. For example, [Ne III]λ3869 is currently only typically detected in lower-metallicity, higher-excitation sources. The [Ne III]λ3869/[O II]λ3727 ratio is used as an empirical metallicity tracer that is insensitive to dust extinction; however, the limitations in detecting [Ne III]λ3869 mean the samples currently available are not representative of all $z \sim 2$ star-forming galaxies. Another example are faint auroral lines (e.g., [O III]λ4363). As discussed in this thesis, the nebular metallicity of star-forming galaxies at $z > 1$ are usually estimated from ratios of strong emission-lines (e.g., Hβ, [O III]λ5008, Hα, [N II]λ6585) that have been calibrated based on local observations. However, the flux ratio of the auroral line to its corresponding strong line feature (e.g., [O III]λ4363/[O III]λ5008) can directly probe the metallicity of the ISM. However, at the present time, there are only 5 detections (i.e., $\geq 3\sigma$) of [O III]λ4363 at $z > 1.5$, as it is too faint for current telescopes (e.g., Keck). JWST and ELTs should help significantly with detecting valuable weaker

lines like [Ne III]λ3869 and auroral lines such as [O III]λ4363. Rest-UV spectroscopy is essential for constraining the stellar metallicity of a galaxy. Therefore, combining rest-optical and rest-UV spectra is vital for obtaining a complete understanding of the full suite of physical and chemical properties of a galaxy, which is necessary to build calibrations between empirical emission-line ratios and key physical quantities (e.g., gas-phase oxygen abundance). The massive influx of data from these new observatories and instruments will significantly increase our knowledge of our Universe's past and present.

Bibliography

Aalto S., Garcia-Burillo S., Muller S., Winters J. M., van der Werf P., Henkel C., Costagliola F., Neri R., 2012, A&A, 537, A44

Abazajian K. N., et al., 2009, ApJS, 182, 543

Adelberger K. L., Steidel C. C., Shapley A. E., Hunt M. P., Erb D. K., Reddy N. A., Pettini M., 2004, ApJ, 607, 226

Alonso-Herrero A., et al., 2016, MNRAS, 455, 563

Andrews B. H., Martini P., 2013, ApJ, 765, 140

Antonucci R. R. J., Miller J. S., 1985, ApJ, 297, 621

Asplund M., Grevesse N., Sauval A. J., Scott P., 2009, ARA&A, 47, 481

Azadi M., et al., 2017, ApJ, 835, 27

Baldwin J. A., Phillips M. M., Terlevich R., 1981, PASP, 93, 5

Balestra I., et al., 2010, A&A, 512, A12

Balogh M. L., Morris S. L., Yee H. K. C., Carlberg R. G., Ellingson E., 1999, ApJ, 527, 54

Barnes J. E., Hernquist L. E., 1991, ApJ, 370, L65

Barnes J. E., Hernquist L., 1996, ApJ, 471, 115

Barthelmy S. D., et al., 2005, Space Sci. Rev., 120, 143

Belli S., Newman A. B., Ellis R. S., 2017, ApJ, 834, 18

Bian F., Kewley L. J., Dopita M. A., 2018, ApJ, 859, 175

Bian F., Kewley L. J., Groves B., Dopita M. A., 2020, MNRAS, 493, 580

Blumenthal K. A., Barnes J. E., 2018, MNRAS, 479, 3952

Bouwens R. J., et al., 2016, ApJ, 833, 72

Bradford C. M., et al., 1999, in Cox P., Kessler M., eds, ESA Special Publication Vol. 427, The Universe as Seen by ISO. p. 861

Brammer G. B., van Dokkum P. G., Coppi P., 2008, ApJ, 686, 1503

Brinchmann J., Pettini M., Charlot S., 2008, MNRAS, 385, 769

Bruzual G., Charlot S., 2003, MNRAS, 344, 1000

Calzetti D., Armus L., Bohlin R. C., Kinney A. L., Koornneef J., Storchi-Bergmann T., 2000, ApJ, 533, 682

Cappellari M., 2017, MNRAS, 466, 798

Cappellari M., Emsellem E., 2004, PASP, 116, 138

Cardelli J. A., Clayton G. C., Mathis J. S., 1989, ApJ, 345, 245

Chabrier G., 2003, PASP, 115, 763

Clark C. J. R., et al., 2019, MNRAS, 489, 5256

Clegg P. E., et al., 1996, A&A, 315, L38

Cohen R. D., Osterbrock D. E., 1981, ApJ, 243, 81

Coil A. L., et al., 2015, ApJ, 801, 35

Conroy C., Gunn J. E., 2010, ApJ, 712, 833

Contini M., 2012, MNRAS, 426, 719

Cox T. J., Jonsson P., Somerville R. S., Primack J. R., Dekel A., 2008, MNRAS, 384, 386

Cullen F., et al., 2019, MNRAS, 487, 2038

Dai Y. S., et al., 2021, ApJ, 923, 156

Di Matteo T., Springel V., Hernquist L., 2005, Nature, 433, 604

Di Matteo P., Combes F., Melchior A. L., Semelin B., 2007, A&A, 468, 61

Di Matteo P., Bournaud F., Martig M., Combes F., Melchior A. L., Semelin B., 2008, A&A, 492, 31

Diamond-Stanic A. M., Rieke G. H., Rigby J. R., 2009, ApJ, 698, 623

Diaz A. I., Prieto M. A., Wamsteker W., 1988, A&A, 195, 53

Donevski D., et al., 2020, A&A, 644, A144

Du X., et al., 2018, ApJ, 860, 75

Durret F., Bergeron J., 1988, A&AS, 75, 273

Edelson R. A., Malkan M. A., 1986, ApJ, 308, 59

Eldridge J. J., Stanway E. R., Xiao L., McClelland L. A. S., Taylor G., Ng M., Greis S. M. L., Bray J. C., 2017, PASA, 34, e058

Ellison S. L., Patton D. R., Simard L., McConnachie A. W., 2008, AJ, 135, 1877

Erb D. K., Shapley A. E., Pettini M., Steidel C. C., Reddy N. A., Adelberger K. L., 2006a, ApJ, 644, 813

Erb D. K., Steidel C. C., Shapley A. E., Pettini M., Reddy N. A., Adelberger K. L., 2006b, ApJ, 647, 128

Erkens U., Appenzeller I., Wagner S., 1997, A&A, 323, 707

Esdaile J., et al., 2021, ApJ, 908, L35

Falstad N., et al., 2015, A&A, 580, A52

Farrah D., et al., 2013, ApJ, 776, 38

Fensch J., et al., 2017, MNRAS, 465, 1934

Ferland G. J., et al., 2017, Rev. Mexicana Astron. Astrofis., 53, 385

Fernández-Ontiveros J. A., Spinoglio L., Pereira-Santaella M., Malkan M. A., Andreani P., Dasyra K. M., 2016, ApJS, 226, 19

Feruglio C., Maiolino R., Piconcelli E., Menci N., Aussel H., Lamastra A., Fiore F., 2010, A&A, 518, L155

Fischer J., et al., 2010, A&A, 518, L41

Fluetsch A., et al., 2019, MNRAS, 483, 4586

Freeman W. R., et al., 2019, ApJ, 873, 102

Gilli R., Vignali C., Mignoli M., Iwasawa K., Comastri A., Zamorani G., 2010, A&A, 519, A92

Gnerucci A., et al., 2011, A&A, 533, A124

Golombek D., Miley G. K., Neugebauer G., 1988, AJ, 95, 26

González-Alfonso E., Smith H. A., Fischer J., Cernicharo J., 2004, ApJ, 613, 247

González-Alfonso E., Smith H. A., Ashby M. L. N., Fischer J., Spinoglio L., Grundy T. W., 2008, ApJ, 675, 303

González-Alfonso E., et al., 2012, A&A, 541, A4

González-Alfonso E., et al., 2014, A&A, 561, A27

González-Alfonso E., et al., 2015, ApJ, 800, 69

González-Alfonso E., et al., 2017a, PASA, 34, e054

González-Alfonso E., et al., 2017b, ApJ, 836, 11

González-Martín O., et al., 2015, A&A, 578, A74

Goodrich R. W., 1989, ApJ, 342, 224

Goodrich R. W., Osterbrock D. E., 1983, ApJ, 269, 416

Goodrich R. W., Veilleux S., Hill G. J., 1994, ApJ, 422, 521

Grogin N. A., et al., 2011, ApJS, 197, 35

Hainline K. N., Shapley A. E., Greene J. E., Steidel C. C., 2011, ApJ, 733, 31

Hao C.-N., Kennicutt R. C., Johnson B. D., Calzetti D., Dale D. A., Moustakas J., 2011, ApJ, 741, 124

Harshan A., et al., 2020, ApJ, 892, 77

Hatziminaoglou E., Hernán-Caballero A., Feltre A., Piñol Ferrer N., 2015, ApJ, 803, 110

Heckman T. M., 1980, A&A, 500, 187

Helou G., Walker D. W., 1988, NASA RP-1190, 7, 0

Hernán-Caballero A., et al., 2015, ApJ, 803, 109

Ho L. C., Filippenko A. V., Sargent W. L. W., 1993, ApJ, 417, 63

Ho L. C., Filippenko A. V., Sargent W. L. W., 1997, ApJS, 112, 315

Hopkins P. F., Hernquist L., Cox T. J., Kereš D., 2008, ApJS, 175, 356

Hopkins P. F., et al., 2010, ApJ, 724, 915

Hopkins P. F., Quataert E., Murray N., 2011, MNRAS, 417, 950

Hopkins P. F., Kereš D., Oñorbe J., Faucher-Giguère C.-A., Quataert E., Murray N., Bullock J. S., 2014, MNRAS, 445, 581

Hopkins P. F., et al., 2018, MNRAS, 480, 800

Horstman K., et al., 2021, MNRAS, 501, 137

Houck J. R., et al., 2004, ApJS, 154, 18

Jeong M.-S., et al., 2020, ApJ, 902, L16

Johnson B., et al., 2021, dfm/python-fsps: python-fsps v0.4.1rc1, doi:10.5281/zenodo.4737461, https://doi.org/10.5281/zenodo.4737461

Joint Iras Science W. G., 1994, VizieR Online Data Catalog, p. II/125

Juneau S., et al., 2014, ApJ, 788, 88

Kartaltepe J. S., et al., 2015, ApJS, 221, 11

Kashino D., et al., 2013, ApJ, 777, L8

Kashino D., et al., 2017, ApJ, 835, 88

Kashino D., et al., 2019, ApJS, 241, 10

Kauffmann G., et al., 2003, MNRAS, 346, 1055

Kegel W. H., Hertenstein T., Quirrenbach A., 1999, A&A, 351, 472

Kennicutt Robert C. J., et al., 2003, PASP, 115, 928

Kessler M. F., et al., 1996, A&A, 500, 493

Kewley L. J., Dopita M. A., Sutherland R. S., Heisler C. A., Trevena J., 2001, ApJ, 556, 121

Kewley L. J., Dopita M. A., Leitherer C., Davé R., Yuan T., Allen M., Groves B., Sutherland R., 2013, ApJ, 774, 100

Koekemoer A. M., et al., 2011, ApJS, 197, 36

Koski A. T., 1978, ApJ, 223, 56

Kraemer S. B., Wu C.-C., Crenshaw D. M., Harrington J. P., 1994, ApJ, 435, 171

Kriek M., et al., 2008, ApJ, 677, 219

Kriek M., van Dokkum P. G., Labbé I., Franx M., Illingworth G. D., Marchesini D., Quadri R. F., 2009, ApJ, 700, 221

Kriek M., et al., 2015, ApJS, 218, 15

Kriek M., et al., 2016, Nature, 540, 248

Lacy J. H., et al., 1982, ApJ, 256, 75

Law D. R., Steidel C. C., Shapley A. E., Nagy S. R., Reddy N. A., Erb D. K., 2012, ApJ, 745, 85

Lee J. C., Hwang H. S., Lee M. G., Kim M., Kim S. C., 2011, MNRAS, 414, 702

Leung G. C. K., et al., 2017, ApJ, 849, 48

Lilly S. J., Carollo C. M., Stockton A. N., 2003, ApJ, 597, 730

Liu X., Shapley A. E., Coil A. L., Brinchmann J., Ma C.-P., 2008, ApJ, 678, 758

Lofthouse E. K., Kaviraj S., Conselice C. J., Mortlock A., Hartley W., 2017, MNRAS, 465, 2895

Lotz J. M., Jonsson P., Cox T. J., Croton D., Primack J. R., Somerville R. S., Stewart K., 2011, ApJ, 742, 103

Luo B., et al., 2008, ApJS, 179, 19

Madau P., Dickinson M., 2014, ARA&A, 52, 415

Magnelli B., et al., 2020, ApJ, 892, 66

Malkan M. A., 1986, ApJ, 310, 679

Malkan M. A., Jensen L. D., Rodriguez D. R., Spinoglio L., Rush B., 2017, ApJ, 846, 102

Man A. W. S., Toft S., Zirm A. W., Wuyts S., van der Wel A., 2012, ApJ, 744, 85

Man A. W. S., Zirm A. W., Toft S., 2016, ApJ, 830, 89

Mannucci F., Cresci G., Maiolino R., Marconi A., Gnerucci A., 2010, MNRAS, 408, 2115

Mantha K. B., et al., 2018, MNRAS, 475, 1549

Masters D., et al., 2014, ApJ, 785, 153

Masters D., Faisst A., Capak P., 2016, ApJ, 828, 18

McLean I. S., et al., 2012, in Ground-based and Airborne Instrumentation for Astronomy IV. p. 84460J, doi:10.1117/12.924794

McLure R. J., et al., 2018, MNRAS, 476, 3991

Meixner M., et al., 2018, in Ootsubo T., Yamamura I., Murata K., Onaka T., eds, The Cosmic Wheel and the Legacy of the AKARI Archive: From Galaxies and Stars to Planets and Life. pp 59–65

Meurer G. R., Heckman T. M., Calzetti D., 1999, ApJ, 521, 64

Miller J. S., Goodrich R. W., 1990, ApJ, 355, 456

Momcheva I. G., et al., 2016, ApJS, 225, 27

Moreno J., Torrey P., Ellison S. L., Patton D. R., Bluck A. F. L., Bansal G., Hernquist L., 2015, MNRAS, 448, 1107

Moreno J., et al., 2019, MNRAS, 485, 1320

Morris S. L., Ward M. J., 1988, MNRAS, 230, 639

Moshir M., et al., 1990, in Bulletin of the American Astronomical Society. p. 1325

Moshir M., Kopman G., Conrow T. A. O., 1992, IRAS Faint Source Survey, Explanatory supplement version 2

Mostardi R. E., Shapley A. E., Steidel C. C., Trainor R. F., Reddy N. A., Siana B., 2015, ApJ, 810, 107

Moustakas J., Kennicutt Robert C. J., Tremonti C. A., Dale D. A., Smith J.-D. T., Calzetti D., 2010, ApJS, 190, 233

Nakajima K., Ouchi M., Shimasaku K., Hashimoto T., Ono Y., Lee J. C., 2013, ApJ, 769, 3

Newman A. B., Belli S., Ellis R. S., Patel S. G., 2018a, ApJ, 862, 125

Newman A. B., Belli S., Ellis R. S., Patel S. G., 2018b, ApJ, 862, 126

Oke J. B., Lauer T. R., 1979, ApJ, 230, 360

Osterbrock D. E., 1977, ApJ, 215, 733

Osterbrock D. E., 1981, ApJ, 249, 462

Osterbrock D. E., Dahari O., 1983, ApJ, 273, 478

Osterbrock D. E., Martel A., 1993, ApJ, 414, 552

Osterbrock D. E., Miller J. S., 1975, ApJ, 197, 535

Osterbrock D. E., Pogge R. W., 1985, ApJ, 297, 166

Ott S., 2010, in Mizumoto Y., Morita K. I., Ohishi M., eds, Astronomical Society of the Pacific Conference Series Vol. 434, Astronomical Data Analysis Software and Systems XIX. p. 139 (arXiv:1011.1209)

Pannella M., et al., 2015, ApJ, 807, 141

Patton D. R., Ellison S. L., Simard L., McConnachie A. W., Mendel J. T., 2011, MNRAS, 412, 591

Patton D. R., Torrey P., Ellison S. L., Mendel J. T., Scudder J. M., 2013, MNRAS, 433, L59

Pérez-Montero E., 2014, MNRAS, 441, 2663

Persson S. E., et al., 2013, PASP, 125, 654

Pettini M., Pagel B. E. J., 2004, MNRAS, 348, L59

Phillips M. M., Charles P. A., Baldwin J. A., 1983, ApJ, 266, 485

Pilbratt G. L., et al., 2010, A&A, 518, L1

Pilyugin L. S., Vílchez J. M., Mattsson L., Thuan T. X., 2012, MNRAS, 421, 1624

Poglitsch A., et al., 2010, A&A, 518, L2

Popping G., et al., 2022, arXiv e-prints, p. arXiv:2204.08483

Price S. H., et al., 2014, ApJ, 788, 86

Price S. H., et al., 2016, ApJ, 819, 80

Price S. H., et al., 2020, ApJ, 894, 91

Rangwala N., et al., 2011, ApJ, 743, 94

Reddy N. A., Erb D. K., Steidel C. C., Shapley A. E., Adelberger K. L., Pettini M., 2005, ApJ, 633, 748

Reddy N. A., Steidel C. C., Pettini M., Adelberger K. L., Shapley A. E., Erb D. K., Dickinson M., 2008, ApJS, 175, 48

Reddy N. A., Pettini M., Steidel C. C., Shapley A. E., Erb D. K., Law D. R., 2012, ApJ, 754, 25

Reddy N. A., et al., 2015, ApJ, 806, 259

Reddy N. A., et al., 2018, ApJ, 853, 56

Reddy N. A., et al., 2020, ApJ, 902, 123

Reddy N. A., et al., 2022, ApJ, 926, 31

Roelfsema P. R., et al., 2018, PASA, 35, e030

Rudie G. C., et al., 2012, ApJ, 750, 67

Rudie G. C., Steidel C. C., Pettini M., Trainor R. F., Strom A. L., Hummels C. B., Reddy N. A., Shapley A. E., 2019, ApJ, 885, 61

Runco J. N., Malkan M. A., Fernández-Ontiveros J. A., Spinoglio L., Pereira-Santaella M., 2020, ApJ, 905, 57

Runco J. N., et al., 2021a, arXiv e-prints, p. arXiv:2112.09715

Runco J. N., et al., 2021b, MNRAS, 502, 2600

Sanders R. L., et al., 2015, ApJ, 799, 138

Sanders R. L., et al., 2016, ApJ, 816, 23

Sanders R. L., et al., 2018, ApJ, 858, 99

Sanders R. L., et al., 2020a, MNRAS, 491, 1427

Sanders R. L., et al., 2020b, ApJ, 888, L11

Sanders R. L., et al., 2021, ApJ, 914, 19

Schawinski K., Treister E., Urry C. M., Cardamone C. N., Simmons B., Yi S. K., 2011, ApJ, 727, L31

Schöier F. L., van der Tak F. F. S., van Dishoeck E. F., Black J. H., 2005, A&A, 432, 369

Scudder J. M., Ellison S. L., Torrey P., Patton D. R., Mendel J. T., 2012, MNRAS, 426, 549

Scudder J. M., Ellison S. L., Momjian E., Rosenberg J. L., Torrey P., Patton D. R., Fertig D., Mendel J. T., 2015, MNRAS, 449, 3719

Shapley A. E., Coil A. L., Ma C.-P., Bundy K., 2005, ApJ, 635, 1006

Shapley A. E., et al., 2015, ApJ, 801, 88

Shapley A. E., et al., 2019, ApJ, 881, L35

Shapley A. E., Cullen F., Dunlop J. S., McLure R. J., Kriek M., Reddy N. A., Sanders R. L., 2020, ApJ, 903, L16

Shapley A. E., et al., 2022, ApJ, 926, 145

Shivaei I., et al., 2015, ApJ, 815, 98

Shivaei I., et al., 2020, ApJ, 899, 117

Shivaei I., et al., 2022, ApJ, 928, 68

Shuder J. M., 1980, ApJ, 240, 32

Shuder J. M., Osterbrock D. E., 1981, ApJ, 250, 55

Skelton R. E., et al., 2014, ApJS, 214, 24

Somerville R. S., Davé R., 2015, ARA&A, 53, 51

Spinoglio L., Malkan M. A., 1992, ApJ, 399, 504

Spinoglio L., Malkan M. A., Rush B., Carrasco L., Recillas-Cruz E., 1995, ApJ, 453, 616

Spinoglio L., Malkan M. A., Smith H. A., González-Alfonso E., Fischer J., 2005, ApJ, 623, 123

Spinoglio L., Pereira-Santaella M., Dasyra K. M., Calzoletti L., Malkan M. A., Tommasin S., Busquet G., 2015, ApJ, 799, 21

Spinoglio L., et al., 2017, PASA, 34, e057

Spoon H. W. W., Marshall J. A., Houck J. R., Elitzur M., Hao L., Armus L., Brandl B. R., Charmandaris V., 2007, ApJ, 654, L49

Spoon H. W. W., et al., 2013, ApJ, 775, 127

Stanway E. R., Eldridge J. J., 2018, MNRAS, 479, 75

Steidel C. C., Adelberger K. L., Shapley A. E., Pettini M., Dickinson M., Giavalisco M., 2003, ApJ, 592, 728

Steidel C. C., Shapley A. E., Pettini M., Adelberger K. L., Erb D. K., Reddy N. A., Hunt M. P., 2004, ApJ, 604, 534

Steidel C. C., et al., 2014, ApJ, 795, 165

Steidel C. C., Strom A. L., Pettini M., Rudie G. C., Reddy N. A., Trainor R. F., 2016, ApJ, 826, 159

Stone M., Veilleux S., Meléndez M., Sturm E., Graciá-Carpio J., González-Alfonso E., 2016, ApJ, 826, 111

Strom A. L., Steidel C. C., Rudie G. C., Trainor R. F., Pettini M., Reddy N. A., 2017, ApJ, 836, 164

Strom A. L., Steidel C. C., Rudie G. C., Trainor R. F., Pettini M., 2018, ApJ, 868, 117

Strom A. L., Rudie G. C., Steidel C. C., Trainor R. F., 2022, ApJ, 925, 116

Sturm E., et al., 2011, ApJ, 733, L16

Tanaka M., et al., 2019, ApJ, 885, L34

Tasca L. A. M., et al., 2014, A&A, 565, A10

Tody D., 1986, in Crawford D. L., ed., Society of Photo-Optical Instrumentation Engineers (SPIE) Conference Series Vol. 627, Instrumentation in astronomy VI. p. 733, doi:10.1117/12.968154

Tody D., 1993, in Hanisch R. J., Brissenden R. J. V., Barnes J., eds, Astronomical Society of the Pacific Conference Series Vol. 52, Astronomical Data Analysis Software and Systems II. p. 173

Toft S., Gallazzi A., Zirm A., Wold M., Zibetti S., Grillo C., Man A., 2012, ApJ, 754, 3

Toft S., et al., 2017, Nature, 546, 510

Tommasin S., Spinoglio L., Malkan M. A., Smith H., González-Alfonso E., Charmandaris V., 2008, ApJ, 676, 836

Tommasin S., Spinoglio L., Malkan M. A., Fazio G., 2010, ApJ, 709, 1257

Topping M. W., Shapley A. E., Reddy N. A., Sanders R. L., Coil A. L., Kriek M., Mobasher B., Siana B., 2020a, MNRAS, 495, 4430

Topping M. W., Shapley A. E., Reddy N. A., Sanders R. L., Coil A. L., Kriek M., Mobasher B., Siana B., 2020b, MNRAS, 499, 1652

Topping M. W., et al., 2021, MNRAS, 506, 1237

Tran H. D., Miller J. S., Kay L. E., 1992, ApJ, 397, 452

Tremonti C. A., et al., 2004, ApJ, 613, 898

Turner M. L., Schaye J., Steidel C. C., Rudie G. C., Strom A. L., 2014, MNRAS, 445, 794

Vaceli M. S., Viegas S. M., Gruenwald R., de Souza R. E., 1997, AJ, 114, 1345

Vazdekis A., Sánchez-Blázquez P., Falcón-Barroso J., Cenarro A. J., Beasley M. A., Cardiel N., Gorgas J., Peletier R. F., 2010, MNRAS, 404, 1639

Veilleux S., Osterbrock D. E., 1987, ApJS, 63, 295

Veilleux S., Kim D. C., Sanders D. B., Mazzarella J. M., Soifer B. T., 1995, ApJS, 98, 171

Veilleux S., et al., 2009, ApJS, 182, 628

Veilleux S., et al., 2013, ApJ, 776, 27

Ventou E., et al., 2017, A&A, 608, A9

Véron-Cetty M. P., Véron P., 2010, A&A, 518, A10

Véron-Cetty M. P., Joly M., Véron P., 2004, A&A, 417, 515

Walter F., et al., 2007, ApJ, 661, 102

Werner M. W., et al., 2004, ApJS, 154, 1

Whitaker K. E., Pope A., Cybulski R., Casey C. M., Popping G., Yun M. S., 2017, ApJ, 850, 208

Williams R. J., Quadri R. F., Franx M., van Dokkum P., Labbé I., 2009, ApJ, 691, 1879

Williams R. J., Quadri R. F., Franx M., 2011, ApJ, 738, L25

Wilson T. J., et al., 2019, ApJ, 874, 18

Winkler H., 1992, MNRAS, 257, 677

Worthey G., 1994, ApJS, 95, 107

Worthey G., Ottaviani D. L., 1997, ApJS, 111, 377

Wright S. A., Larkin J. E., Graham J. R., Ma C.-P., 2010, ApJ, 711, 1291

Wu Y., Charmandaris V., Huang J., Spinoglio L., Tommasin S., 2009, ApJ, 701, 658

Yeh S. C. C., Verdolini S., Krumholz M. R., Matzner C. D., Tielens A. G. G. M., 2013, ApJ, 769, 11

York D. G., et al., 2000, AJ, 120, 1579

Zick T. O., et al., 2018, ApJ, 867, L16

van Dokkum P. G., Brammer G., 2010, ApJ, 718, L73

van de Sande J., et al., 2013, ApJ, 771, 85

van der Wel A., et al., 2014, ApJ, 788, 28